THE UNIVERSITY OF SHEFFIELD

Department of Infection, Immunity & Cardiovascular Disease

Faculty of Medicine, Dentistry & Health

Thesis submitted in partial fulfilment of the requirements for the degree of

DOCTOR OF PHILOSOPHY

Endothelial responses to shear stress differs in healthy aortas and atherosclerotic plaques

By

Ziqi Zhou

Supervised by Prof Paul C Evans and Dr Maria Fragiadaki

October 2022

Abstract

Shear stress is the parallel force generated by blood flow. Endothelial cells (ECs) are capable of sensing shear stress and converting it into biochemical signals. Atherosclerosis initiates preferentially at regions with low shear stress (LSS), whereas regions with high shear stress (HSS) are atheroprotected. However, conflicting data exists regarding the progression of plaque formation, with the suggestions that high or low shear may act as drivers of this process (Samady et al., 2011; Stone et al., 2012).

In this thesis, a new 3-dimensional (3D) imaging technique was developed, including CUBIC (Clear Unobstructed Brain/Body Imaging Cocktails and Computational analysis) clearing and light sheet imaging, coupled with computational fluid dynamics to validate the suitability of eNOS as a marker for identifying HSS ECs in both healthy arteries and plaques. Moreover, single-cell RNA sequencing (scRNA seq) was used to compare the transcriptome profiles of eNOS ^{high} HSS ECs in healthy aortas and plaques. The scRNAseq analysis revealed a significant difference in the transcriptional profile of eNOS ^{high} ECs between healthy aorta and plaques. Further, various mechanosensing genes (including Selp, Nt5e, Klk10, Nox4, Heg1 and Bmp4) exhibited differential expression in eNOS ^{high} ECs from wild type (WT) mice, *ApoE*$^{-/-}$ mice exposed to normal diet (ND) and *ApoE*$^{-/-}$ mice exposed to a high fat diet (HFD). Both *in vivo* and *in vitro* experiments were conducted to validate the scRNAseq findings. These experiments demonstrated that Kallikrein related peptidase 10 (KLK10), guanylate binding protein 3 (GBP3) and CD74 were upregulated by HSS, and their expression was dramatically reduced in plaques. Overall, the results indicate that the transcriptional profiles of EC exposed to HSS differ between healthy arteries and plaques, suggesting that atherosclerosis may affect endothelial mechanosensing mechanisms.

Acknowledgements

I feel very fortunate to have Prof. Paul Evans and Dr. Maria Fragiadaki as my supervisors, they are role models in my long academic journey of PhD. Many thanks to Prof. Paul for his guidance, support and encouragement for my study. As a role model, he always has a passion on science. As a teacher, he makes every effort possible to help me on my project. As an instructor, he always shares the knowledge about atherosclerosis and shear stress to me. Many thanks to Dr. Maria, she always gives me lots of useful advice in the project presentation meetings.

I would also like to thank all the members in Evan's lab, without their help, these three years would be really difficult for me. I would like to thank Dr. Mannekomba R Diagbouga, Dr. Jovana Serbanovic-Canic, Dr. George Bowley, Dr. Hannah Roddie, Dr Celin Souilhol, Dr. Yan Chen and Miss Priscila Hirschfeld, for their help and support in the lab. Special thanks to Dr. Blanca Tardajos Ayllon and Dr. Daniela Pirri for their help and advice. It is extremely helpful for my project. I would also like to thank Dr. Jolanda Wentzel, Dr. Torsten Schenkel and Dr. Junxi Wu for their help and support on the shear stress map project. Also, many thanks to Dr. Mark J Dunning, for his help with the analysis of scRNA-seq data. Finally, I would like to thank Dr. Darren Robinson, Dr. Nick Van Hateren and Dr. Colin Gray, for their help with imaging issues.

Last but not least, I would like to express my gratitude to my family: My mum Yarong Sun and my dad Yiguo Zhou, for their unwavering love and constant encouragement. I am also deeply grateful to my sisters: Dr. Huihui Sun and Yinghui Qi, for their love and support during the challenging times in Covid-19 pandemic. Furthermore, I extend my appreciation to my friends Longdan Hao, Dr. Siyu Tian and my cat, Er Miao, for always being there for me. Lastly, special thanks to my boyfriend Dr. Zijiang Yang, for his love and technique support throughout these years.

List of Publications

Conferences:

1. **Ziqi Zhou**, Nicholas Van-Hateren, Sheila Francis, Maria Fragiadaki, Paul Evans, 2021. Light sheet imaging to analysis the spatial distribution of proteins in atherosclerotic plaques. Heart, Volume 107.
2. **Ziqi Zhou**, Junxi Wu, Jolanda Wentzel, Torsten Schenkel, Mannekomba Diagbouga, Michael Simons, Maria Fragiadaki, Paul Evans, 2022. Endothelial cell profile in responses to high shear stress is different in healthy arteries and plaques. Heart, Volume 108.

Paper:

Celine Souilhol, Blanca Tardajos Ayllon, Xiuying Li, Mannekomba Diagbouga, **Ziqi Zhou**, Lindsay Canham, Hannah Roddie, Daniela Pirri, Emily V Chambers, Mark J Dunning, Mark Ariaans, Jin Li, Yun Fang, Helle F Jørgensen, Michael Simons, Rob Krams, Johannes Waltenberger, Maria Fragiadaki, Victoria Ridger, Sarah De Val, Sheila E. Francis, Timothy JA Chico, Jovana Serbanovic-Canic, Paul C Evans, 2022. JAG1-NOTCH4 mechanosensing drives atherosclerosis. ScienceAdvances. Volume 8, Issue 35.

Table of Contents

Index of Figures

Index of Tables

Abbreviations

APC	Antigen presenting cells
Apo	Apolipoproteins
ASPA	Animal Scientific Procedures Act
$ApoE^{-/-}$	ApoE knockout mice
BMP4	Bone morphogenetic protein 4
CVD	Cardiovascular disease
CTL	Cytotoxic T lymphocytes
CLARITY	Clear Lipid-exchanged Acrylamide Tissue hydrogel
DA	Descending aorta
EC	Endothelial cells
eNOS	Endothelial nitric oxide synthase
ERK5	Extracellular-signal-regulated protein kinase 5
EndMT	Endothelial to mesenchymal transition
EndICLT	Endothelial to immune cell- like phenotypes transition
GS-IVUS	gray scale coronary intravascular ultrasound
GBP3	Guanylate binding protein 3
GO	Gene ontology
HSS	High shear stress
HFD	High fat diet
HCAEC	Human coronary artery endothelial cells
HAEC	Human aortic endothelial cells
HEG1	Heart of glass/ Heart Development Protein With EGF Like Domains 1
HTRA1	High Temperature Requirement A serine peptidase 1
IFNIC	Type 1 interferon inducible cells
IFN	Interferon
IVUS	Coronary intravascular ultrasound
KLF2	Kruppel-like factor 2
KLF4	Kruppel-like factor 4
KLK10	Kallikrein-related peptidase 10

LSS	Low shear stress
LDL	Low-density lipoproteins
$Ldlr^{-/-}$	LDL receptor deficient mice
LOSS	Low oscillatory shear stress
LCA	Left carotid artery
LCCA	Left common carotid artery
MHC II	Major histocompatibility complex II
MKK5	Mitogen-activated protein kinase kinase 5
MEF2	Myocyte enhancer factor
NLRP3	NLR family pyrin domain containing 3
NF- kB	Nuclear factor kappa-B
Nt5e	5'-Nucleotidase
NOX4	NADPH Oxidase 4
NO	Nitric oxide
NES1	Normal epithelial cell specific 1
ND	Normal diet
OA	Oleic Acid
oxLDL	oxidized LDL
OPT	Optical Projection Tomography
OSS	Oscillatory shear stress
PECAM1	Platelet and endothelial cell adhesion molecule 1
PAEC	Porcine aorta endothelial cells
PFA	Paraformaldehyde
PSA	Prostate specific antigen
PI3K	Phosphatidylinositol 3-kinase
ROS	Reactive oxygen species
RCA	Right carotid artery
STAT1	Signal transducer and activator of transcription 1
SMC	Smooth muscle cell
Selp	Selectin P
Sc-RNA seq	Single cell RNA sequencing
t-SNE	t-distributed stochastic neighbour embedding
T_{reg} cells	Regulatory T cells

TGF-β	Transforming growth factor-β
TLR	Toll like receptors
T_H1 cells	T helper 1
T_H2 cells	T helper 2
T_H17 cells	T helper 17
TNF	Tumor necrosis factor
VCAM1	Vascular cell adhesion molecule 1
VSMC	Vascular smooth muscle cells
VEGFR	Vascular endothelial growth factor receptors
VE-cadherin (CDH5)	Vascular endothelial cadherin
WSS	Wall shear stress
WT	Wild type
3D	Three-dimensional
2D	Two-dismensional
3DISCO	3D imaging of solvent-cleared organs

Chapter 1. Introduction

1.1 ATHEROSCLEROSIS AND SHEAR STRESS

1.1.1 Atherosclerosis

Cardiovascular disease (CVD) is a leading cause of mortality, with the American Heart Association reporting approximately 17.9 million deaths in 2015. Moreover, it is projected that CVD-related deaths will rise to over 23.6 million by 2030 (Benjamin et al., 2018). Developing novel treatments for CVD requires understanding of their pathology. Currently available therapies for CVD involve the use of antiplatelet drugs, lipid-lowering drugs and antihypertension medications (Flora & Nayak, 2019). Howerer, these treatments still have limitations including drug resistance, inadequate biological efficacy and low water solubility (Deng et al., 2020).

Atherosclerosis is a leading contributor to CVD and it results from the accumulation of extracellular matrix, lipids and other inflammatory materials within arterial walls (Xu et al., 2019). The development of atherosclerosis involves chronic vascular inflammation (Chen et al., 2020). Here, inflammatory signalling cascades are initiated through the activation of endothelial cells by cytokines, oxidized low-density lipoproteins (LDLs) and other pro-inflammatory substances. As a consequence, the surface of ECs expresses adhesion molecules and chemokines, which co-ordinate the recruitment of inflammation-related cells such as monocytes (Xu et al., 2019). Monocytes transmigrate through the subendothelial intima of blood vessels and differentiate into macrophages. These macrophages accumulate lipids (particularly oxidized LDL), and transform into lipid-laden foam cells, which is the early stage of atherosclerosis known as fatty streaks (Kasikara et al., 2018). Concomitant with a continuous deposition of lipids and extracellular matrix, as well as migration and proliferation of cells, the fatty streaks progress over time and develop into atherosclerotic plaques (Brown et al., 2016). Atherosclerotic plaques can either have a high risk of rupture, known as unstable plaques, or a low risk of rupture, referred to as stable plaques. Unstable plaques are typically charaterized by factors that increase the risk of rupture, such as extensive plaque necrosis, a thin fibrous cap and spotty calcification (Brown et al., 2016). The rupture of unstable plaques is the main reason that causing clinical cardiovascular events such as stroke, unstable angina, myocardial infarction and even sudden heart arrest.

Recent studies have revealed that atherosclerosis is a chronic inflammatory disease that involves a complicated interaction between lipids accumulation, endothelial dysfunction,

SMC migration and proliferation, innate immune response and adaptive immune response (Zălar et al., 2019). In the beginning of atherosclerosis, low shear stress (LSS) triggers endothelial dysfunction through inflammatory pathways. LSS results in the accumulation of NF-κB molecules, leading to an inflammatory response on endothelium (Theofilis et al., 2021). In atherosclerosis, two types of immune responses are involved: innate immune response and adaptive immune response. The innate immune response is rapid but unspecific, generating numerous types of immune cell constitutively (Hansson et al., 2002). In atherosclerosis, the accretion of cholesterol and lipoproteins usually activates the innate immune response. Adhesin molecules like vascular cell adhesion molecule 1 (VCAM1) are upregulated and attract immune cells towards ECs (Mohmmad-Rezaei et al., 2021). As shown in Figure 1.1, monocytes are rare in healthy aortas. However, elevated cholesterol levels in blood induces systemic monocytosis, whereby monocytes differentiate into macrophages (Roy et al., 2022). Macrophages have the ability to take up lipoproteins and transform into foam cells, contributing to the formation of atherosclerotic plaques (Tabas & Lichtman, 2017).

Adaptive immune responses have high specificity (Hansson et al., 2002), at this stage, T cells and dendritic cells govern the immune process by identifying foreign antigens and initiating a immune response with high specificity (Miteva et al., 2018). As shown in Figure 1.2, the unstable plaque is largely composed of foam cells, T cells, dendritic cells and red blood cells (Noonan, 2020). B cells are absent in the intima but present in the adventitia of arteries (Mallat & Binder, 2022). The adaptive immune response consists of T cell subsets, including $CD4^+$ T cells and $CD8^+$ T cells. $CD8^+$ T cells contain cytotoxic T lymphocytes (CTLs), which have the ability to induce inflammation and apoptosis, ultimately leading to plaque instability (Roy et al., 2022). $CD4^+$ T cells are composed of various subsets including regulatory T cells (T_{reg} cells), T helper 1 (T_H1 cells), T helper 2 (T_H2 cells) and T helper 17 (T_H17 cells). T_H1 cells are known to exert pro-atherosclerotic effects by promoting inflammation and vascular smooth muscle cells (VSMC) proliferation. Conversely, T_H2 cells have been found to have anti-atherosclerotic effects, such as dampening VCAM1 expression, increasing collagen formation, increasing production of atheroprotective antibodies and inducing anti-inflammatory macrophages to clear oxidized LDL (oxLDL) (Roy et al., 2022). The functions of T_H17 cells are currently subject to debate, as they have been found to exhibit both atheroprotective and pro-atherosclerotic roles, they can both increase inflammation and improve plaque

stability (Brauner et al., 2018; Nordlohne et al., 2018). T_{reg} cells, on the other hand, are capable of regulating T cells activation by secreting transforming growth factor-β (TGF-β) and interleukin 10 (IL-10) (Roy et al., 2022). T_H1 cells, T_H2 cells, T_H17 cells and CTL all have the ability to release interferon related molecules. The activation and regulation of T cells and adaptive immune responses are controled by dentritic cells, which is dependent on toll-like receptors present in dendritic cells (Roy et al., 2022). An increase in the density and diversity of immune cells, inflammation, and lipid accumulation can result in the destabilisation of plaques. The death of macrophages may lead to the formation of necrotic cores, whereas the existence of leaky neo-vessels can cause intraplaque haemorrhage, these mechanisms can ultimately lead to plaque rupture (Noonan, 2020).

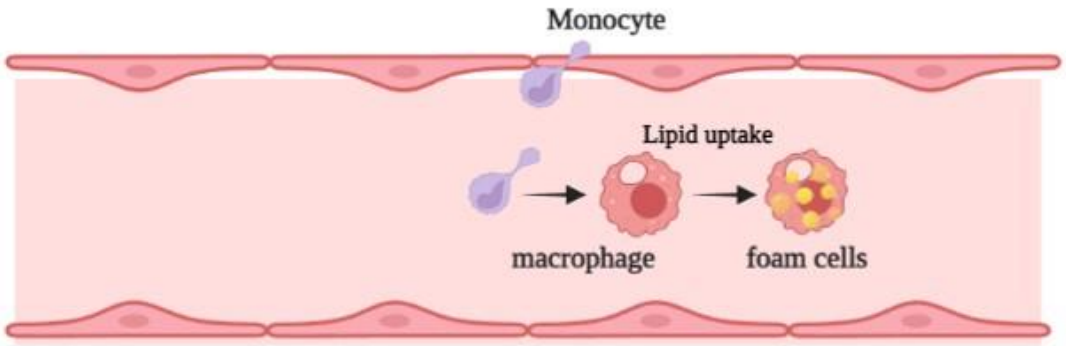

Figure 1. 1 Role of monocytes and macrophages in innate immunity of atherosclerosis. Monocytes can be attracted and differentiate into macrophages, macrophages uptake lipids and become foam cells.

Figure 1. 2 Role of T cells, dendritic cells in adaptive immunity of atherosclerosis. Unstable plaques contain immune cells like T cells, foam cells and dendritic cells. T cells include regulatory T cells (T_{reg} cells), T helper 1 (T_H1 cells), T helper 2 (T_H2 cells), T helper 17 (T_H17 cells) and cytotoxic T lymphocytes (CTLs). T cells that have pro-atherosclerotic roles are labeled with red, T cells that have atheroprotective roles are labeled with green.

1.1.2 Lipids in atherosclerosis

As previously mentioned, lipids play an important role in atherosclerosis, with oxLDL being taken up by macrophages and transforming into foam cells. Recent research suggests that hypercholesterolemia may induce innate immune cells to maintain a long term pro-inflammatory phenotype that can aggravate atherosclerosis (Pirillo et al., 2018). Indeed, lipids accumulation in monocytes can promote their migration and adhesion, resulting in the development of atherosclerosis (Khan et al., 2016). Elevated lipids levels in the bloodstream have also been shown to modify endothelial barrier properties, increase vascular permeability and trigger the accumulation of LDL, leading to plaque formation (Mundi et al., 2018). Additionally, lipid rafts, which are plasma membrane microdomains composed of cholesterol and sphingolipids, play important roles in the inflammation mechanism underlying atherosclerosis. (Lemaire-Ewing et al., 2012). Studies have discovered that lipid rafts are capable of regulating immune cells activation and inflammation by assisting in the formation of immunological synapses that contain toll like receptors (TLR) and T cell receptors (Varshney et al., 2016). Lipid rafts are also participating in antigen presentation by harbouring major histocompatibility complex II (MHCII), thereby enhancing the efficiency of antigen presenting cells (APC)-mediated T cells proliferation and activation (Eren et al., 2006).

Apolipoproteins (Apo) are integral to lipoprotein metabolism, with the Apo family including ApoA, ApoB, ApoC and ApoE. The liver predominantly produces ApoE, with 5-10% produced by macrophages (Linton et al., 1998). Serving as a ligand for lipoprotein receptors, ApoE has crucial roles in clearing very low density lipoproteins and residual chylomicrons, making it essential in inhibiting plaque formation. Consequently, ApoE knockout mice (*ApoE*$^{-/-}$) is widely used in atherosclerosis studies (Zhang et al., 1992), as these mice have higher cholesterol levels and exhibit more severe atherosclerotic plaque formation in a relatively short time compared with other mice models like LDL receptor deficient mice (Ldlr$^{-/-}$) (Nakashima et al., 1994). Notably, *ApoE*$^{-/-}$ mice have been observed to develop atherosclerotic lesions even on a normal diet (Lo Sasso et al., 2016).

1.1.3 Endothelial cell reponses to wall shear stress (WSS) in atherosclerosis

Many risk factors for atherosclerosis have been defined such as age, gender, high cholesterol, hypertension and high blood sugar. Although they act over the whole body, it is observed that plaques have patchy distribution and different blood flow patterns can influence plaque formation. The formation of most plaques occurs in disturbed flow, such

as branches and bends of arteries (Niu et al., 2019). On the other hand, plaques are not usually found in regions exposed to laminar flow (such as regions of straight and unbranching parts of arteries) (Niu et al., 2019). To explain this observation, two major theories have been reported in the literature. The first theory, given as "the shear stress theory", indicates that as pulsatile blood flow through arterial vasculature, various haemodynamic forces can be generated, such as WSS, cyclic strains and hydrostatic pressures (Topper & Gimbrone, 1999). The second theory is described as "the mass transport theory" (or response to influx theory), which indicates the relationship between bioactive substance uptake rate growth and exposure time. Due to disturbed or low blood flow, the contact time between bioactive components of blood (e.g. nitric oxide (NO) and LDL) and ECs is increased. Therefore, the cells time of potential interaction with atheromatous materials is increased, leading to atherogenesis (Back, 1975). This mass transport theory is also supported by experimental results based on rabbit models, as it is shown that tagged macromolecules experience a higher influx at areas prone to atherosclerosis (e.g. disturbed flow areas) (Tarbell, 2003).

The term 'WSS' refers to a parallel frictional force generated by blood flow and exerted on the endothelial surface of blood vessel (Brown et al., 2016). WSS can be described by magnitude and direction, it is often classified into three types: low shear, low and oscillatory shear and high shear. To be precise, in human arteries a WSS of 1-1.5 Pa is considered physiological HSS, and values less than 0.5 Pa are considered LSS (Kwak et al., 2014). WSS is dependent on the geometry of the blood vessel; As shown in Figure 1.3, LSS normally occurs at the inner curvature of arteries and induces early atherosclerosis by increasing ECs inflammation, apoptosis and vascular permeability, whereas HSS usually occurs at the outer curvature of arteries and is atheroprotective by decreasing ECs inflammation, apoptosis and vascular permeability (Chistiakov et al., 2017). ECs under HSS present elongated and aligned appearance and ECs under LSS present a cobblestone appearance. WSS is also sensitive to stenosis, when there is a atherosclerotic plaque in the blood vessel, increased WSS occurs at the entrance to stenosis while decreased shear stress and oscillatory shear stress (OSS) occurs at the outlet of stenosis (Slagger et al., 2005).

To assess shear stress levels in different regions of the aorta, various studies have utilized computational fluid dynamics to generate shear stress maps across different species including human, mice and pigs (Luong et al., 2016; Serbanovic-Canic et al., 2017; Suo

et al., 2007). Additional approaches to investigate the development of atherosclerosis in the carotid artery involve using causation cuff and partial ligation techniques. As shown in Figure 1.4 A, the application of a constrictive cast to the carotid artery results in low oscillatory shear stress (LOSS) downstream of the stenosis and LSS upstream. This model validates the theory that WSS plays a critical role in atherosclerotic plaque formation and vulnerability (Cheng et al., 2006). Partial ligation can also modify shear stress *in vivo*, as shown in Figure 1.4 B, where ligations are applied to left carotid artery (LCA) while the right carotid artery (RCA) is unligated, leading to a significant reduction in shear stress in the LCA (Dunn et al., 2015).

ECs can be affected by WSS via growth of lamellipodia, reorganization of actin filaments, contraction of stress fibre and cell polarity regulation leading to alteration in their migratory behaviour (S. Li et al., 2002). Additionally, WSS can affect the biological processes of ECs in terms of apoptosis and senescence. A Previous study revealed that ECs senescence can be induced by disturbed flow through p53 dependent signalling pathway (Warboys et al., 2014). ECs apoptosis can be induced at bifurcation points through a series of cascades involving an unfolded protein up-regulation response (Civelek et al., 2009), and by various signalling pathways involving activation of p53 and JNK MAP (mitogen activated protein) kinase (Kwak et al., 2014). On the contrary, apoptosis can be suppressed by laminar flow through up-regulation of protective signalling pathways (Kwak et al., 2014).

Endothelial proliferation rates are different between atheroprone regions and protected sites. Atheroprone regions experience excessive cell proliferation, leading to changes in endothelial gap junction communication, which further induces vascular leakiness, cholesterol permeation and expression of other atherogenic molecules (Ebong & Depaola, 2013). In contrast, ECs in protected sites of healthy arteries remain quiescent to maintain vascular integrity and reduce lesion formation (Schober et al., 2014).

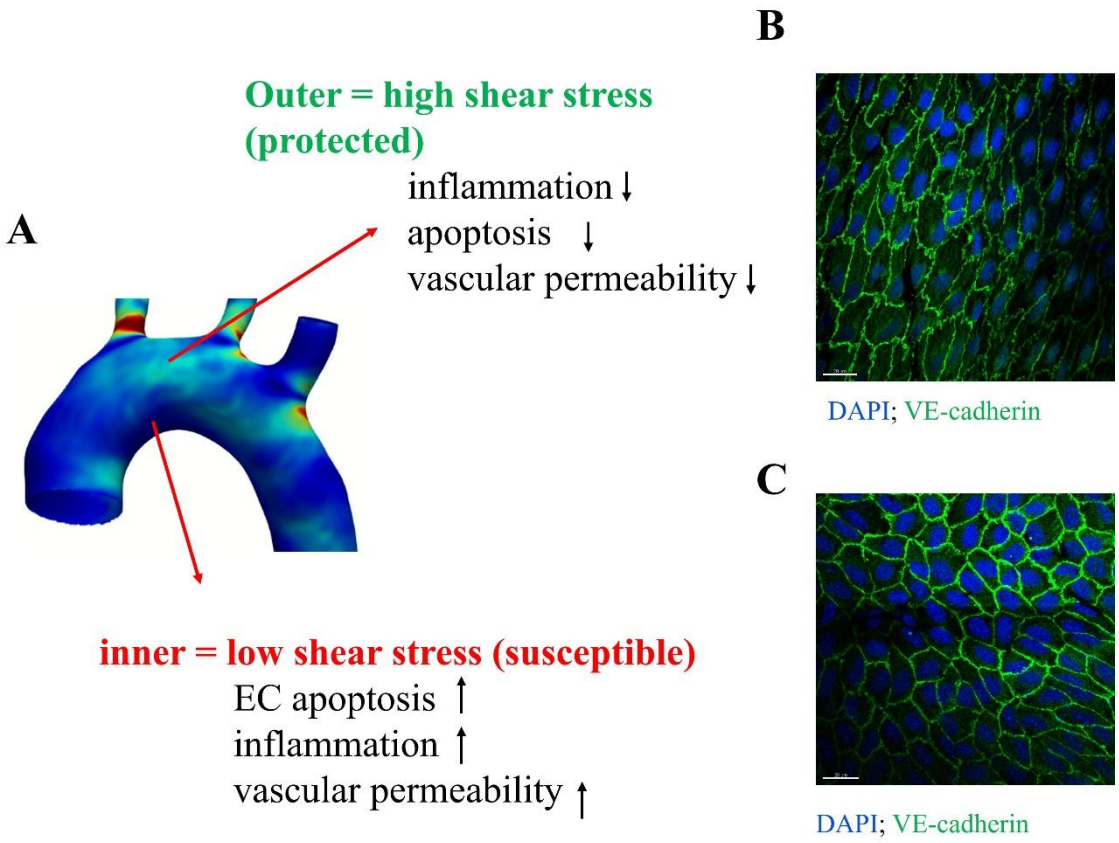

Figure 1. 3 Focal distribution of atherosclerosis in mouse aorta. (A) Atherosclerosis mainly occurs in inner curvature of the mouse aorta (LSS), this atheroprone area is characterized by increased ECs apoptosis, inflammation and vascular permeability. Outer curvature of arteries are atheroprotective (HSS), this region is characterized by decreased ECs apoptosis, inflammation and vascular permeability. (B) ECs under HSS are elongated and aligned. (C) ECs from LSS present a cobblestone appearance. Nuclei are stained with DAPI (blue), and VE-cadherin (CDH5) (green) is endothelial cell marker.

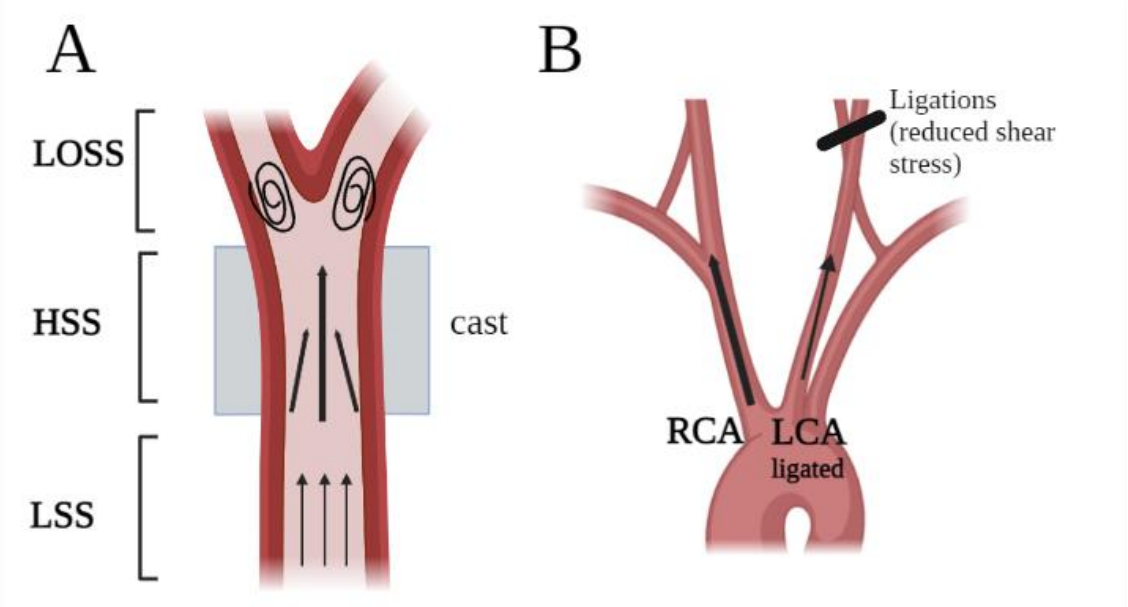

Figure 1. 4 Representative images for constrictive cuff (A) and partial ligation (B) of mouse carotid arteries. (A) Constrictive cast is applied to the carotid, leading to HSS in the cast, LSS in the upstream of the stenosis and LOSS in the downstream of the stenosis. (B) Partial ligation is applied to left carotid artery (LCA), ligations reduce the shear stress in LCA compared with right carotid artery (RCA).

1.1.4 Controversial observations of the role of shear stress in atherosclerosis progression

It is widely acknowledged that WSS controls EC behaviour and is a regulator of early atherogenesis. However, the role of WSS in plaque growth and plaque rupture remains controversial. It is well-accepted that atherosclerosis initiation can be induced by LSS at bends and branches, but a much debated question is the effects of WSS in disease progression, with conflicting data and the effects of high, low and oscillatory WSS (Koskinas et al., 2010). Additional studies of shear stress and plaque progression also report that low and multidirectional WSS induce plaque initiation and plaque progression (Hoogendoorn et al., 2020).These different conclusions are difficult to reconcile, and they could be caused at least partly by technical differences, such as analysis methods and imaging modalities. Other possible contributors include the patient demographics which vary between studies and the time between measurements.

Table 1.1 provides a summary of the findings from multiple studies that have investigated the association between WSS and plaque phenotype. Although these studies did not provide any information on the plaque size, the authors demonstrated that the plaques had features that make them more susceptible to rupture. These features include large plaque size and necrotic core, thin fibrous cap (<65μm) with many macrophages and few smooth muscle cells, angiogenesis, intraplaque hemorrhage and spotty calcification (Samady et al., 2011; Stone et al., 2012).

Ref No.	Study size	Time of follow up (months)	Imaging methods	Results
(Stone et al., 2003)	8 patients (12 arteries)	6	Biplane coronary Angiography and GS-IVUS	LSS—progressive atherosclerosis
(Stone et al., 2007)	13 patients (47 subsegments)	8±2	Biplane coronary Angiography and GS-IVUS	LSS—constrictive, expansive remodelling
(Stone et al., 2012)	506 patients (1,341 arteries)	6-10	Angiography and GS-IVUS	LSS— plaque enlargement, lumen narrowing
(Stone et al., 2018)	697 patients	36-48	3-vessel radiofrequency (RF)-IVUS	LSS— high risk plaque
(Samady et al., 2011)	20 patients Segments (n=2249)	6	Angiography, VH-IVUS and Computational fluid dynamics	HSS—high-risk plaque
(Fukumoto et al., 2008)	20 patients	N/A	3-dimensional intravascular ultra- sound (IVUS), color mapping	HSS — plaque rupture
(Timmins et al., 2017)	20 patients Sectors (n=14235)	6	Angiography, VH-IVUS and Computational fluid dynamics	Low and oscillatory — high-risk plaque
(Koskinas et al., 2010)	5 pigs(diabetic) Segments(n=304)	9	Intravascular ultrasound and Computational fluid dynamics	LSS — initial and progression of plaque

Table 1. 1 description of effects of WSS in plaque rupture. Detailed analysis is shown in following sections :1.1.4.1 to 1.1.4.4.

1.1.4.1 Correlation of LSS with plaque instability

Data from several studies of the same group suggests that LSS is an inducer of plaque rupture (Stone et al., 2003, 2007, 2012). In 2003, the Stone group used biplane coronary angiography and coronary intravascular ultrasound (IVUS) to reconstruct three-dimensional (3D) arteries for computational fluid dynamic assessment of WSS. After 6 months of longitudinal study, twelve arteries in 8 patients were analyzed. It was observed that low WSS was associated with outward remodeling and progressive atherosclerosis (Stone et al., 2003). However, the major drawback of this research is the small study size (twelve arteries, six normal arteries and six arteries with stents). Therefore, firm conclusions cannot be extracted from this study. In 2007, similar methods were used to reconstruct 3D artery geometries in 13 patients. After ten months, it was concluded that LSS was associated with plaque progression and development of high-risk plaque through either expansive remodeling or constrictive remodeling (Stone et al., 2007). This study is still restricted by a small number of patients and only two study time points. Both studies from the Stone group analyzed arteries with lumen obstruction less than 50% while coronary arteries with more obstruction were not investigated.

This group then followed up with a study on a larger number of patients using angiography and gray scale IVUS (GS-IVUS) to rebuild the luminal geometry (Stone et al., 2012). The research suggested that LSS was associated with plaque progression (lumen narrowing and increased plaque area). Although the study number was relatively large (1,341 arteries from 506 patients), it is limited by lack of symptomatic clinical events and therefore a definitive link between WSS and plaque rupture could not be established. Furthermore, since this study uses GS-IVUS rather than radiofrequency IVUS (RF-IVUS), the accuracy of histological correlation could be questionable (Stone et al., 2012).

Another study from Stone's group showing that LSS is associated with high-risk plaque (e.g. thin-cap, lumen narrowing and large plaque burden) (Stone et al., 2018). They studied 697 patients with high-risk acute coronary syndrome and used 3-vessel RF-IVUS (Stone et al., 2018). They followed up 3-4 years, the limitations of this study are only 59% cases were suitable for LSS calculation, which probably resulted in selection bias, sampling error and small sample size (Stone et al., 2018).

1.1.4.2 Correlation of HSS with plaque instability

In contrast to Stone, Samady argued that HSS was the driver of plaque rupture. Virtual histology intravascular ultrasound (VH-IVUS) and computational fluid dynamics were used to reconstruct coronary arteries and calculate WSS (Samady et al., 2011). The patient number was 20 and they were followed up at 6 months (Samady et al., 2011). This longitudinal study found that regions exposed to HSS were associated with the subsequent development of plaques with features of instability (e.g. fibrous tissue regression and increased necrotic core)(Samady et al., 2011). The drawback of this research is that only two time points were analyzed.

Similarly, Fukumoto et al. (2008) also suggested that plaque rupture is driven by localised HSS. Colour mapping was used to demonstrate the WSS, streamlines and blood pressure in reconstructed coronary arteries. 20 patients were selected to build the *in vivo* 3D colour maps. It is the first study to demonstrate localization of HSS on each plaque surface. Most of rupture sites are matched with increased shear stress sites, indicating that HSS stress could trigger plaque rupture (Fukumoto et al., 2008).

It is hard to reconcile these different observations due to technical differences, such as different imaging methods and patient demographics. For example, The stone group studied patients with acute coronary syndrome (unstable angina and myocardial infarction) whereas the Samady group focused on patients with stable angina (Samady et al., 2011; Stone et al., 2018).

1.1.4.3 Correlation of oscillatory shear with plaque instability

Recently, there has been renewed interest in low and oscillatory WSS. Timmins et al. (2017) found evidence that oscillatory shear is also important. In a six-months follow up study of 20 patients, low and oscillatory WSS were found to be associated with regression of fibrous tissue and progression of necrotic core (Timmins et al., 2017). The results suggest that low and oscillatory WSS could lead to the development of high-risk plaque (increasing necrotic core and decreasing fibrous tissue). However, this study is still limited by the small study size and lack of clinical events.

1.1.4.4 Summary

In summary, pre-clinical studies have shown conclusively that WSS is a regulator of plaque progression and the generation of stable or unstable phenotypes. There is agreement that LSS is associated with plaque growth, clinical studies have produced conflicting data over shear stress and instability, because both LSS and HSS have been

associated with the development of plaques with features of instability. There are several possible explanations of these seemingly contradictory observations. From a statistical perspective, of the eight studies mentioned in this thesis, several were limited by small study sizes which may reduce the reliability of observations. In addition, the majority of studies use intravascular ultrasound (IVUS) and computational fluid dynamics. These methods are particularly useful to generate 3D reconstructions of artery and calculate WSS. However, the accuracy of IVUS to detect plaque composition is still questionable (Samady et al., 2011). Moreover, it is hard to determine whether atherosclerosis or other unrelated diseases (e.g. high blood pressure) is the major cause of intimal-medial thickening (Peiffer et al., 2013). A limitation of computational fluid dynamics analysis is lack of standard methods for computational modelling and variation in the use of different metrics of WSS (Peiffer et al., 2013).

Finally, it is plausible that both HSS or LSS conditions can promote plaque instability and therefore that both arguments in the literature are correct. Consistent with this, *in vitro* studies found that cultured EC can be activated by WSS conditions that are either higher or lower than their WSS set-point (Baeyens et al., 2015). In addition, individual plaques contain both HSS and LSS regions which could contain dysfunctional endothelium (Wang et al., 2016).

1.1.5 Light-sheet for imaging cardiovascular system

To image sample in a global level, several tissue clearing techniques were developed in terms of CLARITY (Clear Lipid-exchanged Acrylamide Tissue hydrogel), CUBIC (Clear, Unobstructed and Brain/Body Imaging Cocktails and Computational analysis) and 3DISCO (3D imaging of solvent-cleared organs) (Susaki et al., 2015). While these methods all achieved tissue-clearing, CLARITY has the limitation of being technically challenging, and 3DISCO could lead to signal quenching (Susaki et al., 2015). By contrast, the CUBIC protocol is simple and efficient, clearing method followed by light sheet imaging enables analysis the global level of sample (Susaki et al., 2015). Previous study has evaluated the application of cleared samples followed by light sheet imaging (Ding et al., 2018). This approach offers several benefits, including the ability to expand the field of view, overcome limitation of two dimension and enable high resolution of entire vasculature (Ding et al., 2018).

1.2 SIGNALLING RESPONSES TO SHEAR STRESS

1.2.1 Mechanosensors in atherosclerosis

Vascular ECs sense various shear stress parameters (e.g. HSS, LSS and OSS) through mechanosensors. Mechanosensors can be classified into various types including connexins, integrins, receptor tyrosine kinases like vascular endothelial growth factor receptors (VEGFR), caveolae, adhesion molecules like platelet and endothelial cell adhesion molecule 1 (PECAM1) and vascular endothelial cadherin (VE-cadherin) as well as ion channels (Figure 1. 5) (Kwak et al., 2014). Mechanosensors transform the mechanical information to signalling pathways and influences EC behaviours, such as proliferation, migration, inflammation and apoptosis (Figure 1. 5) (Kwak et al., 2014).

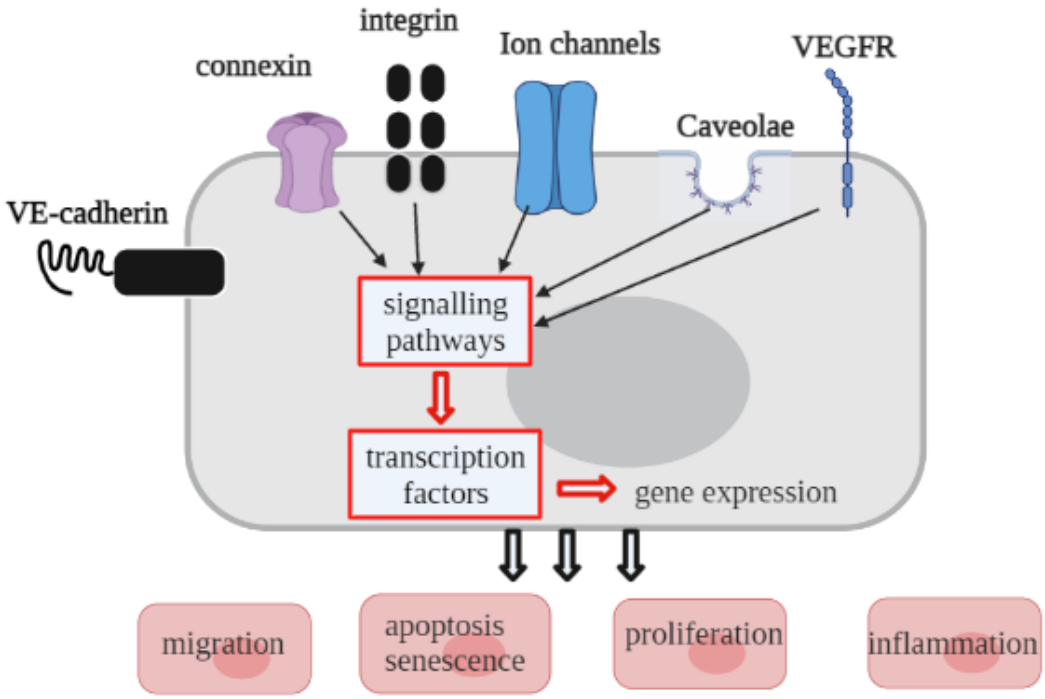

Figure 1. 5 Mechanosensors in vascular endothelium. Shear stress can be sensed by mechanoreceptors (such as VE-cadherin (CDH5), connexin, integrin, ion channels, VEGFR and caveolae at the apical surface) on ECs membrane. Then receptors convert mechanical force into downstream signalling through activating signalling pathways and transcription factors. In the end, signalling pathways lead to ECs migration, inflammation, apoptosis, proliferation and senescence.

1.2.2 HSS markers: Klf2, Klf4, eNOS

Endothelial nitric oxide synthase (eNOS) is induced and activated by HSS (Cheng et al., 2005). Vascular endothelial growth factor receptor (VEGF) can be activated by HSS and phosphorylates eNOS at Ser1177, which leads to the production of NO by eNOS (Dimmeler et al., 1999). NO acts on vascular smooth muscle cells, promoting vasodilation and maintaining ECs homeostasis (Chistiakov et al., 2017). This vasodilatory effect of eNOS-derived NO is cardioprotective, however, the protective role of eNOS is altered in atheroscleorsis. In atherosclerosis, eNOS uncoupling causes it to produce superoxide instead of NO, which ultimately result in endothelial dysfunction (Y. M. Yang et al., 2009).

Kruppel-like factor 2 (KLF2) and Kruppel-like factor 4 (KLF4) are also identified as HSS induced genes by several studies (Lalitha Nayak, Zhiyong Lin and Mukesh K. Jain 2011). KLFs are expressed in both in EC and VSMC. In EC, KLF2 and KLF4 are capable of protecting ECs from inflammation, migration, and thrombus formation (Jain, 2018). In VSMC, KLF4 has essential functions in repressing proliferation and inducing dedifferentiation (Jain, 2018).

1.2.3 KLK10

The Kallikrein-related peptidase 10 (KLK10) was identified as a normal epithelial cell specific 1 (NES1) protein in 1996 (Long, 1996). Due to the fact that NES1 is localized on the same locus as most of the kallikreins family, which is on chromosome 19q13.3-q13.4, the NES1 gene was subsequently named KLK10 (Luo et al., 1998). KLK family members contain 15 serine proteases, thus, KLKs are involved in a wide range of processes including cancer, inflammatory diseases (Sotiropoulou & Pampalakis, 2012), and hypertension (Iwai et al., 2005).

The KLK family are used as biomarkers of various cancer types (Ahn et al., 2008). KLK3 (also named prostate specific antigen, PSA) is the most wildly used in diagnosis of prostate cancer (Lilja et al., 2008). It is also predicted that KLK10 has tumour suppressive function in several cancer types including breast cancer, liver cancer, and esophageal cancer (L. Li et al., 2015).

Recently, Hanjoong Jo's group have found that KLK10 is a shear stress regulated endothelial protein and can protect ECs from atherosclerosis by inhibiting nuclear factor kappa-B (NF-κB) inflammatory pathway (Williams et al., 2022). They showed that

KLK10 has antiinflammatory and atheroprotective roles both *in vivo* and *in vitro,* which revealed that KLK10 may be a therapeutic target to treat atherosclerosis in the future (Williams et al., 2022).

1.3 Project hypothesis

It is hypothesized that rupture-prone plaque phenotypes are promoted by localized regions of high and low shear, which can cause altered EC physiology. It is also hypothesized that endothelial responses to WSS may vary between healthy arteries and plaques. LSS has been found to promote the initiation of atherosclerosis by triggering EC activation, proliferation, senescence and apoptosis. Investigating the role of HSS in the ECs of healthy aortas and plaques is therefore important. To achieve this, a method needs to be developed for isolating HSS ECs from plaques and then comparing them to HSS endothelium from healthy aortas (Figure 1. 6).

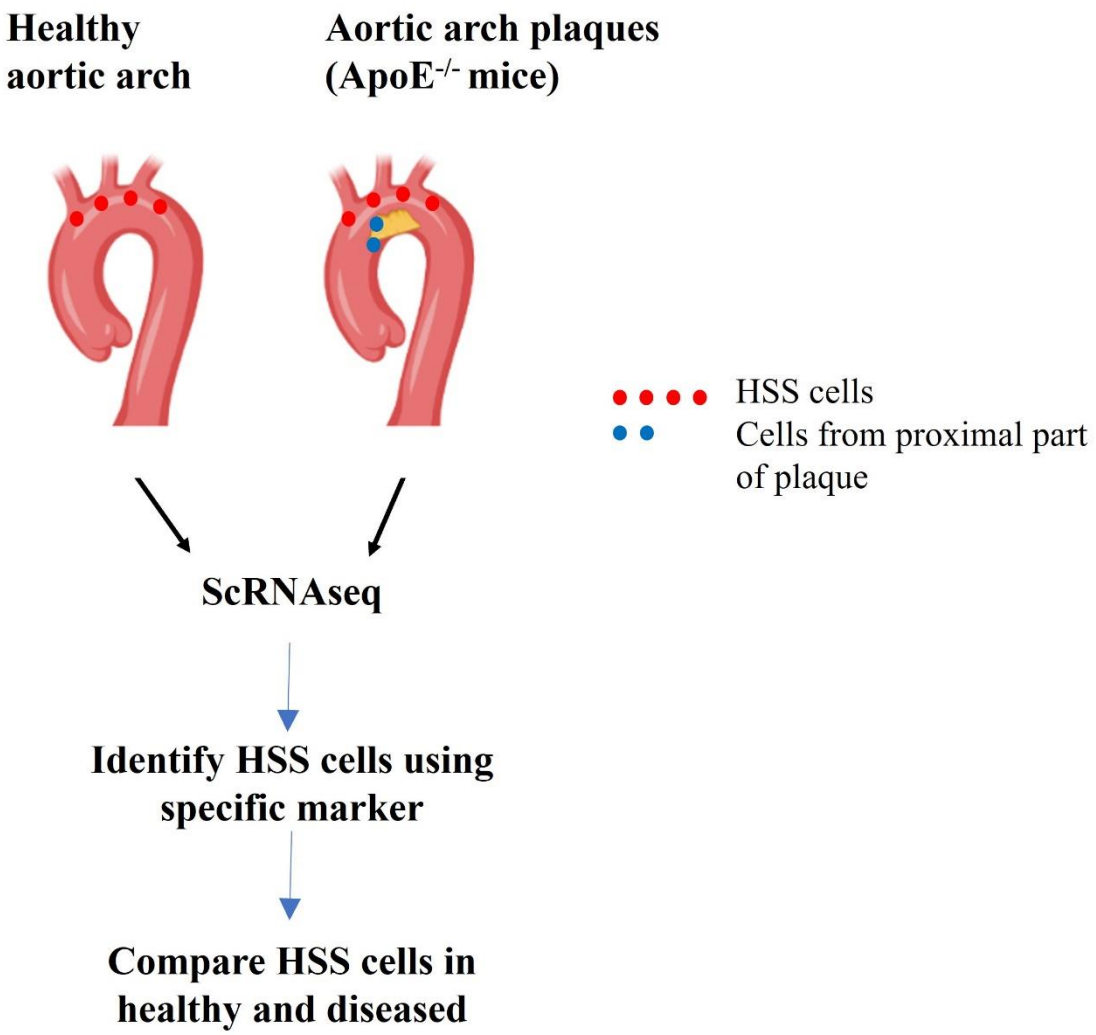

Figure 1. 6 Three steps to perform transcriptome analysis of high shear endothelium in healthy and diseased aorta. Both healthy aortic arch and diseased arch were used to perform scRNAseq, a specific HSS marker was used to identify HSS cells and perform a transcriptome analysis of high shear endothelium in heathy aorta versus diseased aorta.

1.4 Project aims

The aims of this project are to:

1. Map shear stress in healthy and diseased aortas
2. Find a HSS marker in healthy and diseased aortas
3. Use the HSS marker to perform scRNAseq and transcriptome analysis of HSS endothelium in healthy versus diseased aortas
4. Validate the transcriptome analysis by quantifying molecules at the protein level

Chapter2. Materials and Methods

2.1 Reagents

Reagent	Vendor	Cat-Number
96- well plate	Greiner CELLSTAR®	655180
Bovine Serum Albumin	Sigma- Aldrich	A9647-50G
Goat serum	Sigma- Aldrich	G6767
Phosphate Buffered Saline (PBS)	Sigma- Aldrich	P4417
TO-PRO-3 Iodide	Life Technologies	T3605
Pro-Long Gold antifade reagent	Life Technologies	P36930
Concavity slide	GMBH & Co. KG	475505
Glass capillaries	GMBH & Co. KG	701910
DAB Substrate Kit	Cell Signaling Technology	8059
N,N,N',N'-Tetrakis (2-hy droxypropyl)ethylenedia mine (Quadrol)	Sigma	122262-1L
2,2',2''-Nitrilotriethanol (triethanolamine)	Sigma	90278-100ML
Urea	Sigma	15604-1KG
Triton X-100	Sigma	X100-500ML
Sucrose	Fisher	10386100
Mineral oil (RI=1.467)	Sigma	M8410-500ML

2.2 Antibodies

Reagent	Vendor	Cat-Number
9EG7	BD Biosciences	553715
CDH5 (VE-cadherin)	BD pharmingen	555289
STAT1	Thermo Fisher	MA5-15129
CD74	abcam	ab245692
GBP3	Antibodies-online	ABIN6341723
KLK10	Invitrogen	PA5-109887
HEG1	Biossusa	Bs-15449R
NOX4	Novusbio	NB110-58851
eNOS (D9A5L)	Cell Signaling Technology	32027S
Anti-mouse CD31	Dianova	DIA-310
Rabbit IgG	abcam	ab37415
AlexaFlour™488 (donkey anti- rat)	Invitrogen	A21208
AlexaFlour™ 488 (anti-mouse CD31)	Bio Legend	102514
AlexaFlour™ 568 (goat anti- rabbit)	Invitrogen	A11036

2.3 Mice

All animal experiments conducted in this study were performed under the guidelines of the Animal (Scientific Procedures) Act 1986 (ASPA). The study utilized three types of mice: C57BL/6 wild type (WT) mice (N=20), *ApoE*$^{-/-}$ normal diet (ND) mice (N=15;) and *ApoE*$^{-/-}$ high fat diet (HFD) mice (N=15). For light-sheet imaging, *ApoE*$^{-/-}$ HFD mice were given the diet for 16 weeks, while for en face staining, *ApoE*$^{-/-}$ HFD mice were given the diet for 6-8 weeks.

2.4 Immunofluorescent staining

2.4.1 en face staining and confocal microscopy

The Opened aortic segments were dissected and placed in a 96-well plate (Greiner CELLSTAR®). To permeabilize the aortic tissue and block unspecific binding, aortic tissue was incubated in 20% (v/v) goat serum (Sigma-Aldrich) in 0.5% triton-X100 (Sigma) 4 °C overnight. After this step, tissue was washed with PBS three times at 5 minutes' intervals, 100 µl per well.

To stain the segments with primary antibodies. All primary antibodies were diluted in 5% (w/v) Bovine Serum Albumin (BSA, Sigma) in 0.1% PBST. According to the species of the primary antibodies on datasheet, Isotype IgG was used at same concentration of primary antibody for controlling unspecific binding. All aortic segments were incubated with primary antibody (100 µl per well) at 4 °C overnight. Washed with PBS three times at 5 minutes' intervals.

To stain segments with secondary antibodies, goat anti rabbit AlexaFlour™ 568 (Invitrogen) was diluted at 1:200 in 5% (w/v) BSA (Sigma) in 0.1% PBST. The aortic tissue was incubated for 8 hours at 4 °C in cold-room. Segments were washed with PBS (Sigma) three times at 5 minutes' intervals. To identify endothelial cells, segments were incubated with 100 µl of anti-mouse CD31 AlexaFlour™ 488 (Bio Legend), diluted at 1:100 in 5% (w/v) BSA (Sigma) in 0.1% PBST. Segments were incubated overnight at 4 °C. Next, segments were washes with PBS (Sigma) three times at 5 minutes' intervals. To mark cell nucleus, segments were stained with TOPRO-3 Iodide (Life Technologies) and diluted in a final concentration of 1:300 in PBS.

To mount the sample, aortic segments were washes with PBS and mounted with 15 µl Prolong® gold anti-fade reagent (Life Technologies) on a microscopy slide. In detail, the sample was placed endothelial side down onto the coverslip and fixed with nail varnish. To flatten the aortic tissue, slides were pressed with a 1 Kg weight overnight at 4 °C. Immunofluorescent staining was visualized with the use of confocal microscope (Zeiss LSM 510). A 488nm laser can detect excitation of fluorescence to view Alexa Fluor 488. A 543nm laser can detect excitation of fluorescence to view Alexa Fluor 568. A 633nm laser can detect excitation of fluorescence to view TO-PRO-3 nuclear stain. Oil lens at 63X magnification (Plan-Apochromat 63x/1.4 Oil) was used to image samples. Fiji software was used to quantify the fluorescence intensity mean.

2.4.2 en face staining and Airy-scan microscopy

Dissected aortic arch was opened before staining. To mark the HSS region, spring scissors were used to snip off the brachiocephalic artery and cut a 'V' shape into the aortic segments. Then arch was cut along the outer curvature. En face staining process was same as shown in 2.4.1, open aortic arch was mounted using 2% agarose gel. Airy-scan confocal microscope (Zeiss LSM 880) with 10X magnification (EC Plan-Neofluar 10x/0.30 M27) lens were used to image sample. Z-stack and tiled image were

applied to aorta and 405nm laser (DAPI), 488nm laser (Alexa Fluor 488) and 561nm laser (Alexa Fluor 568) were used to image. Fiji software was used to quantify the fluorescence intensity mean.

2.4.3 en face staining of cleared tissues and light-sheet microscopy (adapted from Susaki 2015)

To prepare CUBIC 1 solution, 25% urea (Sigma) was combined with 25% Quadrol (Sigma) in distilled water by using a hot stirrer. After all components were completely dissolved, 15% Triton X-100 (Sigma) was added and mixed by stirrer at room temperature. The final step was to degas the solution about 30 minutes by vacuum desiccator.

To prepare the CUBIC 2 solution, urea (25%, Sigma) and sucrose (50%, Fisher) were added in distilled water and mixed with microwave using a hot stirrer. After all components were completely dissolved, the mixture was cooled to room temperature and added triethanolamine (10%, Sigma). The solution was mixed with stirrer and degassed about 30 minutes.

For optimal clearing of aorta using CUBIC, the protocol was adapted from (Susaki et al., 2015). Arch was immersed in 1 ml of 50:50 water: CUBIC-1 at room temperature for 2-3 hours. Subsequently, 50:50-diluted CUBIC-1 was discarded immediately and added 1 ml of CUBIC-1 (kept in darkroom at room temperature overnight). To stop the clearing procedure, placed arch in a 96-well plate (Greiner CELLSTAR®) and washed arch three times with PBS at 1 hour's intervals in the dark at room temperature. Thereafter, arch was immersed in 1 ml of 50:50 PBS-diluted CUBIC-2 in darkroom at room temperature until it was denser than the solution (i.e. arch sunk to the bottom). The arch was then immersed in 1 ml of CUBIC-2 in darkroom at room temperature overnight. After finishing the clearing step, en face staining was performed as shown in 2.4.1, the aorta was mounted with 2% agarose gel in glass capillary. Samples were imaged through light-sheet microscopy (Zeiss Light-sheet Z.1). 5X magnification (EC Plan-Neofluar 5x/0.16) was used to view the sample, 405 laser (DAPI), 488 laser (Alexa Fluor 488) and 561 laser (Alexa Fluor 568) were used to image aortas. Imaris (9.0.1) software was used to view the data and calculate fluorescence intensity mean.

2.5 Optical Projection Tomography (OPT) imaging and computational fluid dynamics

The fixed aortas were performed CUBIC clearing and lightsheet imaging first, then the same aortas were shipped to Junxi Wu's lab (University of Edinburgh) to perform the OPT imaging (Kirkby et al., 2015). The aorta was embedded in 1.5% low melting agarose, and then dehydrated in 100% methanol overnight. The aorta then was cleared overnight using benzyl alcohol and benzyl benzoate (mixture ratio 1:2 volume/volume), then scanned using OPT imaging, the resolution was set at 1024 x 1024. The voxel size is about 200 μm. The aorta was scanned using GFP1 emission channel.

Murine aorta geometrics were reconstructed using OPT images imported into ITK-snap software and segmented automatically using region competition snakes, then manual adjustment of the segmentation.

Computational fluid dynamics was performed by Jolanda Wentzel's group (Erasmus MC, Rotterdam, the Netherlands) and all equations used in this project were from (Luong et al., 2016). After segmentation in ITK-snap software, the geometry then was imported into 3D slicer to smooth. Flow extensions were added to the geometry using VMTK. The inlet was extended 4 times the radius to ensure a smooth inlet profile. The outlets were extended 3 times the radius to exclude upstream effects of the imposed boundary conditions. Then the geometry was imported into ANSYS ICEM (ANSYS 2021 R1) to generate a mesh. Mesh size of healthy aorta: typical cell size: 0.05 mm, resulting in a mesh with 477858 elements/142384 nodes. Mesh size of diseased aorta: typical cell size: 0.05 mm, resulting in a mesh with 584199 elements/188061 nodes. After meshing, computational fluid dynamic simulation was performed. The flow was modelled as laminar. Inlet profile was performed with steady state simulation with a velocity of 0.26 m/s as a typical flow for mouse aorta, the outlet profile using a flow split of 70%, 16%, 8% and 6% for descending aorta, brachiocephalic artery, left common carotid artery and subclavian artery, respectively (Luong et al., 2016).

2.6 Registration of OPT segmentation and eNOS segmentation

To generate the segmentation for diseased aorta, Jolanda Wentzel's group (Erasmus MC, Rotterdam, the Netherlands) placed 7 landmarks in OPT segmentation and eNOS segmentation and register two segmentations together. The tool for registration is Fiducial

Registration (3D slicer) (Figure 2. 1). For quantification of 3D lightsheet imaging aorta, image was processed in Imaris. To measure the fluorescence intensity, surfaces were created based on anatomy and was marked on the endothelial surface. Each individual slice was used to build the region of interest. Fluorescence intensity mean was quantified using the ‘statistic’ function of the Imaris software. Quantification of 3D lightsheet imaging data was also validated in computation fluid dynamics by Wentzel’s group.

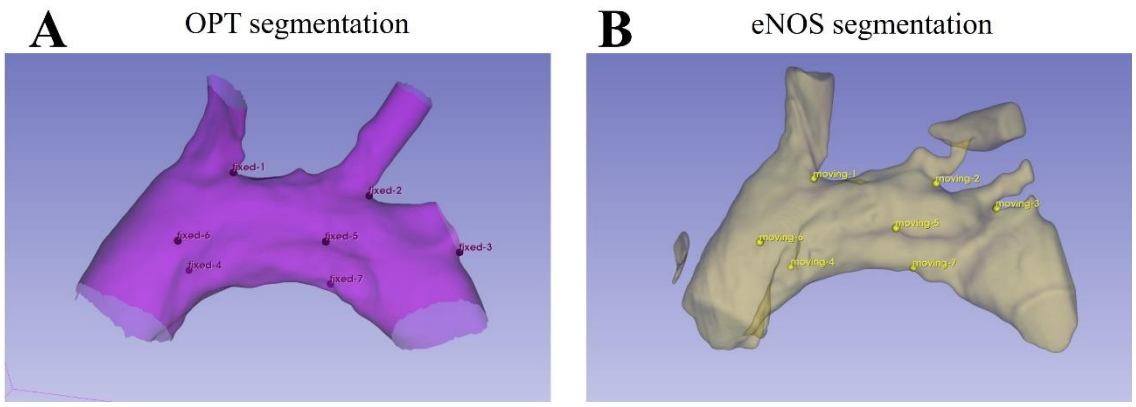

Figure 2. 1 Registration of OPT segmentation (A) and eNOS segmentation (B). 7 landmarks were placed to register two segmentations.

2.7 Generating a 2D shear stress map

The 2D shear stress maps were generated from the 3D shear stress maps. 3D vessel surfaces were cut open and laid flat along the longitudinal axis (Figure 2. 2). As shown in Figure 2. 2, information from 3D map was patched into regions and an average value of the quantity of interest is computed for each region in 2D maps.

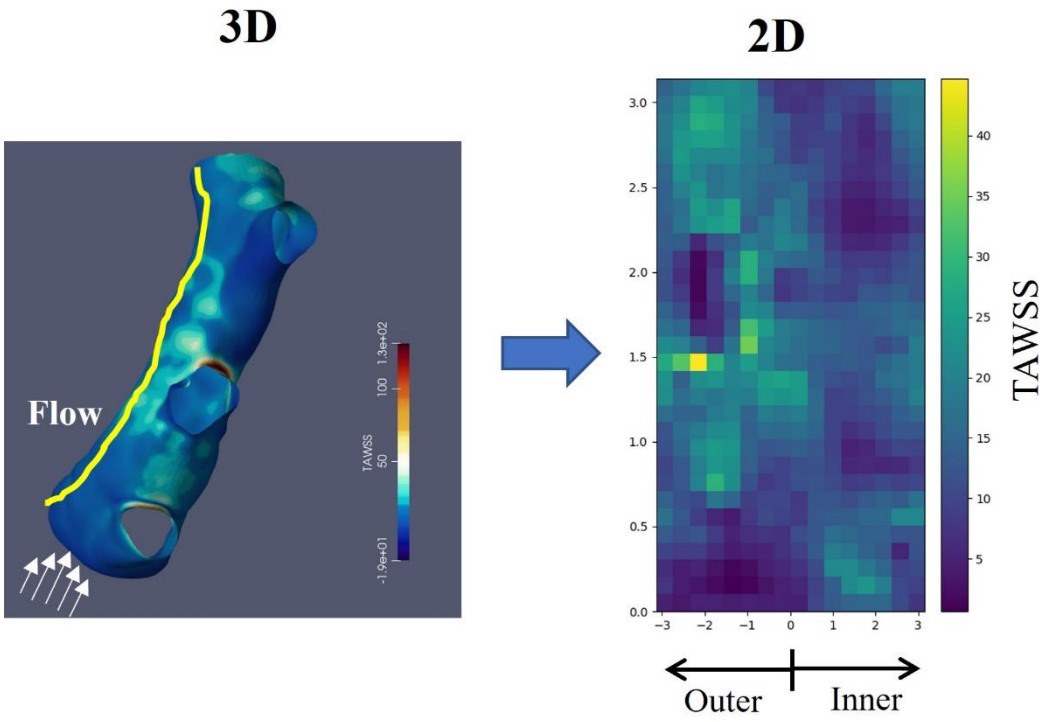

Figure 2. 2 2D shear stress map was generated from 3D shear stress map. 3D vessel surfaces were cut open and laid flat along the longitudinal axis (yellow line).

2.8 Single cell data analysis

The Aortic ECs were analysed by sc-RNAseq by enzymatic digestion, sorting of $CD31^+$ $CD45^-$ cells. Two datasets were integrated together and used in this study. Data from Mike Simon's group (Yale University, USA) was generated from two groups of mice: *ApoE*$^{-/-}$ ND mice and *ApoE*$^{-/-}$ HFD mice (Chen et al., 2019). Data from our group generated by Dr Blanca Tardajos-Ayllon was performed with wildtype (WT) mice. Sort-seq protocol was adapted from (Chen et al., 2019). The whole aorta from WT mice, *ApoE*$^{-/-}$ ND mice and *ApoE*$^{-/-}$ HFD mice were dissected and rinsed in PBS on ice. The aorta was cut into small fragments and digested with enzyme mixture (collagenase, hyaluronidase, DNase I, collagenase type I and elastase) for 1h at 37^{o}C. Cell suspensions were filtered through 40µm cell strainer. FACS staining used Trustain FcX^{TM} (anti-mouse CD16/32) to block unspecific binding of Fc receptors, CD31-AF488, CD45-APC and TOPRO3 (detect dead cells) antibodies. FACS machine sorted $CD31^+$ $CD45^-$ $TOPRO3^-$ cells. Two scRNA-seq count data from both studies were loaded into R (version 4.1) and created into separate R/Seurat (Version 4.1.0) objects. Each dataset was filtered to remove cells that have unique feature counts <200 and that have <5% mitochondrial counts. Only the *ApoE*$^{-/-}$ ND, *ApoE*$^{-/-}$ HFD and WT samples were kept and normalised. Following this, the data were integrated within Seurat to identify or 'anchor' cell populations that are present across the different datasets and reduce any batch differences. Dimensional reduction of the data was carried out using PCA and UMAP and then clustering of the cells was calculated by working out distance metrics of nearest neighbours using the Louvain algorithm. The merged data was analysed using BBrowser 2.10.10.

2.9 Endothelial cells

2.8.1 Isolation of Porcine Aortic Endothelial Cells (PAEC) from porcine aortas

Porcine aorta was placed face down onto the collagenase for 10 minutes digestion (collagenase IV 1mg/mL suspended in M199 (Gibco)). After digestion, using a scalpel to gently scrap the endothelium of porcine aorta, there were two regions to be scraped: Outer curvature (HSS) of porcine aorta and inner curvature (LSS) of porcine aorta. Then the scraped tissue was placed in a 1.5mL Eppendorf tube and centrifuged to get PAECs.

2.8.2 Culture of Human Coronary Artery Endothelial Cells (HCAEC)

HCAECs were purchased from Promocell (Heidelberg, Germany). Cells were cultured using endothelial growth medium MV2. The medium was placed in incubator at 37 ^{o}C and 5% CO_2. After 1 or 2 days, cells were split in a ratio 1:3 or 1:4.

2.8.3 Culture of Human Aortic Endothelial cells (HAEC)

HAECs were purchased from Promocell (Heidelberg, Germany). Cells culture method was same as above-mentioned.

2.10 Flow systems

2.9.1 Orbital shaker system

ECs were grown in 6-well plates and placed onto the orbital shaker system in the incubator at 37^{o}C and 5% CO_2 for 72h (Warboys et al., 2019). The orbital shaker was set at 210rpm. As shown in Figure 2. 3, periphery cells were under HSS and centre cells were under LSS.

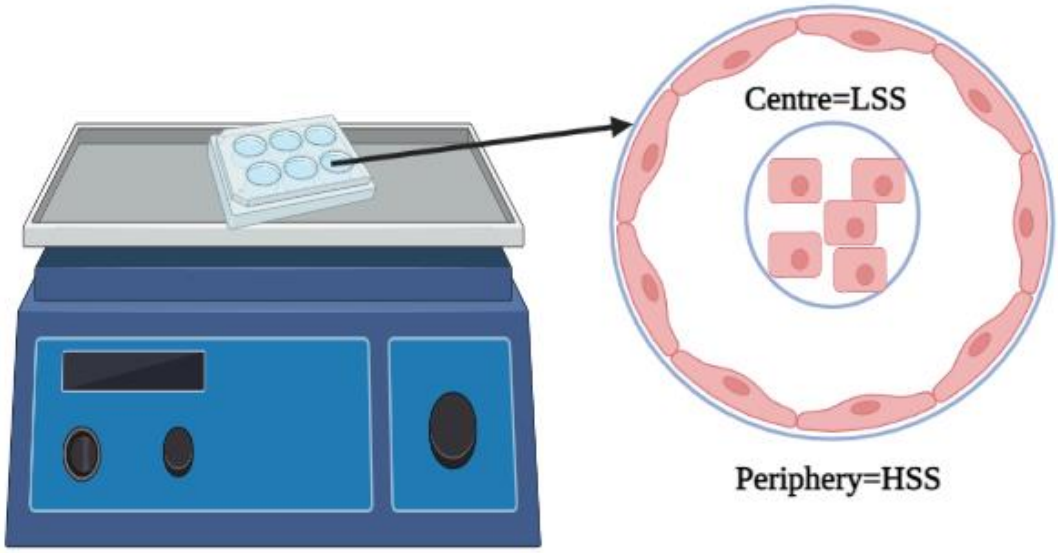

Figure 2. 3 Orbital shaker system. ECs were grown in 6-well plate and exposed to orbital shaker system for 72h. The periphery ECs were under HSS, and centre-localised ECs were under LSS.

2.9.2 Ibidi system

The Ibidi system can reproduce HSS, LSS and OSS in vitro. As shown in Figure 2. 4, the Ibidi pump was set to 1.3 Pa in HSS and 0.5 Pa in LSS and OSS (changing direction with 1 Hz frequency). HCAECs were cultured in specialised channel slides using MV2 media, cells were exposed to flow for 72h in an incubator at 37^{o}C and 5% CO_2.

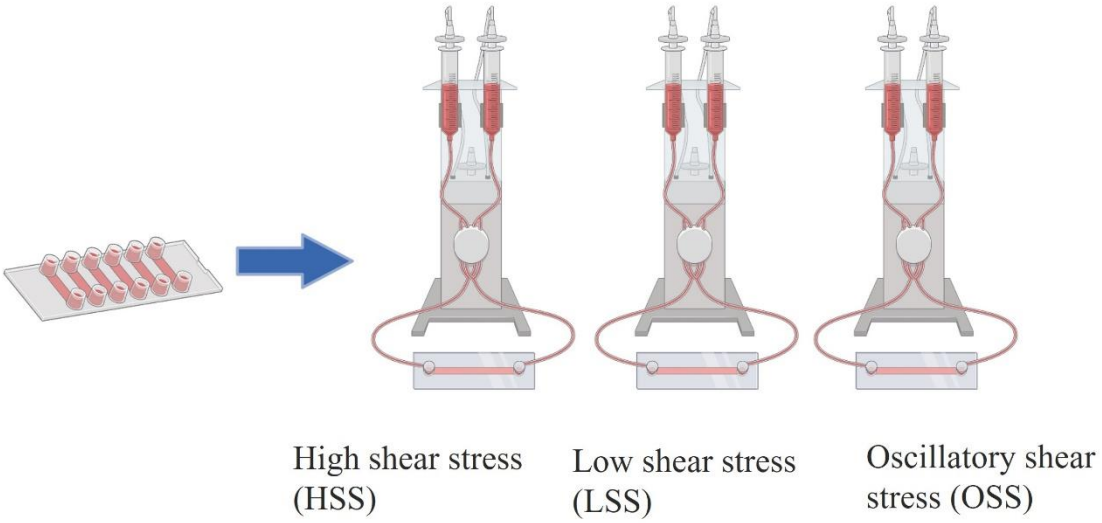

Figure 2. 4 Ibidi flow system. ECs were exposed to the Ibidi system for 72h in an incubator at 37ºC and 5% CO_2. LSS was set to 0.5 Pa and HSS was set to 1.3 Pa. HSS, high shear stress; LSS, low shear stress; OSS, oscillatory stress.

2.11 RNA extraction and cDNA normalization

Cells were collected by centrifugation at 800 *g* for 5 minutes and RNA extraction was performed according to the protocol provided by RNeasy Mini Kit (Cat Number 74104). Cells were lysed with 350 µl Buffer RLT and 70% ethanol. Sample was then transferred to RNeasy Mini spin column and centrifuged for 15 seconds at 8000 *g*, 350 µl Buffer RW1 was then added and the sample was centrifuged for 15 seconds at 8000 *g*. Add 10 µl DNase I stock solution to 70 µl of buffer RDD and mixed gently. After 15 minutes at room temperature, add 350 µl of buffer RW1 and centrifuge it for 15 s at 8000 *g*. Add 500 µl of buffer RPE and centrifuge at 8000 *g* for 15s, add another 500 µl of buffer RPE and centrifuge at 8000 *g* for 2 minutes. Then placed the RNeasy spin column in a new tube and added 50 µl of RNase-free water. The concentration of RNA is determined by NanoDrop ND-1000 (Thermo Scientific).

2.12 Quantitative RT-PCR including primer design

CFX384 Touch™ Real-Time PCR Detection System (Bio-Rad) was used to perform qRT–PCR. SsoAdvanced SYBR Green Supermix (56% v/v; Bio-Rad) and 10 µM gene specific primers were combined with cDNA. Total reaction volume was 20 µl in triplicate. PCR amplification consisted of 3 minutes of denaturation step at 95 °C, then 40 cycles of amplification at 95 °C for 5 seconds and 60 °C for 45 seconds, followed by the final dissociation stage from 65^{o}C to 95^{o}C

The primers were designed in the Primer3 website (http://primer3.ut.ee/). To check the primers are binding specifically, the primer-BLAST website (http://www.ncbi.nlm.nih.gov/tools/primer-blast/) was also used.

The process of cDNA normalisation consists of several formula. The first step is to calsulate the ΔCt, which involves substracting the CT value of the housekeeping gene from the CT value of the gene of interest. To compare cDNA samples from HSS and LSS conditions and express them relative to each other, the ΔCt of HSS is substracted from the ΔCt of LSS, resulting in ΔΔCt, the ΔΔCt of LSS equals to 0. Finally, the fold change is calculated by the formula $2^{-\Delta\Delta Ct}$. In this study, all data is normalised to LSS as it focuses only on gene expression under HSS conditions.

Table 2.1 exhibits all primers used in RT-PCR experiments.

Organism	Gene	Forward primer (5'-3')	Reverse primer (3'-5')	Purpose
H. sapiens	*HPRT*	TTGGTCAGGCAGTATAATCC	GGGCATATCCTACAACAAAC	Housekeeper qRT-PCR
H. sapiens	*Selp*	CAGTGTTTAGCTGCCCAGTG	CTTCCGGTCCAACTAATGCA	EC expression: qRT-PCR
H. sapiens	*Nt5e*	GCATTCCTGAAGATCCAAGCA	AAAGCGGCATGATTGAGAGG	
H. sapiens	*Klk10*	CTGCGGAAACAAGCCACTG	GGTGGTACTTGGGATGGACA	
H. sapiens	*Nox4*	ACACCTCTGCCTGTTCATCT	TGGCCCTTGGTTATACAGCA	
H. sapiens	*Heg1*	GGAAACCCCTATCAGCTTATCA	AGTGCGATGCCTAGGATGAG	
H. sapiens	*Bmp4*	TCTTGAGTATCCTGAGCGCC	CCAGATGTTCTTCGTGGTGG	
H. sapiens	*GBP1*	GAACAGACAAGGGAACAGCC	CCACCACCATAGGCTGTGTA	EC expression: qRT-PCR
H. sapiens	*GBP2*	AAGAGGGAGAAAGCAGTGCA	GGTGTTGTTCCCCAGATCAG	
H. sapiens	*GBP3*	TTCTCCCTGGACTTGGAAGC	TTTGACTGGTACCTTGCGTT	
H. sapiens	*GBP4*	TGGGCGATGTAGAAAAGAGTAA	GTGGTTGATGGTGCTCACG	
H. sapiens	*GBP5*	GCTATCGACCTACTGCACAATG	TGTCAAGGTCGGGTGAGTTT	
H. sapiens	*GBP7*	TGCAGTCACAGGTGGTTATAGA	GCCTGCTTAGCTGCTATGG	
H. sapiens	*Ifit1*	TCCACAAGACAGAATAGCCAGA	CCATTTGTACTCATGGTTGCTG	EC expression: qRT-PCR
H. sapiens	*Bst2*	GTGGAGCGACTGAGAAGAGA	GGGAGCTGGGGTAGTACTTC	
H. sapiens	*Stat1*	GAAAAGCAAGACTGGGAGCA	ACAGGAGGTCATGAAAACGG	
H. sapiens	*Stat2*	GGACATTCAGCCCTTTTCCC	CCCTCTGAGCCTGGATCAAA	
H. sapiens	*Usp18*	ACCTGCTGCCTTAACTCCTT	GCACCGTGATCCTCTTCAAT	
H. sapiens	*CD74*	CTTCCCGGAGAACCTGAGAC	CCAGCTCTCAAAGACCTTCC	
H. sapiens	*IL18*	TCGGGAAGAGGAAAGGAACC	GCCATCTTTATTCCTGCGACA	
H. sapiens	*Casp1*	TCACTGCTTCGGACATGACT	CTTCCCACAAATGCCTTCCC	
H. sapiens	*Casp4*	GCGGAACTGTGCATGATGAG	AGTTCCCCACGGTTTGCAC	
H. sapiens	*GSDMD*	AACTTCCTGACAGATGGGGT	GCTCTCTGTCCAAAAGCTCC	
S. scrofa	*B2M*	GGTTCAGGTTTACTCACGCCAC	CTTAACTATCTTGGGCTTATCG	Housekeeper qRT-PCR
S. scrofa	*Selp*	CAGTATGCAGAGCTGTCAAATG	AGGGTTGGAGCAGTTCATCA	EC expression: qRT-PCR
S. scrofa	*Nt5e*	ACTCATCGCTCAGAAGGTGA	GGTGGGTTGCCTGTGTAAAG	
S. scrofa	*Klk10*	GTCCCTCTTCAATGGCCTCT	ACAGAGGTTTATTGTTCCCGC	
S. scrofa	*Nox4*	CAGAGGGAAAACAGTTGGCG	GTCCTGCTTCATCTCAAAGGT	
S. scrofa	*Heg1*	TTACTCGCCCACAAGTGTCA	CAAGAATGCCGTGATCCTGG	
S. scrofa	*Bmp4*	CCACCACGAAGAACATCTGG	TGGGATGCTGCTGAGGTTAA	

Table 2. 1 PCR primer sequences. Gene specific primers were designed to assess the gene expression in *Homo sapiens* and *Sus scrofa*.

2.13 Statistical analysis

All statistical analysis was performed in Graph Pad Prism 8 Software. Differences between two groups was analysed using t-tests, and differences between more than two groups was performed by ANOVA. P value < 0.05 was considered significant.

Chapter 3. Towards a marker of HSS in healthy and diseased murine aortas

3.1 Introduction

It is well established that atherosclerotic plaques develop at specific sites, including curvatures and bifurcations that are exposed to LSS and disturbed flow. LSS promotes the initiation of atherosclerosis by inducing endothelial cell activation, proliferation, endothelial to mesenchymal transition (EndMT), apoptosis and senescence. By contract, HSS is atheroprotective. However, shear stress control of plaque progression is complex. There are various shear stress profiles associated with plaque, including differences in magnitude, endothelial shear stress gradients, and oscillatory shear stress (Evans et al., 2021), however, the role of shear stress in plaque rupture or erosion is still unclear. Indeed, there is conflicting data on the WSS profiles that trigger plaque rupture with the suggestion that low, high or oscillatory shear stress are the major drivers (Kim et al., 2013; Samady et al., 2011). Thus, developing an unbiased method to investigate the relationship between shear stress, endothelial biology and plaque rupture is vital. An important first step in developing such a method is to define a marker for HSS in healthy and atherosclerotic aortas, because this marker can be used to select and compare HSS cells from healthy and diseased tissues. It is well established that HSS can activate eNOS at the endothelial apical surface through several receptors (Davis et al., 2001, 2004; B. Yang & Rizzo, 2013), thus, this study aim to validate if eNOS can be used as a marker for HSS in both healthy and diseased aortas.

As illustrated in the workflow, I developed a new system to map shear stress and compared it with spatial distribution of endothelial proteins in healthy aorta and plaques in mice (Figure 3.1). I focussed on eNOS as a marker of HSS. The same aorta was used for shear stress mapping and eNOS mapping to allow parallel analysis and registration of shear stress and protein expression. In shear stress mapping, murine aortas were scanned by OPT imaging. Then the segmentation was generated by ITK snap software. We collaborated with Wentzel's group in Erasmus MC hospital to smooth the segmentation and finally shear stress maps were generated by Fluent software. In eNOS mapping, aortic arches were optically cleared by CUBIC solution and eNOS was analysed in 3D by immunofluorescent staining coupled to light-sheet imaging. The shear stress maps and eNOS maps were registered using anatomical landmarks in order to measure the correlation between shear stress values and eNOS levels.

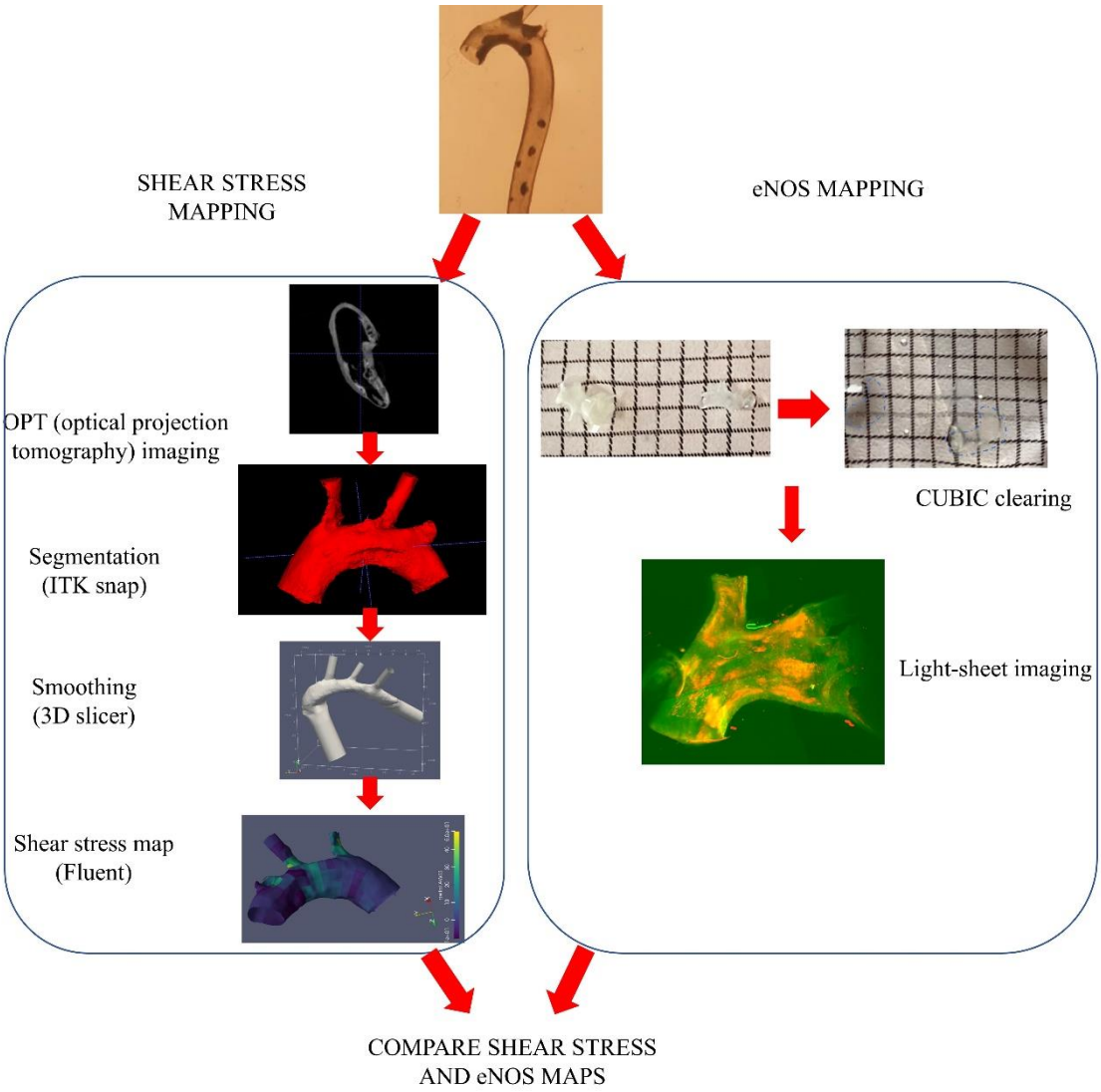

Figure 3. 1 Workflow of building shear stress and eNOS spatial maps in the murine aorta. Representative images are shown from one mouse (*ApoE*$^{-/-}$ mouse exposed to high fat diet for 16 weeks). The same aorta was used for shear stress mapping and eNOS mapping.

3.2 Hypothesis and aims

I hypothesized that ECs exposed to HSS in atherosclerotic plaques behave differently compared to HSS endothelial cells in normal tissue.

To test this hypothesis, I aim to find a marker of HSS that can be used to select and analyse EC exposed to HSS in healthy tissues and atherosclerotic plaques. To identify such a HSS marker I carried out the following aims:

1. Use light-sheet imaging to analyse the spatial distribution of eNOS in healthy and diseased murine aortas.
2. Map shear stress in healthy aorta and atherosclerotic plaques in mice.
3. Develop a system to correlate spatial distribution of eNOS with local shear stress in healthy and diseased aortas.
4. Validate my new methods.

3.3 Light-sheet imaging

3.3.1 Aortic geometry preservation is sub-optimal in Airy-scan confocal scanning

The first aim of this project was to investigate a technique that can preserve murine arterial 3D geometry for mapping of endothelial proteins. To assess this, eNOS was used for en face staining since it is a well-known HSS marker in healthy tissue (Chistiakov et al., 2017). CD31 was used to identify endothelial cells. As it is shown in Figure 3. 2, CD31 staining followed by conventional confocal microscopy determined that endothelial cells under HSS are elongated and under LSS are cubic, which is consistent with previous observations (Depaola et al., 1999). Importantly, the staining using anti-eNOS antibody showed a high relative expression of eNOS at HSS region compared to LSS region in both WT mice and *ApoE*$^{-/-}$ ND mice (Figure 3. 2), whereas IgG control staining gave little fluorescence (Figure 3. 2). Thus, I concluded that en face staining of eNOS was able to identify ECs exposed to HSS in the healthy mouse aorta.

To label the arch in 3D and preserve aortic geometry for computational fluid dynamics analysis, I attempted Airy-scan confocal microscopy of curved tissue in healthy mouse aorta (Figure 3. 3). When eNOS expression was assessed, it was enriched at the HSS region in contrast to the LSS region (Figure 3. 3 A). This observation was consistent in multiple animals since statistical analysis found that eNOS level was significantly enhanced in HSS compared to LSS ($p<0.001$) (Figure 3. 3 B). However, aortic geometry

was sub-optimal in this technique and therefore it cannot be used to register protein with shear stress maps in 3D. Because of this, I next attempted a method where the intact aorta is analysed.

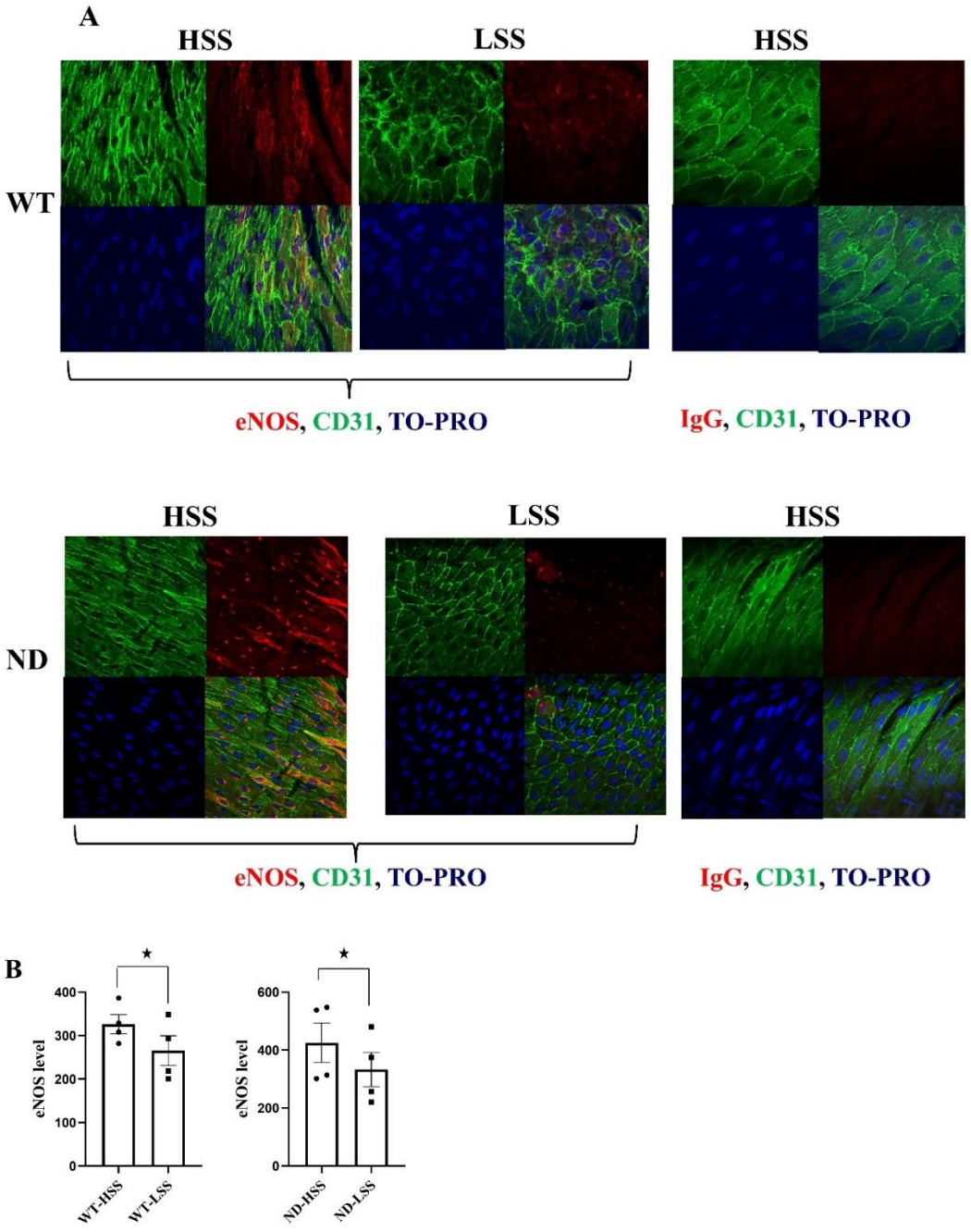

Figure 3. 2 eNOS expression in endothelium correlates with HSS in the aorta of healthy mice. (A) En face staining of aortic arch was performed in C57BL/6 WT mice (N=4). Stained sections were imaged with a confocal microscope at 63X magnification. En face staining of aortic arch was performed in *ApoE*$^{-/-}$ ND mice (normal diet for 6-8 weeks; N=4). Stained sections were imaged with normal confocal microscope at 40X magnification. The arch was stained for CD31 (endothelial marker, green), TO-PRO 3 (nuclear marker, blue), eNOS expression was assessed by immunostaining (red). Rabbit IgG antibody was used to control the non-specific staining. Two regions were chosen to Analyze: outer curvature of arch associated with HSS and inner curvature of arch associated with LSS. (B) Quantification of eNOS level in WT mice and *ApoE*$^{-/-}$ ND mice; paired t-test; * Indicated $p< 0.05$.

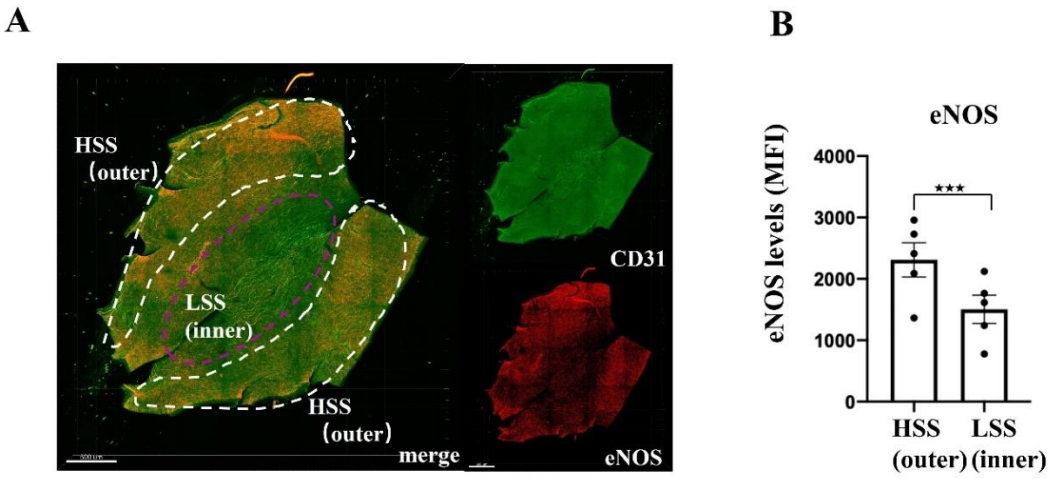

Figure 3. 3. eNOS enrichment at a HSS stress region. (A) en face immunostainings were performed using eNOS antibodies (red), endothelium was stained with CD31 antibodies (green). (N=5 WT mice). After staining, aortas were mounted in cavity slides to partially preserve the curved structure. Z -stack and tiled images of Airy-scan confocal microscopy was obtained, endothelium and specific protein were indicated in green and red, respectively. The co-localization of green and red signals presented as yellow colors. Geometry of arch was reconstructed by using Imaris 3D view tool. The curved tissue was imaged with Zeiss LSM 880 microscope with a 10X lens. Using Image J (Fiji), regions of interest were outlined. (B) The expression of eNOS was quantified at LSS (inner curvature) and HSS (outer curvature) areas of murine aortas. White scale bar, 500 μm. The graph represents the quantification of eNOS levels at LSS (inner curvature of arch) and HSS area (outer curvature of arch). Mean values are presented with standard error of the mean; n=5, *** indicates $p<0.001$, difference between means were analyzed using a paired T-test. Abbreviations: MFI, mean fluorescence index.

3.3.2 Optimisation of Light-sheet microscopy of cleared aortic arches

Classical imaging methods have several restrictions such as providing limited information from 3D and restrict light penetrating deeply through the tissue. With the aim of visualizing the 3D structures in tissues, a modern microscopy technique called light-sheet fluorescence microscopy was attempted, in combination with clearing techniques and en face staining of the murine endothelium. A clearing method was performed to aortic tissue was used based on (Susaki et al., 2015). Clearing procedures and final transparent sample are illustrated in Figure 3. 4 .

Previous studies found that CUBIC solution removed both protein and lipids, which might weaken immunofluorescent staining (Chung et al., 2013). Therefore, optimization of the clearing protocol is an essential step for imaging aortic tissue using the light-sheet approach. To address the issue of fluoresence quenching, the use of 4% paraformaldehyde (PFA) as a post-fixative for the fluorescent label, along with tissue clearing and immunofluorescent staining, is proposed as a potential solution. Furthermore, the order of these steps is considered to be important. To investigate this and find the best approach to image an aortic arch, four methods were attempted as Figure 3. 5.

Light-sheet imaging of arched prepared using Method 1 and Method 2 (first fluorescently labeled then cleared) did not yield strong fluorescent results (Figure 3. 6 A and Figure 3. 6 B). In contrast, staining for eNOS and imaging of tissues prepared with Method 3 and Method 4 (first cleared then fluorescently labeled) generated more promising staining results (Figure 3. 6 C and Figure 3. 6 D). Moreover, eNOS expression was enhanced at the outer curvature (HSS) compared to the inner curvature (LSS) using this approach (Figure 3. 6 C and Figure 3. 6 D), whereas results of Method 1 and Method 2 did not show this pattern (Figure 3. 6 A and Figure 3. 6 B). In conclusion, these data suggested that Method 4 is the optimal approach to analyse endothelial expression of proteins in the mouse aortic arch by means of light-sheet.

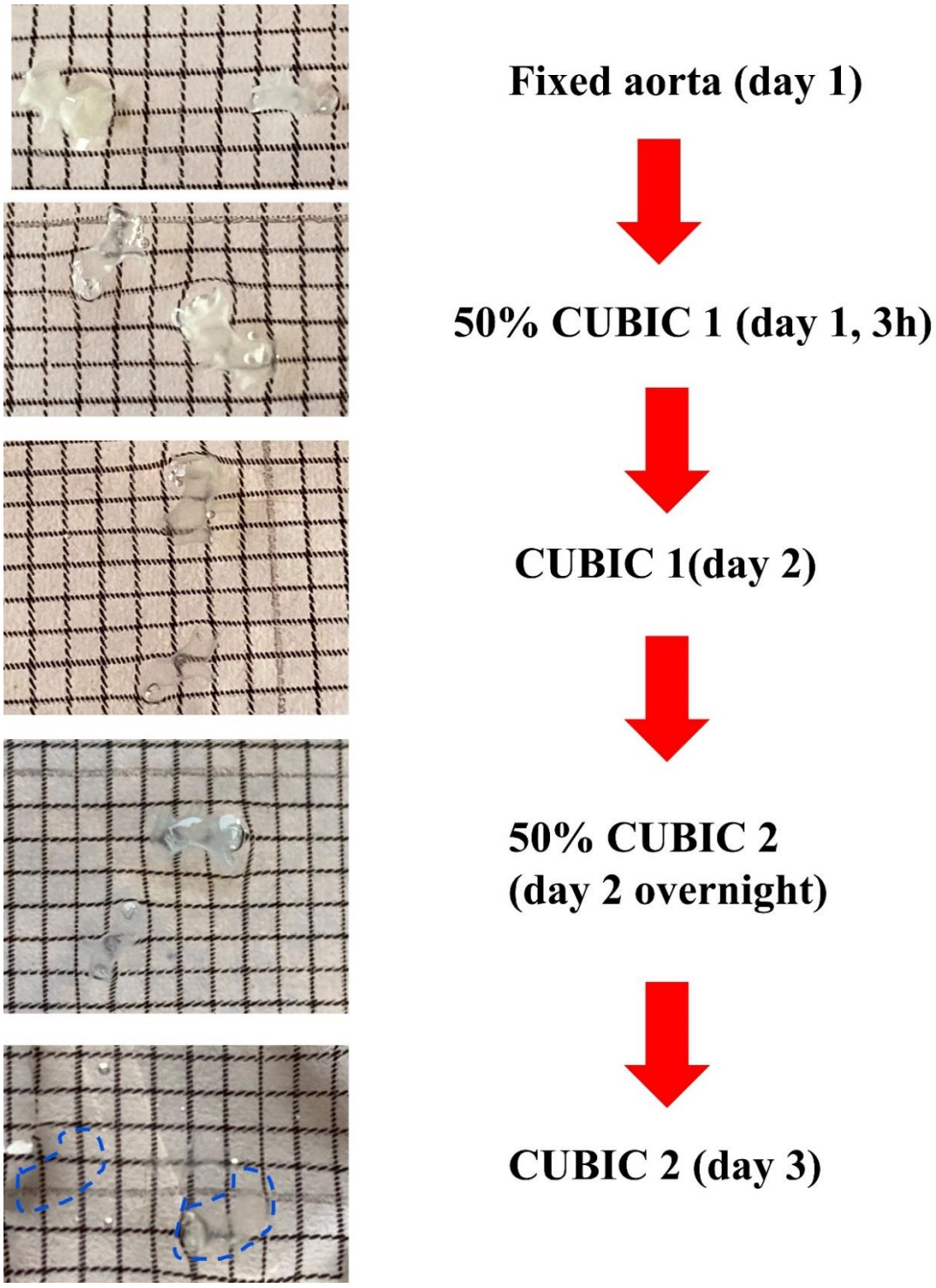

Figure 3. 4 Example of the clearing process. Aortic arches from *ApoE*$^{-/-}$ mice were subjected to CUBIC clearing. CUBIC1 and CUBIC2 protocols involved different reagents. CUBIC1 was a mixture of urea (25wt%), Quadrol (25wt%), Triton X-100 (15wt%) and dH2O. CUBIC 2 was a mixture of urea (25wt%), sucrose (50wt%), triethanolamine (10wt%) and dH2O. 50% CUBIC1 was 50:50 water: CUBIC1 diluted reagents. 50% CUBIC2 was 50:50 PBS: CUBIC2 diluted reagents. The macroscopic appearance of tissues is shown before and after clearing.

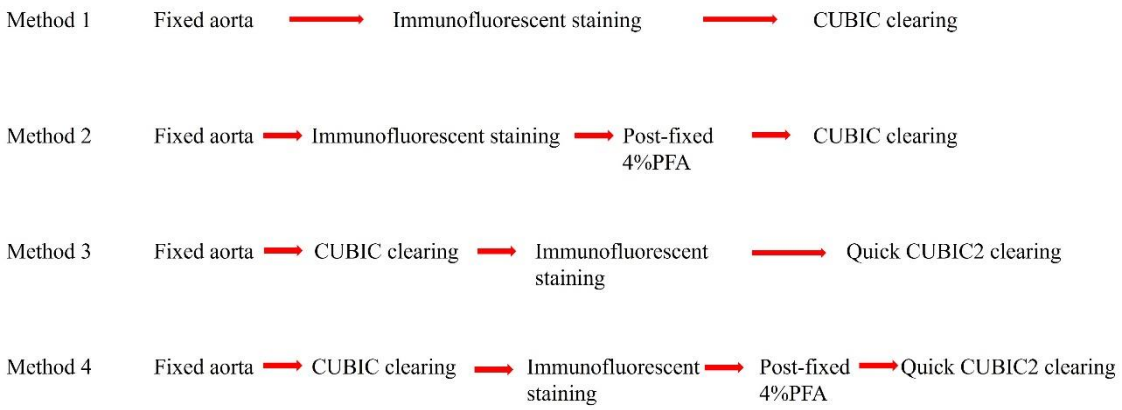

Figure 3. 5 Optimisation of light-sheet microscopy of cleared aortic arches with 4 different methods. Four methods of tissue clearing were compared for immunofluorescent staining and light sheet microscopy of murine aortic tissues.

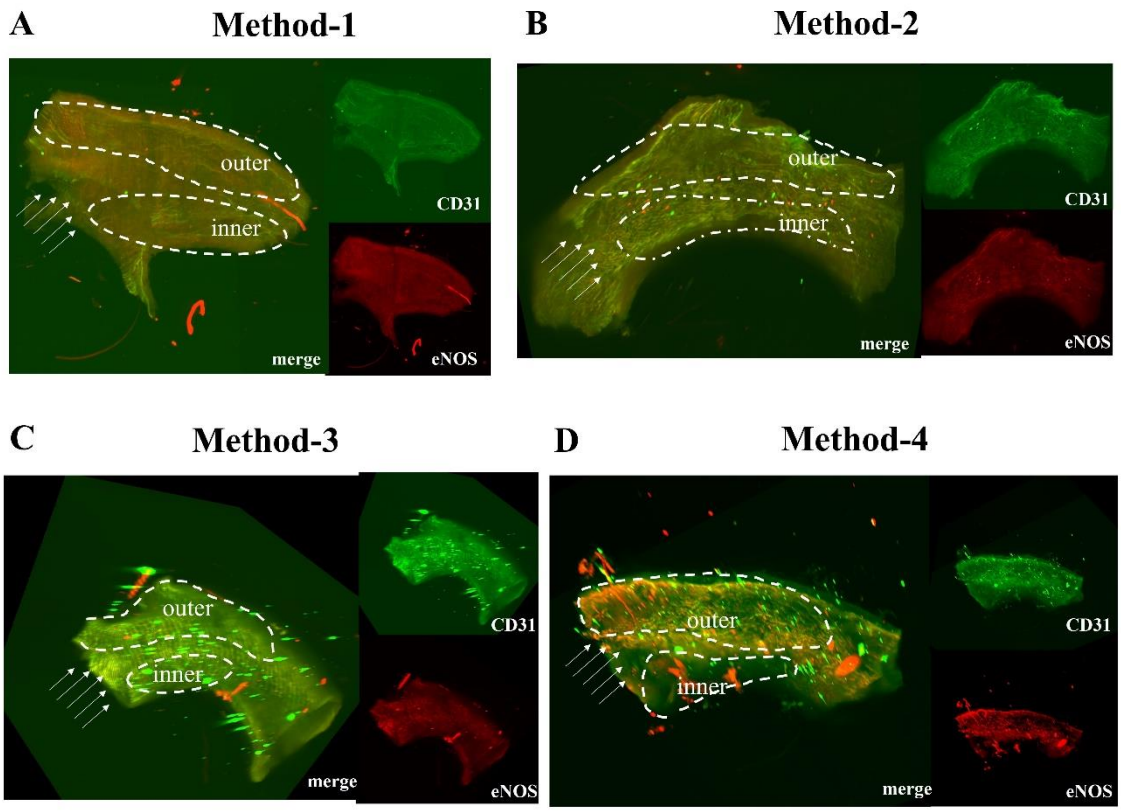

Figure 3. 6 Overview of the results of four methods of optical clearing. Murine aortas of C57BL/6 (healthy) mice were used (n=4). All samples were cleared according to CUBIC immersion protocols (see Figure 3.5). The expression of eNOS (red) was visualized in the aortic arches by en face immunostaining followed by light-sheet imaging (Zeiss light sheet Z.1). Endothelium was stained for CD31 (green). The co-localization of green and red signals presented as yellow colors. HSS region (outer curvature of arch) and LSS region (inner curvature of arch) were recognized by anatomical landmarks. Z stack and tiled images of light sheet microscopy (Zeiss Light sheet Z.1) was obtained, Geometry of arch was reconstructed by using Imaris 3D view tool. (A) Images for Method 1. (B) Images for Method 2. (C) Images for Method 3. (D) Images for Method 4. Imaging condition of representative images in A-D: zoom=0.5x-1x, exposure time=150ms, samples were scanned in four views and each view rotated 90°. Brightness/contrast and 3D constructions of images in A-D were adjusted with software Imaris.

3.3.3 Light-sheet imaging of eNOS in healthy aortas

Having established a technique that can preserve 3D geometry of murine aorta and allow visualization of eNOS expression. eNOS was analyzed by clearing, immunofluorescent staining and light-sheet imaging in several mice.

As shown in Figure 3. 7, in healthy murine aorta, eNOS protein levels were enhanced in the outer curvature of arch compared to inner curvature of arch (N=5 WT; $P<0.01$; Figure 3. 7). The outer curvature of the murine aorta is exposed to relatively high shear values compared to the inner curvature (Suo et al., 2007). Thus, eNOS appears to correlate with HSS in healthy murine aorta.

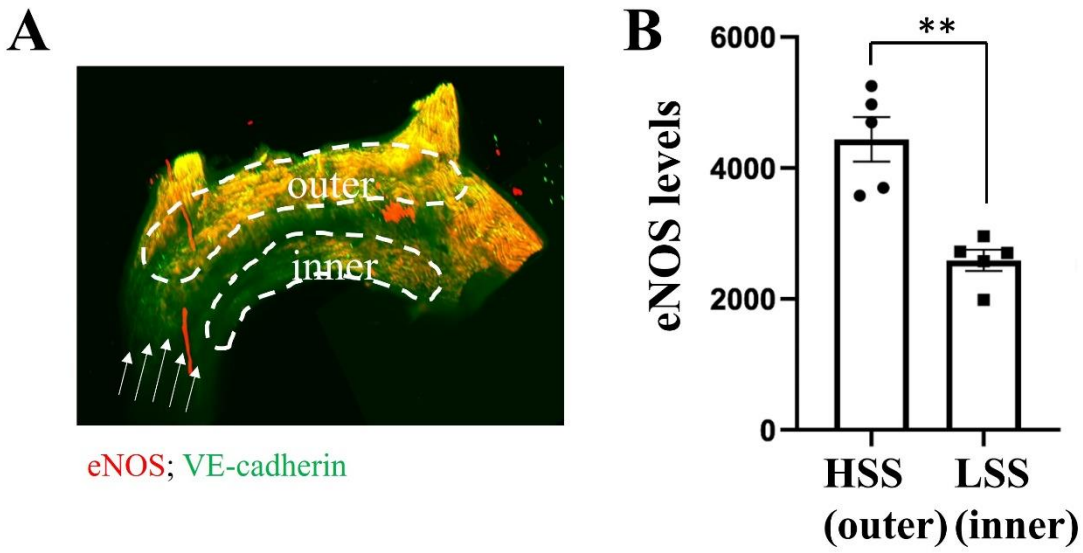

Figure 3. 7 eNOS expression is enhanced at the outer curvature in healthy aorta. (A) eNOS immunofluorescent staining and light-sheet imaging was performed in C57BL/6 mice (n=5). White arrow indicates flow direction. (B) Quantification of eNOS levels at the inner curvature (LSS) and outer curvature (HSS) of healthy aorta. Mean values are presented with SEM, n=5, independent experiments. **p<0.01, paired T-test.

3.3.4 Light-sheet imaging of eNOS in diseased aortas

The spatial distribution of eNOS expression was analysed in aortas from *ApoE*$^{-/-}$ mice (exposed to HFD for 16 weeks) by immunofluorescent staining and light-sheet imaging (Figure 3.8). In *ApoE*$^{-/-}$ mice, eNOS protein levels were enhanced in the outer curvature of arch and in the proximal part of plaque compared to the distal part of plaque (Figure 3. 8 A and C). IgG control staining gave little fluorescence (Figure 3. 8 B) and unspecific binding of plaque is low (N=3; Figure 3. 8 D). The proximal part of the plaque is presumed to be exposed to HSS, whereas the distal portion is presumed to be exposed to LOSS; therefore, we hypothesized that eNOS correlated with HSS in plaques of *ApoE*$^{-/-}$ mice.

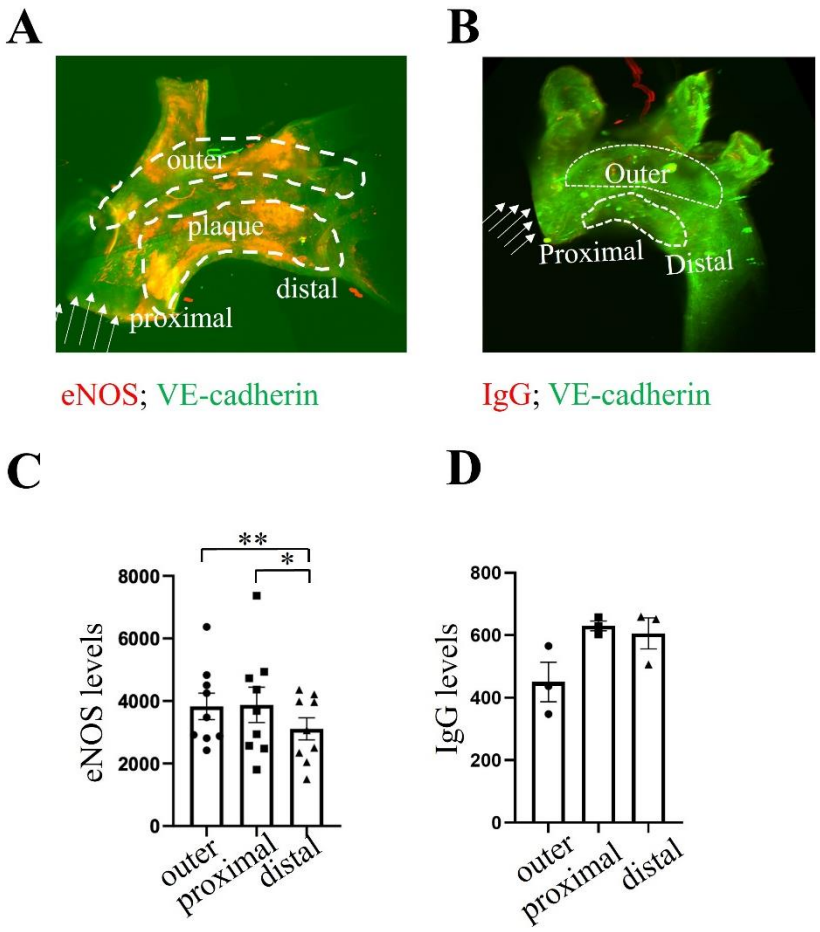

Figure 3. 8 eNOS expression was increased at outer curvature and proximal of plaque in diseased aortas. A) eNOS immunofluorescent staining and light-sheet imaging was performed in *ApoE*$^{-/-}$mice exposed to HFD for 16 weeks, nine animals were studied. eNOS was shown in red, VE-cadherin antibody (CDH5) (green) was used as endothelial marker. B) en face staining and light-sheet imaging was performed in *ApoE*$^{-/-}$mice exposed to HFD for 16 weeks, three animals were studied. Rabbit IgG for eNOS was shown in red and VE-cadherin (CDH5) was shown in green. C) Quantification of eNOS levels at the outer curvature (HSS), proximal of plaque (HSS) and distal of plaque (LSS). Mean values were presented with SEM, N=9, independent experiments. **p<0.01, *p<0.05, paired T-test. D) Quantification of IgG levels in Outer curvature of diseased aorta, proximal and distal region of plaques were presented with SEM (N=3). White arrow indicates flow direction.

3.4 Wall Shear Stress (WSS) maps

3.4.1 Segmentation of healthy aorta

Although mice have been used for shear stress mapping in arteries, the spatial distribution of specific proteins in endothelium has not been correlated precisely with shear stress maps in this model. Thus, I worked with several groups (Wentzel's group, Schenkel's group and Wu's group) to develop a work flow to link OPT imaging, light-sheet imaging, and computational fluid dynamics to correlate shear stress with spatial patterns of protein expression in murine aorta. Figure 3. 9 presents the workflow of light-sheet imaging and segmentation in healthy murine aorta. WT mice (C57BL/6) were scanned using light-sheet imaging (Zeiss Light-sheet Z.1) to obtain murine aortic aortas geometry. The geometry data was opened in Python software and the lumen of the aorta was extracted to build the segmentation. The segmentation was smoothed by Wentzel's group.

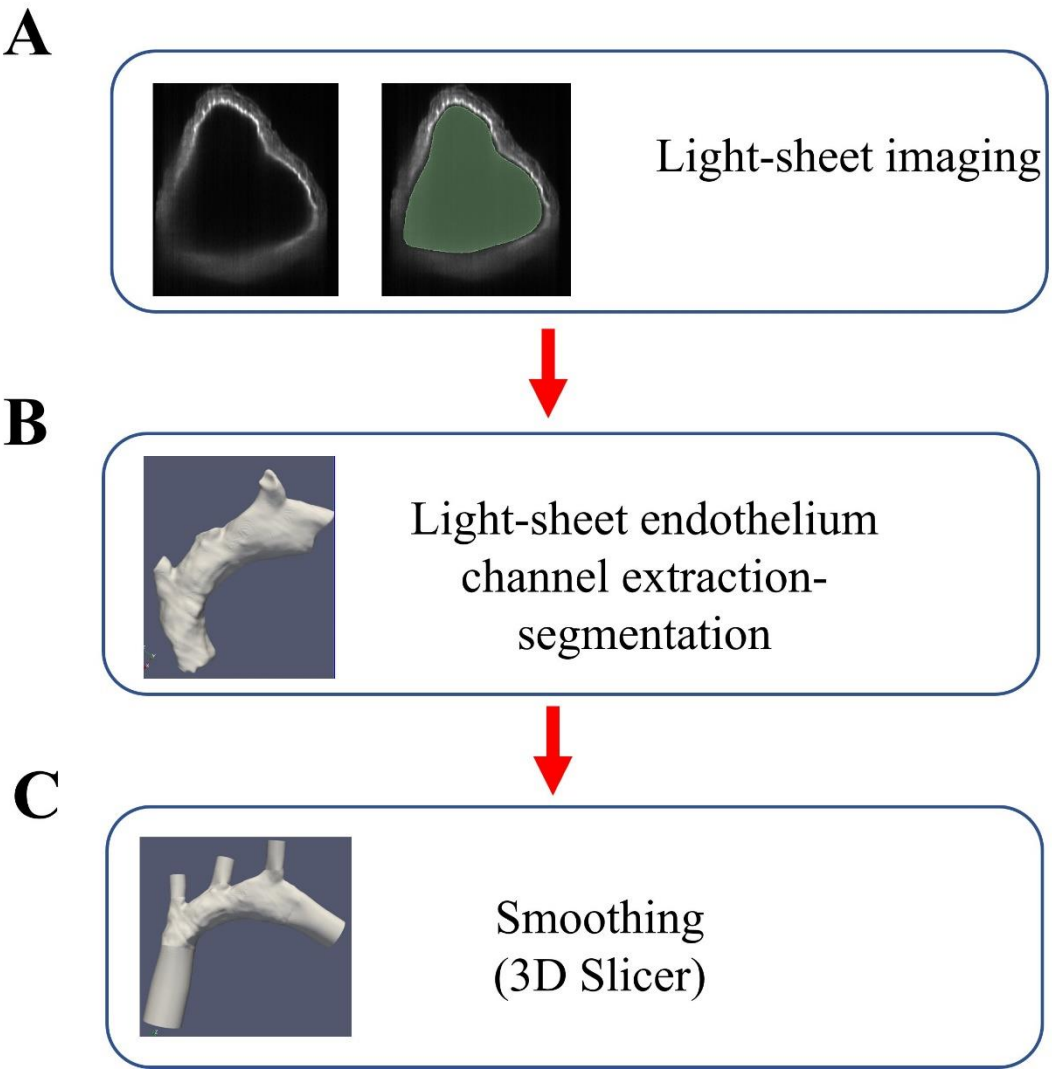

Figure 3. 9 Light-sheet imaging and segmentation workflow in healthy aorta (A) Optical clearing, eNOS immunofluorescent staining and light-sheet imaging were performed on healthy aorta, the 2D geometry data was opened in Python software. (B) The endothelium channel (CDH5) was extracted using Python software to build the segmentation. (C) The segmentation model was smoothed using 3D slicer software.

3.4.1 Computational fluid dynamics in healthy aorta

To make sure the flow that entered and exited the computational fluid dynamics model was fully developed, flow extensions (cylindrical extensions) were added to the outlets and inlets of the healthy aorta with VMTK (Vascular Modelling Toolkit). The inlet was extended 4 times the radius to ensure a smooth inlet profile. The outlet was extended 3 times the radius to exclude upstream effects of the imposed boundary conditions. High quality Meshes were generated in Ansys ICEM software (ANSYS 2021 R1), mesh size of healthy aorta was showed in Figure 3. 10 A, typical cell size was 0.05 mm, resulting in a mesh with 477858 elements/142384 nodes. Steady state simulation for healthy aorta geometry was run in Ansys Fluent software, flow was modelled as laminar flow. Inflow profile was illustrated in Figure 3. 10 B, with a velocity of 0.26m/s as a typical flow for mouse aorta. Outflow used the same flow ratios as in (Luong et al., 2016) (Figure 3. 10 C), the flow splits for biachiocephalic artery, left common carotid artery (LCCA), subclavian artery and descending aorta (DA) are 16%, 8%, 6% and 70% respectively.

The reason why flow extensions were added to computational fluid dynamic model is shown in Figure 3. 11, flow pattern in ascending aorta and descending aorta exhibited high velocity in center and low velocity on both sides, whereas flow pattern in the arch is consistent (Madhavan & Kemmerling, 2018). Thus, adding flow extensions can mimic the flow pattern in murine aorta.

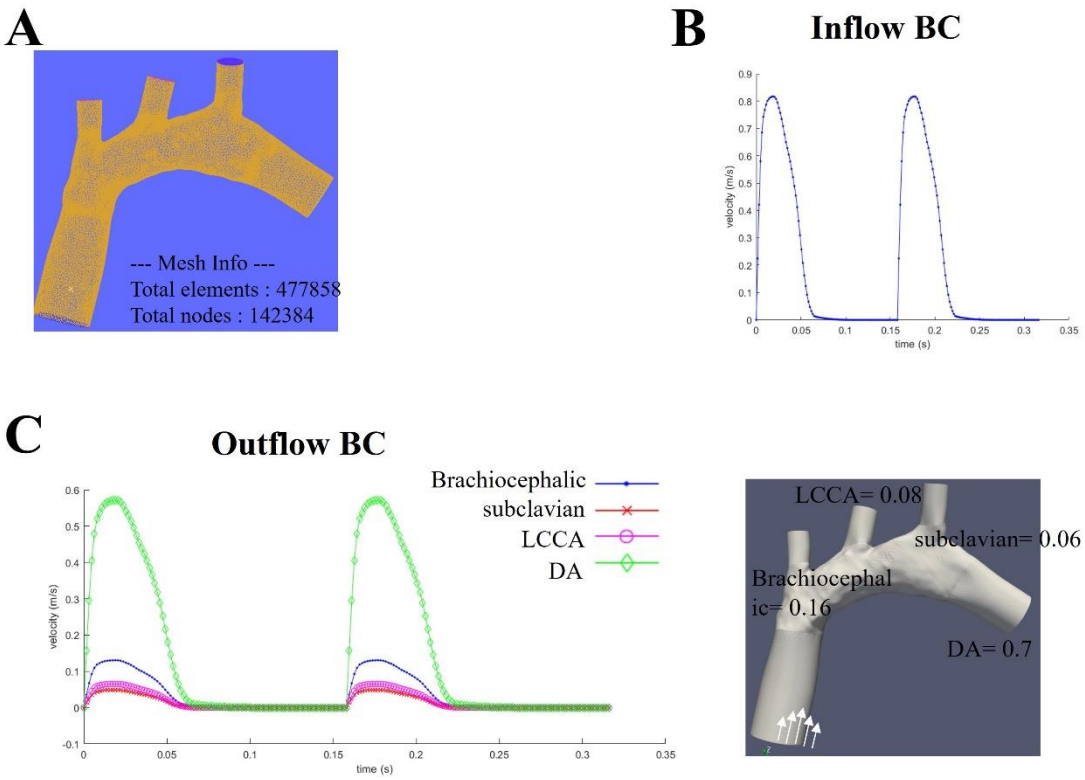

Figure 3. 10 Computational fluid dynamics in healthy aorta. (A) Mesh information of healthy aorta. (B) Inflow BC of healthy aorta. (C) Outflow BC of healthy aorta. White arrow indicates flow direction. Abbreviations: LCCA, left common carotid artery; DA, descending aorta. The definition of BC: When computing the corresponding ratios, these are constant throughout the cardiac cycle and are equal to the ratios.

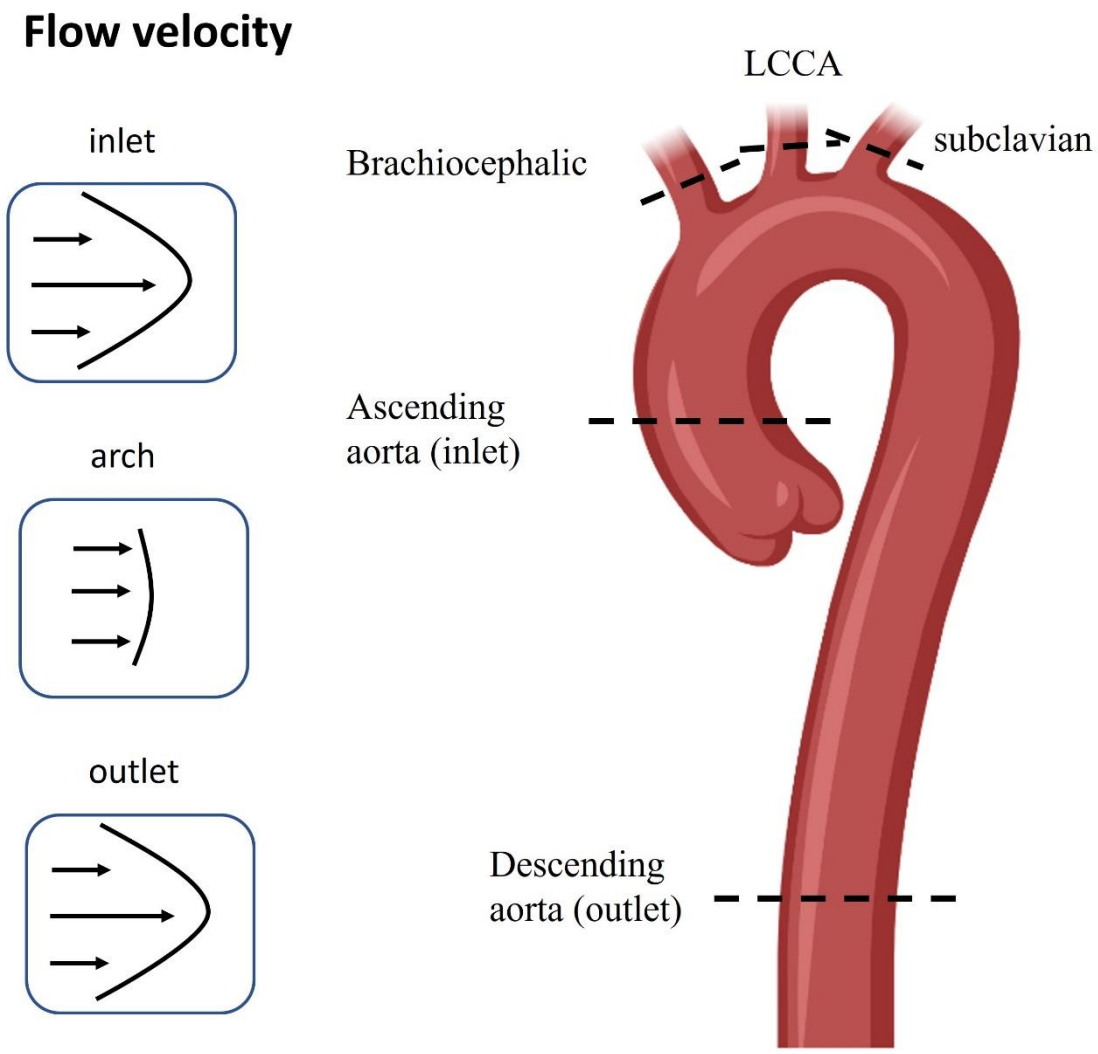

Figure 3. 11 Comparison of different flow velocity pattern between ascending aorta, arch and descending aorta. The flow pattern in inlet and outlet exhibited high velocity in the center and low velocity on both two sides, the flow pattern in arch is consistent.

3.4.2 3D Shear stress map of healthy aorta

To analyse shear stress distribution in the mouse aorta, 3D shear stress map of healthy aorta was generated. As shown in Figure 3. 12, the segmentation was demonstrated in two orientations: outer curvature and inner curvature. The shear stress maps were shown with both high sensitivity and low sensitivity (Figure 3. 13). Consistent with a previous study (Suo et al., 2007), our shear stress map demonstrated that outer curvature has higher shear stress value compared to inner curvature (Figure 3. 13 A and B). Notably, the lateral surface and the entrance of the brachiocephalic artery and left common carotid artery experienced extremely high shear values in healthy aorta (Figure 3. 13 A and B). On the other hand, the lateral surface, and the entrance to the orifice of the left subclavian artery had extremely low shear values in healthy aorta (Figure 3. 13 A). Therefore, these data verify our method for mapping shear stress onto healthy murine aorta is optimal and similar to a previous report (Suo et al., 2007).

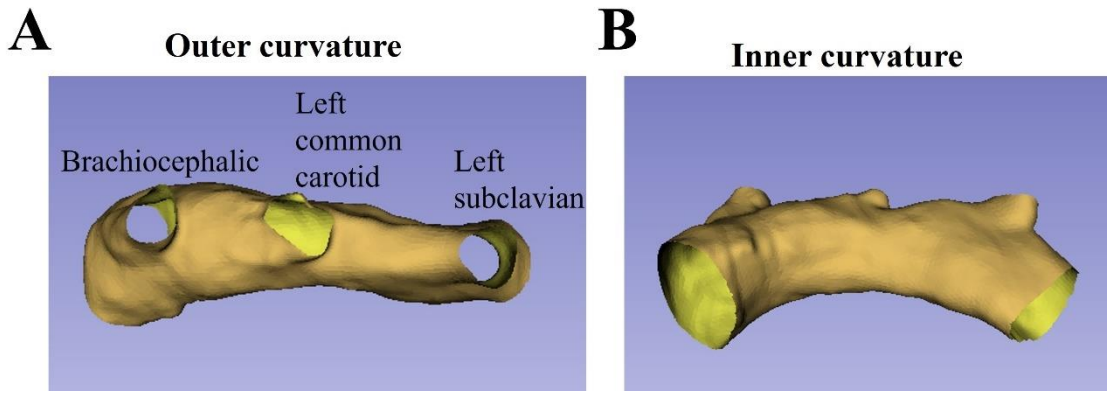

Figure 3. 12 Two orientations of healthy aorta segmentation. (A) View of outer curvature. (B) View of inner curvature.

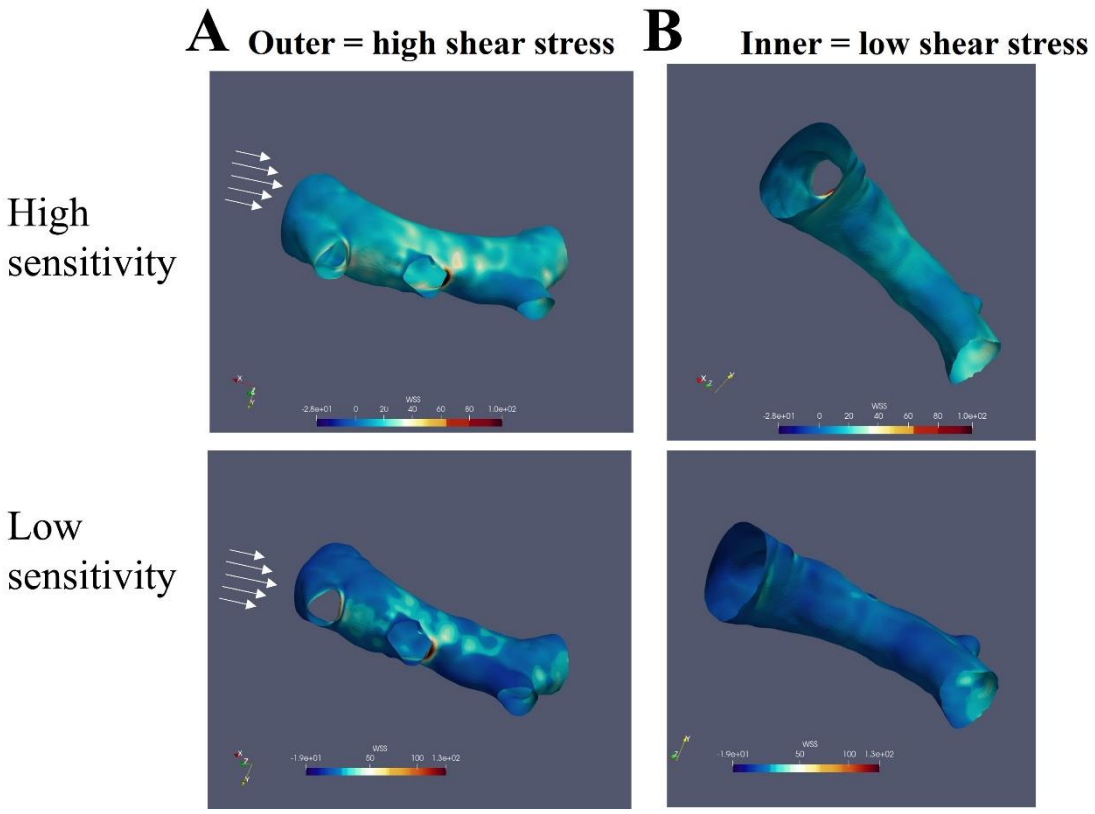

Figure 3. 13 Shear stress map of the healthy murine aorta. Shear stress map was generated by light-sheet imaging followed by computational fluid dynamics. Shear stress map was calculated and mapped on the healthy murine aortic arch geometry. (A) View of outer curvature. (B) View of inner curvature. Representative images are shown from one mouse. Colors were used for scaling the shear stress values. Dark blue indicates LSS; Light blue, white, and yellow indicate HSS. Upper panels were maps with high sensitivity and lower panels were maps with low sensitivity. White arrow indicates flow direction.

3.4.3 Segmentation in diseased aorta

Since the left common carotid artery of diseased aorta (*ApoE*$^{-/-}$ mice exposed to HFD 16 weeks) was deformed during light-sheet mounting, the following techniques were used to perform segmentation to restore diseased aorta geometry. As shown in Figure 3. 14, diseased aortas were stained for eNOS and scanned by light-sheet microscopy and the same aortas were imaged by OPT imaging to allow parallel analysis of eNOS distribution. 3D eNOS expression data from light-sheet imaging was opened in Python software to extract endothelium channel and perform segmentation. Aortic geometry data from OPT imaging was opened in ITK-snap software and perform segmentation. I also used CTvox software to visualize the plaque. Figure 3. 15 shows the surfaces of murine aortic arch (left) and structure of the plaque (right). Some structures (possibly thrombus) in the lumen that did not belong to plaque (marked by red circle in Figure 3. 15) were removed using ITK-snap software during segmentation. Seven registered landmarks were used to perform registration of light-sheet segmentation and OPT segmentation. Two segmentations were registered using Fiducial registration (3D slicer). Smoothing of registered segmentation was performed by Wentzel's group.

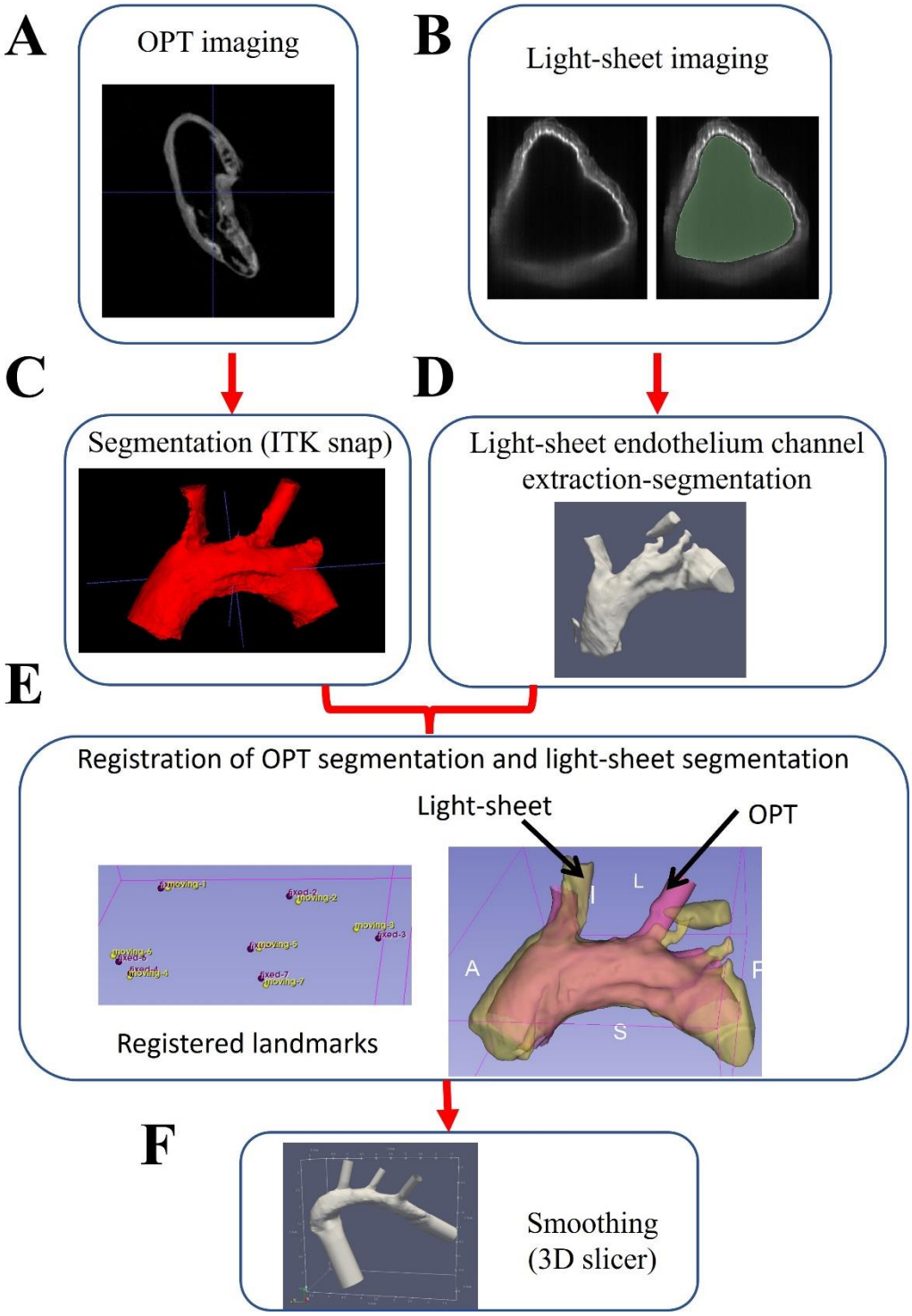

Figure 3. 14 Light-sheet imaging, OPT imaging and segmentation workflow in diseased aorta (A) OPT imaging of diseased aorta. (B) Optical clearing, eNOS immunofluorescent staining and light-sheet imaging were performed on diseased aorta, the 2D geometry data was opened in Python software. (C) Segmentation was generated according to OPT imaging using ITK-SNAP. (D) The endothelium channel (CDH5) was extracted using Python software to build the segmentation. (E) Seven registered markers were used to register OPT segmentation and light-sheet segmentation. (F) The segmentation model was smoothed using 3D slicer software.

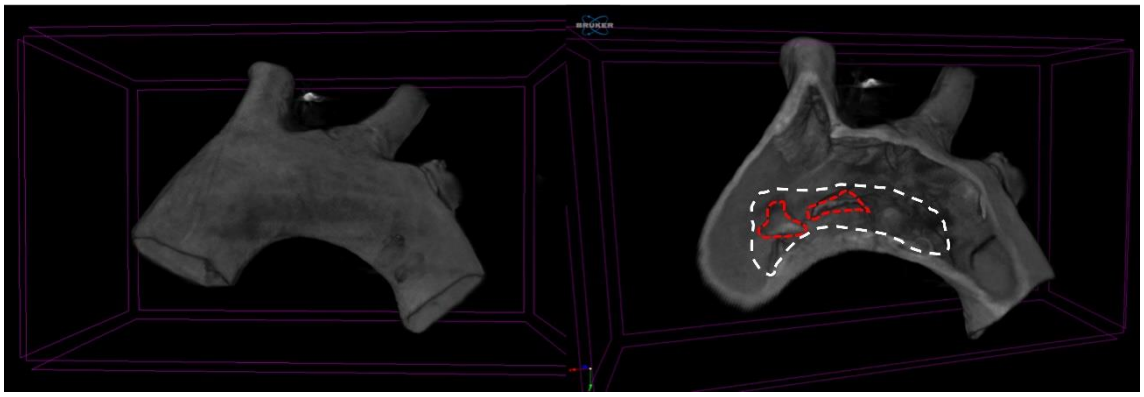

Figure 3. 15 3D reconstruction of aortic arch in *ApoE*$^{-/-}$ HFD mice. OPT images were imported into CTvox software to generate a 3D reconstruction of murine aortic arch and attached plaque. Representative images were from one *ApoE*$^{-/-}$ mice (three *ApoE*$^{-/-}$ mice were studied, exposed to HFD for 16 weeks). The images showed the surfaces of the murine aortic arch (left) and coronal aspect of aortic arch attached plaque. Suspected thrombi were marked with red circle. Plaque was marked with white circle.

3.4.4 Computational fluid dynamics in diseased aorta

To make sure the flow entered and left the computational fluid dynamics model was fully developed, flow extensions (cylindrical extensions) were added to the outlets and inlets of the diseased aorta with VMTK. The inlet was extended 4 times the radius to ensure a smooth inlet profile. The outlet was extended 3 times the radius to exclude upstream effects of the imposed boundary conditions. High quality Meshes were generated in Ansys ICEM software (ANSYS 2021 R1), mesh size of diseased aorta was showed in Figure 3. 16 A, typical cell size was 0.05 mm, resulting in a mesh with 584199 elements/188601 nodes. Steady state simulation for geometry with plaque was run in Ansys Fluent software, flow was modelled as laminar. Inflow profile was demonstrated in Figure 3. 16 B, with a velocity of 0.26m/s as a typical flow for mouse aorta. Outflow used the same flow ratios as in (Luong et al., 2016) (Figure 3. 16 C), the flow splits for biachiocephalic artery, left common carotid artery (LCCA), subclavian artery and descending aorta (DA) are 16%, 8%, 6% and 70% respectively.

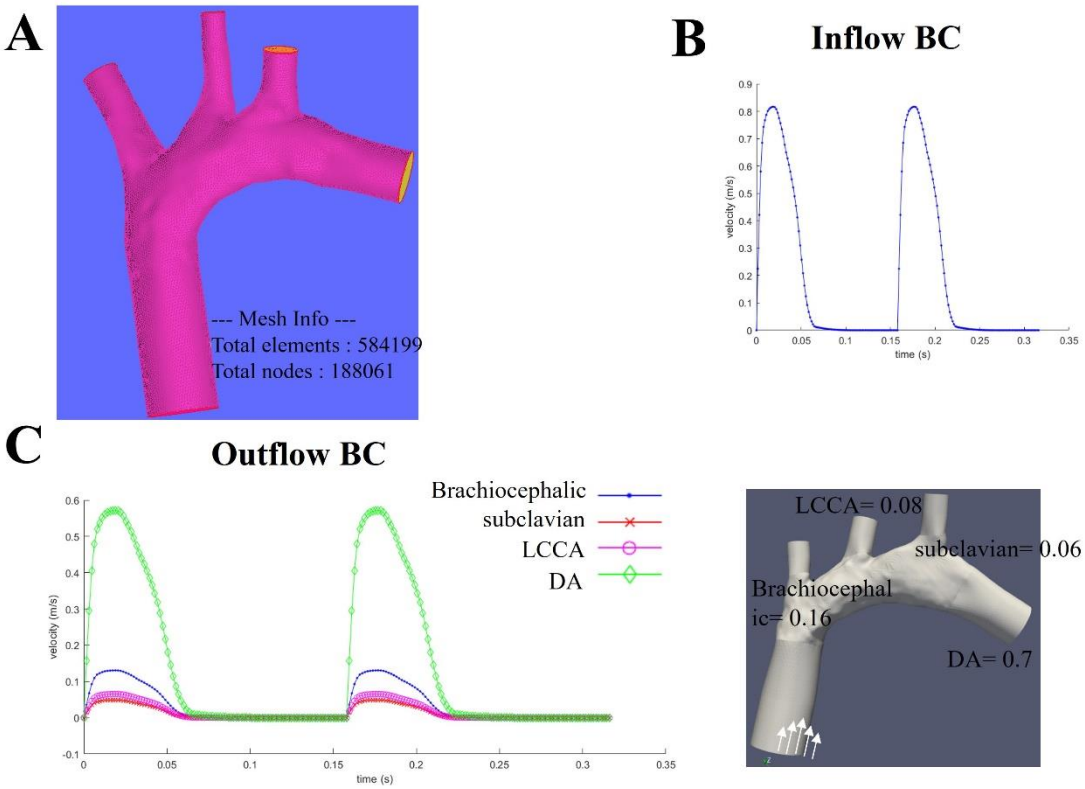

Figure 3. 16 Computational fluid dynamics in diseased aorta. (A) Mesh information of diseased aorta. (B) Inflow BC of diseased aorta. (C) Outflow BC of diseased aorta. White arrow indicates flow direction. Abbreviations: LCCA, left common carotid artery; DA, descending aorta. The definition of BC: When computing the corresponding ratios, these are constant throughout the cardiac cycle and are equal to the ratios.

3.4.5 3D shear stress map of diseased aorta

My study builds on our group's comments about shear stress conditions over atherosclerotic plaques (Evans et al., 2021). Our group hypothesized that endothelial shear stress gradient is higher in the proximal part (upstream) of plaque and oscillatory shear index is higher in the distal part (downstream) of plaque (Evans et al., 2021). To define haemodynamics over plaque in more detail, I used light-sheet imaging, OPT imaging and computational fluid dynamics to characterize shear stress in murine aortic arches with plaques. As shown in Figure 3. 17, the segmentation was demonstrated in two orientations: outer curvature and inner curvature.

Since 3D shear stress map was validated in healthy aorta, I used the same method in diseased aorta, the shear stress maps were shown with both high sensitivity and low sensitivity. (Figure 3. 18). As exhibited in Figure 3. 18 A and B, the outer curvature, brachiocephalic and left common carotid artery of diseased aorta (*ApoE*$^{-/-}$ mice exposed to HFD 16 weeks) are areas of HSS. Shear stress values over plaque are varied, the proximal part of plaque experiences higher shear stress values whereas the distal part of plaque experiences lower shear stress values (Figure 3. 18 A and B).

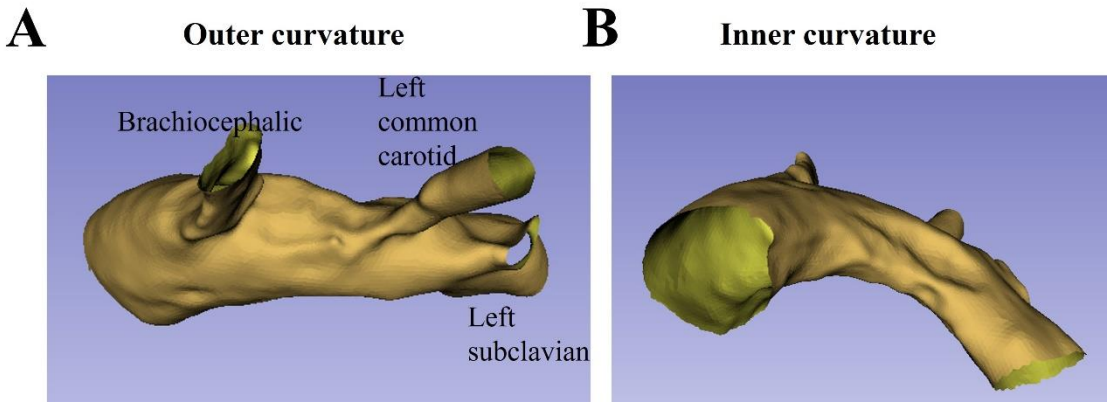

Figure 3. 17 Two orientations of diseased aorta segmentation. (A) View of outer curvature. (B) View of inner curvature.

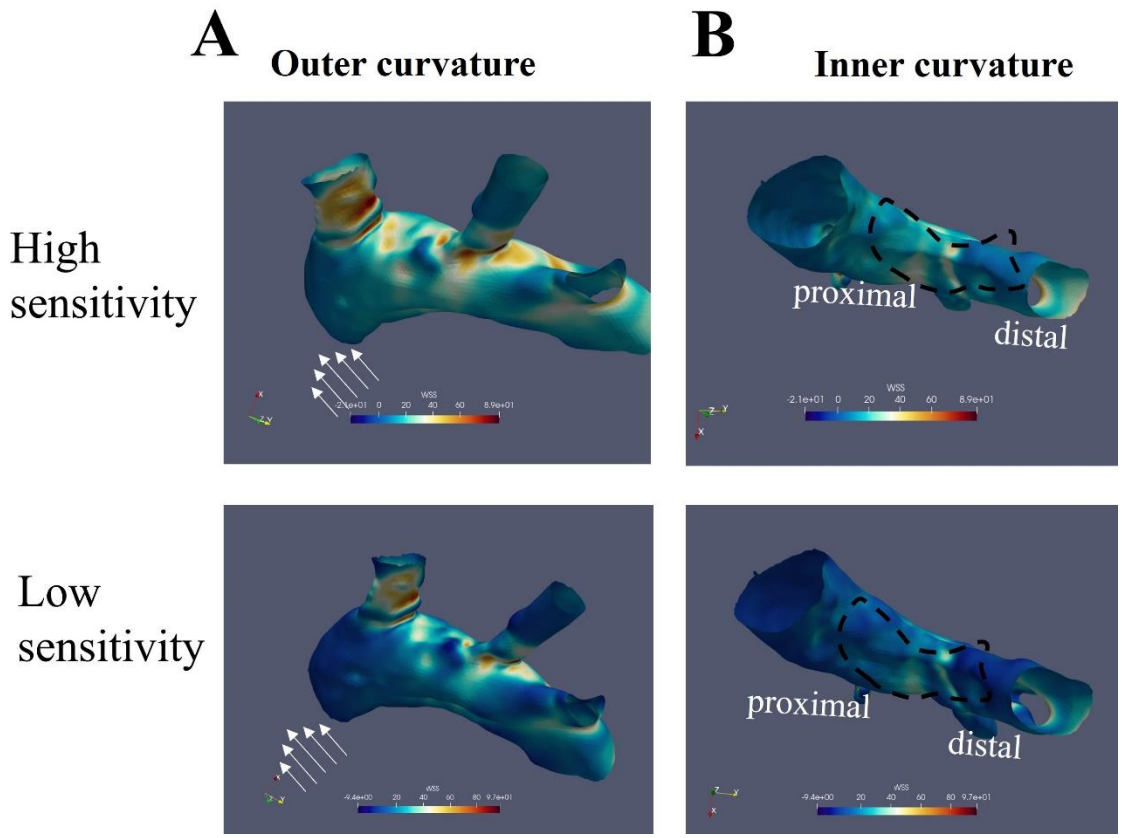

Figure 3. 18 Shear stress map in diseased murine aorta. Shear stress map was generated by OPT imaging followed by computational fluid dynamics, mapped on the diseased murine aortic arch geometry. Shear stress map of diseased mice aorta (*ApoE*$^{-/-}$mice exposed to HFD for 16 weeks). (A) View of outer curvature. (B) View of inner curvature. Colors were used for scaling the shear stress values. Blue indicated LSS; Yellow and red indicated HSS. Upper panels were maps with high sensitivity and lower panels were maps with low sensitivity. White arrow indicates flow direction.

3.5 Registration of shear stress maps and eNOS maps

3.5.1 eNOS intensity mean calculation in healthy aortas

I then sought to calculate eNOS intensity mean values over the lumen surface so that eNOS can be correlated with shear stress. As shown in Figure 3. 19 A and B, the intensity in the CDH5 (endothelial marker) channel and eNOS channel was detected across the aorta. The first step was to define the endothelial layer; to do this, I set an arbitrary intensity threshold of 350 in the CDH5 channel (Figure 3. 20 B), only pixels above this threshold were considered endothelial layer, pixels under the threshold were considered auto-fluorescence. As shown in Figure 3. 20 B, this resulted in an endothelial layer of about -10uM to 75uM thickness. This endothelial definition was subsequently used to compute mean eNOS levels over the structure (Figure 3. 20 C). I also used 2D view of light-sheet imaging to demonstrate why setting the threshold in CDH5 channel can help to define the endothelium spatially. Figure 3. 21 A shows CDH5 channel had auto-fluorescence around the endothelium (blurry green signal). Figure 3. 21 B shows pixels above threshold in CDH5 channel and the structure of the healthy aorta appears clear. The same endothelial definition (about -10uM to 75uM thickness) was applied to eNOS channel, eNOS levels in endothelium were also clear after defining the endothelial layer using CDH5 (Figure 3. 21 C). Figure 3. 21 C also showed the eNOS staining was specific to endothelium.

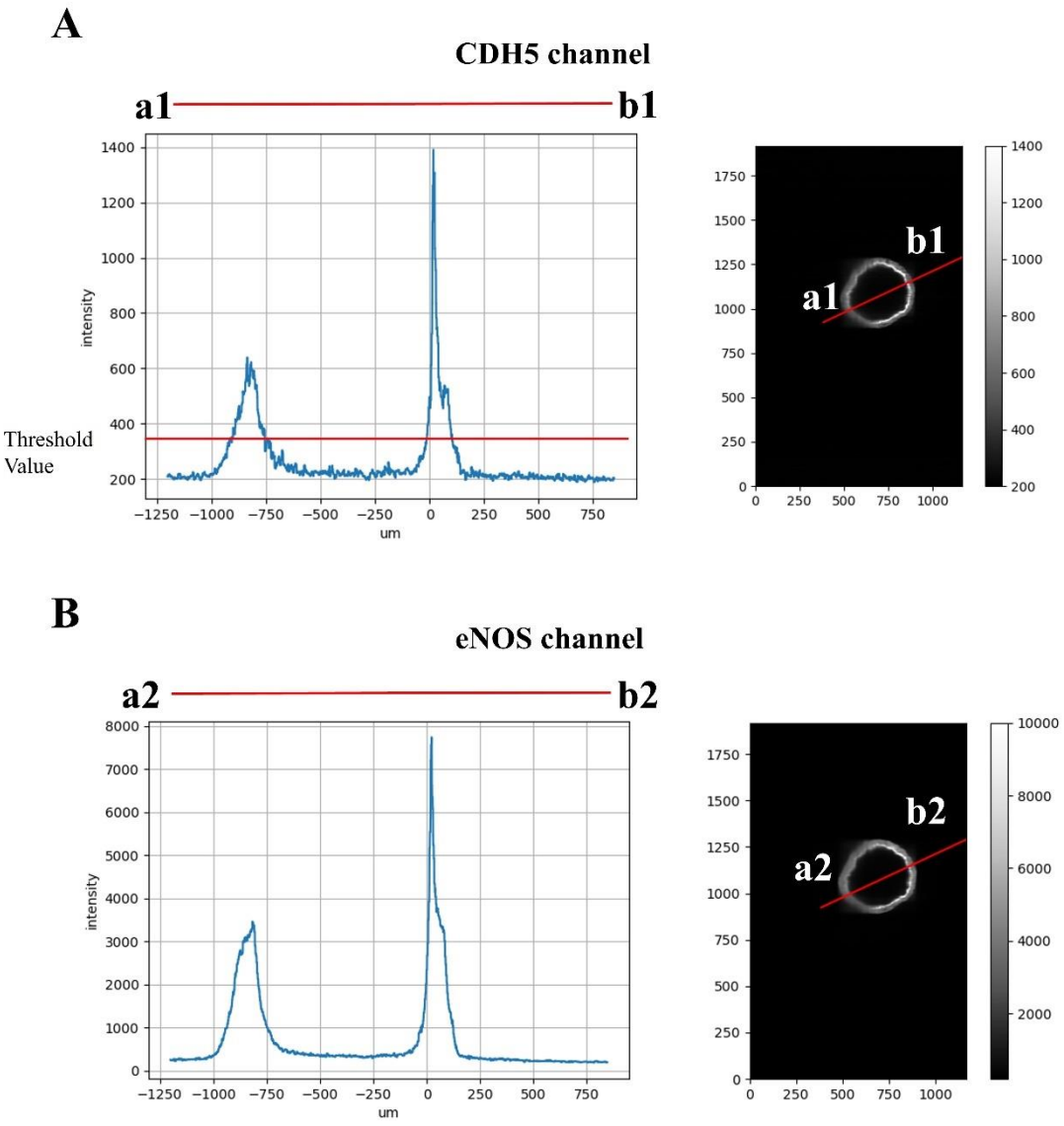

Figure 3. 19 Example for CDH5 and eNOS channel intensity across the healthy aorta. (A) Example of CDH5 channel (intensity plot showed intensity of CDH5 channel across the aorta from a1 to b1). (B) Example of eNOS channel (intensity plot showed intensity of eNOS channel across the aorta from a2 to b2).

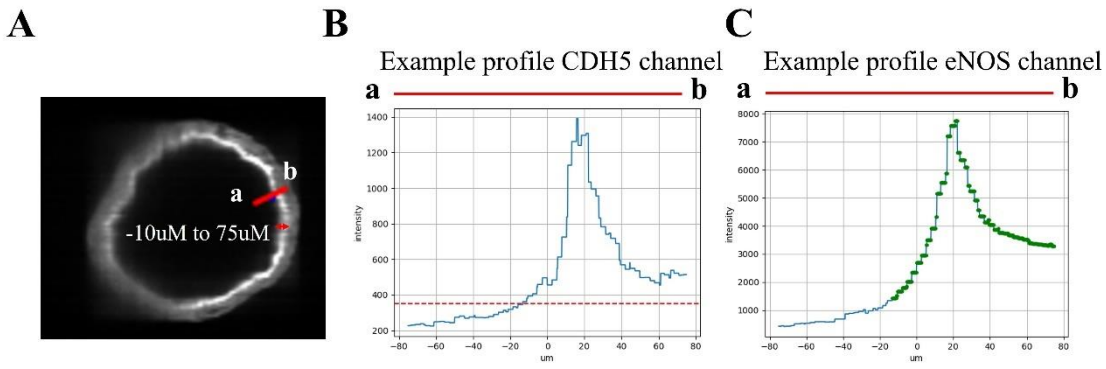

Figure 3. 20 eNOS projection on segmentation surface in healthy aorta (A) Slice was created from light-sheet data, Python software was used to extract pixel intensity of CDH5 channel and eNOS channel. (B) example profile of CDH5 channel, intensity threshold is 350, endothelial layer of about -10uM to 75uM. (C) The same endothelial definition was applied in eNOS channel, ranged from -10uM to 75uM.

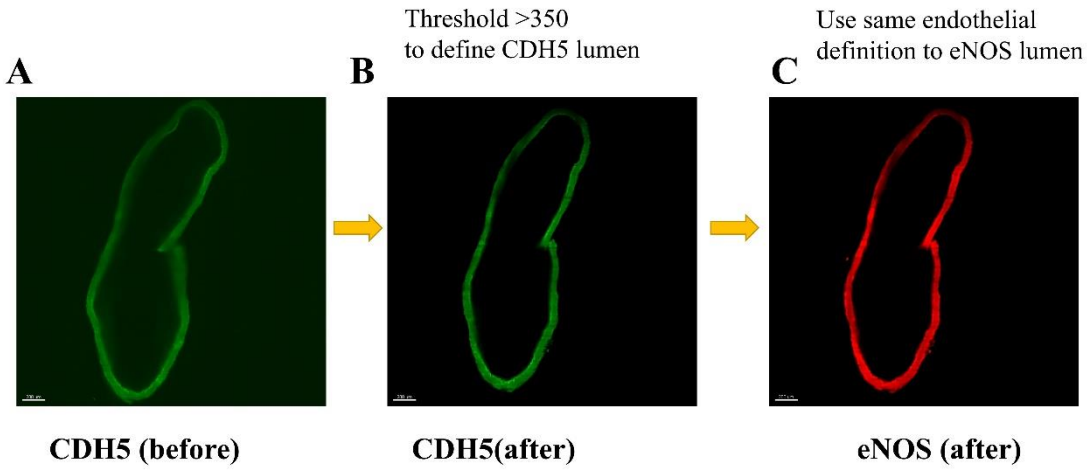

Figure 3. 21 2D view of CDH5 channel and eNOS channel after setting the threshold in healthy aorta. (A) 2D view of CDH5 channel before setting threshold. (B) 2D view of CDH5 channel after setting threshold. (C) 2D view of eNOS channel (endothelial layer of -10uM to 75uM).

3.5.2 eNOS projection on Computational fluid dynamics segmentation in healthy aortas

After computing the mean eNOS values over the aorta surface, I then sought to register the eNOS values onto the segmentation used for computation fluid dynamics.

This registration was important because it allowed me to compare WSS and eNOS values on the same geometry. Figure 3. 22 shows eNOS values projected onto the geometry used for WSS map.

3D eNOS maps were demonstrated with both high sensitivity and low sensitivity (Figure 3. 23 A and B). Figure 3. 23 C and D showed that shear stress values were increased in outer curvature compared to inner curvature in healthy aorta. The outer curvature had higher eNOS values compared to the inner curvature of aortic arch (Figure 3. 23 A and B). Lateral surface of brachiocephalic artery, left common carotid artery (LCCA), and left subclavian artery had extremely high eNOS levels (Figure 3. 23 A and B), high shear stress values were observed in lateral surface of brachiocephalic artery and LCCA (Figure 3. 23 C and D).

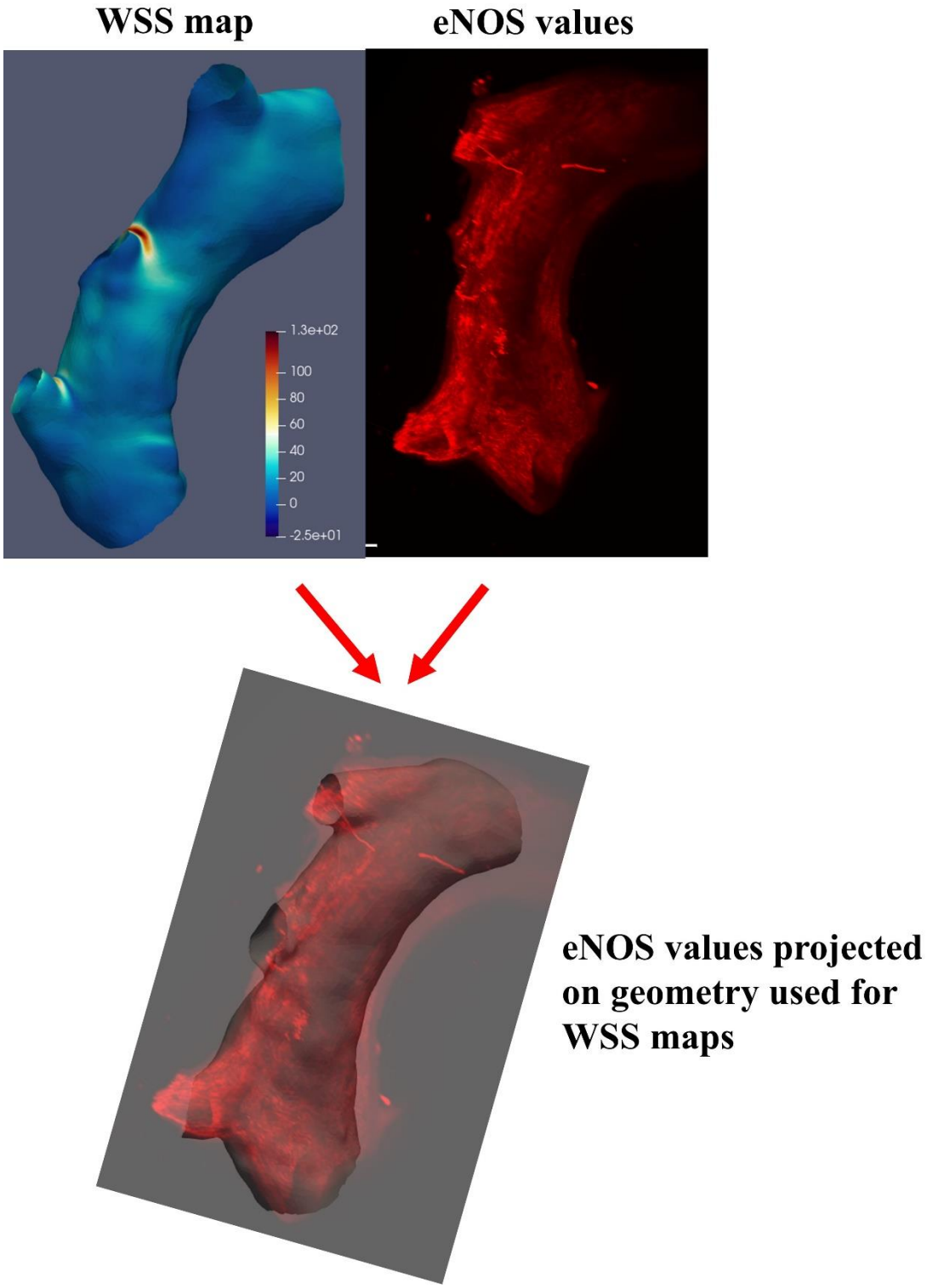

Figure 3. 22 Flow work of eNOS projection on segmentation used for WSS map in healthy aorta. Shear stress map (left) and eNOS channel (right) of light-sheet imaging. Project eNOS values on segmentation used for WSS maps to generate 3D eNOS level maps.

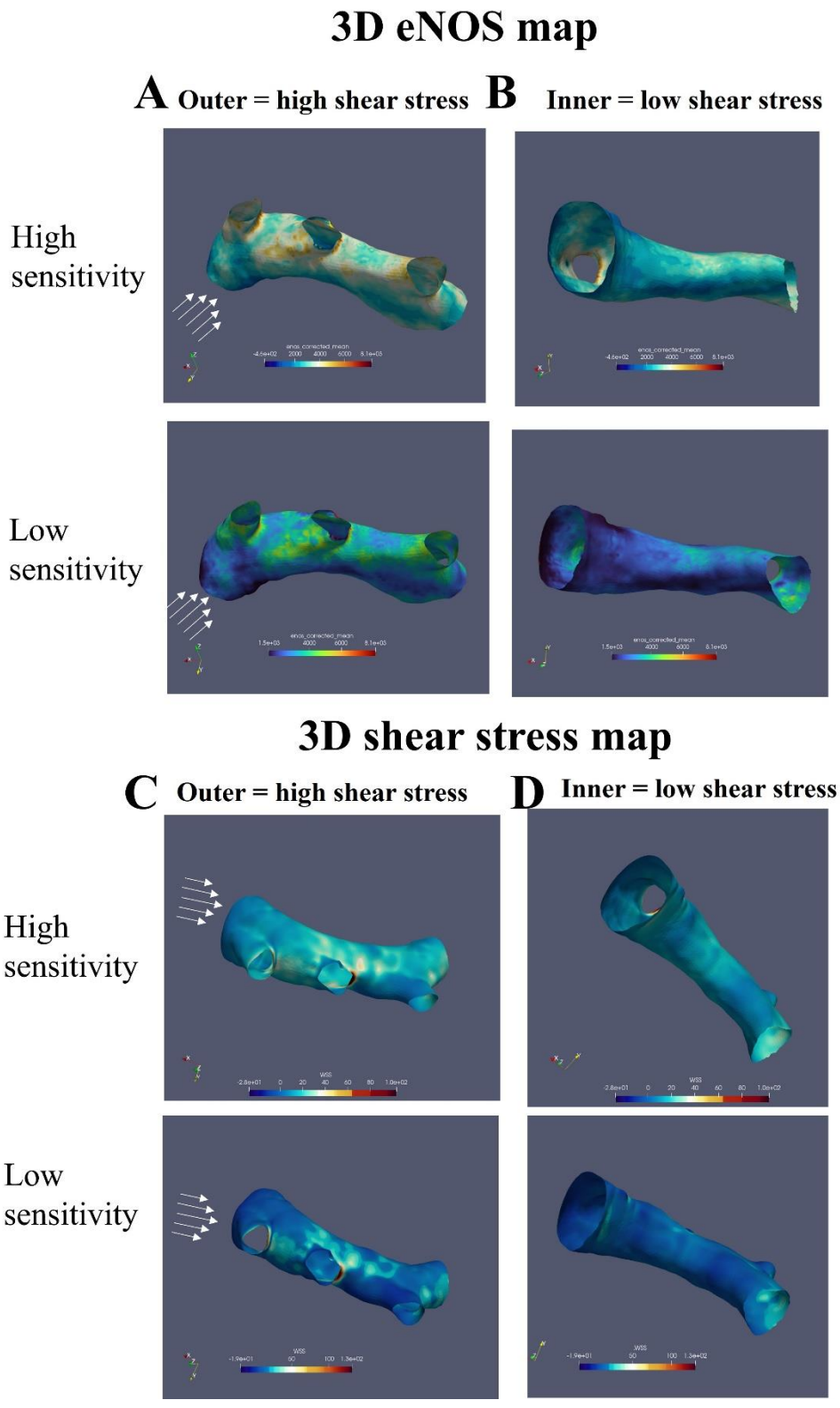

Figure 3. 23 3D WSS map and eNOS level map in healthy aorta (A) View of outer curvature in eNOS map. (B) View of inner curvature in eNOS map. (C) View of outer curvature in shear stress map. (D) View of inner curvature in shear stress map. Upper panels were maps with high sensitivity and lower panels were maps with low sensitivity. WSS, wall shear stress. White arrow indicates flow direction.

3.5.3 2D shear stress map and eNOS correlation in healthy aorta

Next step, to test if eNOS level correlated spatially with HSS at a higher spatial resolution in healthy aortas, a 2-dimensional (2D) shear stress map was generated. The 2D shear stress map was unwrapped over a longitudinal axis (yellow line in Figure 3. 24 A), outer curvature and inner curvature of healthy aorta are shown in Figure 3. 24 B and C.

As shown 2D maps, the outer curvature area of heathy aorta experienced higher shear stress values (Figure 3. 24 B). Part of the inner curvature region (indicated as a white box) was exposed to LSS values (Figure 3. 24 B). Matching shear stress map with eNOS levels suggested that eNOS mean values were enhanced in outer curvature of aorta and decreased in part of the inner curvature region (indicated as a white box) of aorta (Figure 3. 24 C).

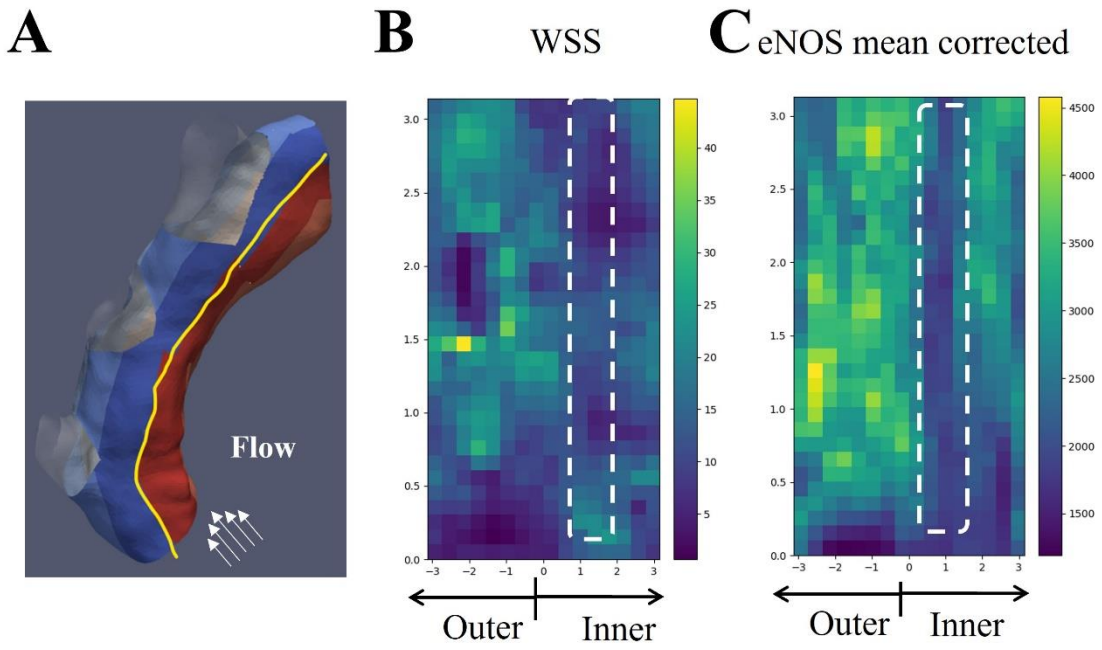

Figure 3. 24 2D maps for eNOS values and shear stress values comparison in healthy aorta. (A) 2D shear stress map was generated; blue region is outer curvature and red region is inner curvature of aorta. (B) to (C) 2D maps. X axis represented outer curvature (0 to -3) and inner curvature (0 to +3) of healthy aorta. Y axis represented wall shear stress value (B) and corrected eNOS mean value (C). WSS, wall shear stress. White arrow indicates flow direction.

3.5.4 Longitudinal averaging plots in healthy aorta

Although shear stress appeared to correlate spatially with eNOS in 2D maps (Figure 3.24), it was important to analyse this relationship quantitatively. To do this, scatter plots were drawn between eNOS mean values and shear stress values. These plots did not show a clear relationship between shear stress and eNOS (Figure 3. 25 A). However, averaging plots longitudinally made the relationship between eNOS levels and shear stress values clearer (Figure 3. 25 B and C). To be more specific, I averaged all shear stress values or eNOS values longitudinally (over the aorta length), the mean values were presented as a blue line (Figure 3. 25 B and C). As illustrated in Figure 3. 25 D, the shear stress value ranged between 12-15.5 Pa. The correlation between shear stress value and eNOS mean value was linear positive ($r=0.55$, $p=0.027$) (Figure 3. 25 D).

The difference between correlation scatter plots and longitudinal averaging is demonstrated in Figure 3. 26 and Figure 3. 27. It was exhibited in Figure 3. 26 C that scatter plots of shear stress values verse eNOS values. For instance, a dot in scatter plot (Figure 3. 26 C) represented one sector about 27 shear stress values in Figure 3. 26 A and one sector about 3500 eNOS values in Figure 3. 26 B.

Apparently, there was quite some ‘noise’ along the length of the aorta, the reason could be due to the presence of side branches or due to the segmentation was not accurate enough. Averaging longitudinally made the eNOS-shear stress correlation became clearer by reducing the effect of the ‘noise’. As shown in Figure 3. 27 E, one dot in the scatter plot (mark with red circle) represented the longitudinally averaged means of shear stress value and eNOS value in Figure 3. 27 C and D.

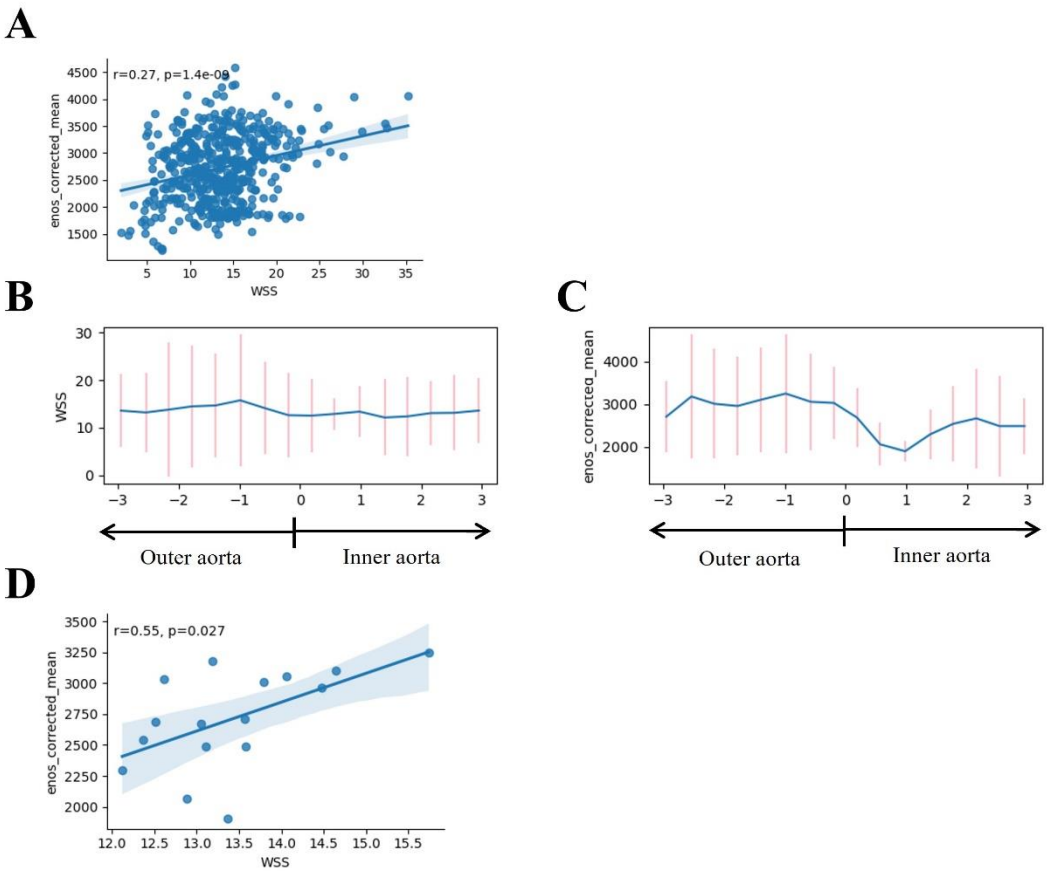

Figure 3. 25 Scatter plots between eNOS levels and WSS values in healthy aorta (A)Scatter plots between eNOS mean values and shear stress values. Longitudinal average plots of (B) shear stress values and (C) eNOS mean values. Red lines represent the standard deviation, blue line represents the mean value. (D) Association plot between shear stress value and eNOS mean values. WSS, wall shear stress.

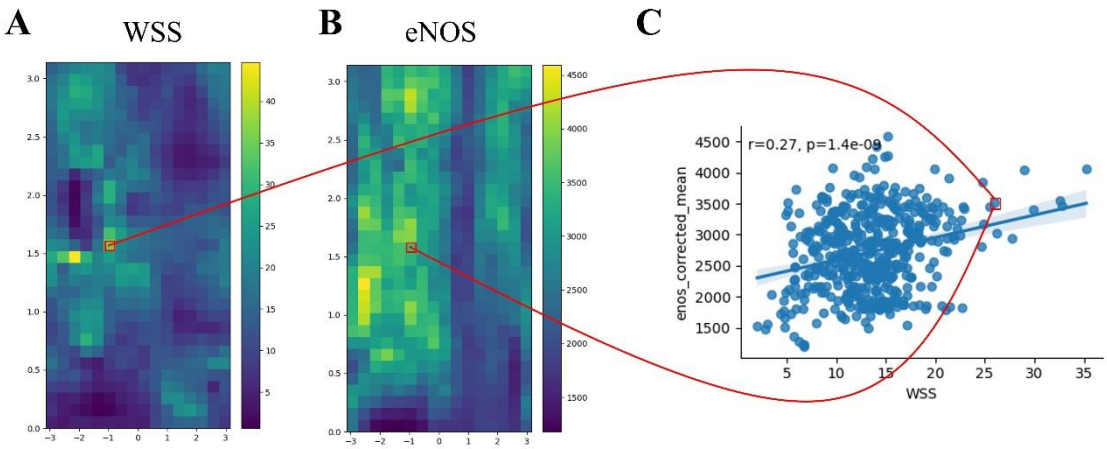

Figure 3. 26 Scatter plot of Wall shear stress map and eNOS map (A) Shear stress map (B) eNOS level map (C) Scatter plots of shear stress value (x-axis) and eNOS value (y-axis) for all sectors.

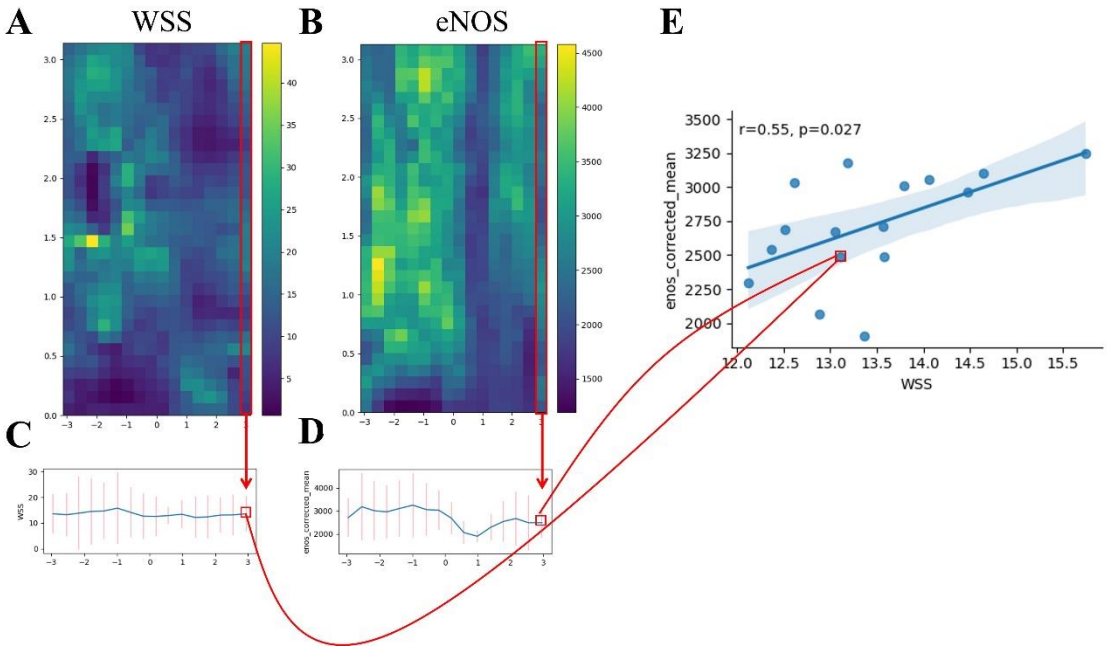

Figure 3. 27 Longitudinal averaging illustration (A) Shear stress map. (B) eNOS level map. (C) Longitudinal average plots of shear stress map. (D) Longitudinal average plots of eNOS level map. (E) Scatter plot of wall shear stress value (x-axis) and eNOS value (y-axis) for averaged profile.

3.5.5 eNOS intensity mean calculation in diseased aortas

I then used the approaches optimized with a healthy aorta to determine if eNOS intensity correlates spatially with shear stress in diseased aorta containing plaque. As shown in Figure 3. 28 A and B, the intensity in CDH5 channel and eNOS channel was detected across the diseased aorta. To define the endothelium spatially, I set an intensity threshold about 255 in CDH5 channel (Figure 3. 29 B), only pixels above this threshold were considered endothelial layer, pixels under the threshold were considered auto-fluorescence. As shown in Figure 3. 29 B, this resulted in an endothelial layer of about -50uM to 80uM thickness. This endothelial definition was used for mean eNOS computation (Figure 3. 29 C). I used 2D view of light-sheet imaging to exhibit why setting threshold in CDH5 channel can help to define endothelium spatially. Figure 3. 30 A showed CDH5 channel had auto-fluorescence around the endothelium (blurry green signal). Figure 3. 30 B showed pixels above threshold in CDH5 channel and structure of diseased aorta was clear. The same endothelial definition was applied to eNOS channel (Figure 3. 30 C). Figure 3. 30 C also showed the eNOS staining was specific to endothelium.

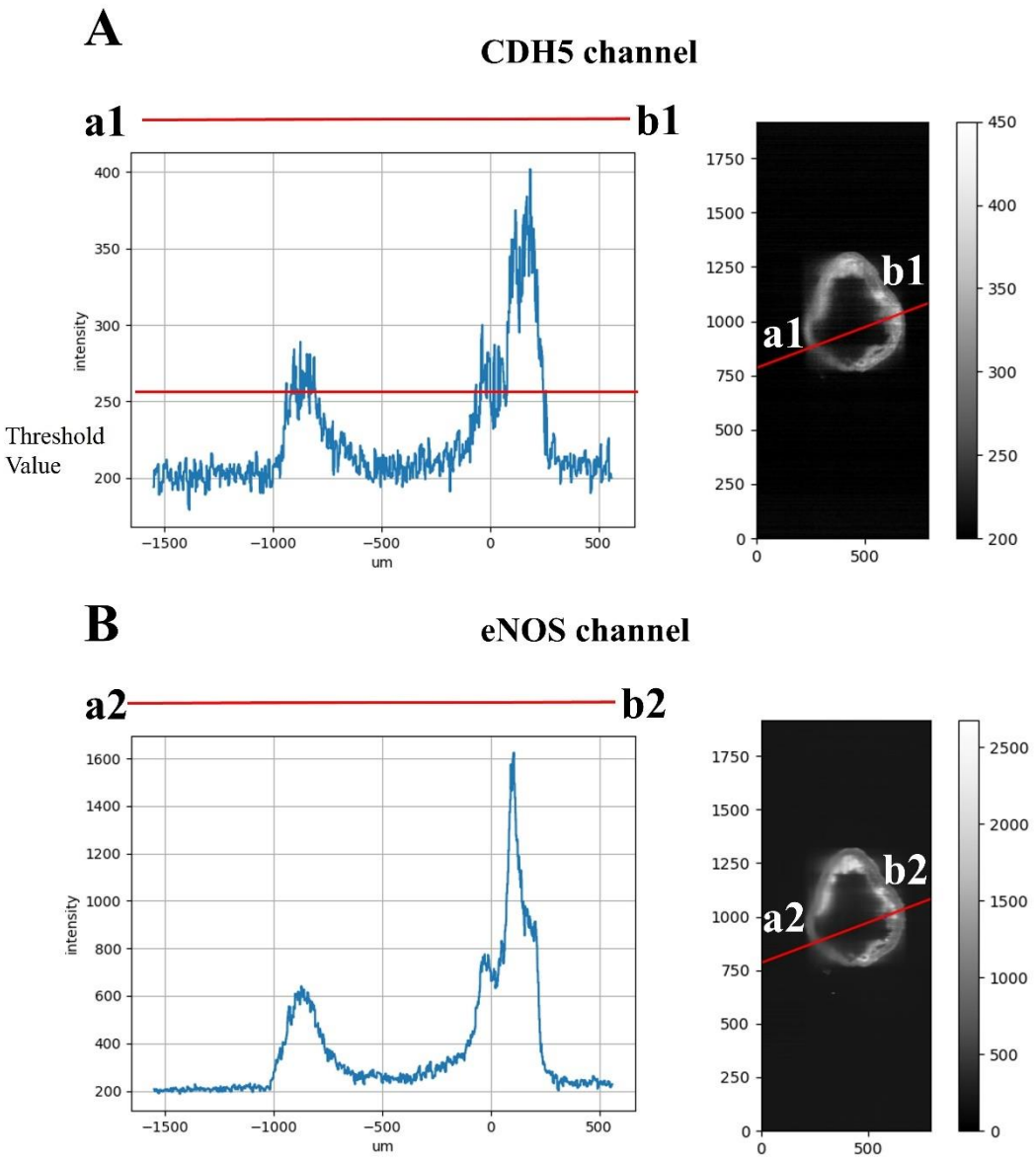

Figure 3. 28 Example for CDH5 and eNOS channel intensity across the diseased aortas (A) Example of CDH5 channel (intensity plot showed intensity of CDH5 channel across the aorta from a1 to b1). (B) Example of eNOS channel (intensity plot showed intensity of eNOS channel across the aorta from a2 to b2).

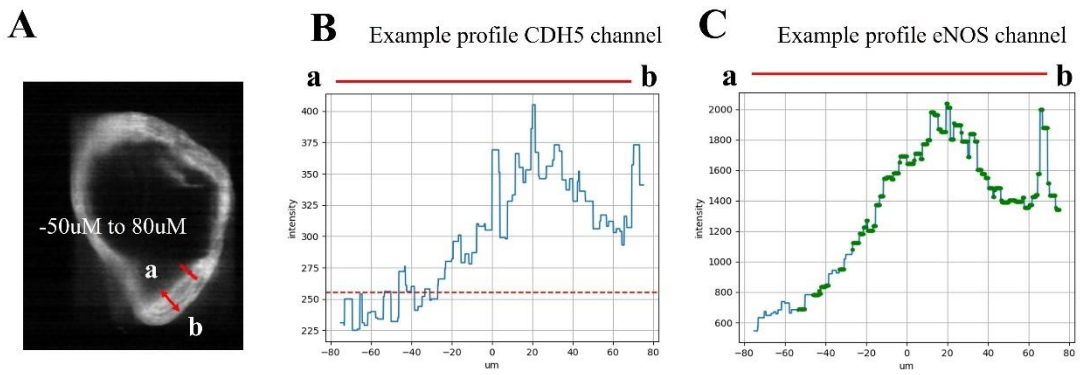

Figure 3. 29 eNOS projection on segmentation surface in diseased aorta (A) Slice was created from light-sheet data, Python software was used to extract pixel intensity of CDH5 channel and eNOS channel. (B) example profile of CDH5 channel, intensity threshold is 255, endothelial layer of about -50uM to 80uM. (C) The same endothelial definition was applied in eNOS channel, ranged from -50uM to 80uM.

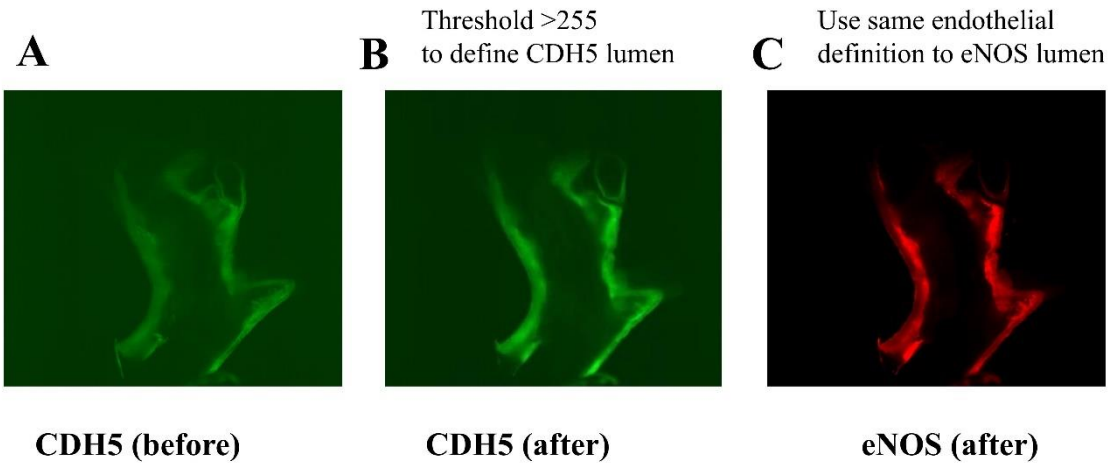

Figure 3. 30 2D view of CDH5 channel and eNOS channel after setting the threshold in diseased aorta. (A) 2D view of CDH5 channel before setting threshold. (B) 2D view of CDH5 channel after setting threshold. (C) 2D view of eNOS channel using same endothelial definition.

3.5.6 eNOS projection on computational fluid dynamics segmentation in diseased aortas

After computing the mean eNOS value in diseased aorta, I then sought to project eNOS values onto segmentation used for WSS map in diseased aortas. Figure 3. 31 shows a shear stress map and eNOS map co-registered in diseased aorta. eNOS values were projected onto shear stress map lumen surface (Figure 3. 31) so that a 3D eNOS values map in diseased aorta was generated.

As shown in plaque thickness map, plaques were observed in the region of brachiocephalic artery, left common carotid artery and in the inner curvature of aortic arch (Figure 3. 32 E and F). WSS maps in diseased aorta have shown that the outer curvature, brachiocephalic and left common carotid artery of diseased aorta had high shear values. On the other hand, shear stress values were decreased in distal part compared to proximal part of plaque (Figure 3. 32 C and D). 3D eNOS maps of diseased aorta were demonstrated with both high sensitivity and low sensitivity, both outer curvature of aortic arch and plaque region had high eNOS values (Figure 3. 32 A and B). Notably, the proximal part of plaque had extremely high eNOS values compared to distal part of plaque (Figure 3. 32 A and B). The entrance of brachiocephalic artery and left common carotid artery also had high eNOS levels (Figure 3. 32 A and B). Therefore, macroscopic analysis suggested a relationship between shear stress and eNOS.

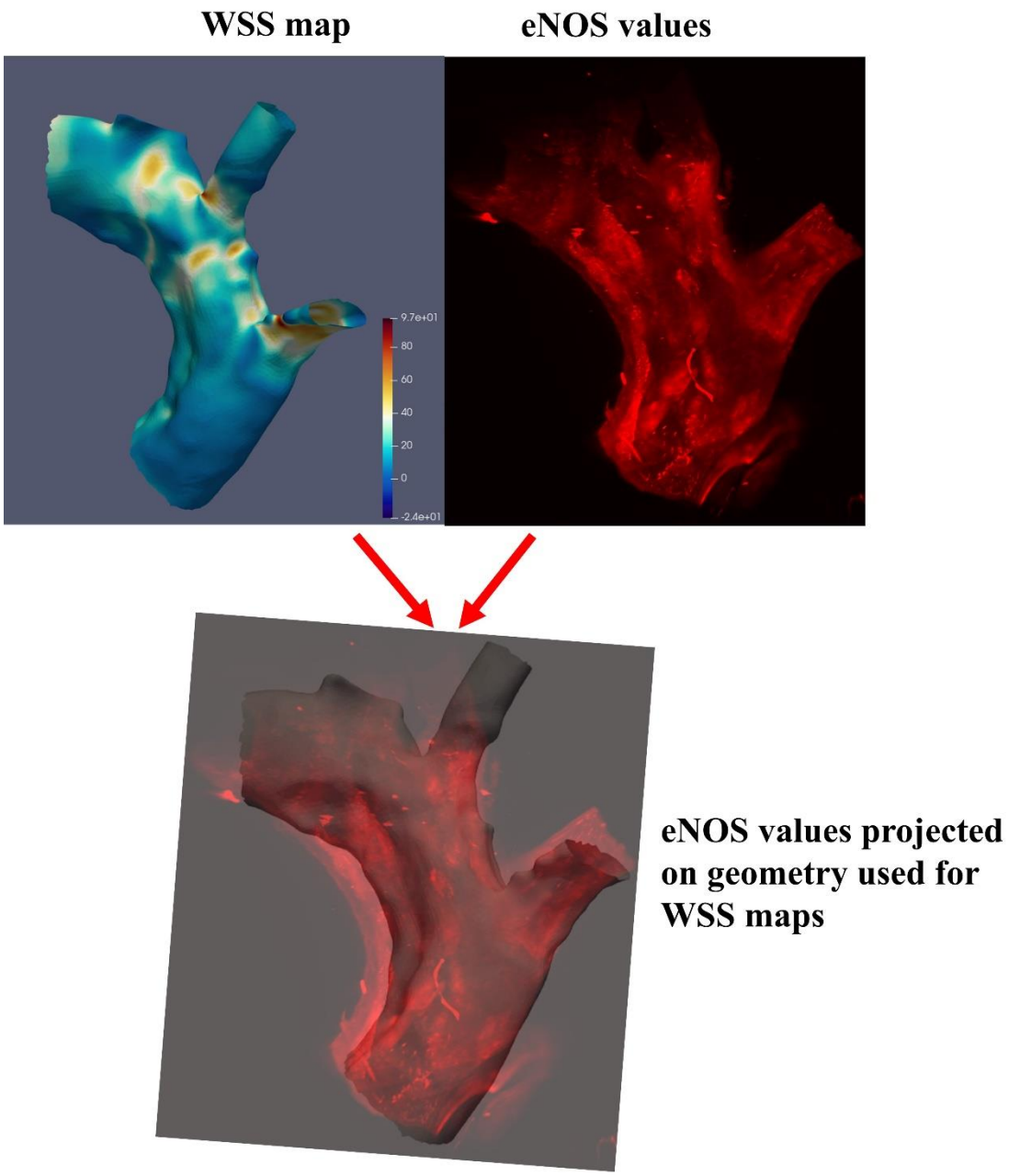

Figure 3. 31 Flow work of eNOS projection segmentation used for WSS map in diseased aorta. Shear stress map (left) and eNOS channel (right) of light-sheet imaging. Project eNOS channel on segmentation used for WSS map.

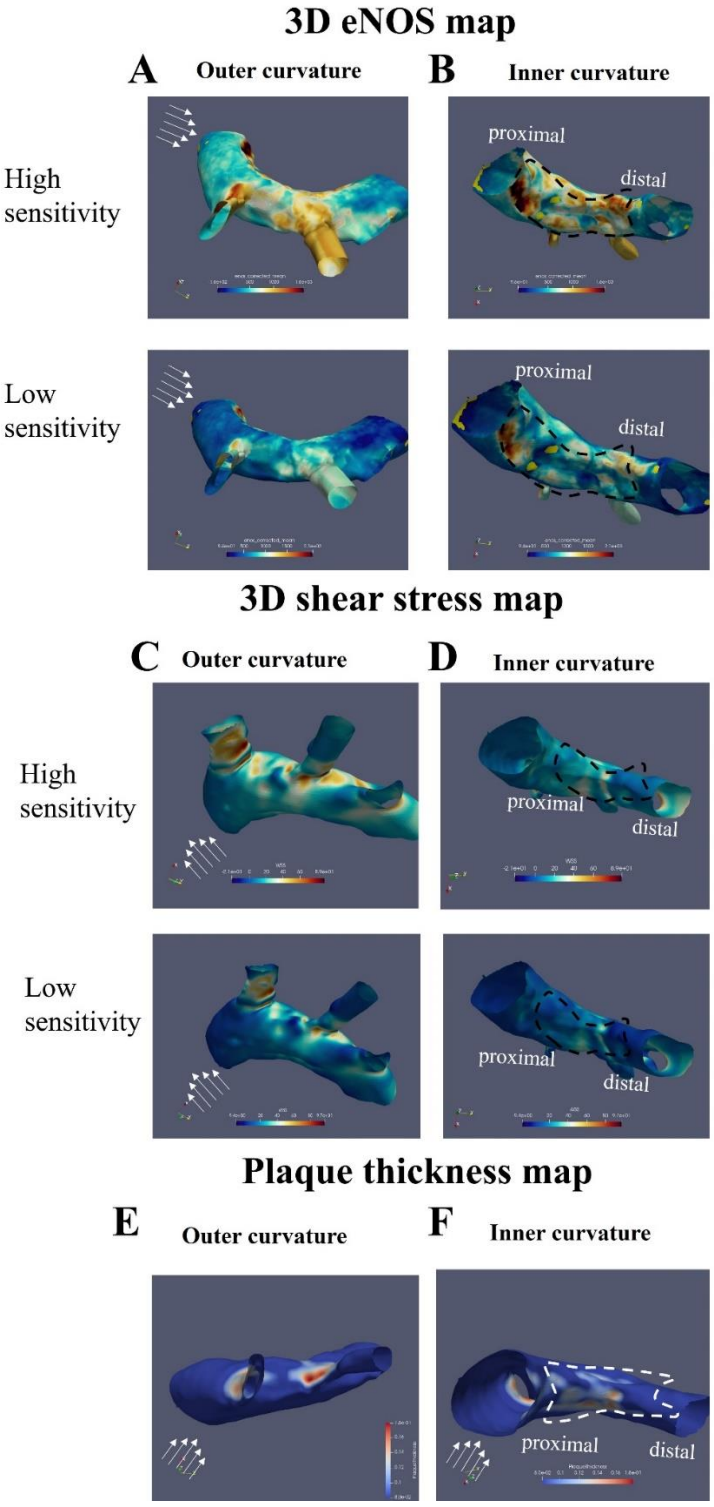

Figure 3. 32 3D eNOS map, WSS map and plaque thickness map. (A) View of outer curvature in eNOS map. (B) View of inner curvature in eNOS map. (C) View of outer curvature in WSS map. (D) View of inner curvature in WSS map. (E) View of outer curvature in plaque thickness map. (F) View of inner curvature in plaque thickness map. (A) to (D): Upper panels were maps with high sensitivity and lower panels were maps with low sensitivity. White arrow indicates flow direction. WSS, wall shear stress.

3.5.7 2D shear stress map and eNOS correlation in diseased aorta

Next step, to test if eNOS level has one to one correlation with HSS in diseased aortas, a 2D shear stress map was generated. The 2D shear stress map was unwrapped longitudinally from the 3D maps (yellow line; Figure 3. 33 A).

As shown in 2D shear stress map, the outer curvature area of diseased aorta experienced higher shear stress values (Figure 3. 33 B). The proximal part of plaque (labelled with red box) was exposed to higher shear stress values compared to distal part of plaque (labelled with white box) (Figure 3. 33 B). Correlating shear stress map with eNOS levels, eNOS mean values were enhanced in outer curvature of aorta and in proximal part of plaque (labelled with red box) (Figure 3. 33 B and D). It was observed that regions of high plaque thickness values were matched with high eNOS levels (Figure 3. 33 C and D). Thus, it appeared that eNOS and shear stress were correlated in the 2D maps, however further work including a quantitative assessment was needed to test this further.

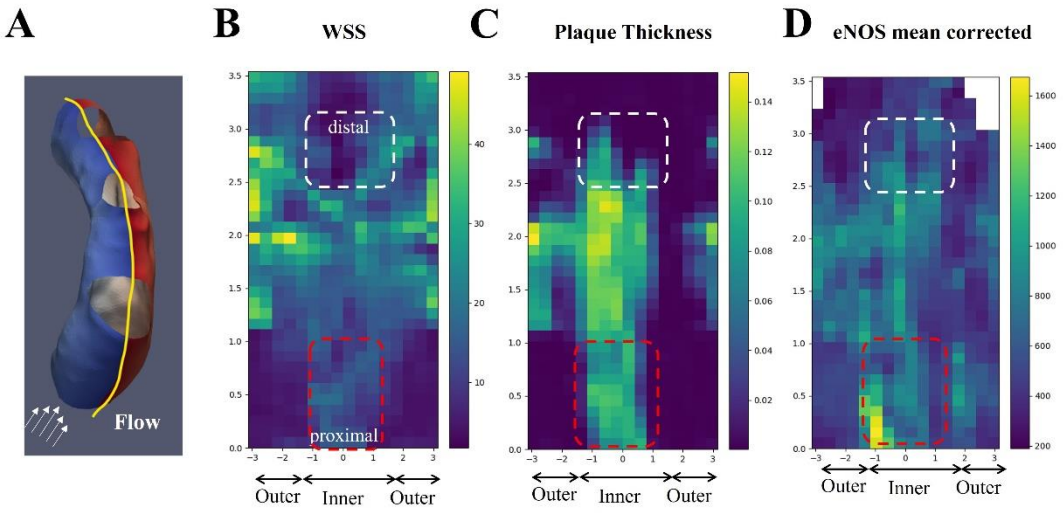

Figure 3. 33 2D maps for eNOS values and shear stress values comparison in diseased aorta. (A) 2D shear stress map was unwrapped over the outer aortic wall (yellow line). (B)-(D)2D map, proximal of plaque (upstream) was marked with red line, distal of plaque (downstream) was marked with white line. WSS, wall shear stress. White arrow indicates flow direction.

3.5.8 Longitudinal averaging plots in diseased aorta

Since the longitudinal averaging method was validated in healthy aorta, I also averaged plots longitudinally in diseased aorta (Figure 3. 34 C, D and E). The correlation between shear stress value and eNOS mean value was less clear compared to healthy aorta (r=0.21, p=0.44; Figure 3. 34 F). However, there was a linear positive correction between plaque thickness and eNOS mean value (r=0.86, p=2.2e-05; Figure 3. 34 G).

Overall, the current approach did not confirm a linear relationship between eNOS and shear stress in the diseased aorta. One possibility is that this is a true reflection of the biology and that eNOS and shear stress do not correlate spatially in plaques. However, it is also possible that this result reflects a technical insufficiency. It occurred to me that the registration between OPT and lightsheet could be inaccurate, and therefore I decided to repeat that analysis using lightsheet imaging as the basis for shear stress mapping.

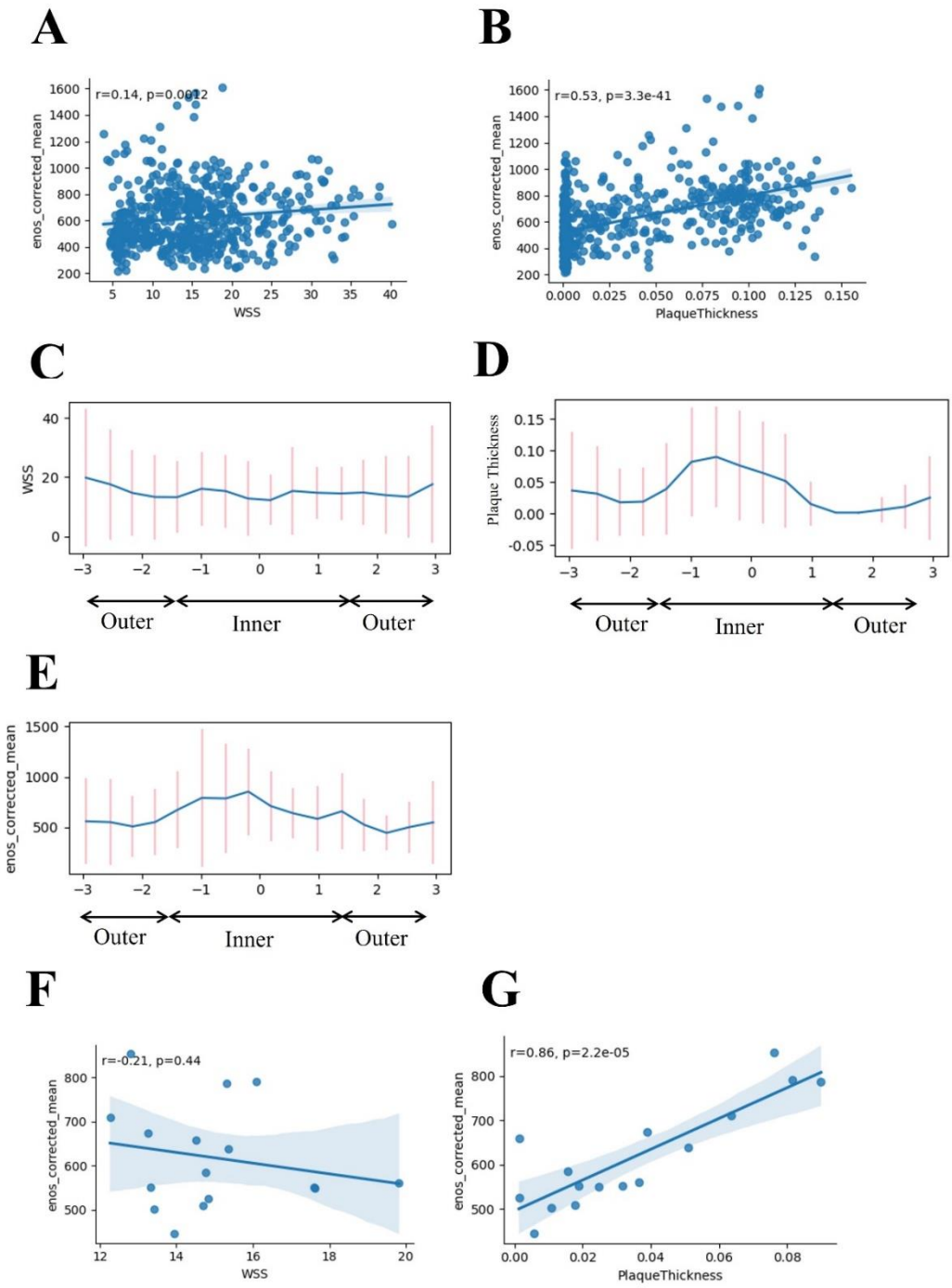

Figure 3. 34 Scatter plots between eNOS levels and WSS values in diseased aorta Scatter plots between (A) eNOS mean values and shear stress values; (B) eNOS mean values and plaque thickness; longitudinal average plots of (C) shear stress values, (D) plaque thickness and (E) eNOS mean values. Red lines represent the standard deviation, blue line represents the mean value. (F)Association plot between shear stress value and eNOS mean values. (G) Association plot between eNOS mean value and plaque thickness.

3.5.9 Computational fluid dynamics projection on eNOS segmentation (new method)

Since registration of OPT imaging and light sheet imaging may be suboptimal for complex structures such as atherosclerotic plaques, a new workflow was attempted where lightsheet imaging was used for both the segmentation for computational fluid dynamic modelling (shear stress) and for eNOS mapping. As shown in Figure 3. 35, lumen narrowing was observed, and shear stress values were increased at the narrow area and outer curvature (Figure 3. 35 C and D). eNOS levels were varied over the plaque, the upstream side of the plaque (proximal) experienced high eNOS levels whereas the downstream side of the plaque (distal) experienced low eNOS levels (Figure 3. 35 A and B).

To correlate shear stress values and eNOS values, 2D maps were generated (Figure 3. 36). It was clear that the proximal part of the plaque experienced higher eNOS values compared to the distal part of plaque in 2D eNOS maps (Figure 3. 36 B). Correlation scatter plots were attempted to reveal the relationship between eNOS levels and shear stress values over plaque (Figure 3. 37 B). I averaged plots longitudinally as Figure 3. 37 A demonstrated and found that the correlation between shear stress value and eNOS mean values was linear positive ($r=0.93$, $p=1.9e-07$; Figure 3. 37 C).

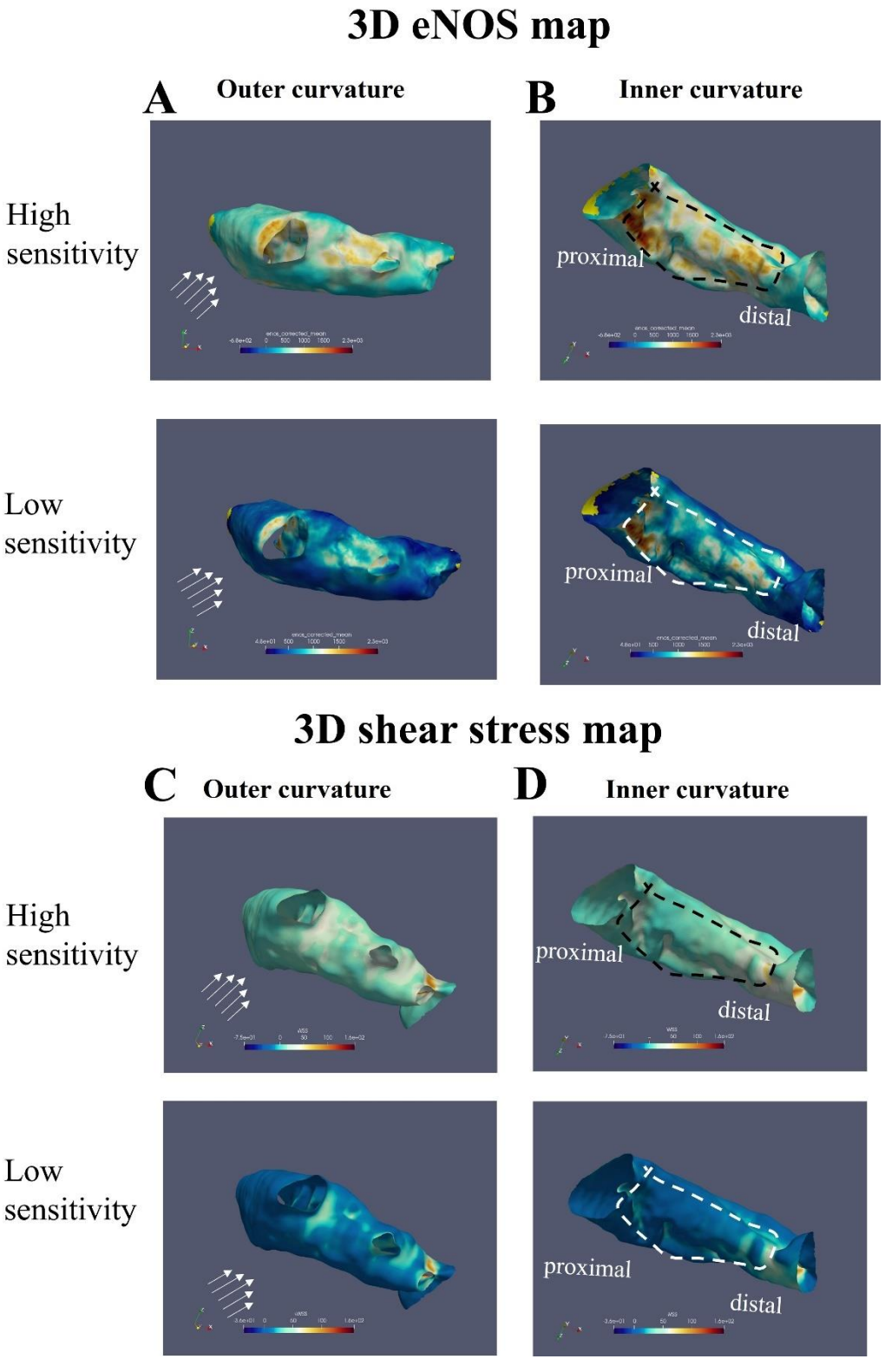

Figure 3. 35 3D wall shear stress map and eNOS level map of diseased aorta in new methods. 3D maps of A) and B) eNOS levels and C) and D) shear stress levels. Shear stress values were calculated and mapped on to eNOS segmentation. White arrow indicates flow direction. Note that images are shown in two orientations, brachiocephalic and left common carotid arteries were cut during segmentation.

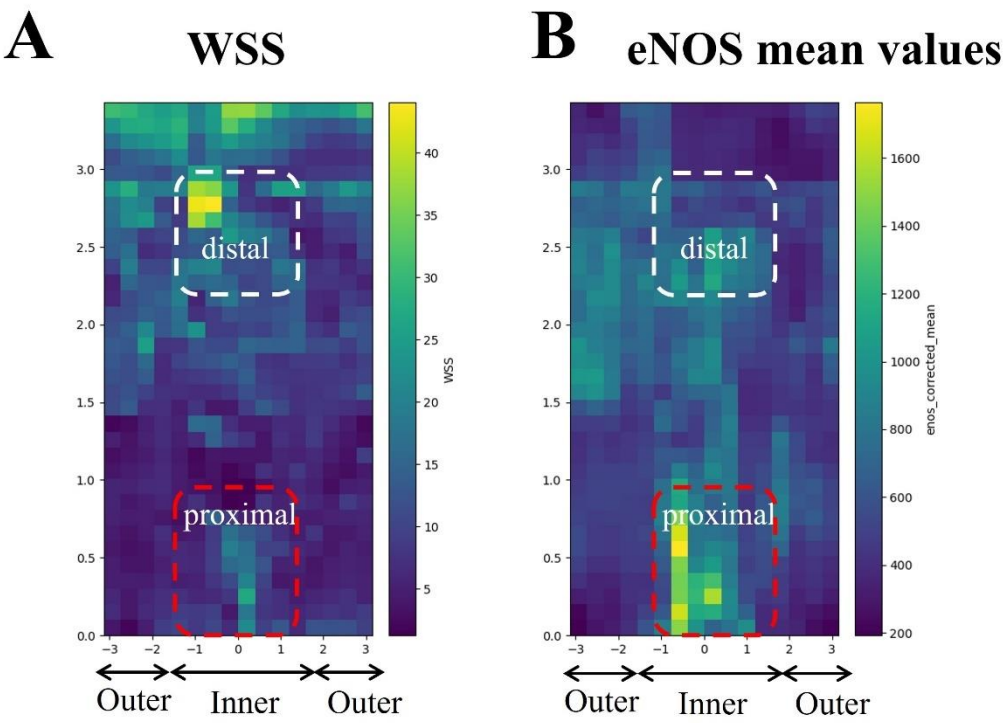

Figure 3. 36 2D maps for eNOS values and shear stress values comparison of diseased aorta in new method. 2D maps of A) Shear stress maps and B) eNOS levels map. Proximal of plaque (upstream) was marked with red line, distal of plaque (downstream) was marked with white line.

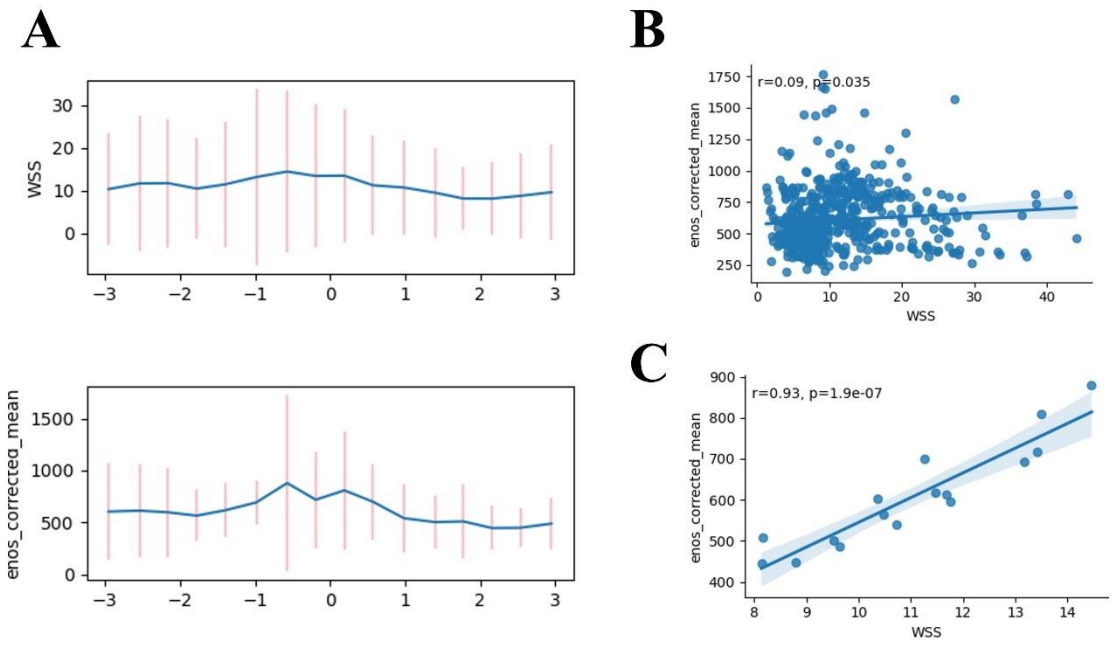

Figure 3. 37 Scatter plots between eNOS levels and WSS values of diseased aorta in new method A) longitudinal average plots of shear stress values and eNOS mean values. Red lines represent the standard deviation, blue line represents the mean value. B) Scatter plots between eNOS mean values and shear stress values. C) Association plot between shear stress value and eNOS mean values.

3.6 Conclusions

I conclude that:

- CUBIC clearing, immunofluorescent staining coupled to light-sheet imaging preserves 3D geometry of aortic arch and can be used to analyse the spatial distribution of specific proteins in the murine aorta.
- A system for analysing the spatial distribution of proteins and correlating them with local shear stress was established both in healthy and diseased aortas.
- Shear stress mapping of healthy aorta confirms outer curvature of healthy aortic arch experiences higher shear stress values compared to inner curvature of arch.
- Shear stress mapping of diseased aorta shows outer curvature experiences higher shear stress values. There was no clear difference in WSS in the proximal part (upstream) of plaque compared to the distal part (downstream) of plaque. However, WSS varied over the plaque and coupled with eNOS levels.
- eNOS expression level is enhanced at outer curvature compared to inner curvature of the healthy murine aortic arch.
- eNOS expression level is upregulated at outer curvature and proximal part (upstream) of plaque compared to distal part (downstream) of plaque in diseased aortas.

The correlation between HSS and ECs in rupture-prone plaque was investigated in this project. Overall, this study confirms eNOS as a HSS marker in healthy aorta, and also revealed a positive correlation between WSS and eNOS levels in atherosclerotic plaques in diseased aorta. In this chapter, two techniques were attempted to preserve arterial 3D geometry in terms of Airy-scan confocal microscopy of curved tissues and light sheet microscopy of CUBIC cleared samples. In summary, CUBIC clearing in combination with light sheet microscopy resulted in efficient clearing and imaging, moreover, it preserved the 3D geometry of arch. Notably, the study establishes a system to couple light-sheet imaging, OPT imaging and computational fluid dynamics to correlate protein expression with local shear stress in both healthy and diseased aortas. Since Jolanda Wentzel's group (Erasmus MC, Rotterdam, the Netherlands) run same simulations in both healthy aorta case and diseased aorta case, the magnitude of shear stress in healthy and diseased aorta is comparable. By comparing the scatter plots, it was observed that the majority of shear stress values for healthy aorta ranged between 5 Pa to20 Pa, with a total range of 5 Pa to 35 Pa. In contrast, the range of shear stress values for diseased aorta was

between 0 Pa to 40 Pa, indicating a higher WSS magnitude in diseased aorta. Moreover, comparing the longitudinal averaging plots showed that healthy aorta had a WSS range of 12.0 Pa to 15.5 Pa, while diseased aorta had a wider range of 8 Pa to 14 Pa, with more low shear stress values. To summarize, all of the results showing that shear stress values are complex and varied over plaque.

3.7 Discussion

3.7.1 eNOS analysis in healthy aorta

The effect of shear stress on the initiation of atherosclerosis is well established, however, the role of shear stress on plaque rupture is controversial. To address this, I planned to detect and isolate HSS endothelial cells in plaques. Therefore, the first aim was to establish a method to identify HSS regions in plaques. In this Chapter, I have explored three methods in terms of normal confocal microscopy of flattened tissue, Airy-scan confocal microscopy of curved tissues and light sheet microscopy combined with CUBIC clearing. All methods confirm that eNOS as a HSS marker in healthy murine aortas.

I also developed a new system to correlate protein levels with local shear stress in healthy aorta. Using this, it was observed that eNOS levels were increased in the outer curvature of healthy murine aorta compared to inner curvature of aorta. Also, shear stress values are higher in the outer curvature compared to inner curvature of the aortic arch. In summary, eNOS correlated with HSS in healthy aorta. Moreover, there was a linear positive correlation between eNOS level and shear stress values in 2D shear stress maps in healthy murine aorta.

Several other studies have shown that elevation of eNOS expression is correlated with HSS (Cai et al., 2004). Endothelial cells sense shear stress by the activation of receptors such as VE-cadherin (CDH5) (vascular endothelial cadherin) and PECAM-1 (Platelet/endothelial cell adhesion molecule-1 (Chistiakov et al., 2017). This signal is converted through phosphatidylinositol 3-kinase (PI3K)/protein kinase B (AKT), mitogen-activated protein kinase kinase 5 (MKK5) and extracellular-signal-regulated protein kinase 5 (ERK5) pathway, which in turn activate myocyte enhancer factor 2 (MEF2), KLF2 and induce eNOS expression (Chistiakov et al., 2017). From a physiological perspective, exposure of endothelial cells to HSS will lead to increased expression of vasodilatory and anti-inflammatory molecules such as eNOS to maintain cardiovascular homeostasis (Chistiakov et al., 2017).

3.7.2 eNOS analysis in plaque

Although eNOS is a HSS marker in healthy aorta, it was not clear if eNOS correlates with HSS in plaque ECs. In plaque ECs, due to the effects of disturbed flow on endothelium around atherosclerotic plaques, it has been suggested that eNOS expression may be downregulated and ROS (reactive oxygen species) is upregulated in endothelial cells (Heo et al., 2011). Thus, it is possible that eNOS does not provide protection in the pathophysiology of atherosclerosis. As a result, it should be careful to use eNOS as a marker for HSS. The relationship between HSS and eNOS in plaques was a major aim of this study.

After validation of light-sheet imaging and computational fluid dynamics in healthy aorta, I used the same method to analyze diseased aorta. It was observed that eNOS levels were enhanced in outer curvature and proximal part (upstream) of plaque compared to distal part (downstream) of plaque in diseased aorta. In terms of shear stress values in diseased aorta, there was no clear difference between proximal part and distal part of plaque. However, shear stress values varied over plaque and coupled with eNOS levels.

It was observed that the spatial distribution of eNOS protein is different in proximal versus distal of plaque. However, when OPT imaging was used to generate shear stress maps, it was observed that WSS and eNOS protein did not have a linear positive correlation in the diseased aorta. A possible reason could be that WSS and eNOS are not correlated over plaques, for instance, there could be high eNOS levels at distal region of plaque (LSS site). Another reason could be due to technical problems that lumen segmentation is not accurate enough, leading to incorrect WSS values and eNOS values. The OPT images of diseased aorta leads to a very irregular lumen surface that is difficult to segment, therefore the resulting segmentation might not be representable of the actual lumen geometry of diseased aorta. To resolve this problem, I projected computation fluid dynamics on eNOS segmentation from light-sheet imaging. This methodology revealed a positive correlation between WSS and eNOS levels in the longitudinal averaging plots.

Thus, it was concluded that eNOS can be used as a marker of HSS in healthy arteries and plaques; a feature that is important for Chapter 4 of this thesis.

Chapter 4. Transcriptome analysis of HSS endothelium in healthy versus diseased aorta

4.1 Introduction

The role of shear stress in controlling atherosclerotic plaque progression is controversial. While there is consensus between different research groups that LSS leads to atherosclerotic plaque growth, there is conflicting data on which shear stress profile induces atherosclerosis progression and plaque rupture with the suggestions that high, low or oscillatory shear stress are the most important drivers (Samady et al., 2011; Stone et al., 2018). However, there is still a lack of understanding of shear stress in plaque rupture, as our group observed, shear stress is the 'dark energy' of the vasculature due to its crucial roles in vascular biology and its effects are largely unrevealed (Evans et al., 2021). These different observations could be because of differences in technology, for instance, different analysis methodology and imaging modalities or differences in patient groups selected. It is well known that HSS confers protection from early atherosclerosis in healthy arteries, and therefore the suggestion from some groups that HSS can drive plaque progression is surprising. However, it is plausible that the effects of HSS may differ between healthy arteries and plaques. Therefore, it is necessary to develop unbiased approaches to assess high shear vascular responses in healthy arteries and plaques.

4.2 Hypothesis and Aims

I hypothesized that endothelial cells in plaques and healthy aorta respond differently to HSS, and these differences could lead to different shear stress profiles in healthy arteries and plaques.

To test this hypothesis, I aim to:

1. Perform scRNA-seq of healthy normocholesterolemic mice (WT mice), mice with hypercholesterolemia (*ApoE*$^{-/-}$ mice exposed to normal diet; ND) and mice with extreme hypercholesterolemia (*ApoE*$^{-/-}$ mice exposed to high fat diet; HFD).
2. Since eNOS was validated as a HSS marker in healthy arteries and plaques (Chapter 3), I will identify EC exposed to HSS by computationally selecting eNOS^{high} cells.
3. Compare the transcriptome in HSS EC (eNOS^{high}) in WT mice, *ApoE*$^{-/-}$ ND mice and *ApoE*$^{-/-}$ HFD mice.

4.3 ScRNA-seq of WT mice, *ApoE*$^{-/-}$ ND mice and *ApoE*$^{-/-}$ HFD mice

To analyse scRNA-seq data of WT mice, *ApoE*$^{-/-}$ ND mice and *ApoE*$^{-/-}$ HFD mice, our group collaborated with Simon's group and merged two datasets together (method described in Chapter 2). The scRNA-seq data from Simon's group was performed with four groups of mice: *ApoE*$^{-/-}$ ND mice, *ApoE*$^{-/-}$ HFD mice, *TGF-βR*$^{iEC\text{-}ApoE}$ ND mice and *TGF-βR*$^{iEC\text{-}ApoE}$ HFD mice (note that data from *TGF-βR* was removed since I was not interested in this particular feature). Studies have illustrated cholesterol levels in WT mice, *ApoE*$^{-/-}$ ND mice and *ApoE*$^{-/-}$ HFD mice. For instance, a study showed that *ApoE*$^{-/-}$ mice on normal diet have 0.02% cholesterol and *ApoE*$^{-/-}$ mice on high fat diet have 0.15% cholesterol (Chamberlain et al., 2009). In summary, WT mice have healthy aortas with normal cholesterol. *ApoE*$^{-/-}$ ND mice have minimal plaque with high cholesterol. *ApoE*$^{-/-}$ HFD mice have large plaques with very high cholesterol. The high throughout sequencing yielded 3298 cells and 27498 genes. Cells that express "Feature Count" under 1500 or "Library Count" under 3000 were eliminated. 2547 cells and 11326 genes were included in the subsequent analysis.

The scRNA-seq data from our group generated by Dr Blanca Tardajos-Ayllon were generated from two groups of mice: WT mice and *Jag1* KO mice (note that data from *Jag1* was removed since I was not interested in this particular feature). The filtering method was same as Simon's data, yielded 991cells and 1670 genes per cell in dataset. After merging two datasets, only cells from WT mice, *ApoE*$^{-/-}$ ND mice and *ApoE*$^{-/-}$ HFD mice were selected for further analysis (BBrowser 2.10.10).

The scRNA-seq workflow is shown in Figure 4. 1. In both studies, whole aortas from aortic roots to iliac artery were dissected and digested by enzyme mixture to generate single cell suspensions. After antibody staining, FACS was used to sort CD31^{+} CD45^{-} live cells. eNOS^{high} cells in WT mice, *ApoE*$^{-/-}$ ND mice and *ApoE*$^{-/-}$ HFD mice were then selected as HSS endothelium for further analysis.

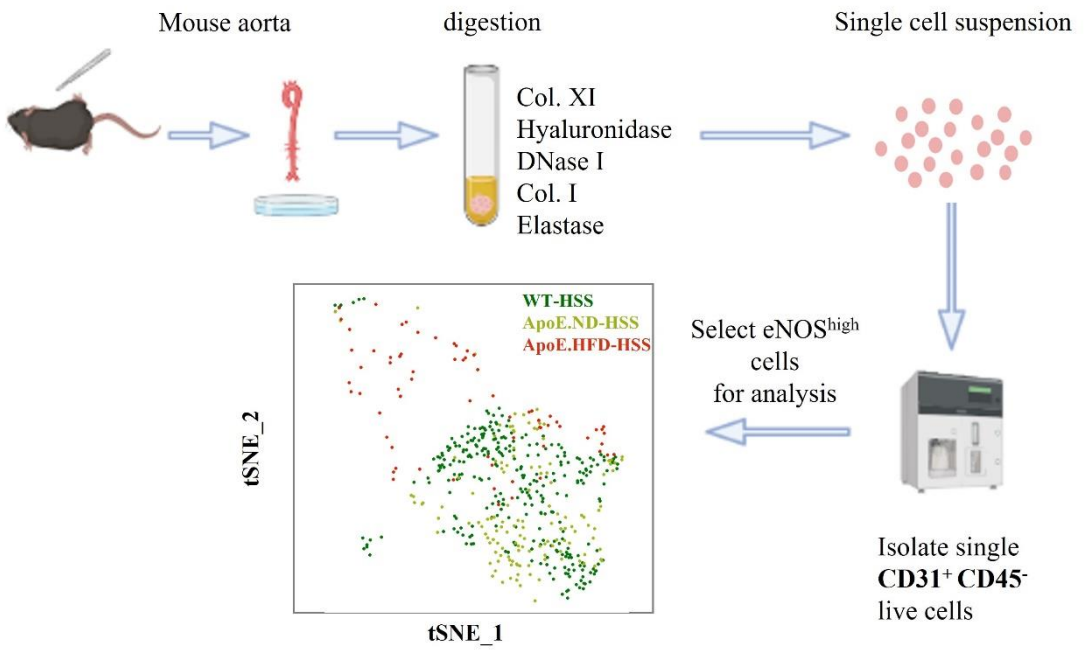

Figure 4. 1 Overview of scRNA-seq workflow. The whole murine aortas were digested by enzyme mixture (Collagenase XI, Hyaluronidase, DNase I, Collagenase I and Elastase) to generate single cell suspension. $CD31^+$ and $CD45^-$ live cells were sorted and sequenced. $eNOS^{high}$ cells were selected as HSS endothelium in WT mice, $ApoE^{-/-}$ ND mice and $ApoE^{-/-}$ HFD mice for further analysis.

4.4 Endothelial clusters and identification of smooth muscle cell (SMC) 'contamination'

As shown in Figure 4. 2, the scRNA-seq analysis identified 10 distinct clusters. Heatmap shows the highest differentially expressed genes for each cluster. Of these, six distinct clusters (0,1,2,3,5,8) were defined as endothelial cells clusters because they exhibit expression of canonical endothelial cell markers (Pecam1, Cdh5 and Vwf). Egfl7 and Ptprb were also known to be endothelial specific genes in angiogenesis (Sun et al., 2017; Usuba et al., 2019). Cluster6 defined as 'fibroblasts' exhibit fibroblasts markers (Lum, Dcn, Gsn). Cluster4 defined as a 'vascular smooth muscle cell cluster' exhibit SMC markers (Myh11, Myl9, Tagln). Cluster7 defined as a lipid cluster exhibit lipid markers (kdr, CD36, Fabp4) and Cluster 9 defined as membrane cluster.

Violin plots showing that SMC markers were enriched in cluster4, which means cluster 4 is identified as SMC contamination (Figure 4. 3 B). The composition of scRNA-seq profile was visualized by Pie chart, there were 26.7% WT cells, 33.3% *ApoE*$^{-/-}$ ND cells, 32.8% *ApoE*$^{-/-}$ HFD cells and 7.2% SMC contamination, and all SMC contamination was excluded from further analysis (Figure 4. 3 A). Clusters were identified in different groups and visualized by t-distributed stochastic neighbour embedding (t-SNE, Figure 4. 3 C). As exhibited in Figure 4. 3 C, endothelial cells from WT mice (green), *ApoE*$^{-/-}$ ND mice (yellow) and *ApoE*$^{-/-}$ HFD mice (red). Cluster 4,6,7,9 had few cells and diverged from the main part of plot (Figure 4. 3 C), in addition, top genes of cluster 6 shown in heatmap (Figure 4. 2) demonstrated that they were composed of SMC and fibroblasts. Therefore, clusters 4,6,7,9 were excluded from further analysis.

t-SNE plots were used to analyse the distribution of endothelial cells from WT mice, *ApoE*$^{-/-}$ ND mice and *ApoE*$^{-/-}$ HFD mice (Figure 4. 3 C). It was observed that distribution of endothelial cells in WT mice, *ApoE*$^{-/-}$ ND mice and *ApoE*$^{-/-}$ HFD mice were very different and non-overlapped (Figure 4. 3 C). Cluster1 was mainly composed of *ApoE*$^{-/-}$ HFD cells, cluster 2 was mainly composed of *ApoE*$^{-/-}$ ND cells and cells from WT mice (Figure 4. 3 C). Endothelial cells from WT mice were also abundant in cluster 0, 3, 5, and 8 (Figure 4. 3 C).

The influence of cholesterolemia on EC subsets was assessed by comparing the contribution of cells from WT mice, *ApoE*$^{-/-}$ ND mice and *ApoE*$^{-/-}$ HFD in each cluster, by number (Figure 4. 4 A) and by percentage of cells (Figure 4. 4 B). Cluster 0,5,8 are

mainly composed of endothelial cells from WT mice, cluster 2 is largely composed of endothelial cells from *ApoE*$^{-/-}$ ND mice, cluster 1 is mainly composed of endothelial cells from *ApoE*$^{-/-}$ HFD mice (Figure 4. 4 A and B).

To understand the function of each endothelial clusters (cluster 0,1,2,3,5,8), cluster-specific functional enriched gene ontology (GO) terms were identified as indicated in Figure 4. 5. For Cluster 0 the top GO terms are related to metabolic and development pathway and leukocyte adhesion (Figure 4. 5 A). For Cluster1 the top GO terms are related to angiogenesis, adhesion, apoptosis and pathways in cancer (Figure 4. 5 B). For Cluster2 the top GO terms are related to antigen presentation and interferon-beta (Figure 4. 5 C). For Cluster3 cells the top GO terms are associated with cell adhesion and insulin-related pathway (Figure 4. 5 D). For Cluster5 the top GO terms are related to cell-matrix adhesion and proliferation (Figure 4. 5 E). For Cluster8 the GO terms include receptor-mediated endocytosis (Figure 4. 5 F).

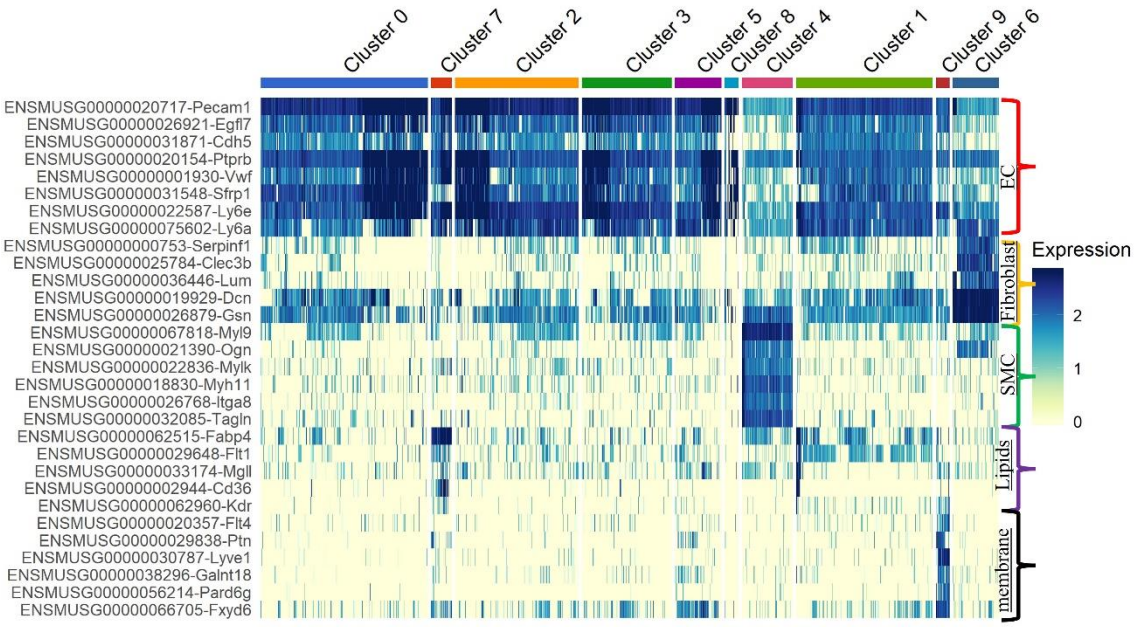

Figure 4. 2 Heatmap of top genes in each cluster. Heatmap demonstrating highly differentially expressed genes in each cluster. Six distinct clusters (0,1,2,3,5, 8) defined as endothelial cells exhibit expression of endothelial cell markers (Pecam1, Cdh5 and Vwf). Cluster6 defined as Fibroblast exhibit fibroblasts markers (Lum, Dcn, Gsn). Cluster4 defined as vascular smooth muscle cell cluster exhibit SMC markers (Myh11, Myl9, Tagln). Cluster7 defined as lipid cluster exhibit lipid markers (kdr, CD36, Fabp4) and Cluster 9 defined as membrane cluster. SMC: smooth muscle cells; EC: endothelial cells.

A

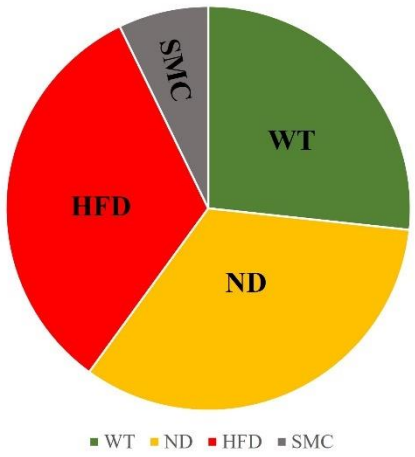

	Total WT	Total Apoe-ND	Total Apoe-HFD	SMC-contamination	Total cells
Cell Number	592	737	726	159	2214
Portion%	26.7%	33.3%	32.8%	7.2%	100%

B

VSMC markers: *Myl9*, *Ogn*, *Mylk*, *Myh11*, *Itga8*, *Tagln*

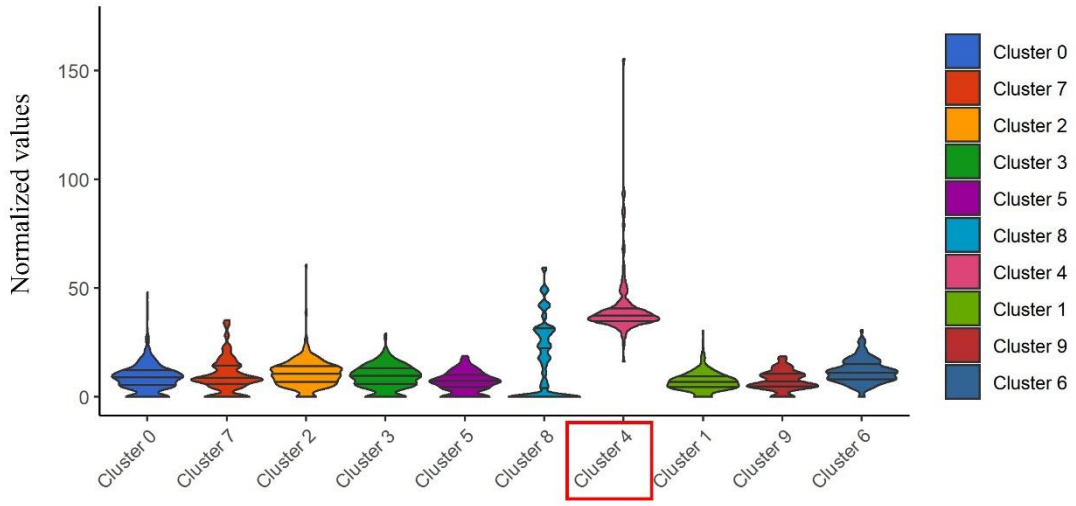

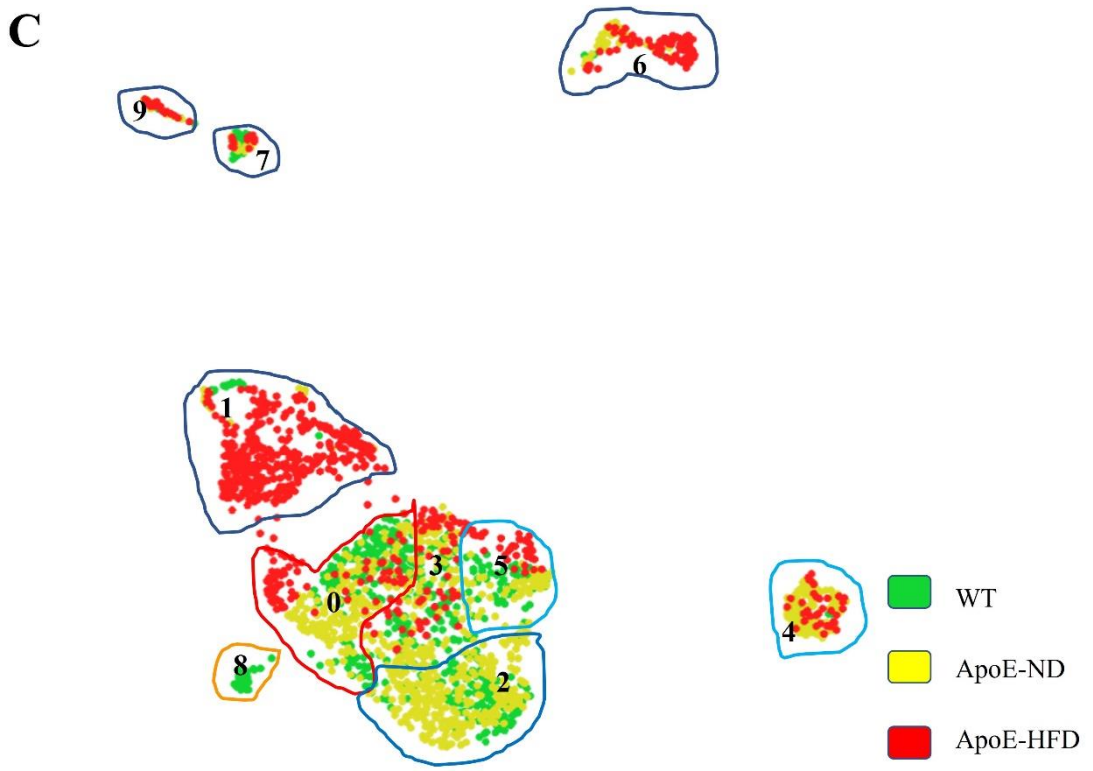

Figure 4. 3 Endothelial clusters identified by scRNA-seq: differences between WT, *ApoE*$^{-/-}$ ND and *ApoE*$^{-/-}$ HFD mice A) Pie chart showing the proportion of single cells that were identified in WT cells, *ApoE*$^{-/-}$ ND cells, *ApoE*$^{-/-}$ HFD cells. B) Violin plot of VSMC markers expression in each cluster. Y-axis represents normalized expression values calculated as a geometric mean of the mean expression values of several markers. C) t-distributed stochastic neighbor embedding (t-SNE) plots showed ten clusters identified from scRNA-seq. Colors summarizing distribution of single cells in WT cells (labeled green), *ApoE*$^{-/-}$ ND cells (labeled yellow), *ApoE*$^{-/-}$ HFD cells (labelled red). Unbiased hierarchical clustering was used to identify clusters. SMC: smooth muscle cells; EC: endothelial cells.

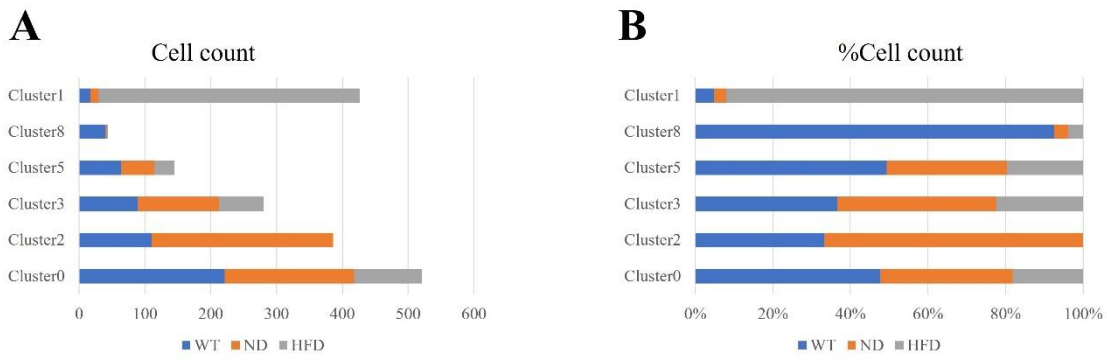

Figure 4. 4 Cluster distribution in WT, *ApoE*$^{-/-}$ ND and *ApoE*$^{-/-}$ HFD mice. Bar graph showing the cell distribution of WT mice, *ApoE*$^{-/-}$ ND mice and *ApoE*$^{-/-}$ HFD mice across endothelial cell clusters, by number of cells (A) and percentage of cells (B). To analyze the clusters composition in an unbiased way, the percentage of cells were calculated by cell number in cluster/cell number in whole RNA-seq profile. For example, cluster 0 have 221 WT cells, %cell count=221/592=37.3% (WT cells in cluster0/total WT cells in whole RNA-seq profile).

A cluster 0

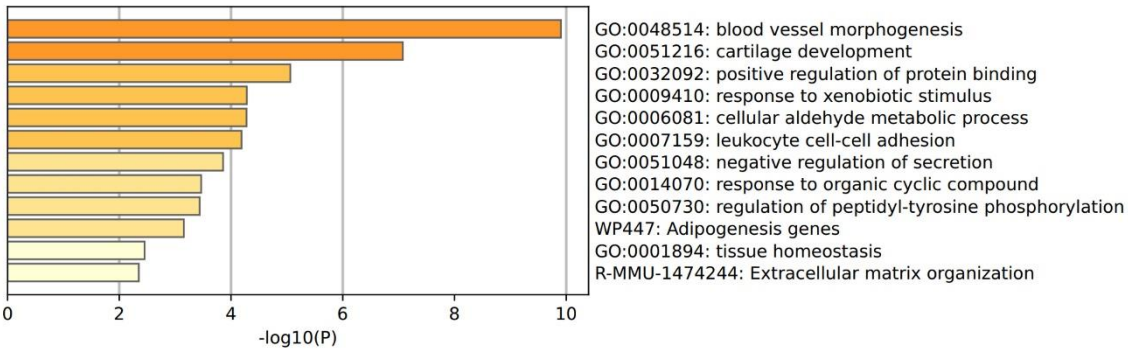

B cluster1

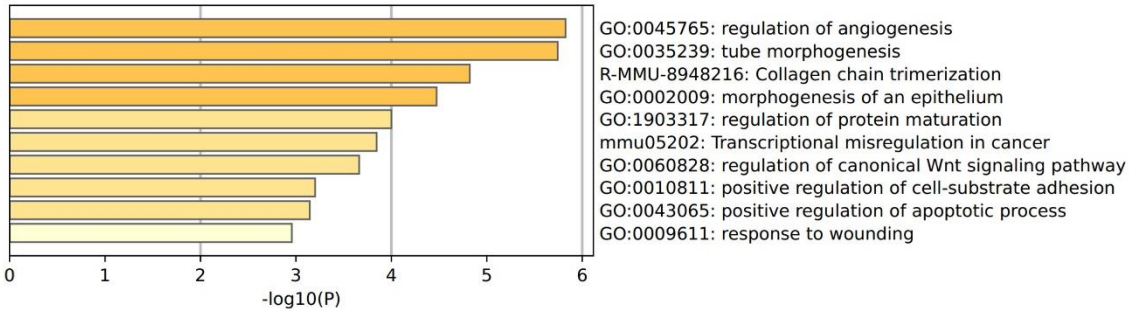

C cluster2

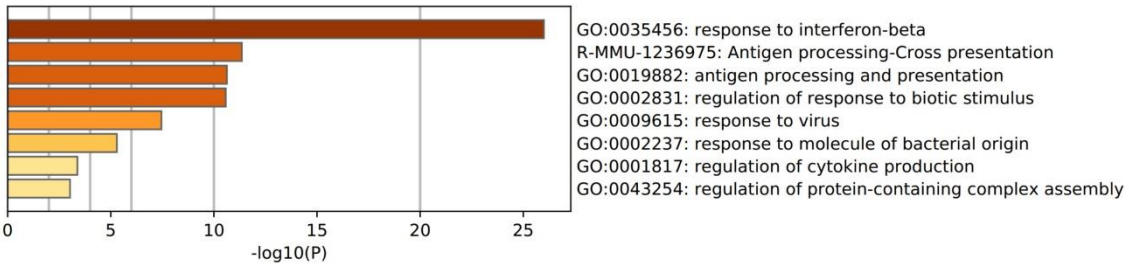

D cluster 3

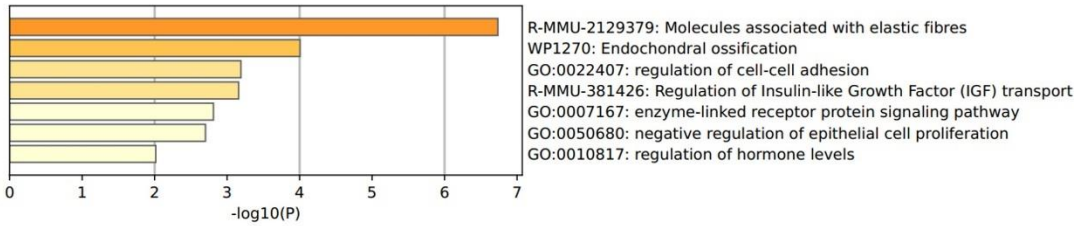

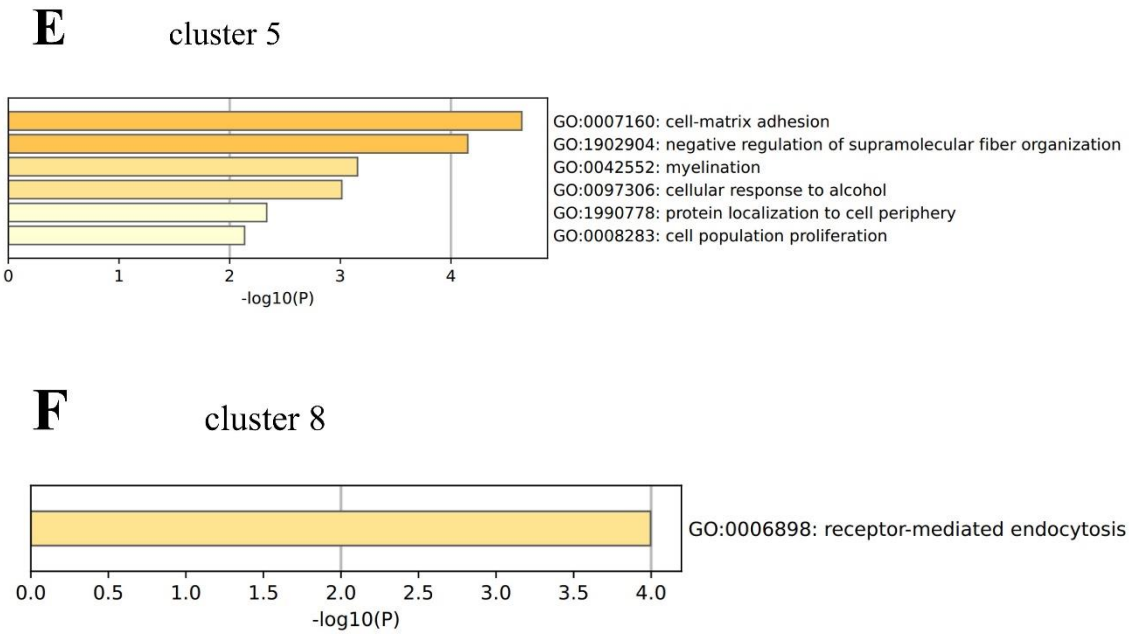

Figure 4. 5 enriched GO terms in each endothelial clusters. A-F summarized GO terms in cluster 0,1,2,3,5,8.

4.5 eNOS ^{high} endothelial cells were selected as HSS cells

To define HSS cells, several HSS markers were visualized using t-SNE plots (Figure 4. 6). It was concluded that eNOS can be used as a marker of HSS in healthy arteries and plaques in Chapter3. There was partial overlap between eNOS, Klf2, Nfe2l2 and Klf4 (HSS stress markers; Figure 4. 6). Therefore, eNOS ^{high} cells were selected as HSS cells and eNOS^{-} cells were selected as LSS cells for further analysis.

As shown in Figure 4. 7 A, eNOS gene expression was demonstrated in endothelial cells from WT mice, *ApoE*$^{-/-}$ ND mice and *ApoE*$^{-/-}$ HFD mice. However, eNOS gene has more expression in endothelial cells from WT mice compared to *ApoE*$^{-/-}$ ND mice and *ApoE*$^{-/-}$ HFD mice. Thus, the definition of HSS cells (eNOS^{high}) was set to eNOS gene expression normalized value >1.6, and the definition of LSS cells (eNOS $^{-}$) was set to eNOS gene expression normalized value=0. To validate if the definition of HSS cells and LSS cells is optimal, averaged expression value from multiple HSS markers and LSS markers were visualized using Violin plots (Figure 4. 8; Figure 4. 9). LSS markers (*Ctgf*, *Bmp4*, *Lmo4*, *Ctps*, *Fosl2*, *Angpt2*, *Ccl2*, *Icam1*, *Sema7a*) were more highly expressed in LSS cells (eNOS^{low}) compared to HSS (eNOS^{high}) cells in WT mice, *ApoE*$^{-/-}$ ND mice and *ApoE*$^{-/-}$ HFD mice (Figure 4. 8). HSS markers expression (*Klf4*, *Mef2c*, *Nfe2l2*, *Klk10*, *Klf2*) were higher in HSS cells compared to LSS cells from WT mice, *ApoE*$^{-/-}$ ND mice and *ApoE*$^{-/-}$ HFD mice (Figure 4. 9). Therefore, these data verified our method for selecting HSS cells and LSS cells based on eNOS expression was justified.

In conclusion, eNOS^{high} and eNOS^{-} cells can be selected as HSS cells and LSS cells. Using this approach, the distribution of HSS cells and LSS cells in each endothelial cell cluster was analysed. Cluster 0, 2 and 5 have more HSS cells, whereas the amount of HSS cells and LSS cells in cluster 1 are equal (Figure 4. 10).

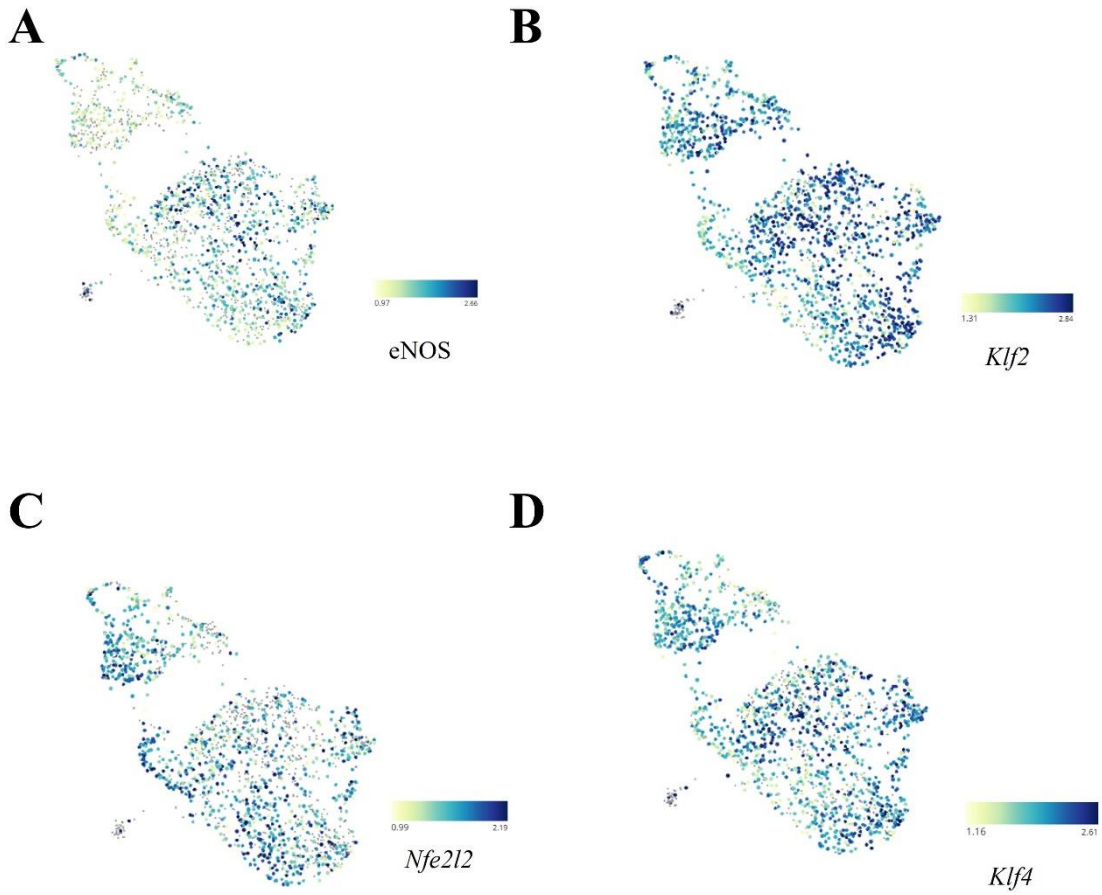

Figure 4. 6 t-SNE plots for HSS markers. t-SNE plots summarizing distribution of HSS markers (eNOS, *Klf2*, *Nfe2l2*, *Klf4*).

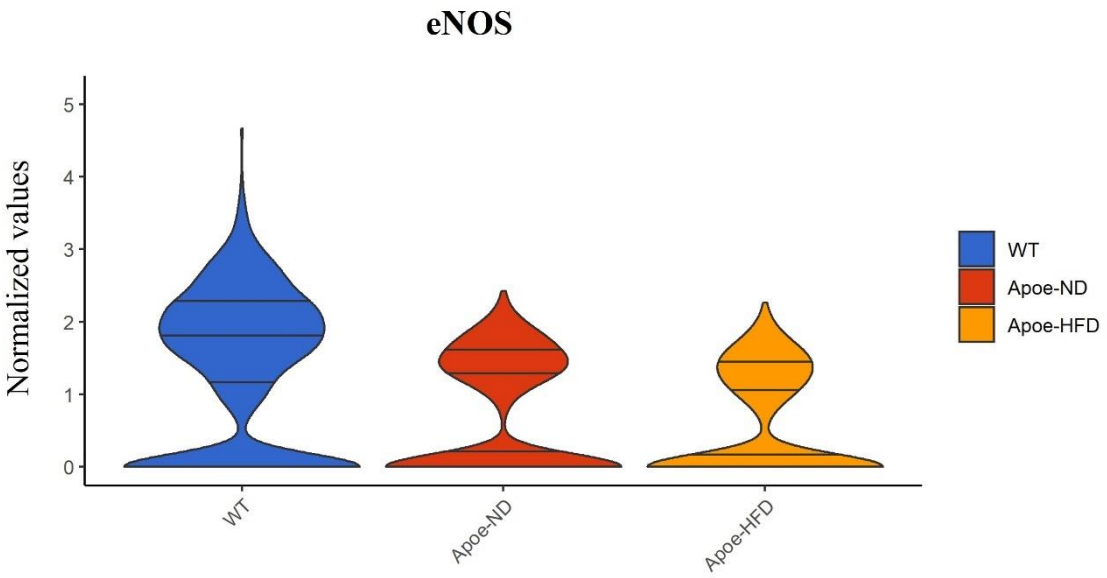

Figure 4. 7 Definition of HSS and LSS cells. Violin plots of normalized expression values for eNOS in endothelial cells from WT mice, *ApoE*$^{-/-}$ ND mice and *ApoE*$^{-/-}$ HFD mice. Violin plot y-axis shows normalized eNOS expression value. B) Definitions of HSS cells and LSS cells from WT mice, *ApoE*$^{-/-}$ ND mice and *ApoE*$^{-/-}$ HFD mice.

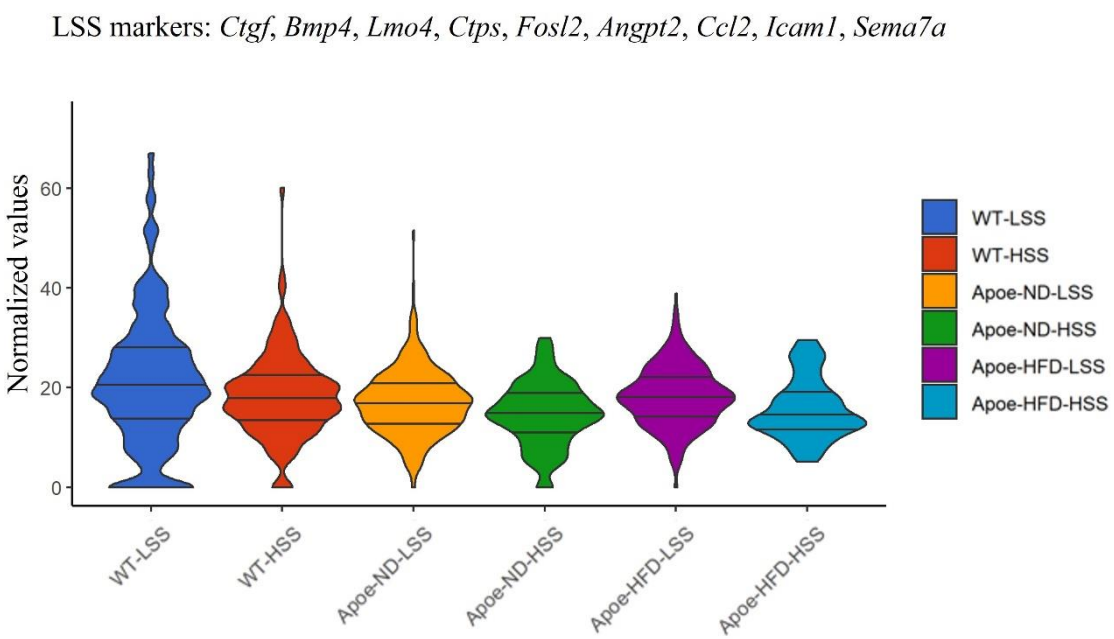

Figure 4. 8 Violin plots for LSS markers in WT Mice, *ApoE*$^{-/-}$ ND mice and *ApoE*$^{-/-}$ HFD mice. WT: wild type; ND: normal diet; HFD: high fat diet; LSS: LSS stress (eNOS^{low} cells); HSS: HSS stress (eNOS^{high} cells).

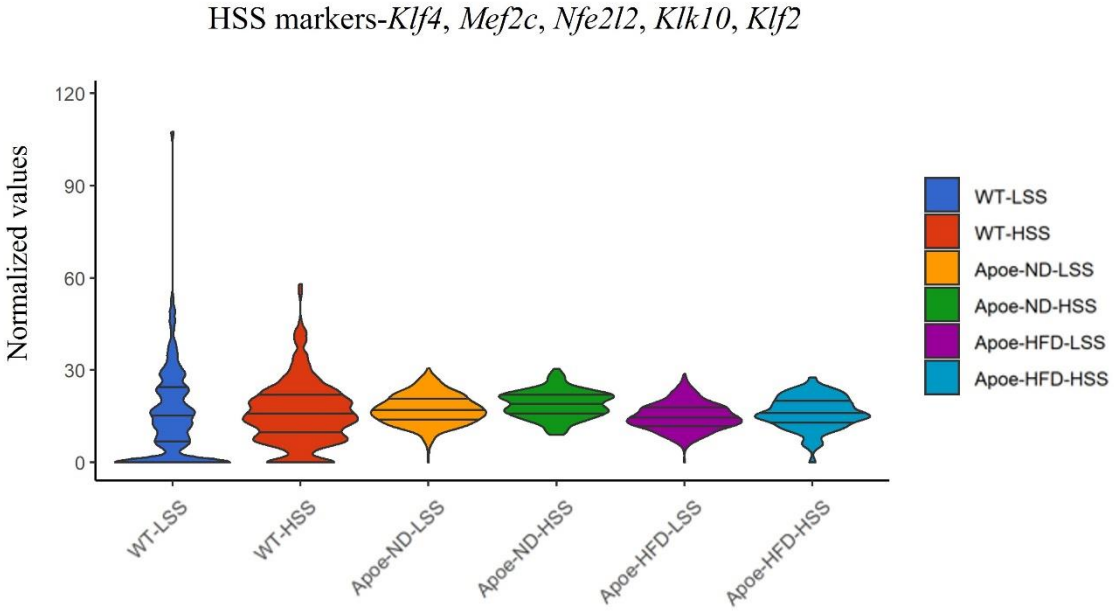

Figure 4. 9 Violin plots for HSS markers in WT Mice, *ApoE*$^{-/-}$ ND mice and *ApoE*$^{-/-}$ HFD mice. WT: wild type; ND: normal diet; HFD: high fat diet; LSS: LSS stress (eNOS^{low} cells); HSS: HSS stress (eNOS^{high} cells).

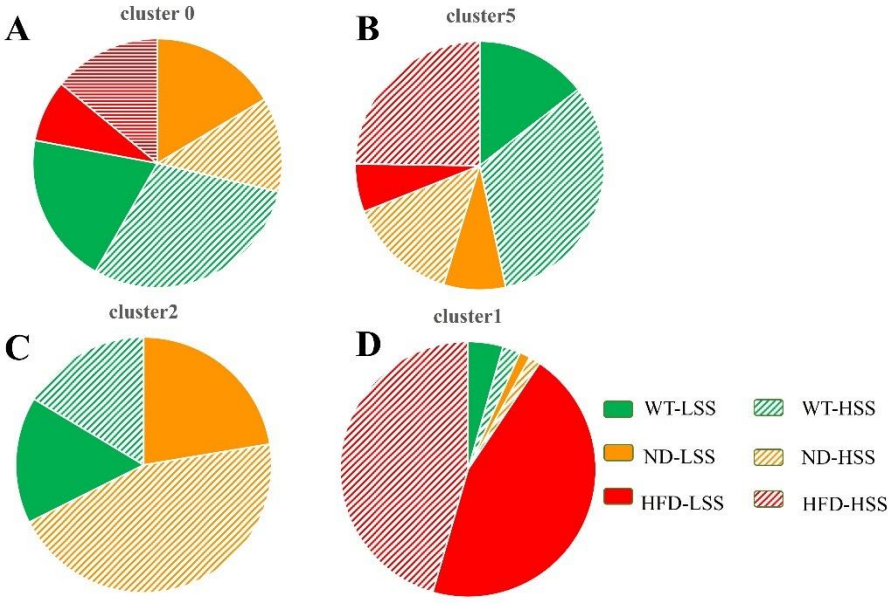

Figure 4. 10 Pie chart showing HSS cells and LSS cells distributions in each cluster. A) Cell distribution of cluster 0. (B) Cell distribution of cluster 5. C) Cell distribution of cluster 2. D) Cell distribution of cluster 1.

4.6 HSS endothelial cells from healthy aorta and plaques have different transcriptome profiles

Having established the definition of HSS cells and LSS cells. I used this to compare the transcriptome profiles of endothelial cells exposed to HSS (Figure 4. 11 A) and LSS (Figure 4. 11 B) in healthy and diseased aorta. It was observed in t-SNE plots that HSS cells (eNOS ^{high}) in diseased aorta had a strikingly different transcriptional profile compared to HSS endothelium (eNOS ^{high}) from WT mice and *ApoE*$^{-/-}$ ND mice (Figure 4. 11 A). There was a distinct population of HSS cells in diseased aorta that diverged from healthy HSS cells (endothelial cells from WT mice and *ApoE*$^{-/-}$ ND mice), I hypothesize that they may be HSS cells in the proximal HSS part of plaque (Figure 4. 11 A). There were some HSS cells in the diseased aorta that overlapped with healthy HSS cells, I hypothesize that they were HSS cells from outer curvature of the aorta from healthy and diseased vessels (Figure 4. 11 A). It was observed in t-SNE plot that LSS cells (eNOS^{low}) in diseased aorta had a strikingly different transcriptional profile compared to LSS endothelium (eNOS^{low}) from WT mice and *ApoE*$^{-/-}$ ND mice (Figure 4. 11 B). There was a distinct population of LSS cells in diseased aorta that diverged from healthy LSS cells (endothelial cells from WT mice and *ApoE*$^{-/-}$ ND mice), I hypothesize that they were LSS cells in the distal part of plaque (Figure 4. 11 B). Cholesterol level seemed to be dominant over WSS for regulation of transcriptional profile, for instance, *ApoE*$^{-/-}$ HFD HSS and *ApoE*$^{-/-}$ HFD LSS clustered together (Figure 4. 11). Also, another possibility should be considered, lipid has effects on eNOS function through several mechanisms including eNOS-caveolin internalization (Chikani et al., 2004), which may provide another explanation on the difference of HSS cells (eNOS ^{high}) in healthy aorta and diseased aortas.

Next, I identified genes that are differentially expressed in eNOS^{high} and eNOS^{low} cells in WT, *ApoE*$^{-/-}$ ND and *ApoE*$^{-/-}$ HFD mice. Only genes that have a large differential expression (Fold change< 0.8 or >1.2) and a very low p value ($P< 10^{-6}$) were included for further analysis (Figure 4. 12 A). Genes with fold change (FC) <0.8 were considered downregulated, and genes with FC >1.2 were considered upregulated. Differentially expressed genes are represented in a pie chart in Figure 4. 12 A; this shows that some differentially expressed genes overlapped between WT group, ND group and HFD group but others were distinct. I conclude that only a minority of genes associated with HSS

stress conditions overlap between WT, *ApoE*$^{-/-}$ ND and *ApoE*$^{-/-}$ HFD mice, whereas the majority of HSS stress genes are specific to WT, *ApoE*$^{-/-}$ ND and *ApoE*$^{-/-}$ HFD mice.

To focus on genes that are specific to WT, *ApoE*$^{-/-}$ ND and *ApoE*$^{-/-}$ HFD mice, genes that were expressed in all of these conditions were excluded from analysis as shown in Figure 4. 12 B. The function of genes correlating with HSS only in healthy endothelium (WT and ND group), and only in diseased endothelium (HFD group) were analysed by identifying gene ontology (GO) terms using the DAVID and Metascape databases. This approach led to the identification of multiple GO terms that were specific to either healthy or plaque endothelium (Figure 4. 13). For plaque endothelium, top GO terms included those related to negative regulation of proliferation, vasculature development and positive regulation of ERK1 and ERK2 (Figure 4. 13 A). ERK1/2 has been found to localize in the cap and basal areas of plaque and have important role in cell proliferation (Hu et al., 2000). For healthy endothelium, top GO terms are associated with metabolic processes and developmental process; I hypothesized these pathways are related to endothelial cells in WT mice (Figure 4. 13 B). Some pathways are related to viral process and immune system process; I hypothesized they are related to endothelial cells in *ApoE*$^{-/-}$ ND mice (Figure 4. 13 B).

Ultimately, I was interested in mechanoreceptors that may differ between health and disease and therefore I focussed on genes encoding cell surface proteins because they are putative mechanoreceptors (Figure 4. 12 B). All 23 putative mechanoreceptors that I selected were visualized via a heatmap (Figure 4. 14). Genes in WT (HSS and LSS), ApoE-ND (HSS and LSS) and ApoE-HFD (HSS and LSS) were clustered separately to demonstrate gene expression differences between WT group, ApoE-ND group and ApoE-HFD group (Figure 4. 14). Genes were organized by expression level, for instance, genes with upregulated expression with increased cholesterol (*ApoE*$^{-/-}$ ND) were plotted on the top of the heatmap, genes with downregulated expression with increased cholesterol (*ApoE*$^{-/-}$ ND) were plotted on the bottom of heatmap (Figure 4. 14). Heatmap also demonstrated that most of putative mechanosensors were lost in plaque (*ApoE*$^{-/-}$ HFD) (Figure 4. 14).

I suspected the loss of mechanosensors due to endothelial dysfunction in plaque. To understand if the endothelial mechanosensor Pecam1 was changed by cholesterol level, the expression of Pecam1 was visualized using Violin plot (Figure 4. 15). The expression

of Pecam1 was similar in HSS cells and LSS cells, violin plot demonstrated dramatically increased expression of Pecam1 in WT group compared to ND group and HFD group (Figure 4. 15). Figure 4. 15 B and C showed that although Pecam1 was expressed in a similar proportion of cells between groups, it was lower in the ND group and HFD group compared to WT.

To visualize how putative mechanosensors were changed by cholesterol level, the expression of all 23 putative mechanosensors were visualized using Violin plot (Figure 4. 16). Putative mechanosensors had more expression in HSS cells compared to LSS cells in all groups of mice. It was also noticed from the violin plot that there was increased expression of putative mechanosensors in WT group compared to ND group and HFD group (Figure 4. 16).

In conclusion, genes that were differentially expressed in HSS versus LSS cells included 23 mechanoreceptors. This group of genes exhibited higher expression in WT mice compared to *ApoE*$^{-/-}$ ND and *ApoE*$^{-/-}$ HFD suggesting that they are altered by hypercholesterolemia. Thus, sensing of shear stress may be altered in conditions of hypercholesterolemia and in plaques compared to healthy arteries.

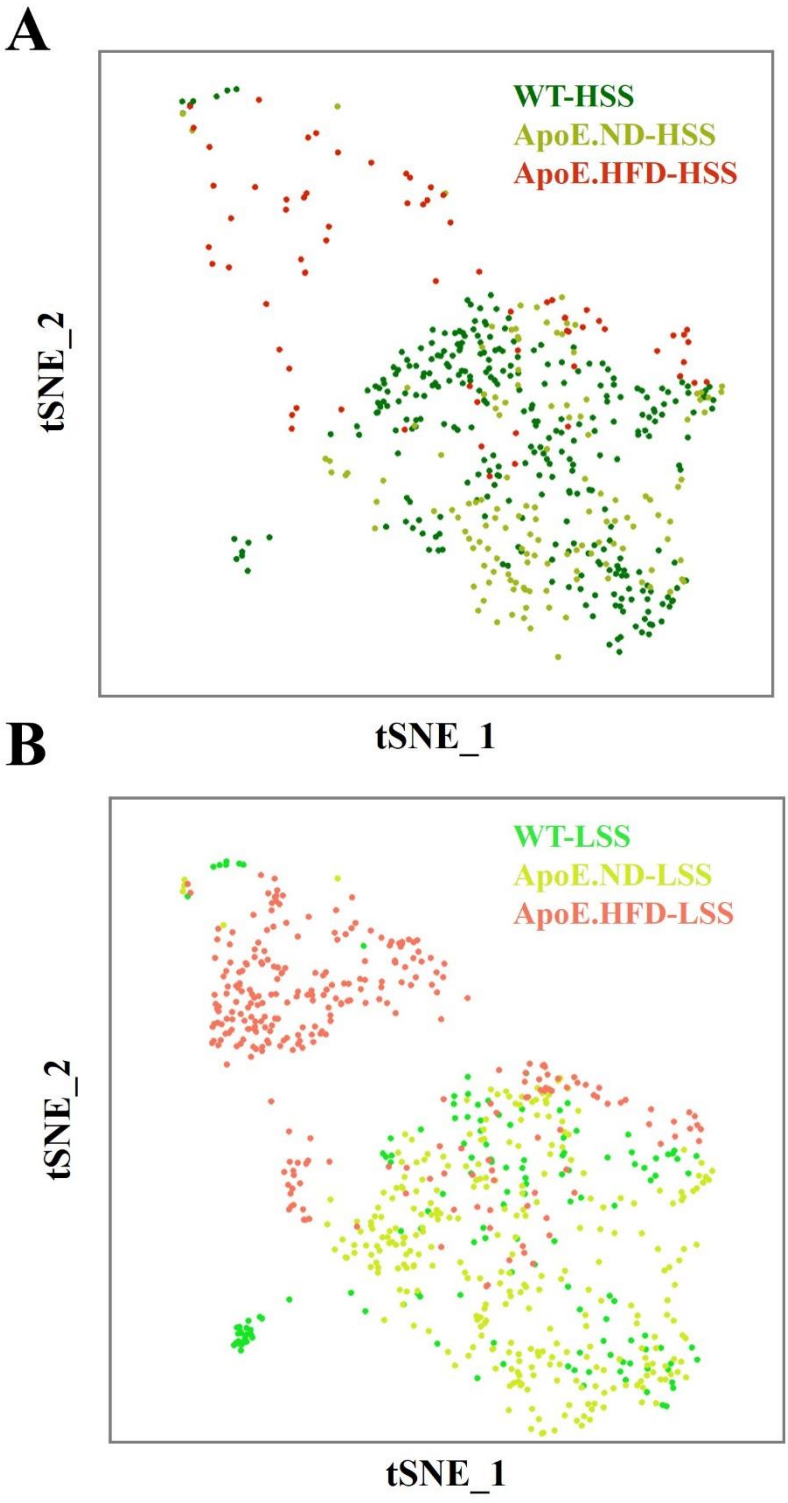

Figure 4. 11 t-SNE plots for HSS cells (A) and LSS cells (B) in WT Mice, *ApoE*$^{-/-}$ ND mice and *ApoE*$^{-/-}$ HFD mice. Cells from WT mice were labelled with green. Cells from *ApoE*$^{-/-}$ ND mice were labelled with yellow. Cells from *ApoE*$^{-/-}$ HFD mice were labelled with red.

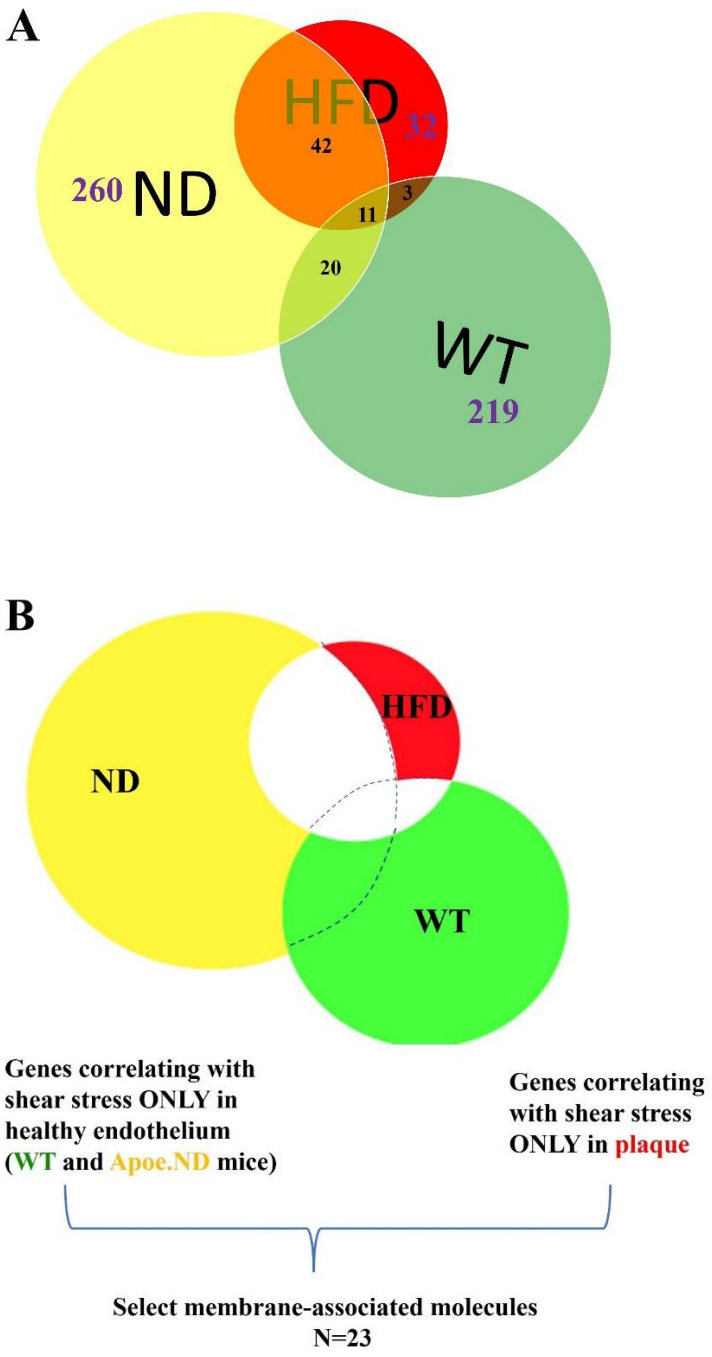

Figure 4. 12 Putative mechanosensors were found in transcriptome analysis of HSS and LSS endothelium in healthy versus disease. (A) Pie chart showing overlapped genes in WT mice, *ApoE*$^{-/-}$ ND mice and *ApoE*$^{-/-}$ HFD mice. (B) Genes correlating with shear stress only in healthy endothelium and only in plaque were included for analysis and membrane-associated genes were selected (N=23).

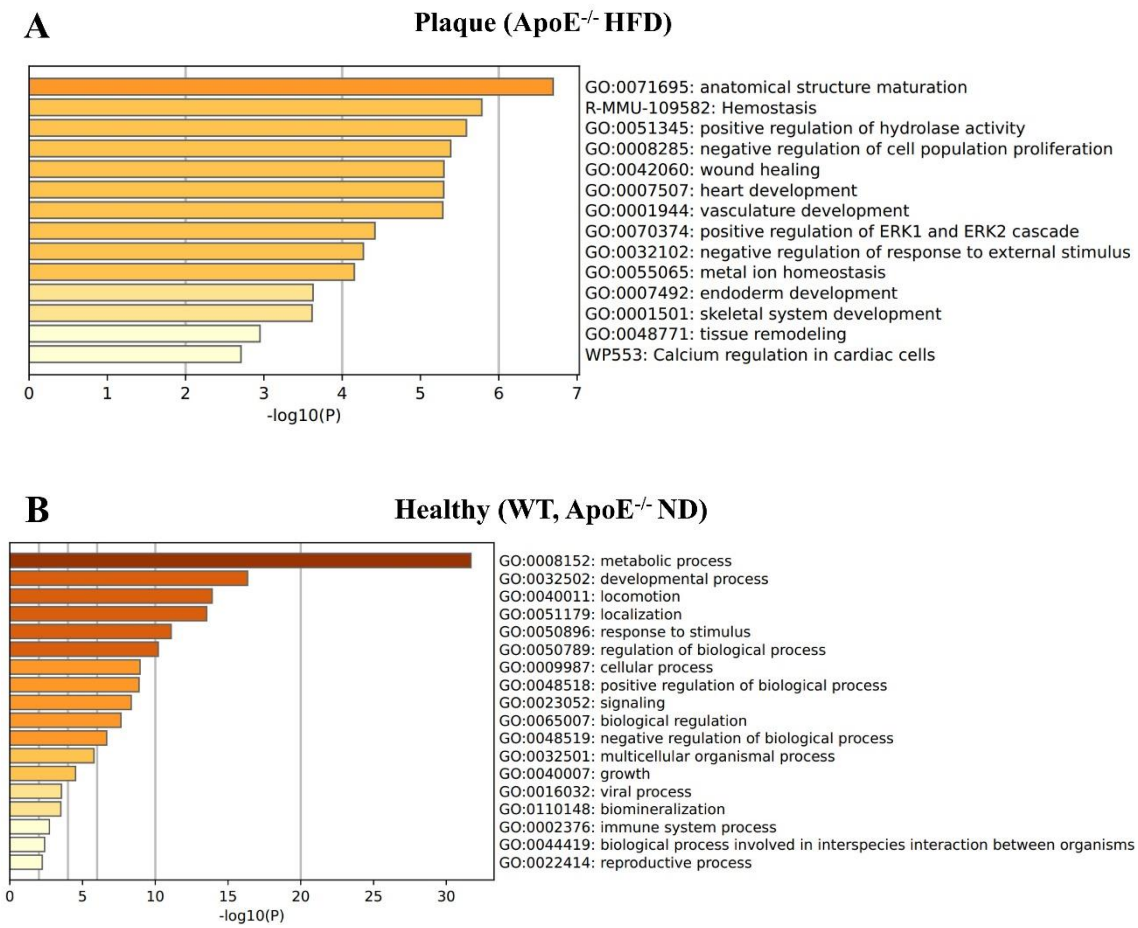

Figure 4. 13 Enriched GO terms in healthy and plaque endothelium. A) GO terms in plaque endothelium. B) GO terms in healthy endothelium.

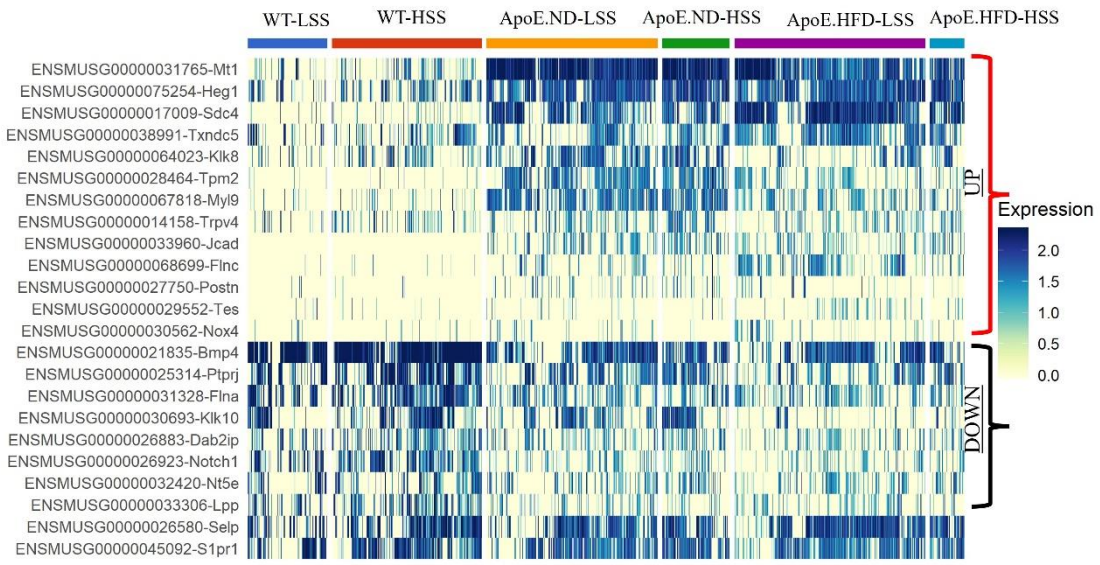

Figure 4. 14 Heatmap for putative mechanoreceptors in HSS and LSS endothelium from WT mice, *ApoE*$^{-/-}$ ND mice and *ApoE*$^{-/-}$ HFD mice. Genes had increased expression in *ApoE*$^{-/-}$ ND mice and *ApoE*$^{-/-}$ HFD mice were marked as UP. Genes had decreased expression in *ApoE*$^{-/-}$ ND mice and *ApoE*$^{-/-}$ HFD mice were marked as DOWN.

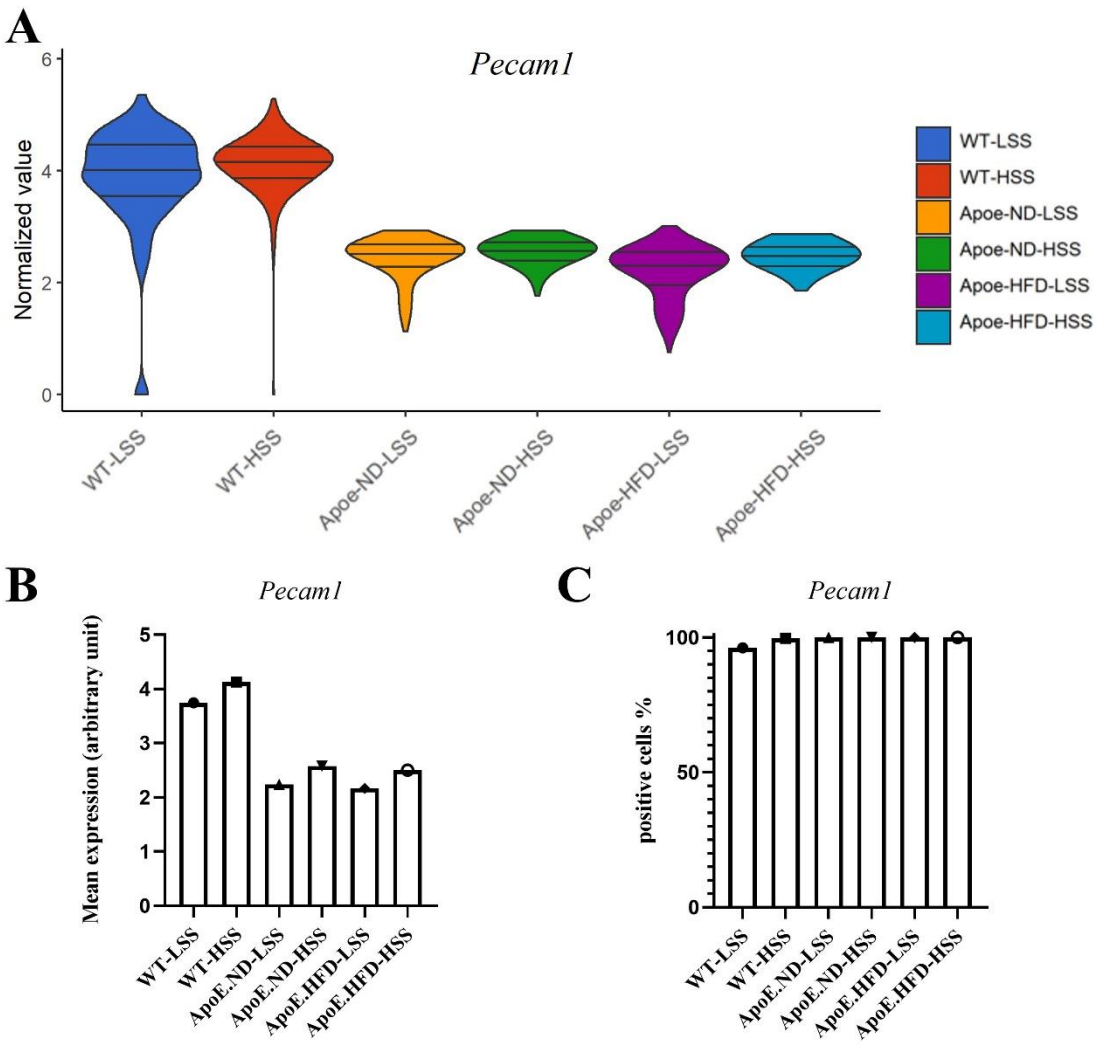

Figure 4. 15 Pecam1 expression in HSS cells and LSS cells from WT Mice, *ApoE*$^{-/-}$ ND mice and *ApoE*$^{-/-}$ HFD mice. (A) Violin plot for Pecam1. (B) Normalized mean expression value. (C) Percentage of positive cells (%).

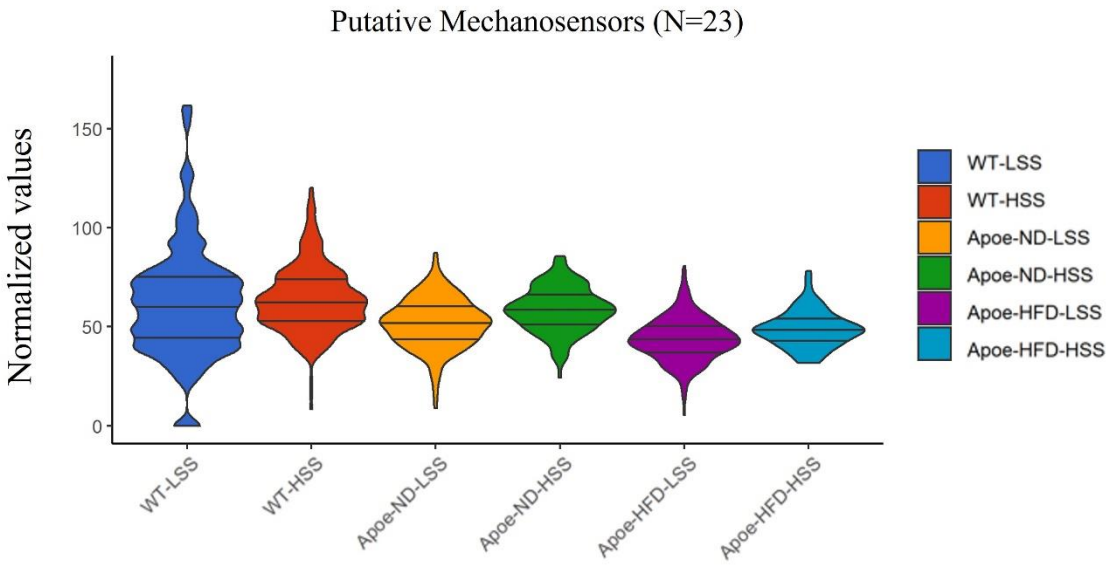

Figure 4. 16 Violin plots for putative mechanosensors in HSS cells and LSS cells from WT Mice, *ApoE*$^{-/-}$ ND mice and *ApoE*$^{-/-}$ HFD mice. Mechanosensitive genes (N=23) used in this analysis were: Mt1, Heg1, Sdc4, Txndc5, Klk8, Tpm2, Myl9, Trpv4, Jcad, Flnc, Postn, Tes, Nox4, Bmp4, Ptprj, Flna, Klk10, Dab2ip, Notch1, Nt5e, Lpp, Selp, S1pr1.

4.7 Six putative mechanoreceptors were selected to explore a mechanism for atheroprogression

I found multiple genes encoding cell surface proteins (called them putative mechanoreceptors) that were differentially expressed in HSS cells (eNOS ^{high} cells) in WT mice and *ApoE*$^{-/-}$ mice on a normal diet (*ApoE*$^{-/-}$ND). Some of these showed an interesting change in *ApoE*$^{-/-}$ mice on a high fat diet (*ApoE*$^{-/-}$HFD). I suspected these differences could explain why plaques and healthy aorta respond differently to shear stress. For instance, a heat map shows that *Selp* (Selectin P) and *Heg1* (Heart Development Protein with EGF Like Domains 1) are HSS genes that have higher expression at plaques, *Klk10* and *Nt5e* (5'-Nucleotidase) are HSS genes that become lost at plaques (Figure 4. 17; red box). *Nox4* (NADPH Oxidase 4) is LSS genes that have higher expression at plaques and *Bmp4* (Bone morphogenetic protein 4) is LSS genes that lost in plaques (Figure 4. 17; red box).

To view the expression change quantitatively, violin plots of six putative mechanoreceptors were used. Violin plot of *Bmp4* (Figure 4. 18), did not show *Bmp4* as a shear stress sensitive gene; *Bmp4* levels were significantly decreased in *ApoE*$^{-/-}$ ND mice and *ApoE*$^{-/-}$ HFD mice (Figure 4. 18 B and C). Violin plot of *Selp* (Figure 4. 19), showed that *Selp* was a HSS gene, and it was increased in plaques (Figure 4. 19 B and C). Violin plot of *Heg1* (Figure 4. 20), showed that *Heg1* was a HSS gene, and it was increased in plaque (Figure 4. 20 B and C). Violin plot of *Nt5e* (Figure 4. 21), showed that *Nt5e* was a HSS gene. *Nt5e* level at LSS site was decreased in *ApoE*$^{-/-}$ ND mice and *ApoE*$^{-/-}$ HFD mice compared to WT mice (Figure 4. 21 B and C). Violin plot of *Nox4* (Figure 4. 22), showed that *Nox4* was a LSS gene, and it was increased at LSS site in *ApoE*$^{-/-}$ ND mice and *ApoE*$^{-/-}$ HFD mice compared to WT mice (Figure 4. 22 B and C). Violin plot of *Klk10* (Figure 4. 23), showed that *Klk10* was a HSS gene, the expression level was higher in WT mice and *ApoE*$^{-/-}$ ND mice and dramatically decrease in plaque (Figure 4. 23 B and C).

In conclusion, As shown in Figure 4. 24, it is well established that HSS is protective and LSS induces plaque formation in the initiation of atherosclerosis. Some shear stress genes are expressed differently between healthy arteries and plaques, these differences could be a mechanism for atheroprogression. Some HSS genes including *Selp* and *Heg1* have higher expression in plaques, other HSS genes including *Klk10* and *Nt5e* are lost in

plaques (Figure 4. 24). Some LSS genes e.g. *Nox4* have higher expression in plaques, other LSS genes e.g. *Bmp4* are lost in plaques (Figure 4. 24). These genes expression are altered in conditions of hypercholesterolemia and in plaques compared to healthy arteries, and this could be a mechanism for atheroprogression.

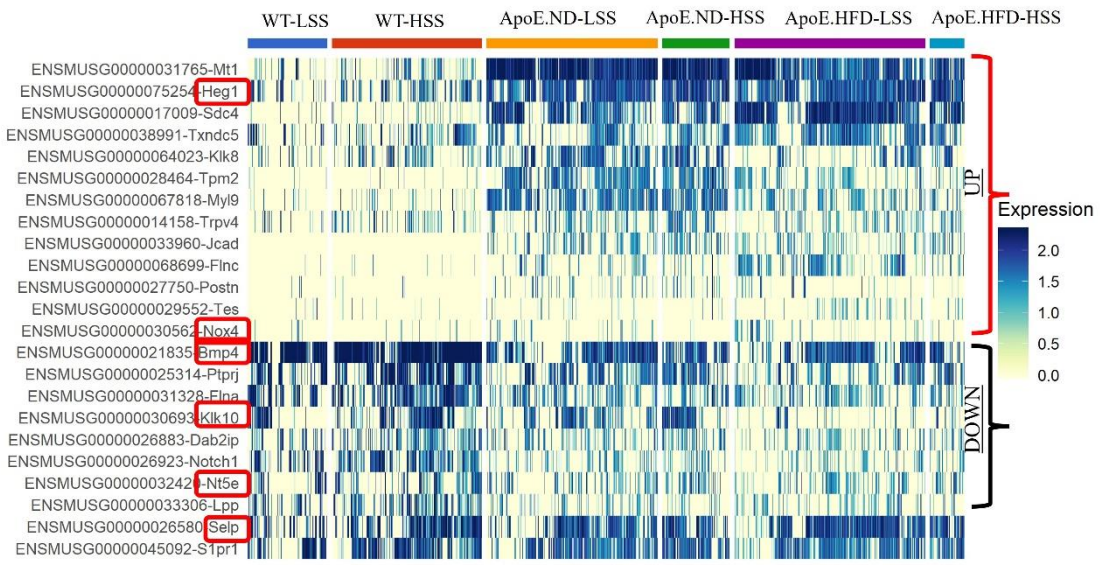

Figure 4. 17 Heatmap showing shear stress correlated genes are different in healthy aorta versus plaque. Genes had increased expression in *ApoE*$^{-/-}$ ND mice and *ApoE*$^{-/-}$ HFD mice were marked as UP. Genes had decreased expression in *ApoE*$^{-/-}$ ND mice and *ApoE*$^{-/-}$ HFD mice were marked as DOWN. Six putative mechanoreceptors were marked with red box.

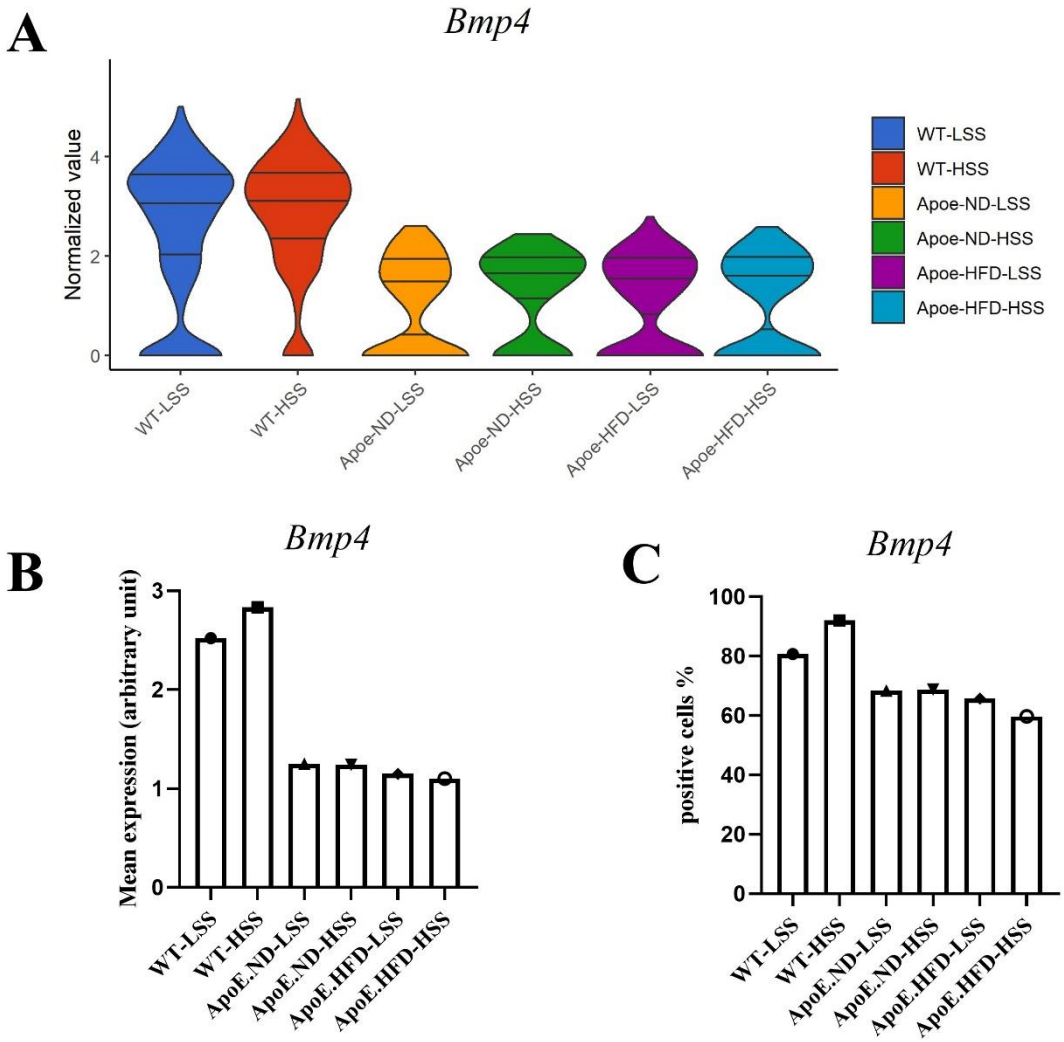

Figure 4. 18 *Bmp4* expression in HSS cells and LSS cells from WT Mice, *ApoE*$^{-/-}$ ND mice and *ApoE*$^{-/-}$ HFD mice. A) Violin plot for Bmp4. (B) Normalized mean expression value. (C) Percentage of positive cells (%).

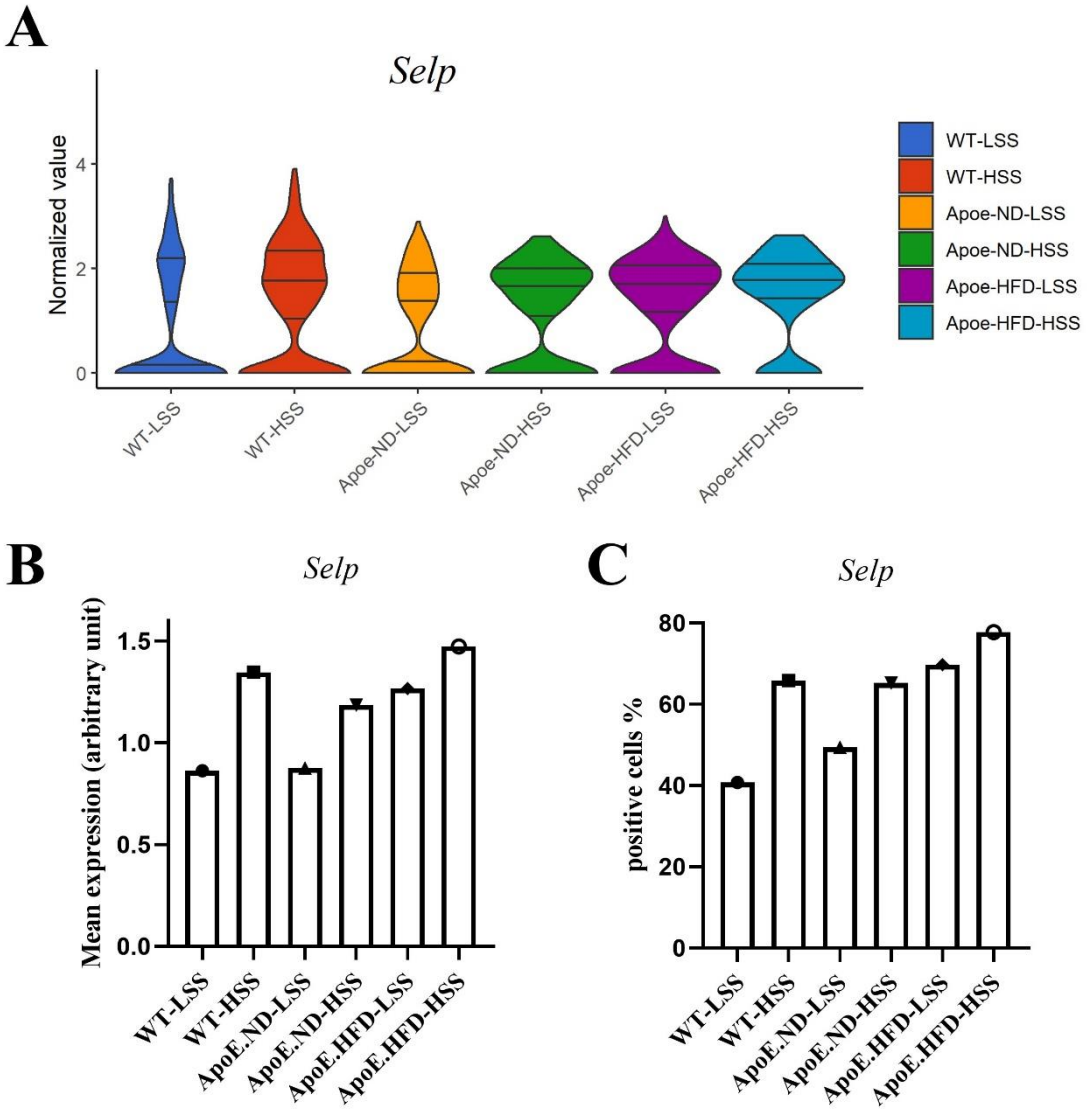

Figure 4. 19 *Selp* expression in HSS cells and LSS cells from WT Mice, *ApoE*$^{-/-}$ ND mice and *ApoE*$^{-/-}$ HFD mice. A) Violin plot for Selp. (B) Normalized mean expression value. (C) Percentage of positive cells (%).

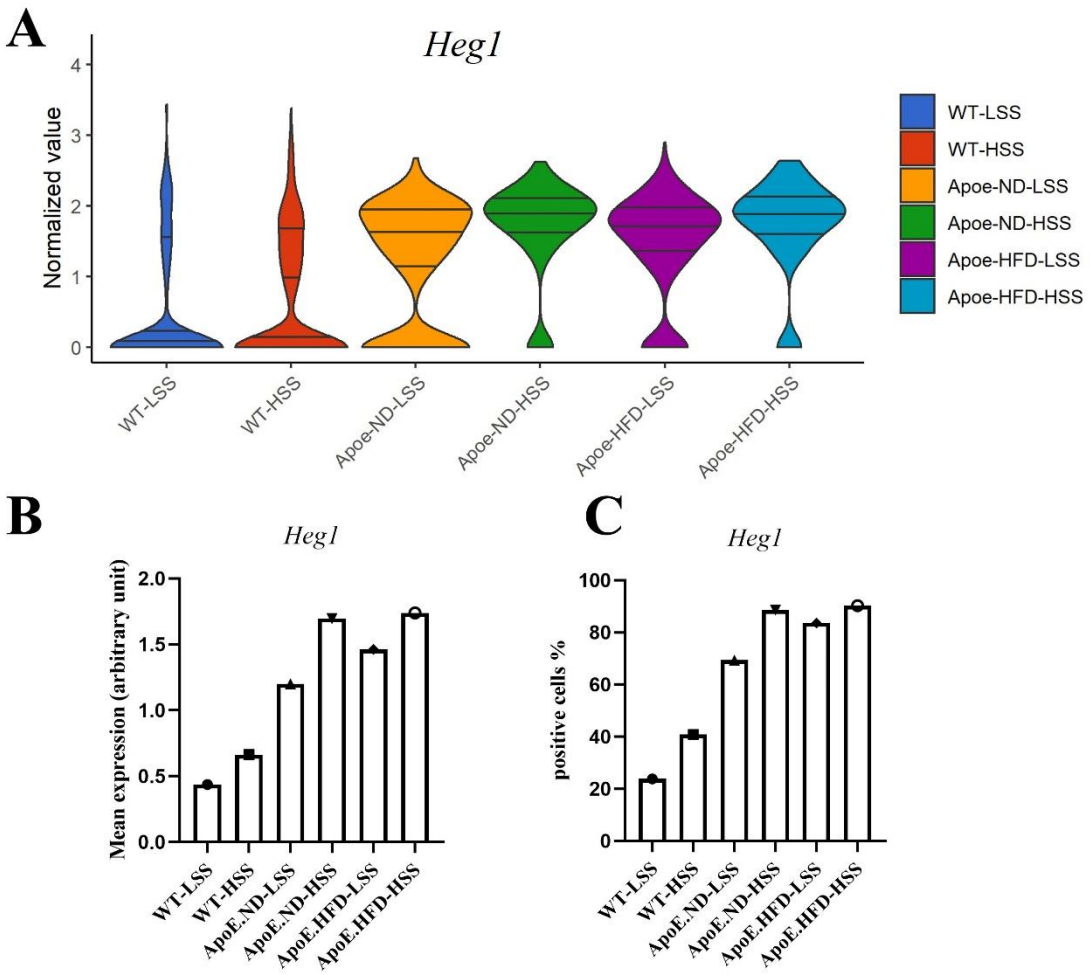

Figure 4. 20 *Heg1* expression in HSS cells and LSS cells from WT Mice, *ApoE*$^{-/-}$ ND mice and *ApoE*$^{-/-}$ HFD mice. A) Violin plot for Heg1. (B) Normalized mean expression value. (C) Percentage of positive cells (%).

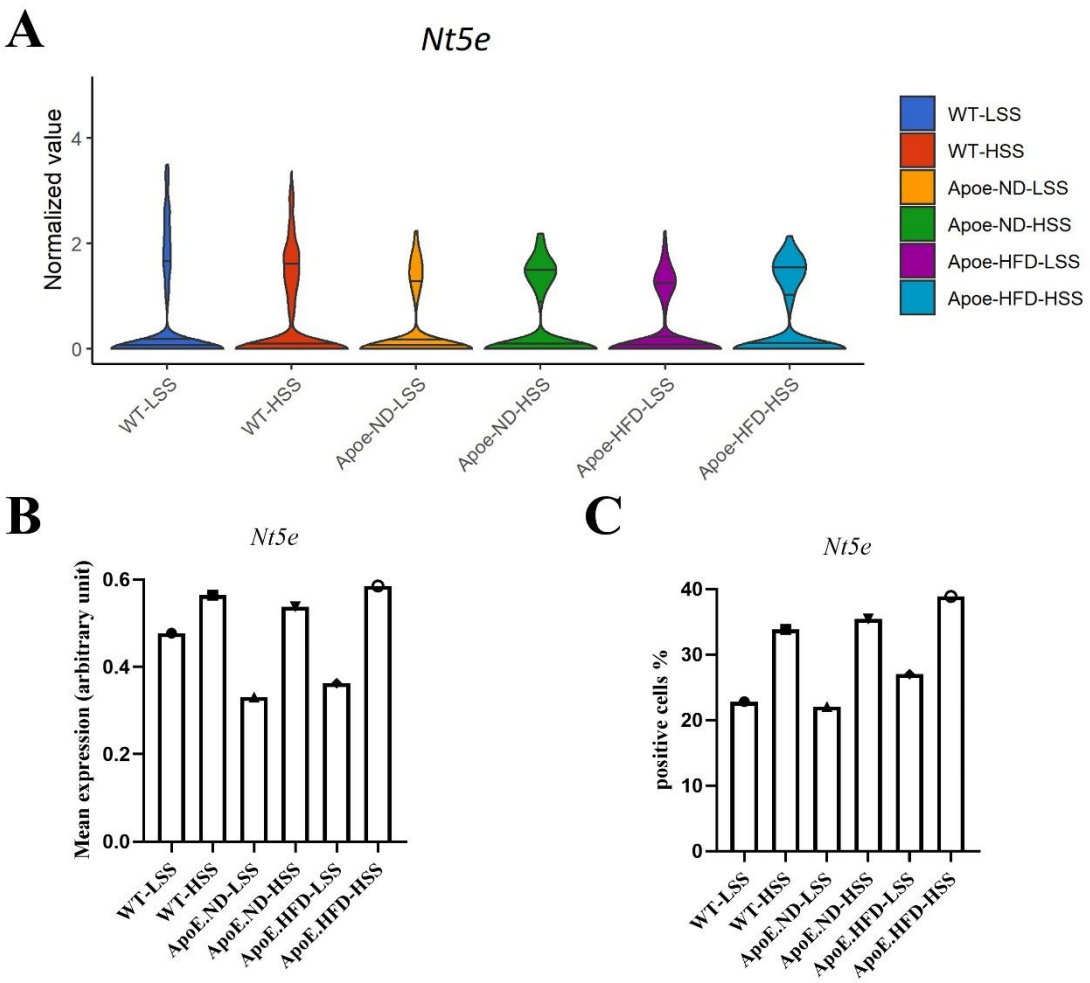

Figure 4. 21 *Nt5e* expression in HSS cells and LSS cells from WT Mice, *ApoE*$^{-/-}$ ND mice and *ApoE*$^{-/-}$ HFD mice. A) Violin plot for Nt5e. (B) Normalized mean expression value. (C) Percentage of positive cells (%).

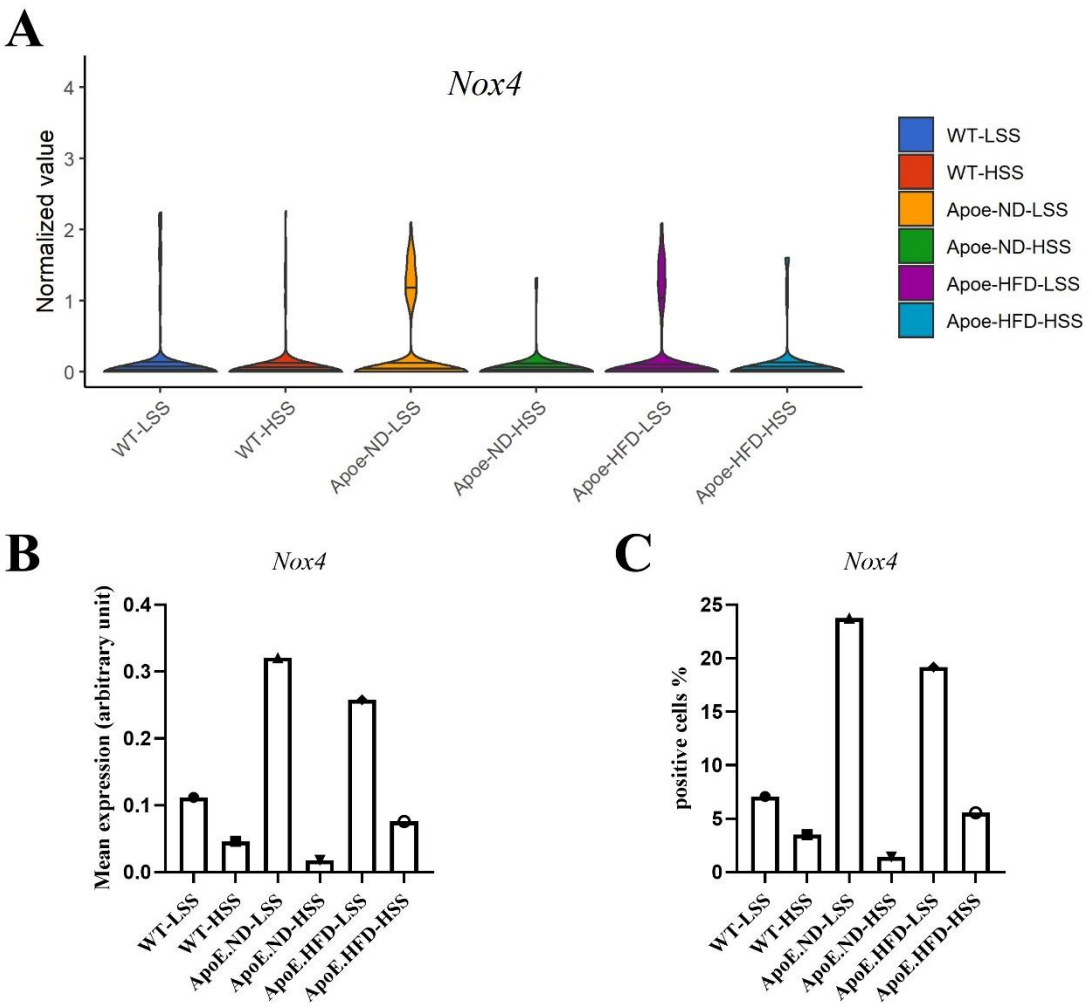

Figure 4. 22 *Nox4* expression in HSS cells and LSS cells from WT Mice, *ApoE*$^{-/-}$ ND mice and *ApoE*$^{-/-}$ HFD mice. A) Violin plot for Nox4. (B) Normalized mean expression value. (C) Percentage of positive cells (%).

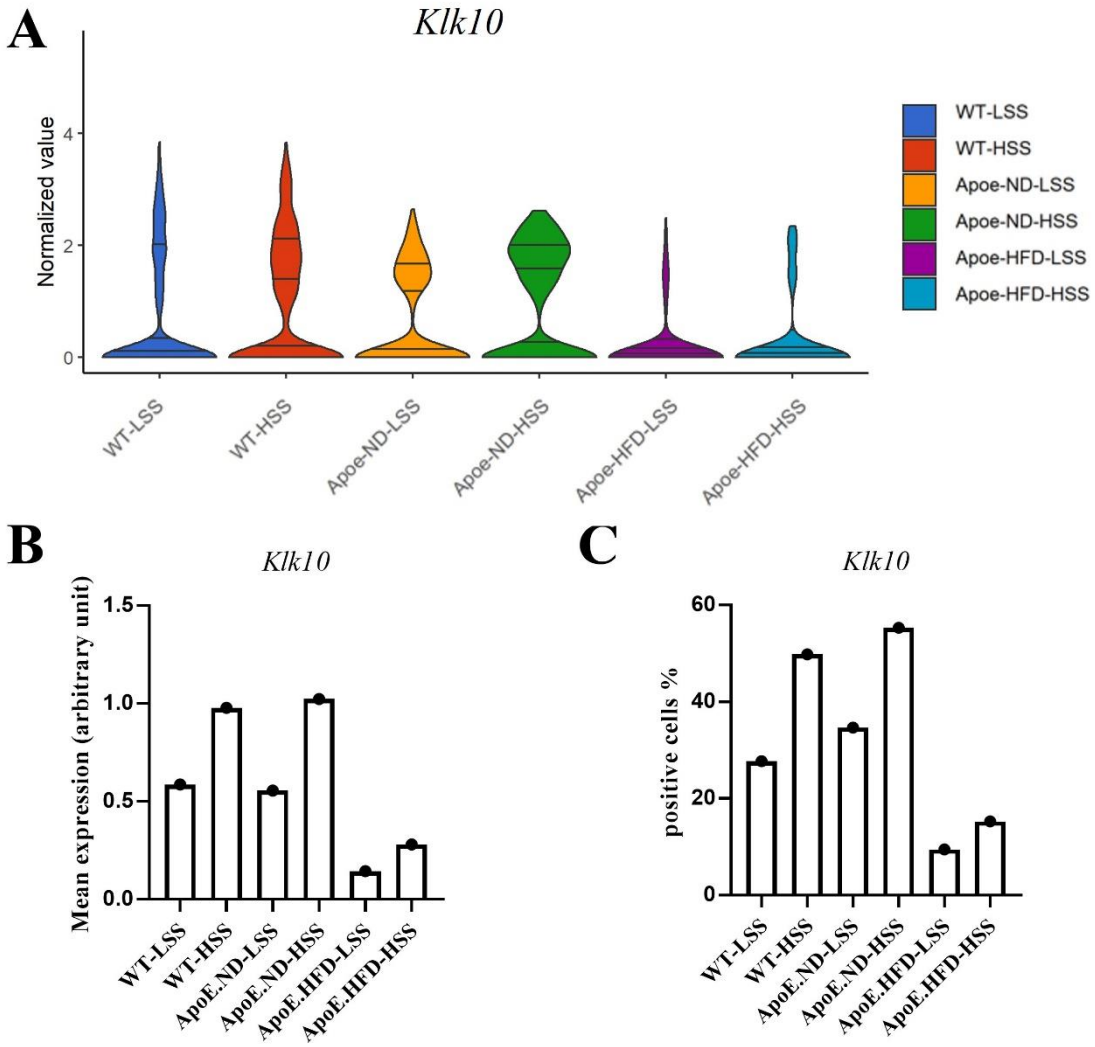

Figure 4. 23 *Klk10* expression in HSS cells and LSS cells from WT Mice, *ApoE*$^{-/-}$ ND mice and *ApoE*$^{-/-}$ HFD mice. A) Violin plot for *Klk10*. (B) Normalized mean expression value. (C) Percentage of positive cells (%).

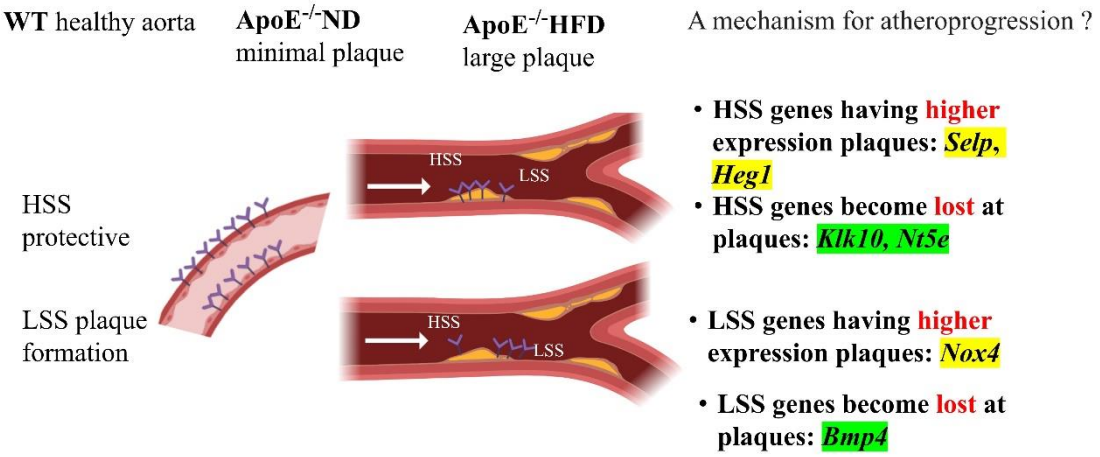

Figure 4. 24 Shear stress regulation of genes is different in WT Mice, *ApoE*$^{-/-}$ ND mice and *ApoE*$^{-/-}$ HFD mice. HSS genes and LSS genes are differentially expressed in plaques, which may suggest a mechanism for atheroprogression.

4.8 GBP and Interferon related genes were enriched in Cluster 2

I analysed cluster 2 in detail because it contained only cells from WT and *ApoE*$^{-/-}$ ND mice and cells were lost from plaque (*ApoE*$^{-/-}$ HFD mice). I compared cluster 2 with the whole scRNA-seq profile to find the upregulated and downregulated genes. I defined upregulated genes as Fold change>1.2 and P value<10^{-8}, downregulated genes as Fold change <0.8 and P value<10^{-8}. Top upregulated and down regulated genes were listed in Figure 4. 25, GBP (Guanylate Binding Protein) protein and IFN (interferon) genes are largely composed of cluster 2, and antigen processing and presentation genes like *Cd74*. For top downregulated genes, positive regulation of endothelial cells migration genes like *Lgmn* and *Hmox1*, positive regulation of vasculature development genes like *Lrg1*, *C3*, *Mdk* and *Hmox1* are mainly downregulated. t-SNE plots showed that GBP protein and interferon genes were only enriched in cluster 2 (Figure 4. 25).

Cluster 2 specific functional enrichment of gene ontology terms (GO terms) revealed the functional pathway of upregulated genes and down regulated genes (Figure 4. 26). Multiple GO terms related to interferon-beta, antigen processing and presentation pathway were enriched in Cluster 2 upregulated genes. t-SNE and violin plots showed that multiple GBP protein and interferon genes (*Gbp3*, *Stat1*, *Iigp1*, *Tap1*, *Gbp5*, *Gbp6*, *Cd74*, *Gbp2*, *Bst2*, *Gbp7*, *Gbp4*, *Irf1*) were enriched in cluster 2 (Figure 4. 27 and Figure 4. 28). Heatmaps of scaled expression in Figure 4. 29, showed that many IFN regulated genes had a similar pattern of expression, for instance, *Klk10*, *Tap1*, *Stat1* and *Gbp3* were increased in *ApoE*$^{-/-}$ ND mice and lost their expression in plaque (*ApoE*$^{-/-}$ HFD mice) (Figure 4. 29). *Cd74* and *Gbp4* lost their expression when cholesterol level was increased (Figure 4. 29; *ApoE*$^{-/-}$ ND and *ApoE*$^{-/-}$ HFD).

To view these gene expression change in a quantitative way, violin plots of GBP and interferon genes were generated, y axis showed normalized expression level and percent value of positive cells. As shown in Figure 4. 30, violin plot did not show *Cd74* as a shear stress sensitive gene, *Cd74* levels were decreased in *ApoE*$^{-/-}$ ND mice and were significantly decreased in *ApoE*$^{-/-}$ HFD mice (Figure 4. 30 B and C). It was observed in Figure 4. 31 that *Gbp4* was a HSS gene and it had higher expression level in WT mice and *ApoE*$^{-/-}$ ND mice compared to *ApoE*$^{-/-}$ HFD mice (Figure 4. 31 B and C). It was observed that *Gbp3* was a HSS gene and its expression level was significantly increased in *ApoE*$^{-/-}$ ND mice and lost in plaque (Figure 4. 32 B and C). Violin plot did not show

Stat1 as a shear stress sensitive gene, its expression level was low in endothelial cells and lost in *ApoE*$^{-/-}$ HFD mice (Figure 4. 33 B and C).

GBPs have important roles in promoting host defense against bacterial by inducing an inflammation-associated programmed cell death called pyroptosis (Wandel et al., 2020). The scRNAseq analysis in this chapter shows that cluster2 are mainly composed of endothelial cells from *ApoE*$^{-/-}$ ND mice. GBP genes, interferon genes and genes related to antigen presentation are enriched in this cluster. Interestingly, all these genes are lost in plaque. GBPs and interferons gene expression are altered in conditions of hypercholesterolemia and in plaques compared to healthy arteries, this could be a mechanism for atheroprogression.

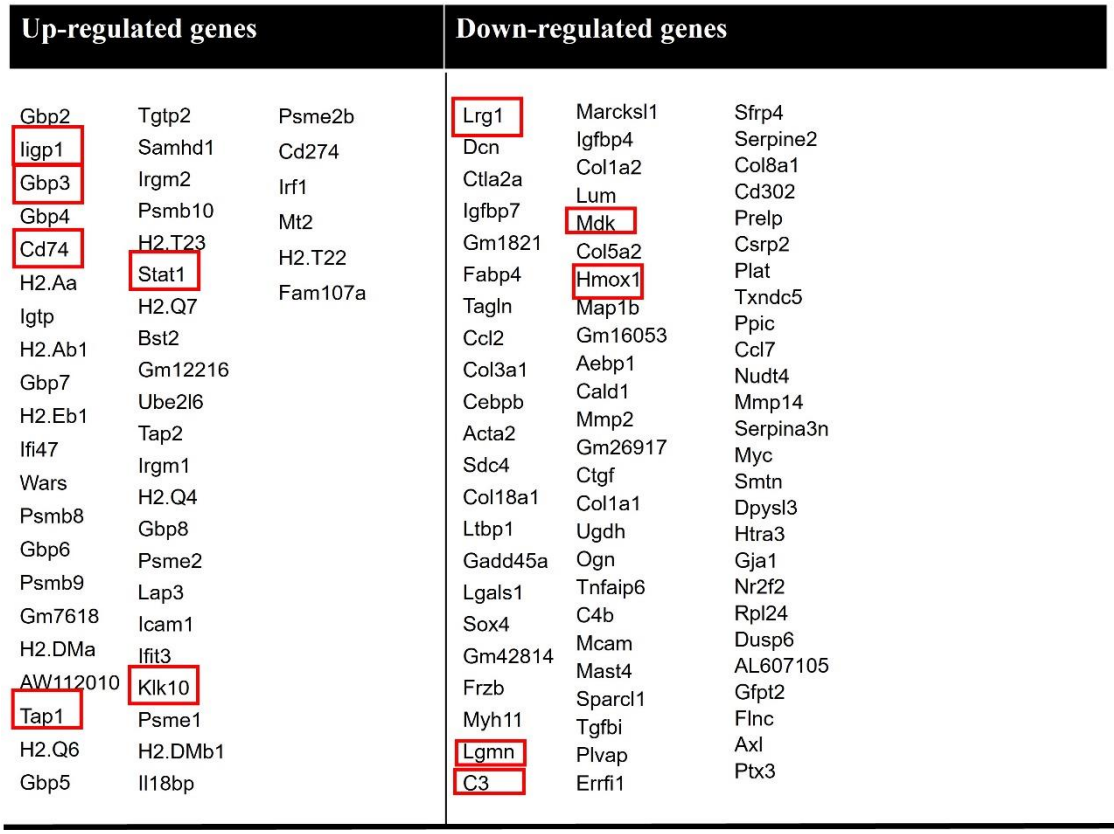

Up-regulated genes			Down-regulated genes		
Gbp2	Tgtp2	Psme2b	Lrg1	Marcksl1	Sfrp4
Iigp1	Samhd1	Cd274	Dcn	Igfbp4	Serpine2
Gbp3	Irgm2	Irf1	Ctla2a	Col1a2	Col8a1
Gbp4	Psmb10	Mt2	Igfbp7	Lum	Cd302
Cd74	H2.T23	H2.T22	Gm1821	Mdk	Prelp
H2.Aa	Stat1	Fam107a	Fabp4	Col5a2	Csrp2
Igtp	H2.Q7		Tagln	Hmox1	Plat
H2.Ab1	Bst2		Ccl2	Map1b	Txndc5
Gbp7	Gm12216		Col3a1	Gm16053	Ppic
H2.Eb1	Ube2l6		Cebpb	Aebp1	Ccl7
Ifi47	Tap2		Acta2	Cald1	Nudt4
Wars	Irgm1		Sdc4	Mmp2	Mmp14
Psmb8	H2.Q4		Col18a1	Gm26917	Serpina3n
Gbp6	Gbp8		Ltbp1	Ctgf	Myc
Psmb9	Psme2		Gadd45a	Col1a1	Smtn
Gm7618	Lap3		Lgals1	Ugdh	Dpysl3
H2.DMa	Icam1		Sox4	Ogn	Htra3
AW112010	Ifit3		Gm42814	Tnfaip6	Gja1
Tap1	Klk10		Frzb	C4b	Nr2f2
H2.Q6	Psme1		Myh11	Mcam	Rpl24
Gbp5	H2.DMb1		Lgmn	Mast4	Dusp6
	Il18bp		C3	Sparcl1	AL607105
				Tgfbi	Gfpt2
				Plvap	Flnc
				Errfi1	Axl
					Ptx3

Figure 4. 25 Table showing upregulated and downregulated genes in cluster 2. Genes with fold change >1.2 and P value $<10^{-8}$ was considered as upregulated, genes with fold change <0.8 and P value $<10^{-8}$ was considered as downregulated.

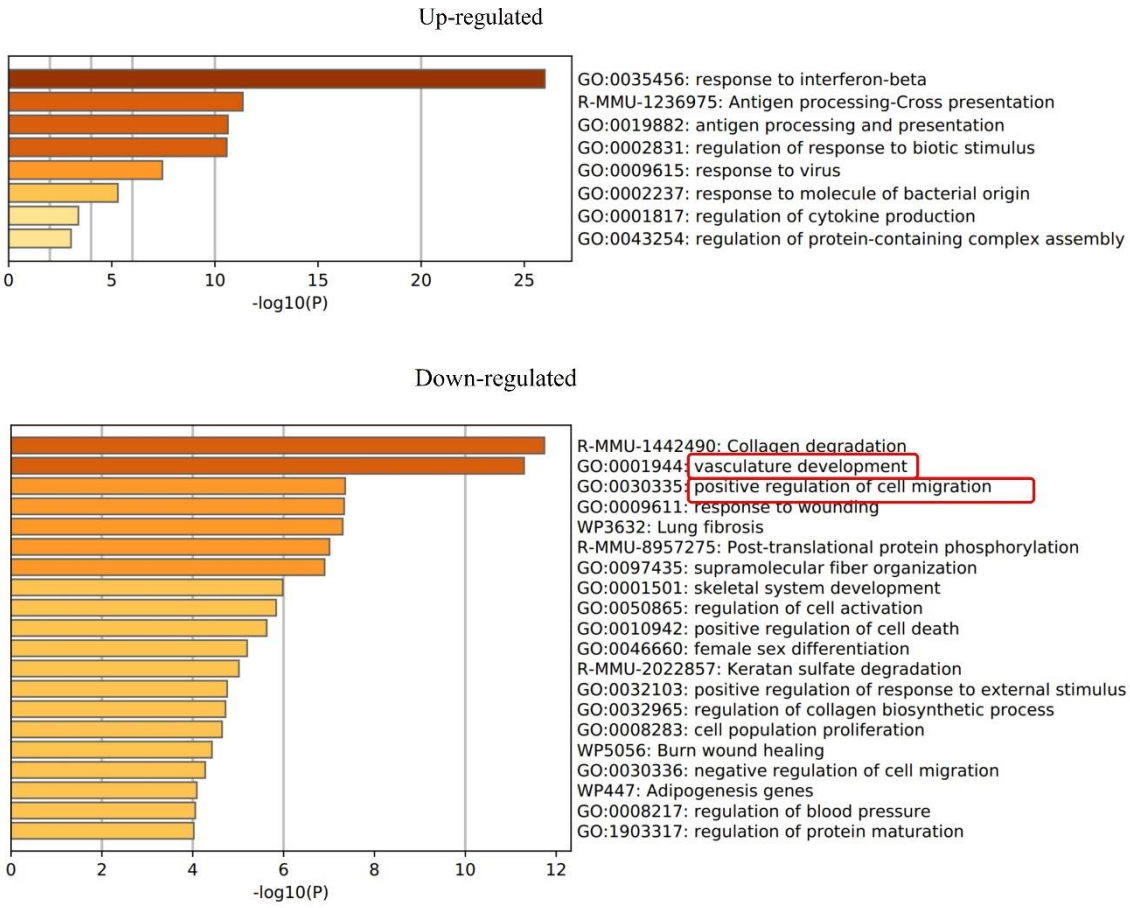

Figure 4. 26 Charts represented upregulated and downregulated GO terms in cluster 2.

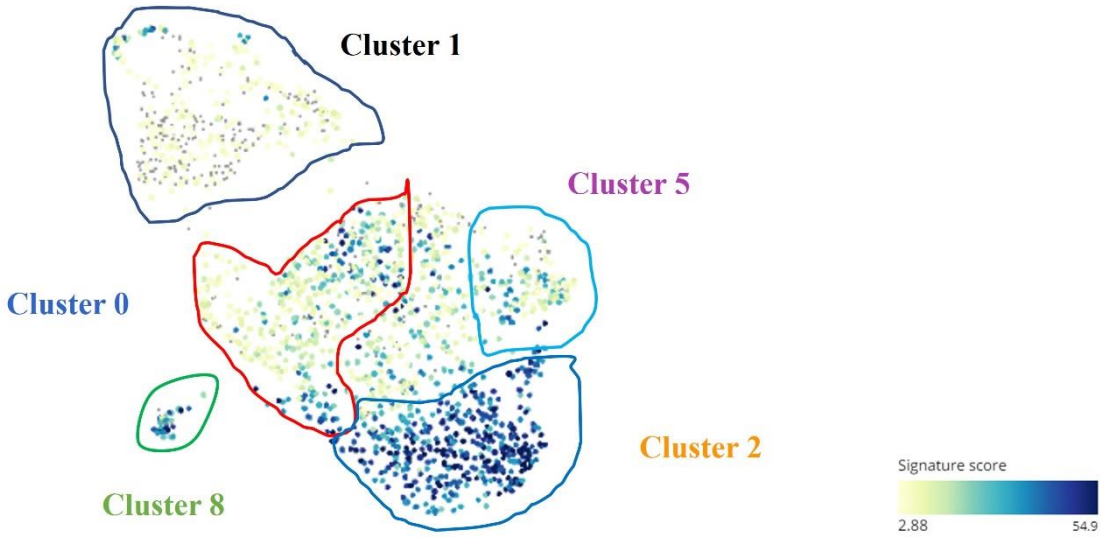

Figure 4. 27 t-SNE plots showing GBPs and interferon genes were enriched in cluster 2. Cd74, Gbp2, Gbp3, Stat1, Iigp1, Bst2, Gbp7, Tap1, Gbp5, Gbp6, Gbp4 and Irf1 were enriched in cluster 2.

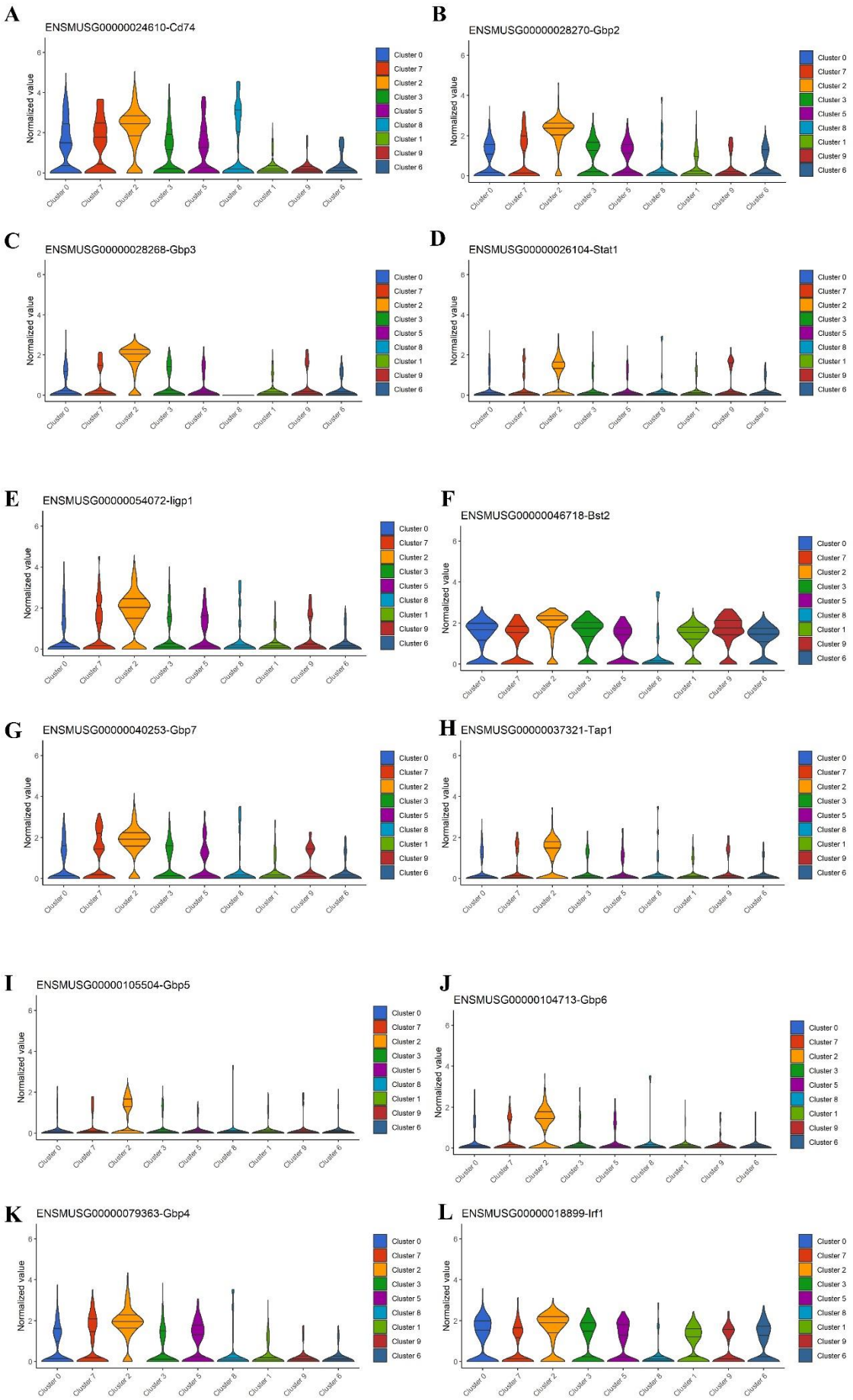
A
ENSMUSG00000024610-Cd74
B
ENSMUSG00000028270-Gbp2
C
ENSMUSG00000028268-Gbp3
D
ENSMUSG00000026104-Stat1
E
ENSMUSG00000054072-Iigp1
F
ENSMUSG00000046718-Bst2
G
ENSMUSG00000040253-Gbp7
H
ENSMUSG00000037321-Tap1
I
ENSMUSG00000105504-Gbp5
J
ENSMUSG00000104713-Gbp6
K
ENSMUSG00000079363-Gbp4
L
ENSMUSG00000018899-Irf1
Normalized value
Cluster 0
Cluster 7
Cluster 2
Cluster 3
Cluster 5
Cluster 8
Cluster 1
Cluster 9
Cluster 6

Figure 4. 28 Violin plots for GBP protein and interferon genes in each cluster. Cluster 4 was removed due to SMC contamination. Violin plots for Cd74 (A), Gbp2(B), Gbp3(C), Stat1(D), Iigp1(E), Bst2(F), Gbp7(G), Tap1(H), Gbp5(I), Gbp6(J), Gbp4(K), Irf1(L).

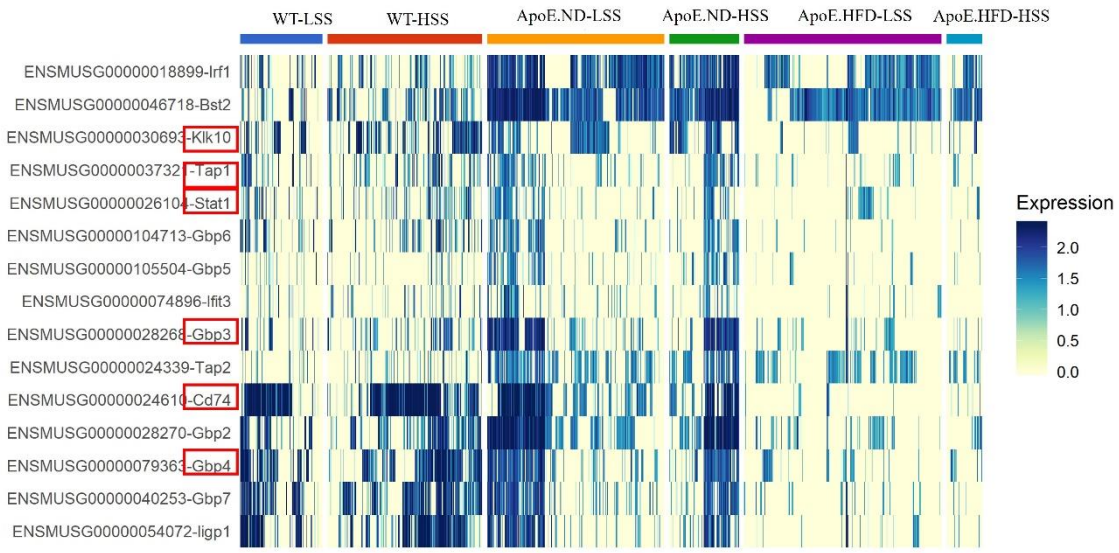

Figure 4. 29 Heatmap of top genes upregulated in cluster 2. Genes with same pattern were marked by red box.

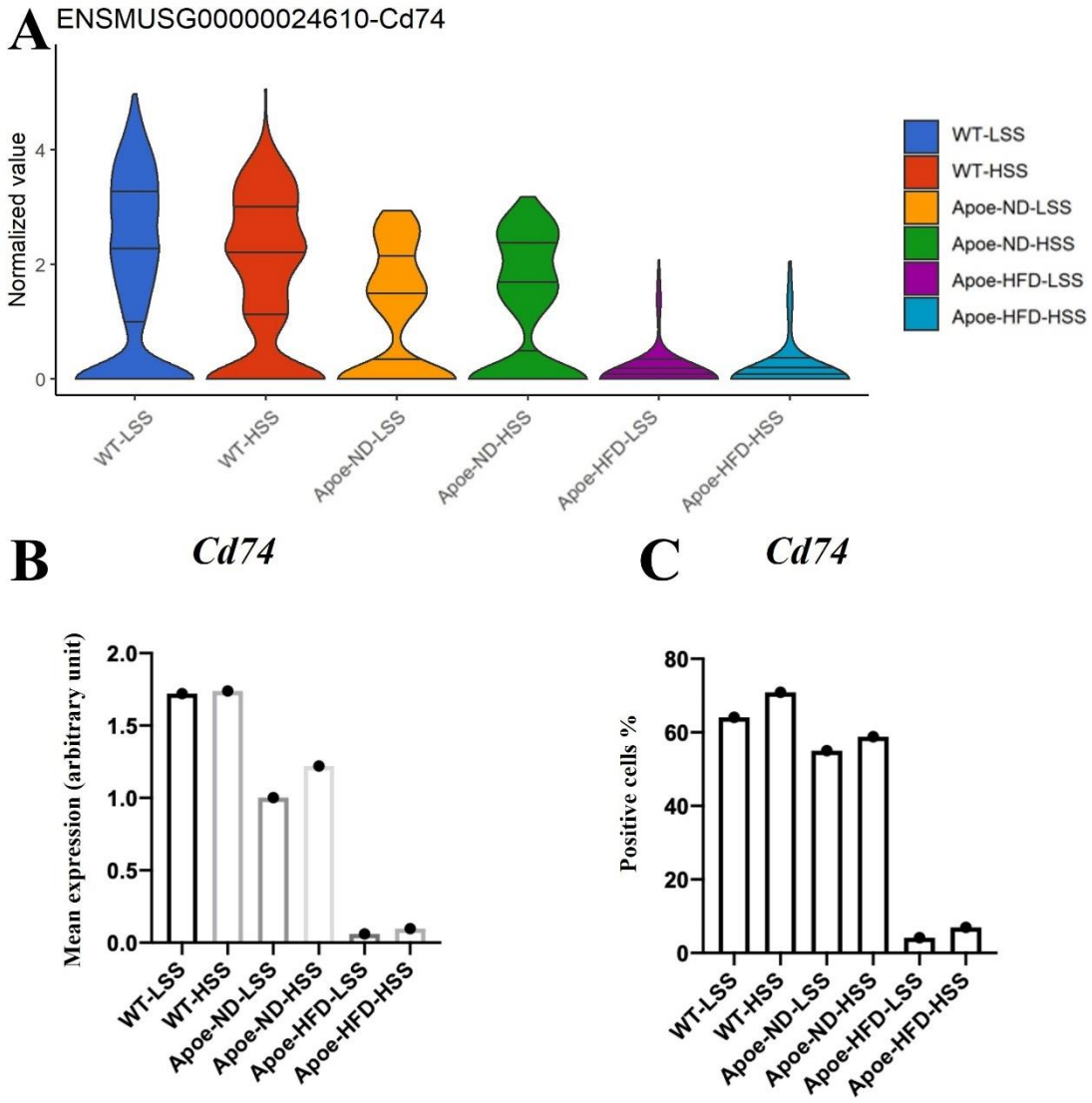

Figure 4. 30 *Cd74* expression in HSS cells and LSS cells from WT Mice, *ApoE*$^{-/-}$ ND mice and *ApoE*$^{-/-}$ HFD mice. A) Violin plot for Cd74. (B) Normalized mean expression value. (C) Percentage of positive cells (%).

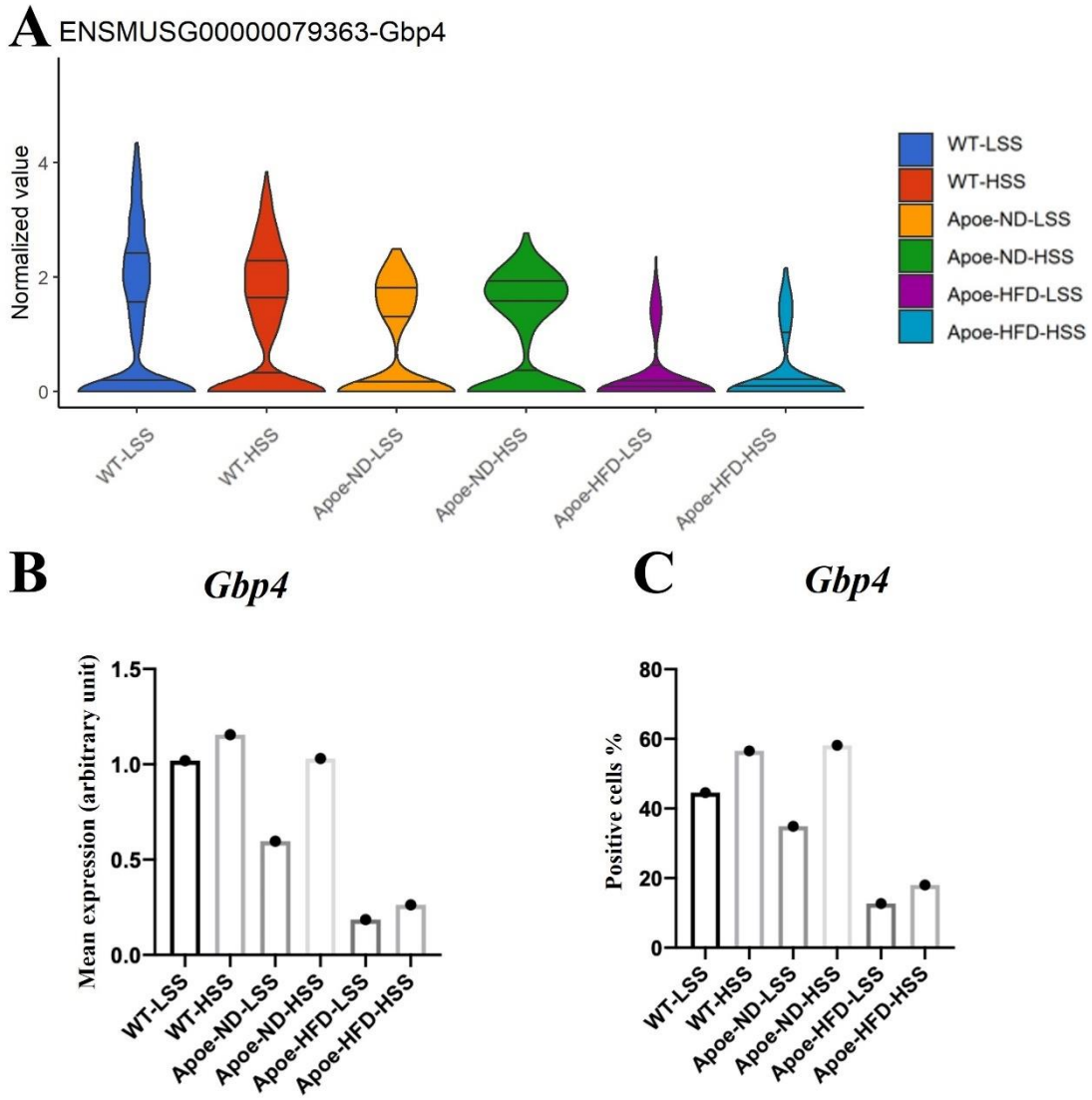

Figure 4. 31 *Gbp4* expression in HSS cells and LSS cells from WT Mice, *ApoE*$^{-/-}$ ND mice and *ApoE*$^{-/-}$ HFD mice. A) Violin plot for Gbp4. (B) Normalized mean expression value. (C) Percentage of positive cells (%).

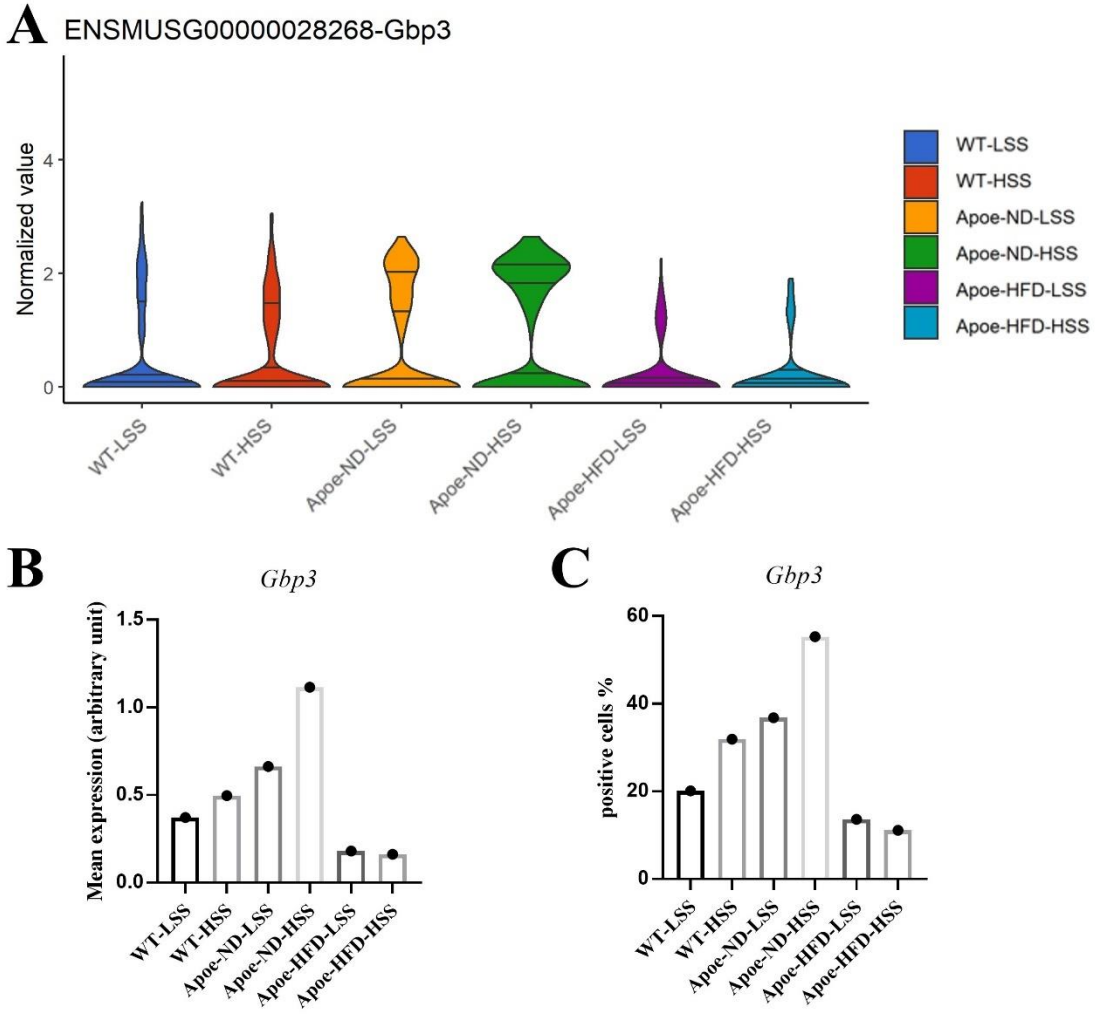

Figure 4. 32 *Gbp3* expression in HSS cells and LSS cells from WT Mice, *ApoE*$^{-/-}$ ND mice and *ApoE*$^{-/-}$ HFD mice. A) Violin plot for Gbp3. (B) Normalized mean expression value. (C) Percentage of positive cells (%).

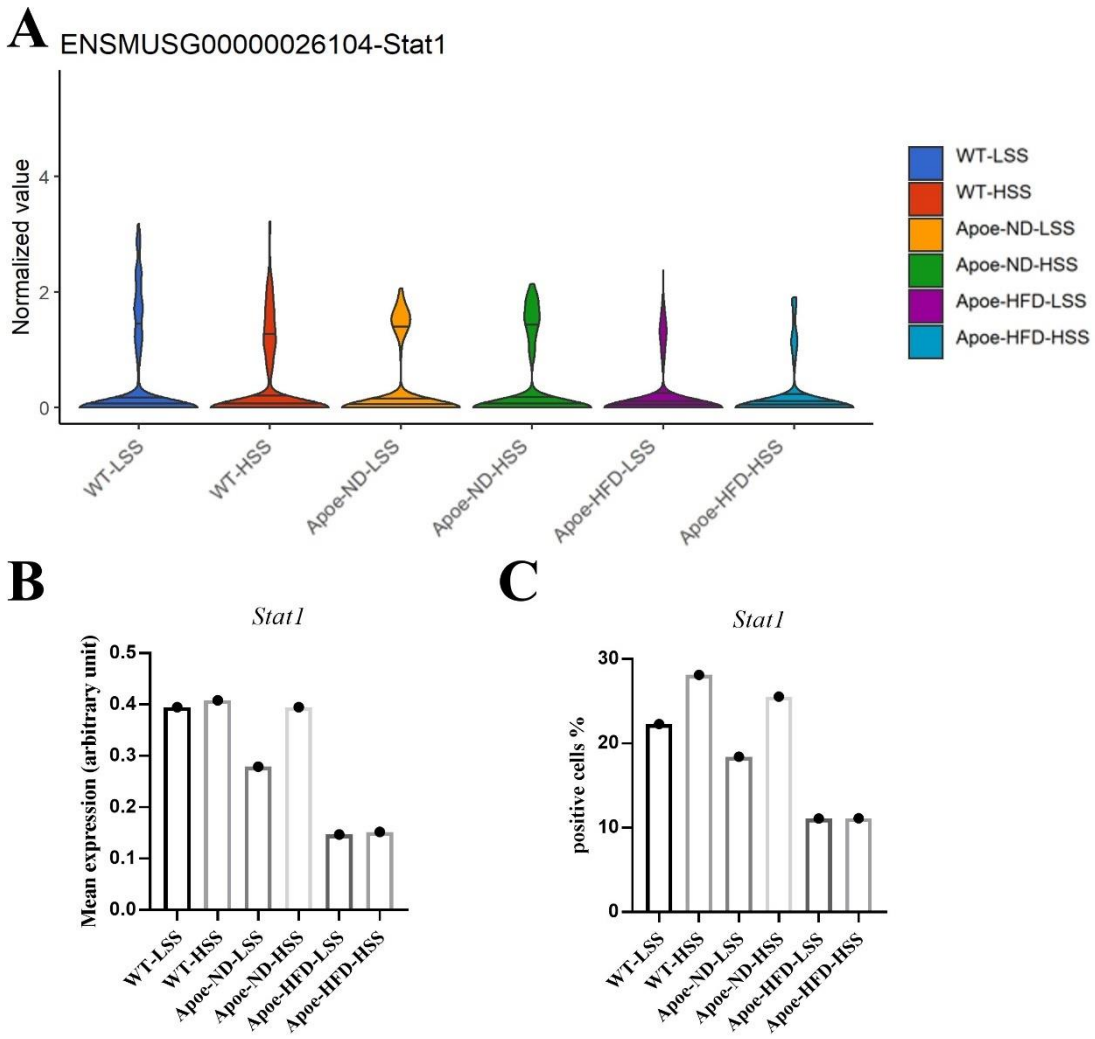

Figure 4. 33 *Stat1* expression in HSS cells and LSS cells from WT Mice, *ApoE*$^{-/-}$ ND mice and *ApoE*$^{-/-}$ HFD mice. A) Violin plot for Stat1. (B) Normalized mean expression value. (C) Percentage of positive cells (%).

4.9 Conclusion

I conclude that:

- eNOS can be used as a HSS marker in scRNAseq profiling analysis of endothelial cells in WT mice, *ApoE*$^{-/-}$ ND mice and *ApoE*$^{-/-}$ HFD mice
- HSS cells (eNOS ^{high}) in healthy aorta had a strikingly different transcriptional profile compared to HSS cells (eNOS ^{high}) in plaques
- Multiple genes including putative mechanoreceptors are differently expressed under HSS and LSS conditions
- Some shear stress genes are different in WT mice, *ApoE*$^{-/-}$ ND mice and *ApoE*$^{-/-}$ HFD mice
- *Klk10*, GBP and interferon genes are enriched in a *ApoE*$^{-/-}$ ND cluster and disappeared in plaques.
- These differences could explain why plaques and healthy aorta respond differently to shear stress, and may also show lipids have effects on eNOS function.

4.10 Discussion

4.10.1 Summary of the differentially expressed genes

Pathways that sense and respond to shear stress in later stage of atherosclerosis are important because they could explain the mechanism of plaque progression towards rupture. To further understand the pathway of plaque progression, I focussed on several genes that exhibit altered expression levels between WT mice, *ApoE*$^{-/-}$ ND mice and *ApoE*$^{-/-}$ HFD mice. Here I provide a summary of the major described roles of several of these differentially expressed genes:

Some studies have shown that BMP4 is a mechanosensitive and pro-inflammatory protein (Sorescu et al., 2003; Souilhol et al., 2020). Laminar flow reduced Bmp4 expression, whereas oscillatory flow induced the expression (Sorescu et al., 2003). In mice and human cells, BMP4 expression was increased at LSS region (Souilhol et al., 2020). Souilhol et al showed that BMP4 is the upstream regulator of HoxB9 and BMP4-HoxB9 pathway can induce inflammation by increasing TNF (tumor necrosis factor) and NFκB expression, moreover, this signalling pathway is enhanced in hypercholesterolaemic environment (Souilhol et al., 2020). However, my scRNA-seq data did not show BMP4 differently expression under LSS. One possible explanation is that LSS cells in my study did not include those with intermediate eNOS expression, and this may have obscured expression difference with HSS.

KLK10, a secreted serine protease was discovered as a tumor suppressor in testicular cancer and breast cancer (Kioulafa et al., 2009; Meyts & Jung, 2001). Recently, a study also found that KLK10 as a vitamin D-responsive gene (J. Lu et al., 2005). Williams et al found that KLK10 serves as a protective protein in atherosclerosis, they showed that KLK10 is enhanced in HSS endothelium in mice, and my observation are consistent with this (Williams et al., 2022). In Williams' study, they also found the KLK10 anti-inflammatory signalling pathway: HTRA1 (high temperature requirement A serine peptidase 1) cleaves and activates KLK10, leading to the inhibition of NFκB and therefore reducing inflammation (Williams et al., 2022).

GBPs and interferon related genes were also found differentially expressed in my scRNA-seq analysis, these genes were enriched in a *ApoE*$^{-/-}$ ND cluster and disappeared in plaques. Many studies have revealed the relationship between GBP protein, interferon related genes and MHC II (CD74). As shown in Figure 4. 34, IFN can recruit and

phosphorylate STAT1 and then promote interferon related gene transcription (Boshuizen & De Winther, 2015). During bacterial infection, it was found that the noncanonical NLRP3 inflammasome signalling pathway is depended on IFN-induced GBP proteins: IFN can activate GBPs and then induce NLRP3 inflammasome and release IL-1β (Gomes et al., 2018; Sharma & Kanneganti, 2016). Also, it was found that IFNγ-STAT1 signalling pathway can induce MHC II expression (X. B. Lu et al., 2019). The signalling pathways discussed suggest that GBPs and IFN genes may play important roles in the immune response in atherosclerotic plaque. However, the relationship between WSS and GBPs remains unknown, it has been reported that LSS can activate STAT1 and induce endothelial damage (Zhu et al., 2020).

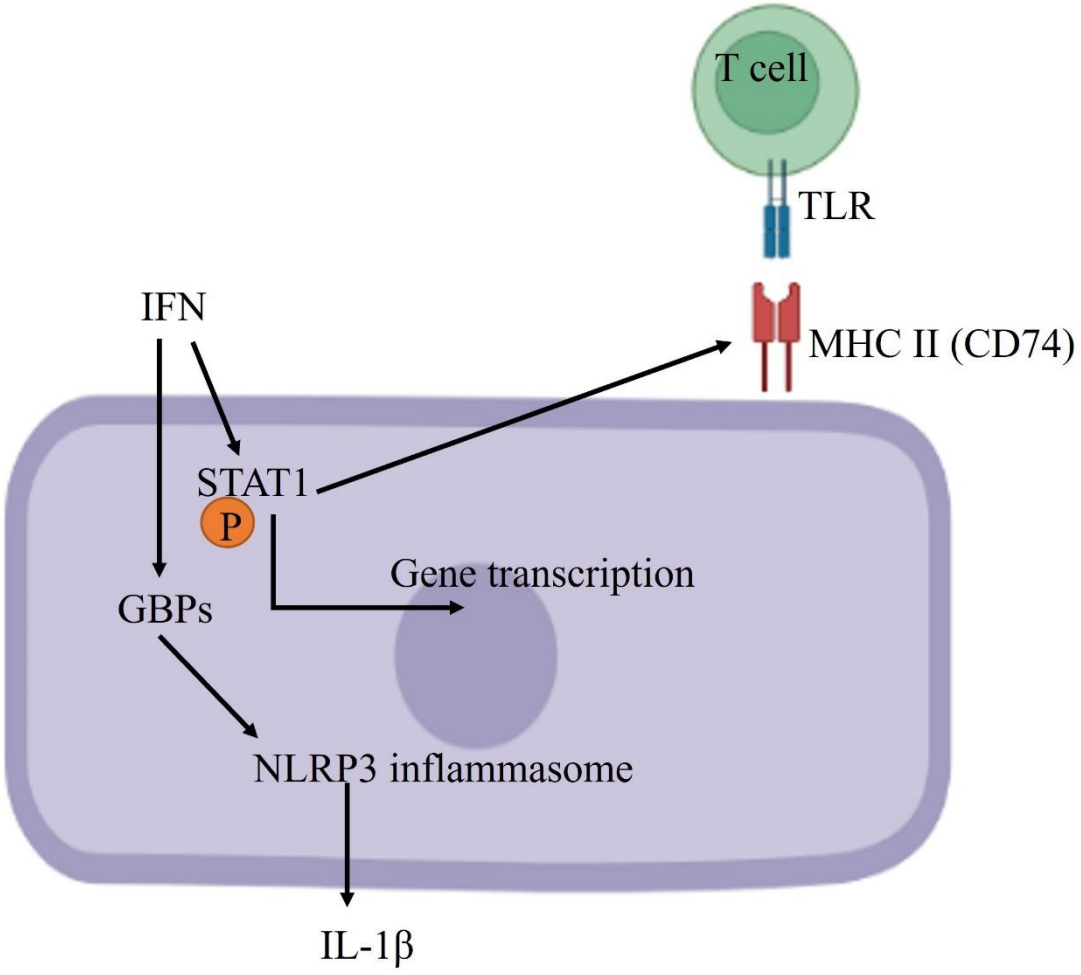

Figure 4. 34 GBPs and interferon related genes signaling pathway IFN can recruit and phosphorylate STAT1 and then promote interferon related gene transcription. IFN can also activate GBP proteins and induce NLRP3 inflammasome and release IL-1β. The IFN-STAT1 pathway can induce MHC II expression. Abbreviation: IFN, interferon; STAT1, signal transducer and activator of transcription 1; MHC II, major histocompatibility complex class II; GBP, guanylate binding proteins.

4.10.2 HSS may not be protective in plaque

Studies suggested that LSS promotes the initiation of plaques and HSS is protective, however, HSS may not be protective in late stage of atherosclerosis (Samady et al., 2011). Samady et al showed that HSS is associated with plaque destabilization (e.g. fibrous tissue regression and necrotic core progression) (Samady et al., 2011). My transcript analysis is consistent with Samady's group studies. All these genes expression in HSS are different between healthy arteries and plaques. Figure 4. 35 summarized these changes, athero protective genes like *Klk10* is disappeared in plaque, and pathogenic genes like *Heg1* have more expression in plaque. I suspected these differences could explain why healthy arteries and plaques respond differently to shear stress. One interesting possibility is that HSS may not be protective in the plaque progression stage. Another possibility is that lipids may have effects on eNOS function and cause the difference between HSS cells (eNOS ^{high}) and LSS cells.

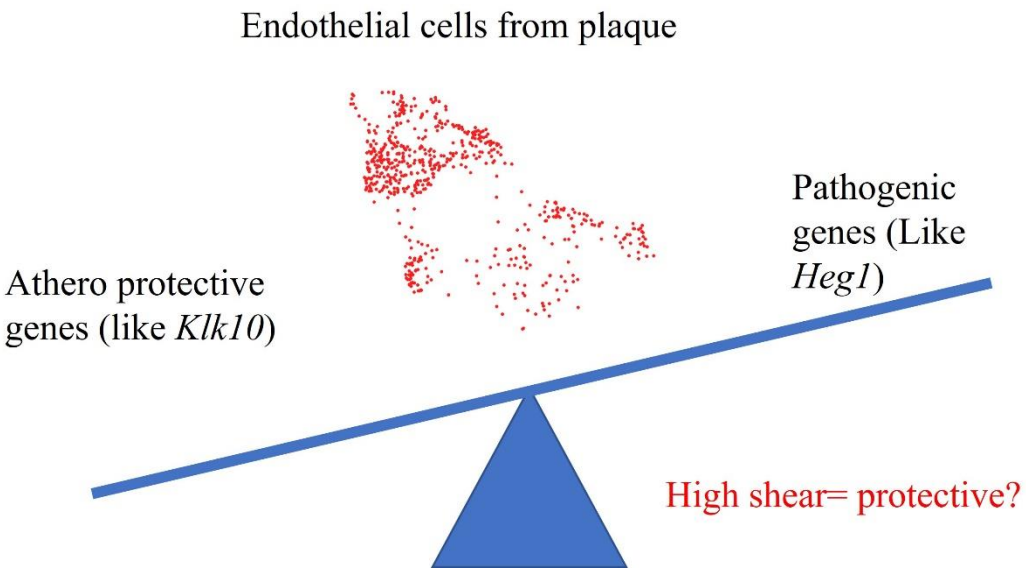

Figure 4. 35 Hypothesis for shear stress regulated genes in plaque progression stage. Athero protective genes like *Klk10* was decreased in HSS, whereas pathogenic genes like *Heg1* was increased.

4.10.3 eNOS expression in plaques

The vasoprotective factor eNOS is crucial for vascular health, however, eNOS expression is reduced in plaques due to eNOS uncoupling (Förstermann & Li, 2011). Despite the reduction in eNOS expression in plaques, previous studies have demonstrated eNOS staining in mice aortic sections (Yeh et al., 2022). Specifically, immunofluorescence staining of eNOS in both WT mice and *ApoE*$^{-/-}$ mice revealed reduced eNOS expression in plaques (Rodella et al., 2013). Consistent with these studies, my technology in this project allowed me to visualize that eNOS expression is expressed at high shear region of diseased aorta. However, it is important to consider that the interaction between lipids and eNOS may impact eNOS function through several mechanisms (Chikani et al., 2004), which could have effects on targeting HSS cells (eNOS ^{high} cells) in plaque.

4.10.4 Are changes in endothelial cell subsets due to plasticity?

This study compares the transcriptome profiles of HSS ECs in healthy and diseased aortas. It is demonstrated that some genes including KLK10, GBP3 and CD74 may be part of the mechanosensing system and are regulated by shear stress, these genes are lost in plaques suggesting that ECs sense shear stress differently in healthy and diseased aortas and their transcriptome profiles are altered by increasing cholesterol.

Several studies have shown that ECs have plasticity and heterogeneity in response to disease-related stimulus like hypertension, hyperlipidemia and altered shear stress (Aditya Sreemadhav Kalluri, 2019). A study from Hanjoong Jo's group used partial ligation to compare transcriptome profiles from ligated carotid with transcriptome profiles from un-ligated carotid; that analysis found that altered shear stress transform ECs from atheroprotective phenotype to proatherogenic phenotype, this reprograming process includes endothelial cell to mesenchymal transition (EndMT) and endothelial cells to immune cell- like phenotypes transition (EndICLT) (Andueza et al., 2020). In this study, they found that cell phenotypes in acute disturbed flow and chronic disturbed flow were different, suggesting this transition depends on time and environment (Andueza et al., 2020). They also demonstrated that Stat1 is a new flow sensitive gene, and chronic disturbed flow can induce Cd74 expression in ECs (Andueza et al., 2020), which validates my work in thesis. Another study also supported the EndICLT theory, vascular ECs can express MHC class I and MHC class II molecules and present antigen presentation roles (Al-Soudi et al., 2017).

Because of these considerations, I hypothesize that the changes in the expression of immune regulators (CD74, GBPs, STAT1) could be due to alterations in EndICLT. One possibility is that EndICLT may be enhanced at regions of HSS by hypercholesterolemia but then reversed in established plaques (explaining the differences in expression between WT, *ApoE*$^{-/-}$ ND and *ApoE*$^{-/-}$ HFD mice). The alternative explanation is that EC populations change due to turnover (i.e. loss of one subset and gain of another) instead of transition. These possibilities are not mutually exclusive and it is likely that changes are partly due to phenotypic transition and partly due to subset loss and growth. One way to discriminate between this is to perform cell tracking studies using fluorescently labelled endothelial cells to determine if they change or are replaced in hypercholesterolemia.

The limitation of my transcriptome profiling analysis is when I selected HSS cells and LSS cells, I only considered eNOS ^{high} and eNOS^{low} cells, the endothelial cells that have eNOS intermediate expression was not included, thus, the validation for scRNAseq data is necessary. Also, the effect of lipids and their metabolites on eNOS expression is not considered in this project. To address this, immunostaining of aortic arch in WT mice, *ApoE*$^{-/-}$ ND mice and *ApoE*$^{-/-}$ HFD mice will be described in next Chapter.

Chapter 5. Validation of scRNA-seq results

5.1 Introduction

Several studies have focused on the effects of haemodynamic forces on endothelial function and physiology to understand the mechanism of plaque erosion and rupture (Thondapu et al., 2021). However, the interaction between plaque and shear stress is still poorly understood. According to my scRNA-seq analysis, there are some genes including GBP genes, interferon genes and athero-protective gene *Klk10* that are enriched in healthy aorta but reduced in plaques. Here, I carried out several analyses using *in vitro* and *in vivo* models in attempt to validate these scRNAseq observations. Understanding the signalling pathway of these genes may provide insight into why vascular endothelial cells sense shear stress differently in healthy aortas versus plaques.

5.2 Hypothesis and Aims

I hypothesized that some mechanosensing genes are expressed differently between healthy aorta and plaques and understanding the regulation of these genes will help to understand plaque responses to shear stress.

To test this hypothesis, I aim to:

1. Validate the scRNA-seq data in vitro by using flow systems and cultured human EC or porcine EC.
2. Validate the scRNA-seq data in vivo by immunostaining of aortas in WT mice, *ApoE*$^{-/-}$ ND mice and *ApoE*$^{-/-}$ HFD mice.

5.3 IN VITRO ANALYSES

In these studies, flow was applied to human coronary artery EC (HCAEC), human aortic EC (HAEC) or porcine aortic EC (PAEC).

5.3.1 Flow regulation of gene expression in cultured human endothelial cells

To determine if shear stress can regulate putative mechanosensing genes (Selp, Nt5e, Klk10, Nox4, Heg1 and Bmp4) expression *in vitro*, I assessed their expression using HCAECs exposed to LSS (4 dynes/cm2) or HSS (13 dynes/cm2) by using an Ibidi® parallel plate system. HCAECs were exposed to these shear stress conditions for 72 hours.

Following cDNA synthesis, qRT-PCR was performed to assess gene expression level using human gene specific primers. Expression of *SELP*, *NT5E*, *NOX4* and *HEG1* varied between donors and there was no clear difference between LSS and HSS (Figure 5. 1 A, B, D, E). The *KLK10* expression in HCAEC seemed to be higher in low shear compared to high shear (Figure 5. 1 C), which differs with the results obtained in scRNA-seq analysis. BMP4 levels were enriched in LSS compared to HSS (Figure 5. 1 F).

Then expression of interferon genes in HAECs exposed to LSS (4 dynes/cm2) and HSS (13 dynes/cm2) were assessed using the Ibidi® system. Their expression varied between different human donors (Figure 5.2). *BST2*, *STAT1* and *STAT2* expression were not significantly different in HAEC exposed to LSS and HSS (Figure 5. 2 A, B and C). It is also observed that *CD74* expression in HAEC was increased in HSS compared to LSS (Figure 5. 2 D), which is consistent with the results obtained at the scRNA-seq analysis.

Then I tested expression of GBP genes in HCAECs exposed LSS (4 dynes/cm2) and HSS (13 dynes/cm2) by using the Ibidi® system. The trend of *GBP4* expression in HCAEC was enhanced in high shear compared to low shear (Figure 5. 3 D), *GBP3* expression was enriched in HSS compared to LSS (Figure 5. 3 C), which is consist with the results obtained at the scRNA-seq analysis. The expression of *GBP1*, *GBP2*, *GBP5* and *GBP7* varied in different donors (Figure 5. 3 A, B, E and F).

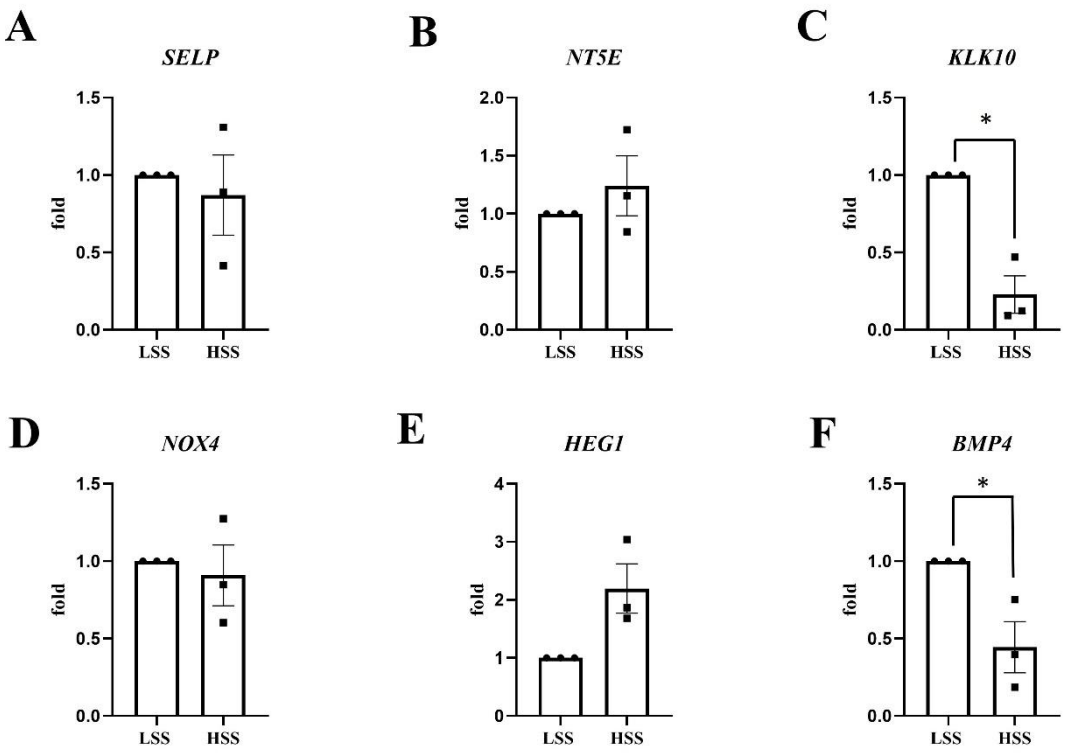

Figure 5. 1 cDNA levels of six putative mechanosensing genes in LSS and HSS conditions in HCAECs. HCAECs were exposed to LSS or HSS for 72 h prior to quantitation of gene expression by qRT-PCR. Data are shown for *SELP* (A), *NT5E* (B), *KLK10* (C), *NOX4* (D), *HEG1* (E) and *BMP4* (F). The housekeeping gene is HPRT. n=3, mean with SEM. Differences between means were analyzed using a paired t-test and significant differences are indicated.

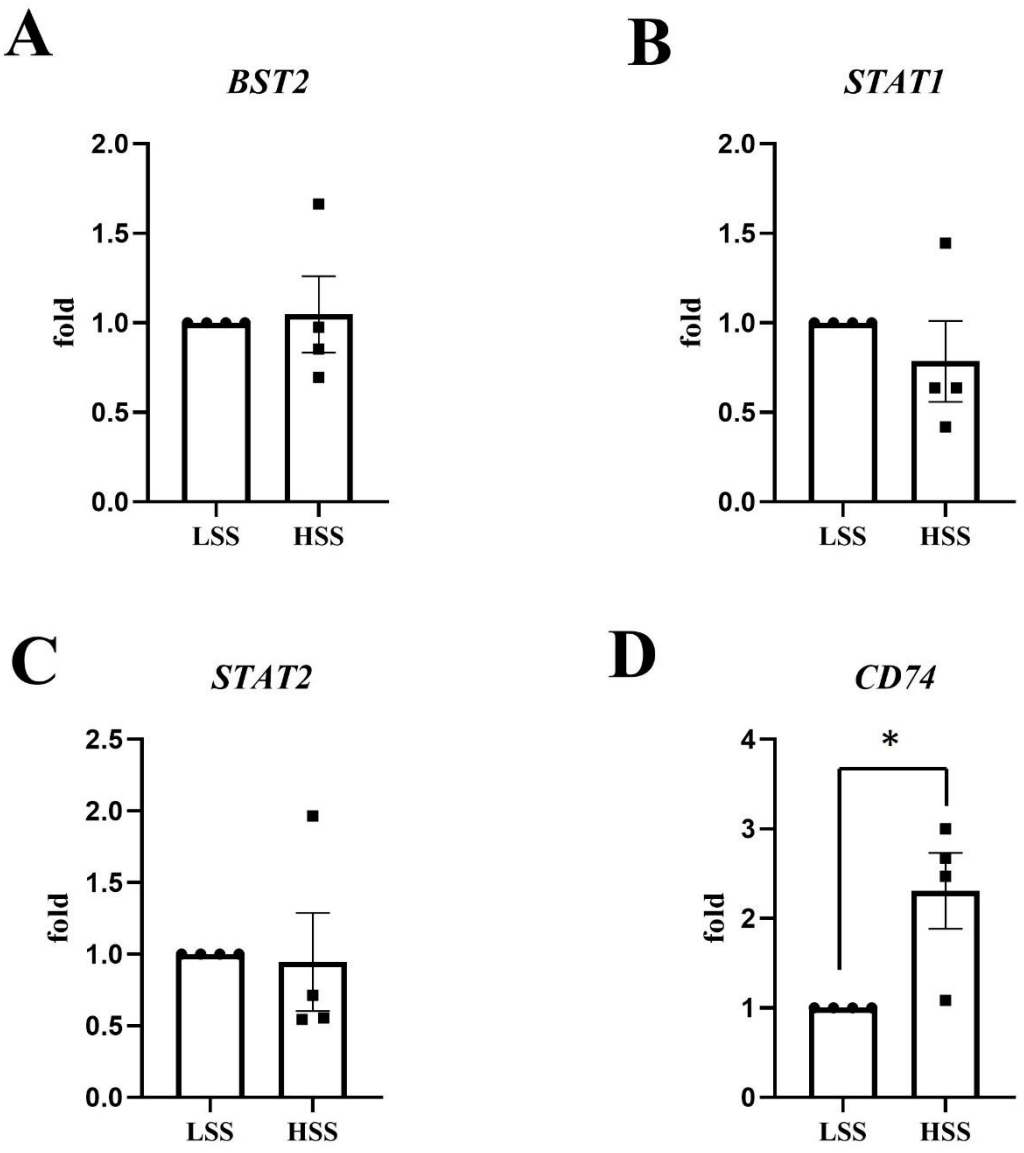

Figure 5. 2 Interferon genes cDNA levels in LSS and HSS in human aortic endothelial cells (HAECs). HAECs were exposed to LSS or HSS for 72 h prior to quantitation of gene expression by qRT-PCR. Data are shown for *BST2* (A), *STAT1* (B), *STAT2* (C), and *CD74* (D). The housekeeping gene is HPRT. n=4, mean with SEM. Differences between means were analysed using a paired t-test and significant differences are indicated.

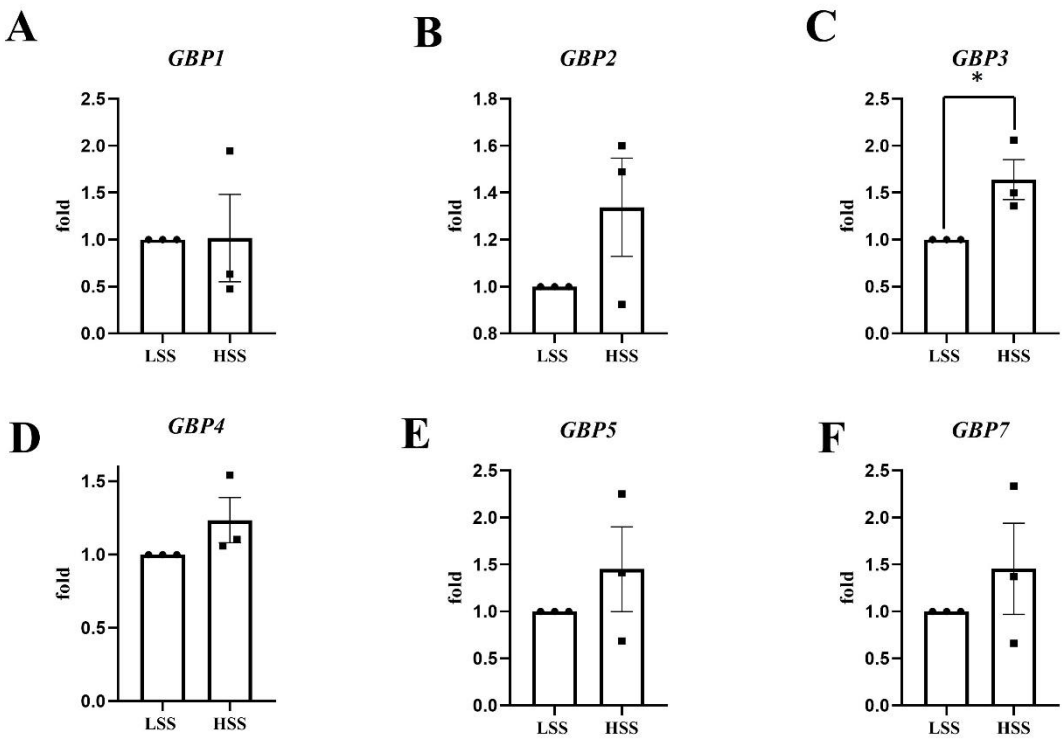

Figure 5. 3 GBPs cDNA levels in LSS and HSS in human coronary artery endothelial cells (HCAECs). HCAECs were exposed to LSS or HSS for 72 h prior to quantitation of gene expression by qRT-PCR. Data are shown for *GBP1* (A), *GBP2* (B), *GBP3* (C), *GBP4* (D), *GBP5* (E) and *GBP7* (F). The housekeeping gene is HPRT. n=3, mean with SEM. Differences between means were analysed using a paired t-test and significant differences are indicated.

5.3.2 Flow and free fatty acid regulation of gene expression in cultured porcine endothelial cells

Hypercholesterolemia is associated with elevated plasma triglycerides which are converted by endothelial cells into free fatty acids. It was found that increased oleic acid (OA) levels can induce lipid accumulation and foam cell formation (Ma et al., 2011). Therefore, it was analysed whether the presence of OA has effects on the responses of EC to flow. Porcine aorta endothelial cells (PAECs) were were treated with OA to mimic the free fatty acid environment. PAECs were simultaneously exposed to flow using the orbital shaker system, cells from the centre of walls were exposed to LSS and cells from periphery of walls were HSS. qRT-PCR was then carried out to quantify the expression of putative mechanosensing genes (Selp, Nt5e, Klk10, Nox4, Heg1 and Bmp4).

By assessing the qRT-PCR results, it is revealed that the expression of *SELP*, *NT5E*, *NOX4*, *HEG1* and *BMP4* were not different between HSS (periphery) and LSS (centre) with or without OA treatment (Figure 5. 4 A, B, D, E and F). Interestingly, the trend of *KLK10* expression was increased in HSS (periphery) compared to LSS (centre) in vehicle, also, the expression was elevated in HSS (periphery) after OA treatment (Figure 5. 4 C), which is consistent with scRNA-seq results.

In summary, most of the genes were not regulated by WSS in cell culture condition. The except was *KLK10* which was enhanced under HSS when treated with OA. Also, *CD74* and *GBP3* expression were elevated in HSS in HAECs and HCAECs. Because of this, I next attempted to validate my scRNA-seq data by en face staining in mice, since mice may mimic physiology better than the *in vitro* condition.

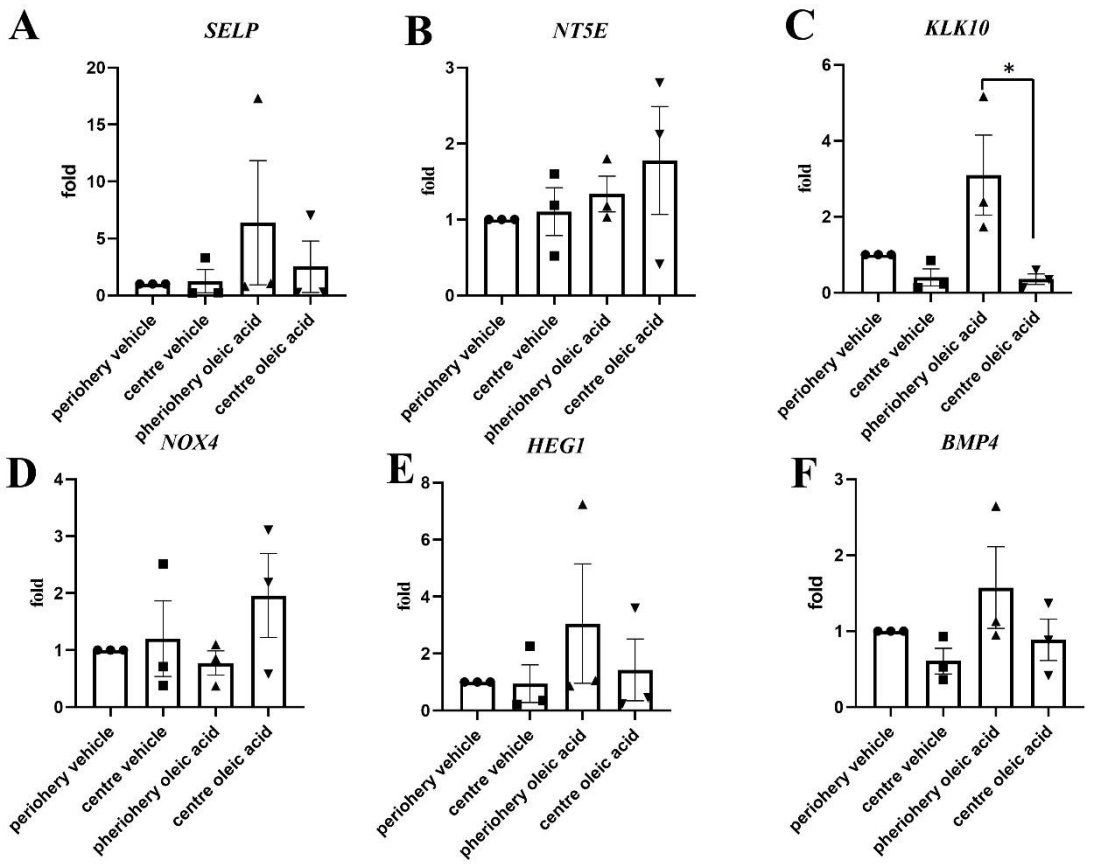

Figure 5. 4 Six mechano-sensing genes cDNA levels in LSS and HSS of porcine aorta, with and without OA treatment. PAECs were isolated from centre and periphery and performed orbital shaker experiment prior to quantitation of gene expression by qRT-PCR. Data are shown for *SELP* (A), *NT5E* (B), *KLK10* (C), *NOX4* (D), *HEG1* (E) and *BMP4* (F). The housekeeping gene is B2M. n=3, mean with SEM. Differences between means were analysed using a two-way ANOVA and significant differences are indicated.

5.4 IN VIVO ANALYSES

5.4.1 Immunostaining of STAT1 in wild-type mice did not show enrichment under different shear stress conditions

To investigate if signal transducer and activator of transcription 1 (STAT1) protein levels are regulated by shear stress in vivo, immunostaining of STAT1 in WT mice was performed. STAT1 expression was not enriched in endothelial cells and the staining (red signal) crossed the CDH5 (VE-cadherin) signal, indicating that it is not from EC and more likely is from immune cells (Figure 5. 5). Thus, I did not include STAT1 for further study.

5.4.2 HEG1 may be slightly enriched at the HSS site

To investigate if heart of glass (HEG1) protein levels are enriched under specific shear stress conditions in vivo, immunostaining of HEG1 in WT mice was performed in 6-8 weeks old C56BL/6 mice. Regions of the aortic arch exposed to high shear stress (HSS; outer curvature) and low shear stress (LSS; inner curvature) were stained using anti-HEG1 antibodies. It was found that staining was heterogeneous in endothelial cells, under high shear stress, some cells have nuclear positive staining, whereas other cells have cytoplasmic and perinuclear positive staining under low shear stress (Figure 5. 6). The isotype rabbit IgG showed little fluorescence (Figure 5. 6 C). Quantification of staining in showed no significant difference between HSS and LSS regions (N=5, p=0.09, Figure 5. 6 D). More significantly, it is reported in the literature that HEG1 is a junction protein (Kreuk et al., 2016). My HEG1 protein expression is heterogeneous and weak in endothelial cells and only small difference between HSS and LSS were seen; therefore, HEG1 was not pursued further.

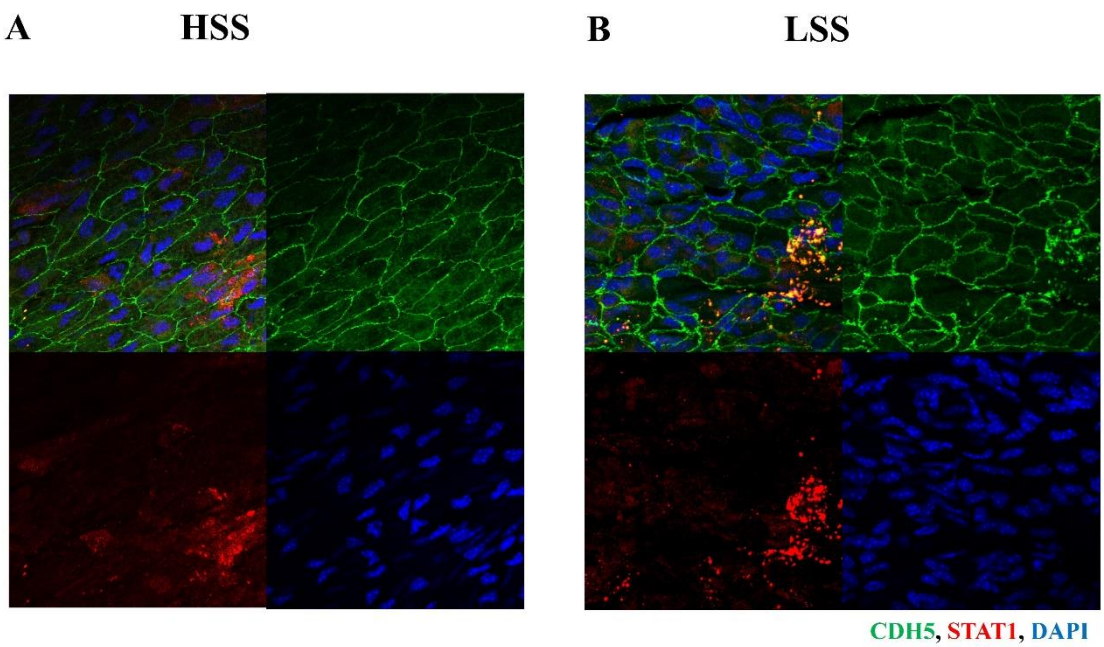

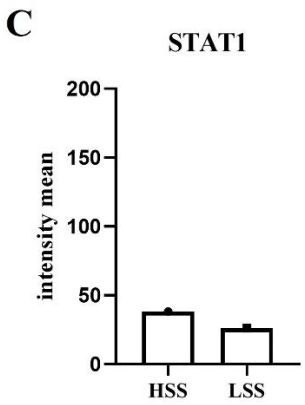

Figure 5. 5 STAT1 expression is not enriched in endothelial cells from WT mice. (A)-(B) En face staining of aortic arch was performed in C57BL/6 WT mice (N=1). The arch was stained for CDH5 (endothelial marker, green), DAPI (nuclear marker, blue) and STAT1 (red). Stained sections were imaged by confocal microscopy at 40X magnification. Two regions were analyzed outer curvature of arch associated with HSS (A) and inner curvature of arch associated with LSS (B). (C) Quantification of STAT1 fluorescence intensity at the HSS regions (outer curvature of arch) and LSS regions (inner curvature of arch) of murine aorta (N=1).

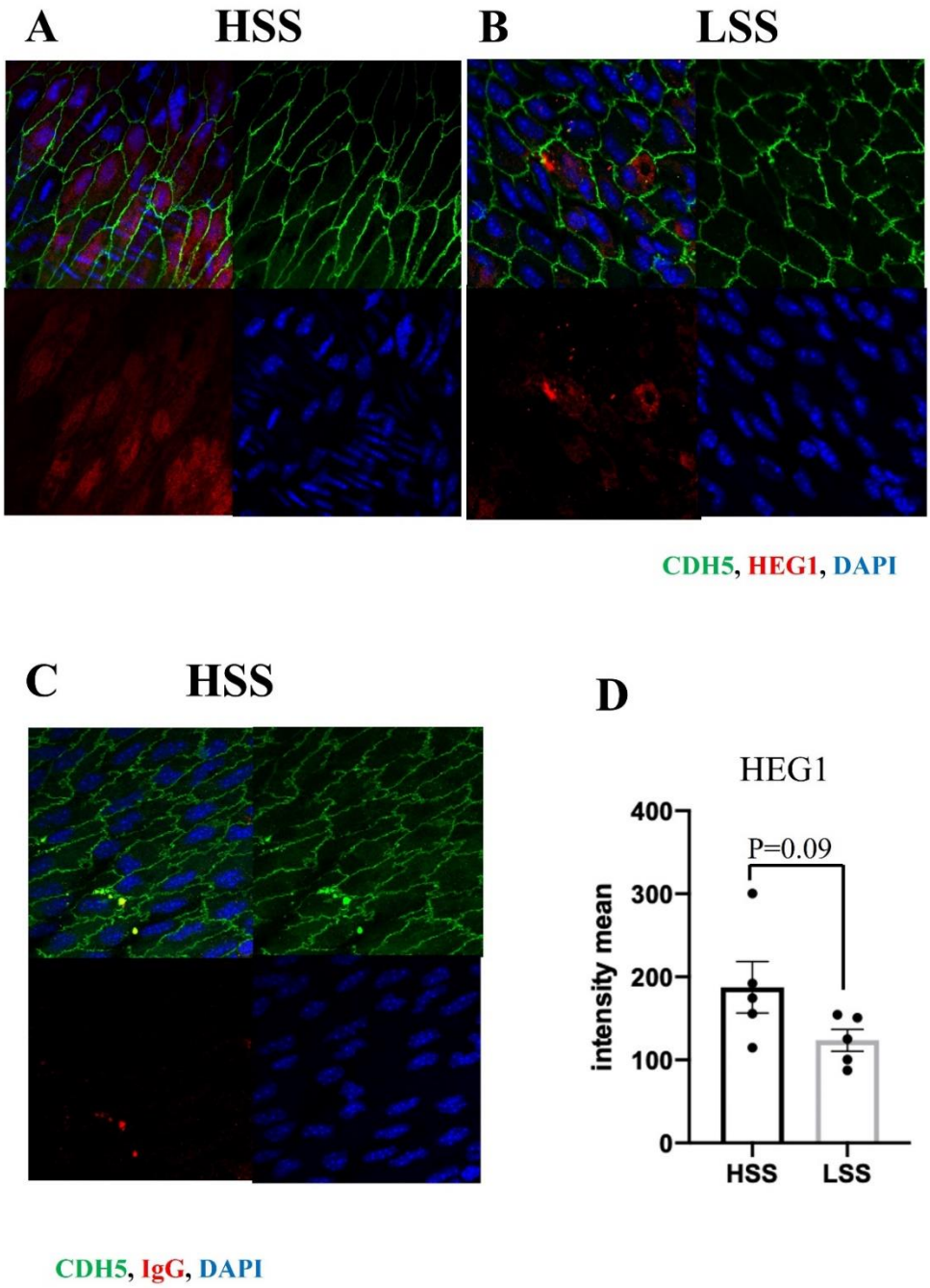

Figure 5. 6 HEG1 may be enriched at HSS regions of the WT mice. (A)-(B) En face staining of aortic arch was performed in C57BL/6 WT mice (N=5). The arch was stained for CDH5 (endothelial marker, green), DAPI (nuclear marker, blue) and HEG1 (red). Stained sections were imaged by confocal microscopy at 40X magnification. Two regions were analyzed outer curvature of arch associated with HSS (A) and inner curvature of arch associated with LSS (B). (C) en face staining of IgG. (D) Quantification of HEG1 fluorescence intensity at the HSS regions (outer curvature of arch) and LSS regions (inner curvature of arch) of murine aorta. Mean values are shown with standard error of the mean (SEM); N=5, paired T-test.

5.4.3 Immunostaining of KLK10 in WT, ApoE$^{-/-}$ ND and ApoE$^{-/-}$ HFD mice

To understand if shear stress and cholesterol levels regulate KLK10 protein expression levels in vivo, immunostaining of murine endothelium was performed in 6-8 weeks old C57BL/6 WT mice, *ApoE*$^{-/-}$ ND mice and *ApoE*$^{-/-}$ HFD mice. Regions exposed to high shear (descending aorta) and low shear (brachiocephalic artery) were stained for KLK10. The KLK10 signal was nuclear positive (Figure 5. 7). KLK10 protein levels were higher at HSS regions compared to LSS regions of the murine aorta in WT mice and *ApoE*$^{-/-}$ ND mice (Figure 5. 7). KLK10 and CDH5 co-staining showed that KLK10 protein expression was significantly reduced at the endothelial layer in atherosclerotic plaques (Figure 5. 7 C and F). An isotype rabbit IgG was used to be negative control for KLK10 in WT mice, *ApoE*$^{-/-}$ ND mice and *ApoE*$^{-/-}$ HFD mice, staining gave little fluorescence, with little change in *ApoE*$^{-/-}$ ND mice and *ApoE*$^{-/-}$ HFD mice (Figure 5. 8). KLK10 fluorescence intensity values normalised against the rabbit IgG control values, confirmed that KLK10 protein levels are enriched in high shear regions and the expression is dramatically decreased in plaques (Figure 5. 7 G, N=4, two-way ANOVA).

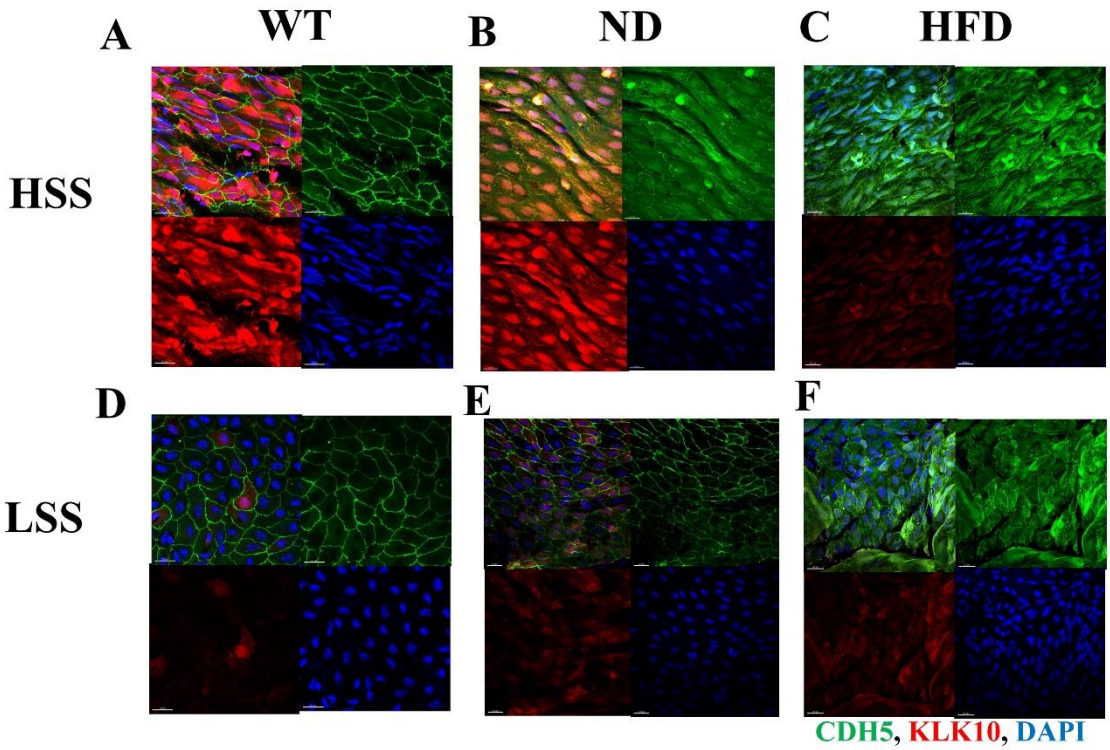
A
WT
B
ND
C
HFD
HSS
D
E
F
LSS
CDH5, KLK10, DAPI

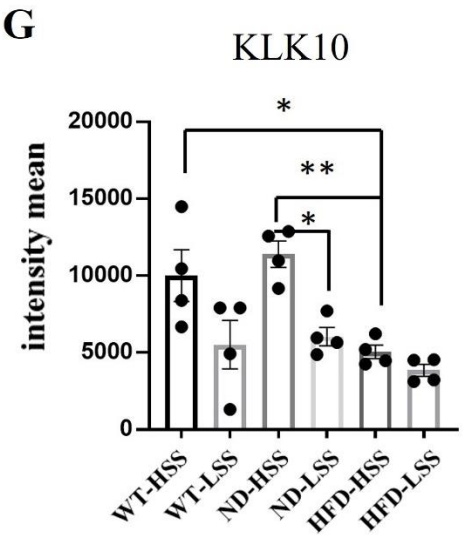
G
KLK10
intensity mean
20000
15000
10000
5000
0
*
**
*
WT-HSS
WT-LSS
ND-HSS
ND-LSS
HFD-HSS
HFD-LSS

Figure 5. 7 KLK10 protein levels are enriched at HSS regions of the WT murine aorta and *ApoE*$^{-/-}$ ND murine aorta and decreased in *ApoE*$^{-/-}$ HFD murine aorta. (A)-(F) En face staining of brachiocephalic and descending aorta was performed in C57BL/6 WT mice, *ApoE*$^{-/-}$ ND mice and *ApoE*$^{-/-}$ HFD mice using anti-KLK10, N=4. The murine tissue was stained for CDH5 (endothelial marker, green), DAPI (nuclear marker, blue), KLK10 (red). Stained sections were imaged with Airy-scan confocal microscope at 40X magnification, Z-stack of images were obtained. Two regions were chosen to Analyze: descending aorta associated with HSS (A)-(C) and brachiocephalic artery associated with LSS (D)-(F). (G) Quantification of KLK10 fluorescence intensity at the HSS regions (descending aorta) and LSS regions (brachiocephalic artery) in WT mice, *ApoE*$^{-/-}$ ND mice and *ApoE*$^{-/-}$ HFD mice, values are normalized against the isotype rabbit IgG control. Mean values are shown with standard error of the mean (SEM); N=4, two-way ANOVA.

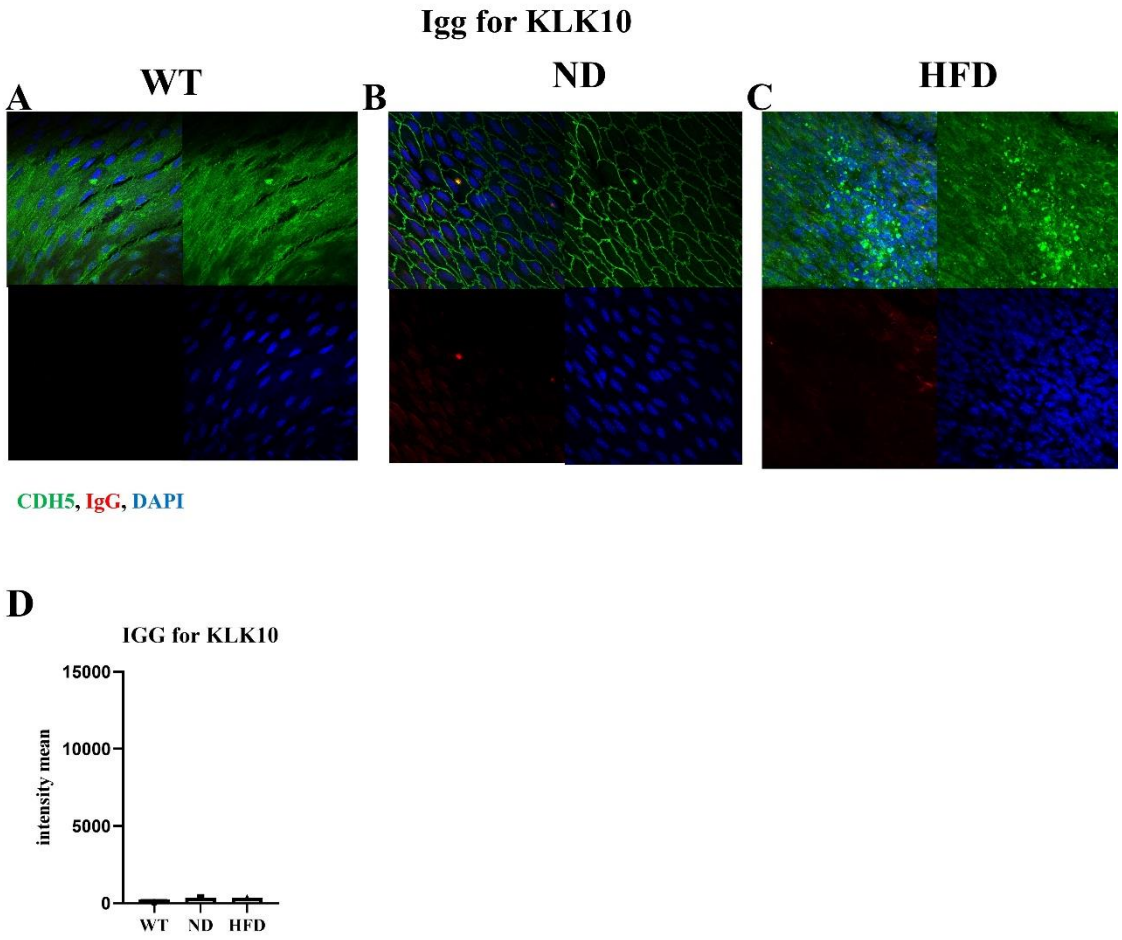

Figure 5. 8 Immunostaining of IgG for KLK10 in WT mice, *ApoE*$^{-/-}$ ND mice and *ApoE*$^{-/-}$ HFD mice. (A)-(C) En face staining controls of descending aorta WT mice, *ApoE*$^{-/-}$ ND mice and *ApoE*$^{-/-}$ HFD mice (N=1) by incubating them with total rabbit IgG. Stained sections were imaged with Airy-scan confocal microscope at 40X magnification, Z-stack of images were obtained. The murine tissue was stained for CDH5 (endothelial marker, green), DAPI (nuclear marker, blue), IGG for KLK10 expression was assessed by immunostaining (red). (A) At HSS region in WT mice. (B) At HSS region in *ApoE*$^{-/-}$ ND mice. (C) At HSS region in *ApoE*$^{-/-}$ HFD mice. Abbreviations: WT, wild type mice; ND, *ApoE*$^{-/-}$ ND mice; HFD, *ApoE*$^{-/-}$ HFD mice. (D) Quantification of isotype rabbit IgG fluorescence intensity at descending aorta in WT mice, *ApoE*$^{-/-}$ ND mice and *ApoE*$^{-/-}$ HFD mice.

5.4.4 Immunostaining of GBP3 in WT, ApoE$^{-/-}$ ND and ApoE$^{-/-}$ HFD mice

To know if shear stress and cholesterol levels regulate GBP3 protein expression level in vivo, immunostaining of murine endothelium was performed; 6-8 weeks old C57BL/6 WT mice, *ApoE*$^{-/-}$ ND mice and *ApoE*$^{-/-}$ HFD mice were used. Regions exposed to HSS (outer curvature of primary aortic arch) and LSS (inner curvature of primary aortic arch) were stained for GBP3. The GBP3 signal had Golgi positive staining (Figure 5. 9). GBP3 protein levels were higher at HSS regions (outer curvature of primary aortic arch) compared to LSS regions (inner curvature of primary aortic arch) of the murine aorta in WT mice and *ApoE*$^{-/-}$ ND mice (Figure 5. 9). GBP3 and CDH5 co-staining showed that GBP3 protein expression was significantly reduced at endothelial layer with atherosclerotic plaques (Figure 5. 9 C and F). An isotype rabbit IgG was used to be negative control for GBP3 in WT mice, *ApoE*$^{-/-}$ ND mice and *ApoE*$^{-/-}$ HFD mice, the IgG signal showed nuclear positive staining, which is different from GBP3 signal pattern, IgG fluorescent values were small, and it was increased in *ApoE*$^{-/-}$ ND mice and *ApoE*$^{-/-}$ HFD mice (Figure 5. 10). GBP3 fluorescence intensity confirmed that GBP3 protein levels are enriched in HSS regions and the expression is dramatically decreased in plaques (Figure 5. 9 G, N=4, two-way ANOVA).

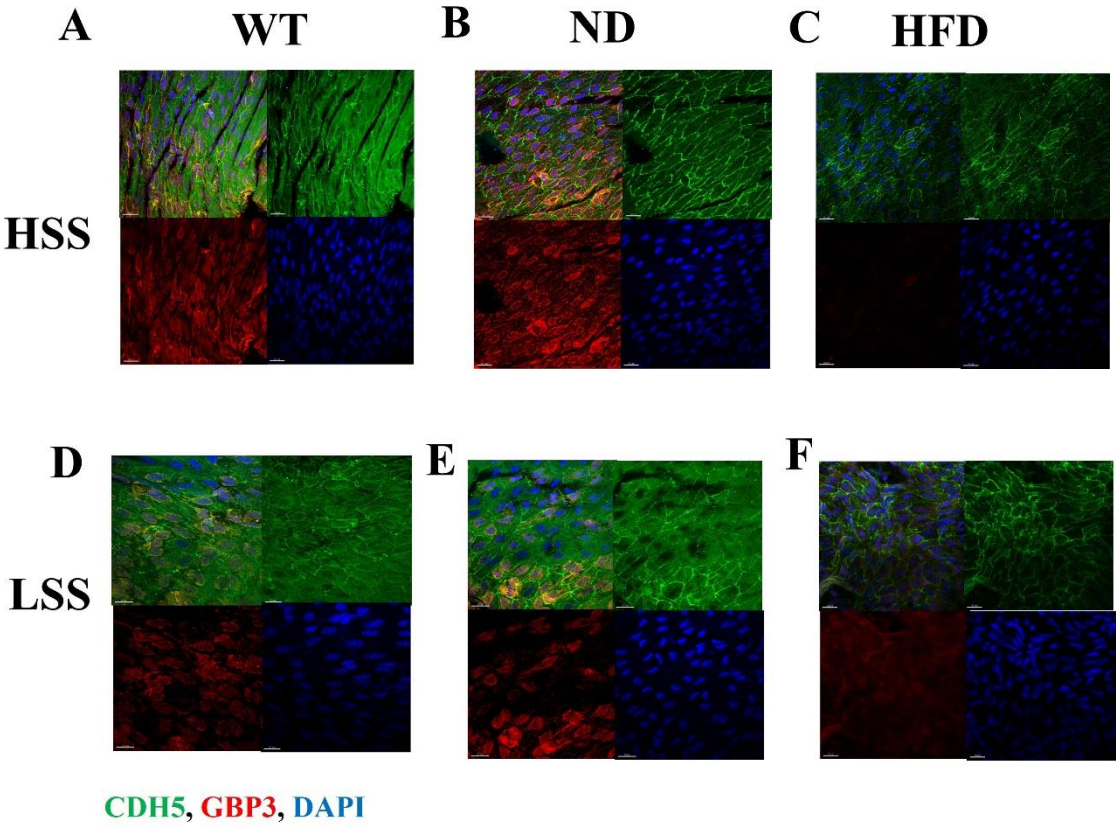
A
WT
B
ND
C
HFD
HSS
D
E
F
LSS
CDH5, GBP3, DAPI

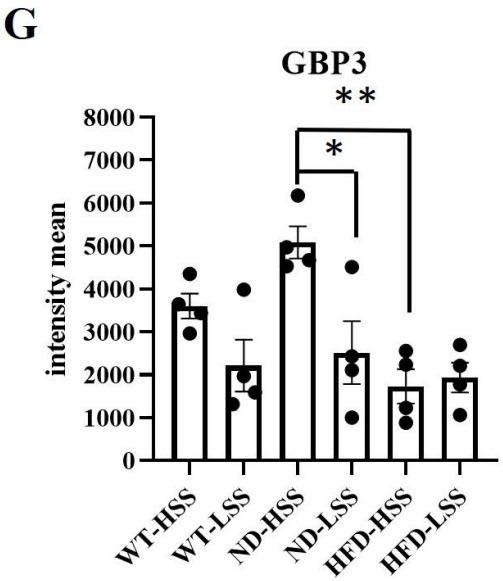
G
GBP3
**
*
intensity mean
8000
7000
6000
5000
4000
3000
2000
1000
0
WT-HSS
WT-LSS
ND-HSS
ND-LSS
HFD-HSS
HFD-LSS

Figure 5. 9 GBP3 protein levels are enriched at HSS regions of the WT murine aorta and *ApoE*$^{-/-}$ ND murine aorta and decreased in *ApoE*$^{-/-}$ HFD murine aorta. (A)-(F) En face staining of primary aortic arch was performed in C57BL/6 WT mice, *ApoE*$^{-/-}$ ND mice and *ApoE*$^{-/-}$ HFD mice, N=4. The murine tissue was stained for CDH5 (endothelial marker, green), DAPI (nuclear marker, blue), GBP3 (red). Stained sections were imaged with Airy-scan confocal microscope at 40X magnification. Two regions were chosen to Analyze: outer curvature of primary aortic arch associated with HSS (A)-(C) and inner curvature of primary aortic arch associated with LSS (D)-(F). (G) Quantification of GBP3 fluorescence intensity at the HSS regions (outer curvature of primary aortic arch) and LSS regions (inner curvature of primary aortic arch) in WT mice, *ApoE*$^{-/-}$ ND mice and *ApoE*$^{-/-}$ HFD mice. Mean values are shown with standard error of the mean (SEM); N=4, two-way ANOVA.

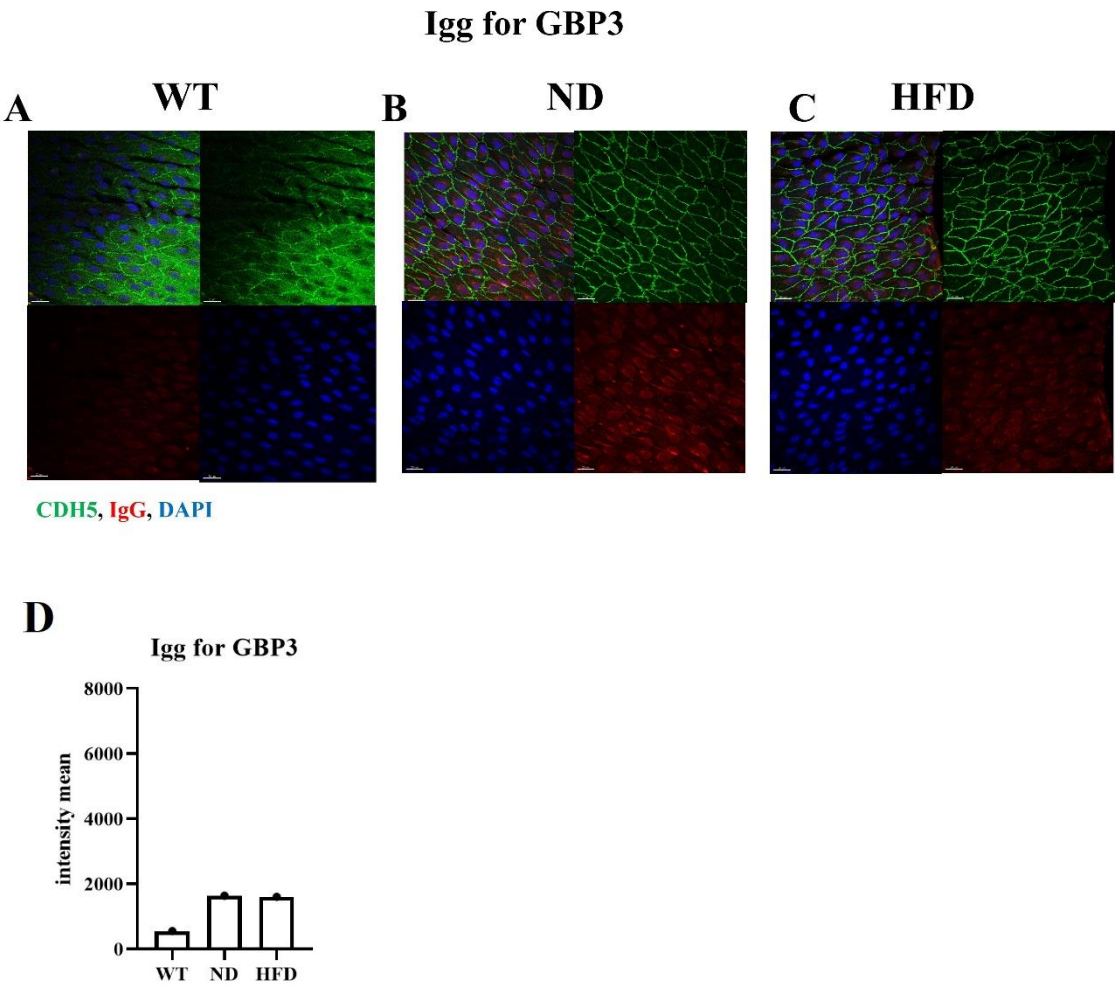

Figure 5. 10 Immunostaining of IgG for GBP3 in WT mice, *ApoE*$^{-/-}$ ND mice and *ApoE*$^{-/-}$ HFD mice. (A)-(C) En face staining controls of descending aorta in WT mice, *ApoE*$^{-/-}$ ND mice and *ApoE*$^{-/-}$ HFD mice (N=1) by incubating them with total rabbit IgG. Stained sections were imaged with Airy-scan confocal microscope at 40X magnification, Z-stack of images were obtained. The murine tissue was stained for CDH5 (endothelial marker, green), DAPI (nuclear marker, blue), IGG for GBP3 expression was assessed by immunostaining (red). (A) At HSS region in WT mice. (B) At HSS region in *ApoE*$^{-/-}$ ND mice. (C) At HSS region in *ApoE*$^{-/-}$ HFD mice. Abbreviations: WT, wild type mice; ND, *ApoE*$^{-/-}$ ND mice; HFD, *ApoE*$^{-/-}$ HFD mice. (D) Quantification of isotype rabbit IgG fluorescence intensity at descending aorta in WT mice, *ApoE*$^{-/-}$ ND mice and *ApoE*$^{-/-}$ HFD mice.

5.4.5 Immunostaining of CD74 in WT, ApoE$^{-/-}$ ND and ApoE$^{-/-}$ HFD mice

To figure out if shear stress and cholesterol level regulate CD74 protein expression level in vivo, immunostaining of murine endothelium was performed; 6-8 weeks old C57BL/6 WT mice, *ApoE*$^{-/-}$ ND mice and *ApoE*$^{-/-}$ HFD mice were used. Regions exposed to HSS (outer curvature of secondary aortic arch) and LSS (inner curvature of secondary aortic arch) were stained for CD74. The CD74 signal had Golgi positive staining (Figure 5. 11). CD74 protein levels were higher at HSS regions (outer curvature of secondary aortic arch) compared to LSS regions (inner curvature of secondary aortic arch) of the murine aorta in WT mice (Figure 5. 11 A and D). CD74 and CDH5 co-staining showed that CD74 protein expression was significantly reduced at endothelial layer in *ApoE*$^{-/-}$ ND mice and *ApoE*$^{-/-}$ HFD mice (Figure 5. 11 B, C, E and F). Since CD74 is also involved in antigen presentation, it was observed the macrophages positive staining in plaques (Figure 5. 11 F). An isotype rabbit IgG was used to be negative control for CD74 in WT mice, *ApoE*$^{-/-}$ ND mice and *ApoE*$^{-/-}$ HFD mice, the IgG signal showed nuclear positive staining, which is different from CD74 signal pattern, IgG fluorescent values were small, and it was increased in *ApoE*$^{-/-}$ ND mice and *ApoE*$^{-/-}$ HFD mice (Figure 5. 12). CD74 fluorescence intensity values confirmed that CD74 protein levels are enriched in HSS regions in WT mice and the expression is dramatically decreased in *ApoE*$^{-/-}$ ND mice and *ApoE*$^{-/-}$ HFD mice (Figure 5. 11 G, N=4, two-way ANOVA).

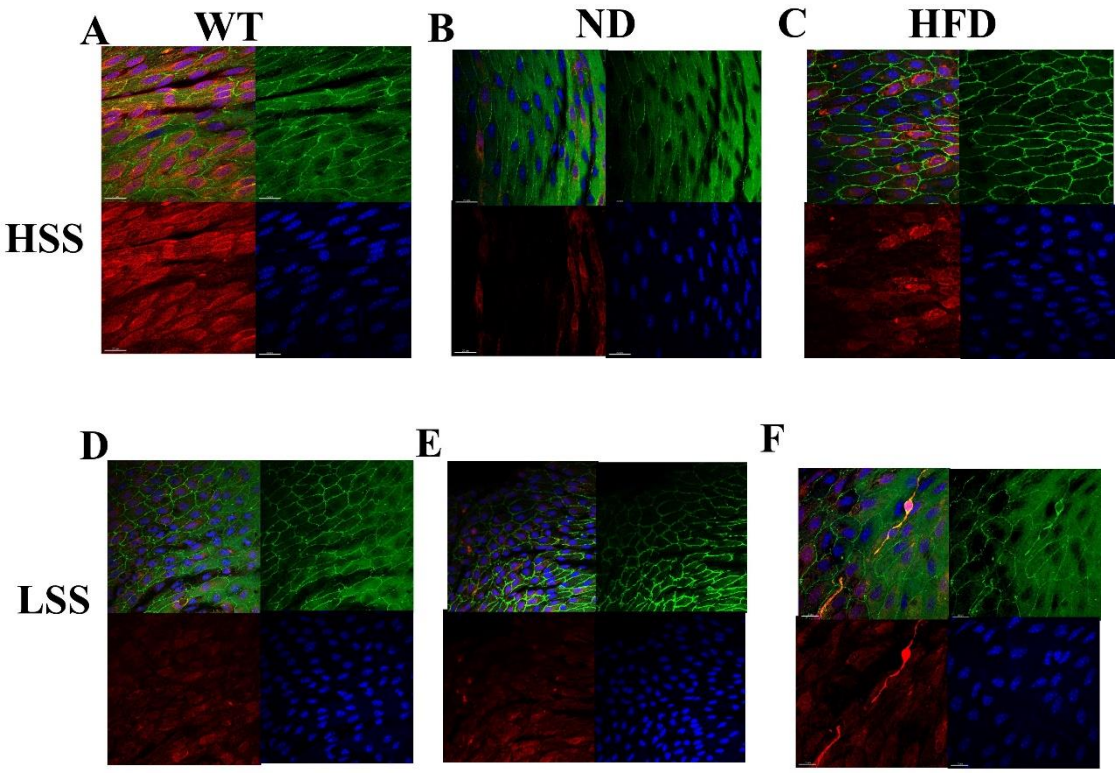

CDH5, CD74, DAPI

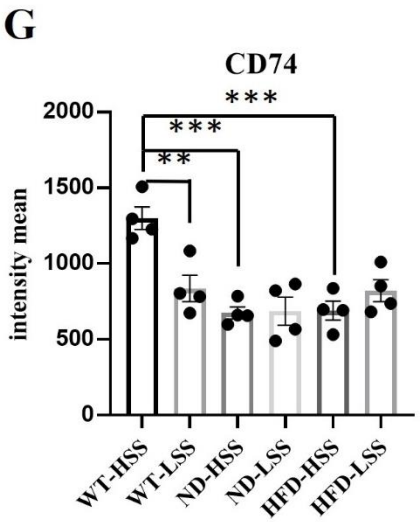

Figure 5. 11 CD74 protein levels are enriched at HSS regions of the WT murine aorta and decreased in *ApoE*$^{-/-}$ ND murine aorta and *ApoE*$^{-/-}$ HFD murine aorta. (A)-(F) En face staining of secondary aortic arch was performed in C57BL/6 WT mice, *ApoE*$^{-/-}$ ND mice and *ApoE*$^{-/-}$ HFD mice, N=4. The murine tissue was stained for CDH5 (endothelial marker, green), DAPI (nuclear marker, blue), CD74 (red). Stained sections were imaged with Airy-scan confocal microscope at 40X magnification. Two regions were chosen to Analyze: outer curvature of secondary aortic arch associated with HSS (A)-(C) and inner curvature of secondary aortic arch associated with LSS (D)-(F). (G) Quantification of CD74 fluorescence intensity at the HSS regions (outer curvature of secondary aortic arch) and LSS regions (inner curvature of secondary aortic arch) in WT mice, *ApoE*$^{-/-}$ ND mice and *ApoE*$^{-/-}$ HFD mice. Mean values are shown with standard error of the mean (SEM); N=4, two-way ANOVA.

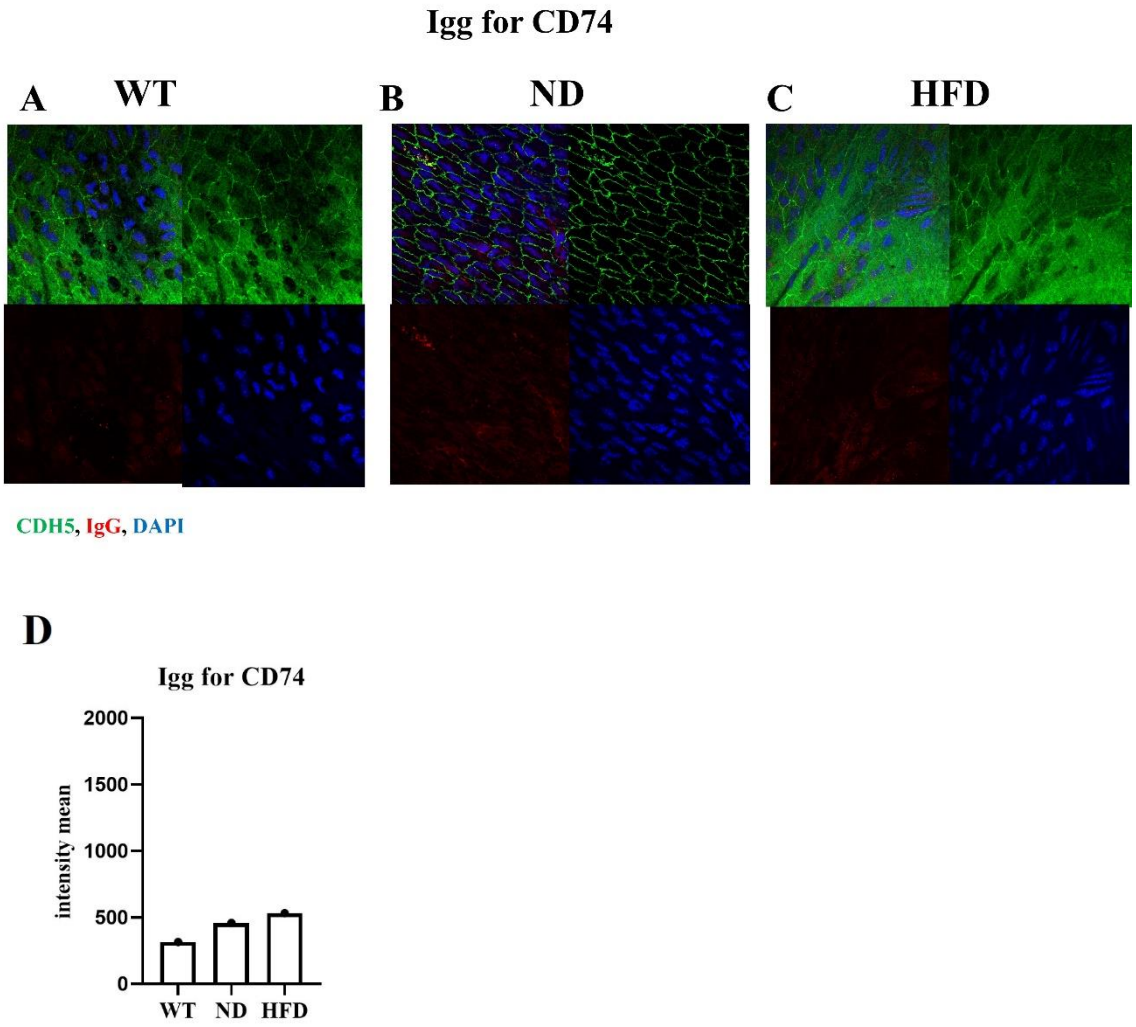

Figure 5. 12 Immunostaining of IgG for CD74 in WT mice, *ApoE*$^{-/-}$ ND mice and *ApoE*$^{-/-}$ HFD mice. (A)-(C) En face staining controls of descending aorta in WT mice, *ApoE*$^{-/-}$ ND mice and *ApoE*$^{-/-}$ HFD mice (N=1) by incubating them with total rabbit IgG. Stained sections were imaged with Airy-scan confocal microscope at 40X magnification, Z-stack of images were obtained. The murine tissue was stained for CDH5 (endothelial marker, green), DAPI (nuclear marker, blue), IGG for CD74 expression was assessed by immunostaining (red). (A) At LSS region in WT mice. (B) At HSS region in *ApoE*$^{-/-}$ ND mice. (C) At HSS region in *ApoE*$^{-/-}$ HFD mice. Abbreviations: WT, wild type mice; ND, *ApoE*$^{-/-}$ ND mice; HFD, *ApoE*$^{-/-}$ HFD mice. (D) Quantification of isotype rabbit IgG fluorescence intensity at descending aorta in WT mice, *ApoE*$^{-/-}$ ND mice and *ApoE*$^{-/-}$ HFD mice.

5.5 Conclusion

I conclude that:

- *Klk10* mRNA levels are increased at high shear regions compared to low shear regions of cultured porcine endothelial cells in the presence of free fatty acid stimulation.
- KLK10 protein levels are upregulated at high shear regions compared to low shear regions of murine aorta *in vivo*.
- KLK10 protein levels are enriched in WT mice and *ApoE*$^{-/-}$ ND mice, and dramatically decreased in plaques.
- GBP3 and CD74 protein levels are upregulated at high shear regions compared to low shear regions of murine aorta *in vivo*.
- GBP3 and CD74 protein levels are enriched in WT mice and *ApoE*$^{-/-}$ ND mice, and dramatically decreased in plaques.

Figure 5. 13 summarized the ScRNA-seq, *in vitro* validation and *in vivo* validation results in this chapter. ScRNA-seq results identifying KLK10 and GBP3 and CD74 have interesting expression changes under shear stress in WT mice, *ApoE*$^{-/-}$ ND mice and *ApoE*$^{-/-}$ HFD mice. Further validation *in vivo* found that KLK10 protein levels were enriched in HSS in WT mice and *ApoE*$^{-/-}$ ND mice, its expression was dramatically decreased in *ApoE*$^{-/-}$ HFD mice. The *in vitro* study showed that KLK10 expression was increased in PAEC under high shear when treated with OA. However, the *in vivo* study showed that KLK10 expression was decreased in *ApoE*$^{-/-}$ HFD mice. The discrepancy between these results could be explained by the lack of immune cell activation in *in vitro* study. Immunity genes identified in scRNA-seq results also were validated in mouse aorta which showed that GBP3 and CD74 protein levels were enhanced in HSS and lost in plaque.

The regulation of KLK10, GBP3 and CD74 levels support the idea that these proteins are part of the mechanosensing system and regulated by shear stress. Immunostaining of KLK10, GBP3 and CD74 in murine aorta showing their expression and mechanosensing function were lost in plaques, suggesting these differences could be the reason that endothelial cells sense shear stress differently in healthy aorta and plaques.

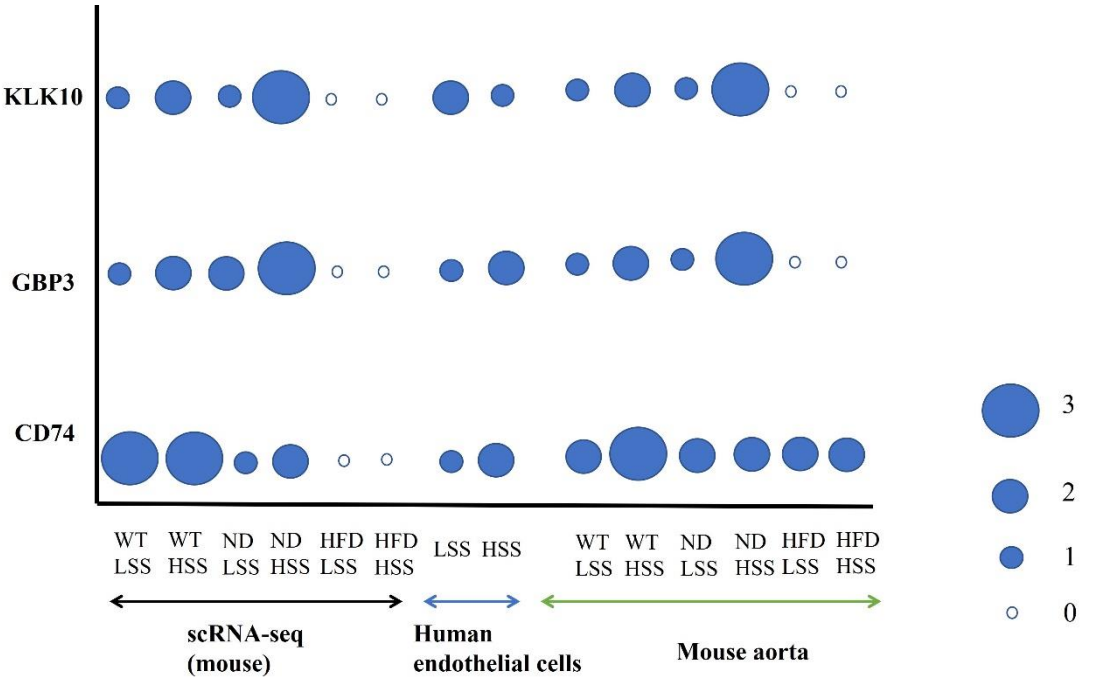

Figure 5. 13 Validation results of KLK10, CD74 and GBP3. Dotplot identifying genes expression levels in scRNA-seq results (mouse), *in vitro* results (validation in HAEC and HCAEC), *in vivo* results (validation in mouse aorta). Dots showed the normalized expression value.

5.6 Discussion

5.6.1 Putative Mechanosensing genes

I have shown that KLK10 protein levels are upregulated in high shear compared to low shear regions *in vivo* and *in vitro*, using cultured human endothelial cells and porcine endothelial cells and immunostaining of the murine aortas. However, it was observed that *KLK10* mRNA level was not enhanced in high shear HCAECs. On the other hand, it was observed that *KLK10* mRNA level was increased in high shear in PAECs. I suspected that it is because *KLK10* mRNA level was not at high levels in my human donors. However, recent research from Hanjoong Jo's group has revealed that KLK10 expression is enhanced by stable flow compared to disturbed flow both *in vivo* and *in vitro*, as determined by multiple techniques including western blot, qPCR, ELISA, and en face staining (Williams et al., 2022). These findings provide further evidence that KLK10 is a flow sensitive protein and is highly expressed in laminar flow. I further confirmed the flow sensitive expression of KLK10 by immunostaining of murine aorta, it was suggested that KLK10 was increased in high shear in WT mice and *ApoE*$^{-/-}$ ND mice and the expression was significantly reduced in *ApoE*$^{-/-}$ HFD mice. Similar observations were shown in other studies, KLK10 levels were dramatically decreased in human coronary arteries with severe plaques compared to those with minimal plaques, the study also showed that KLK10 can inhibit NFκB and thereby reduce inflammation (Williams et al., 2022). Thus, I conclude that KLK10 is an anti-atherogenic protein and its expression is significantly decreased in severe plaques. As shown in Figure 5. 14 A and B, in healthy aortas, KLK10 can protect arteries from atherosclerosis by inhibiting NF-κB and reducing apoptosis and inflammation, however, in aortas with plaques, KLK10 levels are dramatically decreased, the anti-inflammatory pathway is prevented and thereby aggravate atherosclerosis. The upstream mechanisms that lead to the activation of KLK10 are not yet fully understood, however, it is hypothesized that HTRA1 (High Tempreture Requirement A serine peptidase 1) may play a role in cleaving and activating KLK10 in healthy arteries. In atherosclerosis, HTRA1 level is increased and KLK10 expression is reduced, resulting in HTRA1 cleaving KLK10 and inhibiting anti-inflammation pathways (Williams et al., 2022).

Heg1(Heart of Glass) is a heart development protein, and it is a transmembrane receptor that are critical for cardiovascular development (Kreuk et al., 2016). Heg1-Krit1 protein complex can be mechanosensitive and dampen *klf2a* expression (Donat et al., 2018),

which may be pathogenic in atherosclerosis since Klf2 has been shown to be protective in atherosclerosis (Parmar et al., 2006).

STAT1 has important roles with interferons in immunity process through JAK-STAT pathways, but few studies reveal the role of STAT1 in ECs in atherosclerosis. Recently, studies have showed that STAT1 is a negative regulator of angiogenesis in ECs (Battle et al., 2006).

5.6.2 Immune regulators

In this chapter, I have shown that immunostaining of GBP3 and CD74 in mouse aortas have Golgi-like positive staining, recently, it was found that Golgi has crucial roles in innate immunity and initiation of NLRP3 inflammasome activation (Tao et al., 2020). Some interferons inducible GTPases like GBP5 can be promoted by IFN-I and IFN-II in response to virus and bacteria stimulation, and prevent virus replication (Tao et al., 2020). This process suggests that the Golgi-like positive immunostaining is specific.

This chapter shows that CD74 is a flow sensitive protein that is enriched in high shear regions. CD74 was initially discovered as MHC-II antigen presenter, recently, CD74 is found to be involved in proliferation both in cancer cells and endothelial cells. A study found that CD74 as a cognate macrophage migration inhibitory factor (MIF) receptor, can promote proliferation and inhibit apoptosis in hepatocellular carcinoma cells (Wirtz et al., 2021). Another study also showed CD74 can increased proliferation in endothelial cells *in vitro* (Rodor et al., 2021). Since proliferation in endothelial cells under high shear is anti-atherogenic and help to repair blood vessel after injury, I hypothesize that CD74 may have athero-protective roles in healthy arteries and its expression and is significantly decreased in endothelial cells of severe plaques.

The GBPs are a family of guanosine triphosphatases (GTPases) (Liu et al., 2018). GBPs are well known for protecting cells against bacteria by detecting lipopolysaccharide (LPS) (Santos et al., 2018). It has been recently discovered that GBPs play a significant role in pyroptosis, a novel programmed cell death pathway that involves caspase-dependent pathway. It is characterized by forming pores on cell membrane, which leads to the release of IL-1β and IL-18, ultimately causing cell lysis (Man et al., 2017). Among all inflammasomes in pyroptosis, the NLRP3 inflammasome is particularly significant in inflammation and atherosclerosis. It is thought to be regulated by shear stress through F-

actin (Baldrighi et al., 2017). Furthermore, recent research has found that GBP protein can interact with NLRP3 (Baldrighi et al., 2017).

This chapter shows GBP3 is a flow sensitive protein that enriched in high shear regions *in vivo* and *in vitro*. GBP3 immunostaining in murine aorta shows that GBP3 was enriched in HSS and hypercholesterolemia (*ApoE*$^{-/-}$ ND mice) induced GBP3 expression. Thus, I suspected GBP3 may have some pathogenic roles, and oxLDL may be one of the molecules that can upregulate GBPs. However, the function of GBPs in atherosclerosis is still unclear. It is reported in GWAS that GBP3 is related to carotid intima media thickness. Recently, many studies have discovered the function of immunity cells in atherosclerosis. It was found that increased IL-17 expression with reduced IFN- γ can stabilize the plaque structure, on the other hand, increased IL-17 with IFN- γ can lead to plaque progression (Taleb et al., 2015). Clinical studies also found that targeting IL-1 receptor inhibitors and NLRP3 inhibitors can benefit patients with atherosclerosis (Abbate et al., 2020). Thus, I propose the immune cells in atherosclerosis are a 'double edged sword', it depends on the microenvironment of ECs with plaques. As shown in Figure 5. 15, the relationship between GBP3 and CD74 in ECs is still unknown, nevertheless, it was found that interferons can induce both GBP protein and CD74 in macrophages (Marquis et al., 2011). The effects of interferons in ECs are also conflicting, it was found that short-term interferons treatment can prevent apoptosis of ECs, however, long-term interferons stimulation can induce ECs senescence and in the end lead to atherosclerosis (Pammer et al., 2006). On the other hand, CD74 can promote ECs proliferation which is athero-protective. Thus, I propose the role of CD74 and GBP3 in atherosclerosis is conflicting, it depends on the microenvironment of ECs.

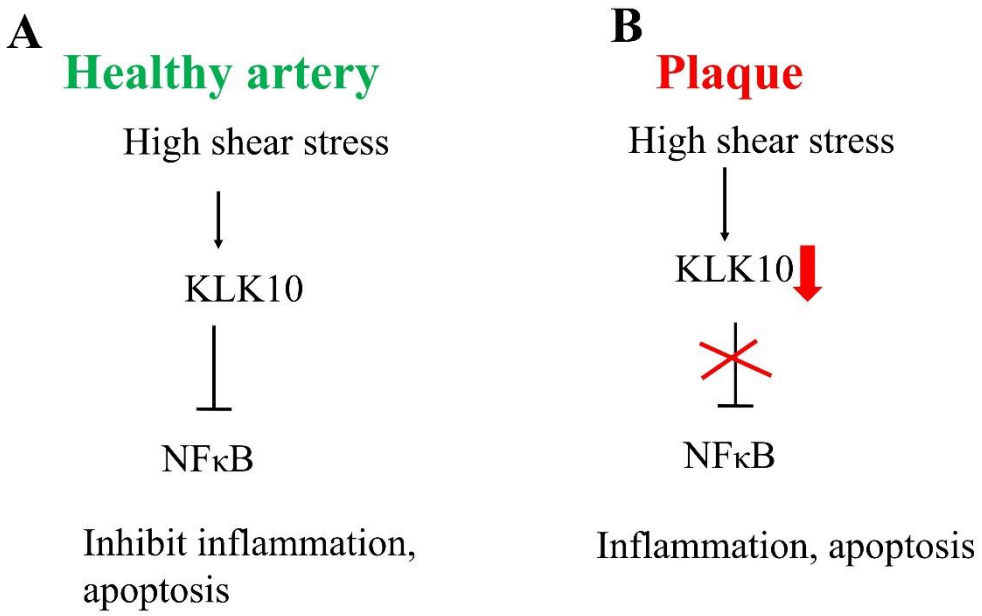

Figure 5. 14 Role of KLK10 in atherosclerosis. In healthy artery, KLK10 cam protect aortas by inhibit NFκB and prevent inflammation, in diseased artery, KLK10 levels are low and the anti-inflammatory pathway is prevented, which leads to atherosclerosis.

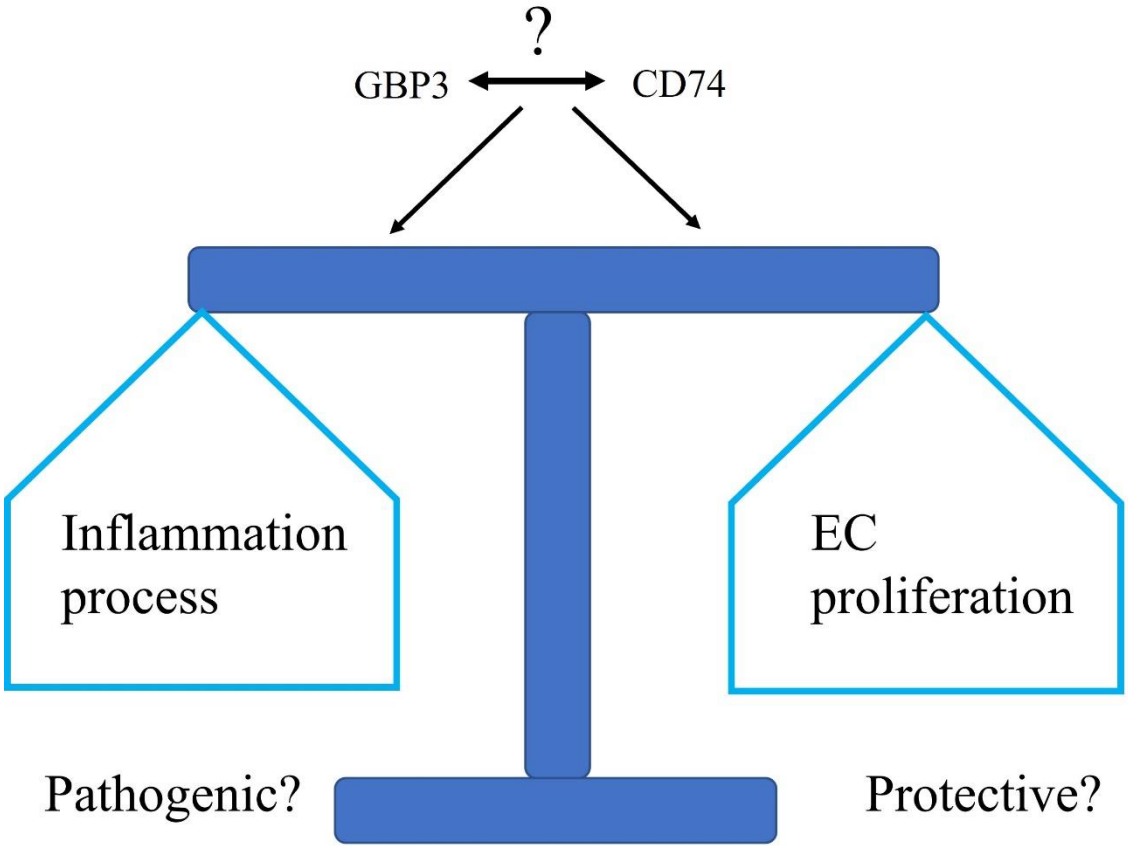

Figure 5. 15 The role of GBP3 and CD74 in atherosclerosis. The relationship between GBP3 and CD74 are still unclear, GBP3 is involved in inflammation process which may be pathogenic, CD74 can promote ECs proliferation which is athero-protective, the role of GBP3 and CD74 in atherosclerosis is still conflicting.

Chapter 6. General discussion

6.1 Major findings

This study established a method using optical clearing, immunostaining coupled with light sheet imaging to analyse spatial distribution of proteins in atherosclerotic plaques. It was found that eNOS can be used as a HSS marker both in healthy aorta and diseased aorta. Moreover, using this method coupled with OPT imaging and computational fluid dynamics has wider use because it can correlate expression of other proteins with shear stress. This innovative technique was not only utilized in this study but was also used to analyze other proteins by our group e.g. JAG1and NOTCH4 (Souilhol et al., 2022). After validating eNOS as a HSS marker, I analysed scRNA-seq data to compare HSS profiles ($eNOS^{high}$) in healthy and diseased aortas. I found several putative mechanosensing genes with an expression level that is altered by shear stress in ECs from WT mice, *ApoE*$^{-/-}$ ND mice and *ApoE*$^{-/-}$ HFD mice. In particular, *Klk10* is a novel atheroprotective gene, it was enriched in HSS in WT mice and *ApoE*$^{-/-}$ ND mice and it disappeared in plaque endothelial cells according to my scRNA-seq analysis. I also found that in my scRNA-seq data, GBPs and interferon related genes were enriched in cluster 2, and all genes were strongly reduced in plaque endothelium. In particular, Gbp3 is related to carotid intima media thickness in GWAS and Cd74 can regulate EC proliferation, suggesting they may play crucial roles in plaque progression. Then, I validated scRNA-seq data at mRNA level and protein level by in vitro analysis (PAEC, HAEC, HCAEC) and *in vivo* analysis (immunostaining of WT mice, *ApoE*$^{-/-}$ ND mice and *ApoE*$^{-/-}$ HFD mice). The validation results showed KLK10, GBP3 and CD74 are differentially expressed at the protein level suggesting that they may be part of the mechanosensing system. Their expression was lost in plaque and this could be a reason that ECs sense shear stress differently in healthy aorta and plaques.

My work is consistent with previous studies that show considerable EC heterogeneity in healthy and diseased arteries (Aditya S. Kalluri et al., 2019). It extends this work by showing that EC exposed to HSS have distinct transcriptional profiles under different conditions. A major conclusion from my study is that the idea that HSS is atheroprotective may be an oversimplification. The reality may be that HSS responses depend on context, in particular levels of lipidemia and growth of plaque.

6.2 Factors that may lead to plaque rupture

It is well known that LSS induces the initiation of atherosclerosis and HSS is protective. However, there is conflicting data on the shear stress profiles that promote plaque rupture with the suggestions that LSS or HSS are the major drivers (Samady et al., 2011; Stone et al., 2012). Because of technical differences including imaging and analysis methods, it is hard to reconcile these different observations. In this study, by comparing the transcriptome profiles of high shear ECs from WT mice, *ApoE*$^{-/-}$ ND mice and *ApoE*$^{-/-}$ HFD mice, it was found that some mechanosensing genes that are enriched in healthy aorta are lost in plaque, and some interferon genes that are enriched in ECs in *ApoE*$^{-/-}$ ND mice are lost in plaque, some atheroprotective genes like KLK10 are lost in plaque. All these findings showed that ECs physiology at high shear regions can be altered by increasing plasma cholesterol levels and the development of atherosclerotic plaques. Thus, I hypothesize that HSS may not be protective in later stage of atherosclerosis and altered shear stress may induce rupture-phone plaque phenotypes by altering ECs physiology.

Recently, Thondapu's group reported a study comparing flow dynamics in eroded plaques and ruptured plaques (Thondapu et al., 2021). They analysed haemodynamics in 19 patients with ruptured plaque and 18 patients with eroded plaque, by using computational fluid dynamic coupled with optical coherence tomography (OCT), they found that layered structure, increased endothelial shear stress gradient (ESSG) and lipids are linked with ruptured plaque independently, whereas, elevated endothelial shear stress (ESS), ESSG and oscillatory shear index (OSI) are linked with eroded plaque independently (Thondapu et al., 2021). Although Thondapu's group and other studies have demonstrated the shear stress profiles in plaque progression, the mechanism of plaque rupture and plaque erosion is still unclear, thus, shear stress is considered to be the 'dark energy' in vasculature, for its crucial roles and largely undiscovered effects (Evans et al., 2021). An important conclusion from my analysis is that vascular responses to shear stress are not uniform; instead they vary between healthy and diseased tissues. Further work is needed to determine the effects of ESSG on KLK10, CD74 GBP3 and other shear regulated proteins.

6.3 KLK10, CD74 and GBP3 as putative therapeutic targets

KLK10 and CD74 have potential atherosclerotic functions. Hanjoong Jo's group showed that KLK10 can inhibit endothelial inflammation through protease activated receptor 1 and 2 signalling pathway (Williams et al., 2022).

Since CD74 is cell membrane receptor of macrophage migration inhibitory factor (MIF), MIF-CD74 interactions have crucial roles in promoting healing from cell injury (Farr et al., 2020). My research showed that KLK10 and CD74 expression was enriched in HSS cells in WT mice, for KLK10, the enrichment was amplified in *ApoE*$^{-/-}$ mice exposed to a normal chow diet. For CD74, the CD74 expression in ECs was decreased whereas the CD74 expression in immunity cells was dramatically increased. Given their function, this suggests that KLK10 and CD74 may protect high shear regions from damage and that this protective mechanism is enhanced under conditions of hypercholesterolemia (Figure 6. 1). This is a potential novel homeostatic pathway. However, the formation of plaques in *ApoE*$^{-/-}$ mice exposed to a high fat diet caused a dramatic reduction in KLK10 and CD74, which may cause disease progression through loss of homeostasis.

On the other hand, the link between GBPs and atherosclerosis suggests that they may contribute to disease progression (Goo et al., 2016). Previous studies have showed that GBP3 and GBP6 expression was induced by chronic hypercholesterolemia, and it was suggested that oxLDL may be one of the molecules that can upregulate GBPs. This induction of GBPs hints at a pathogenic role. Consistently, GBP3 has a significant association with carotid artery intima media thickness in GWAS ($p<10^{-5}$) (Xie et al., 2015), which is a well-known marker for subclinical atherosclerosis (Yeung et al., 2022). Therefore, the development of a plaque may have complex effects on shear -regulated molecules by reducing some positive molecules (e.g. KLK10, CD74) and simultaneously reducing some pathogenic molecules (e.g. GBP3) (Figure 6. 1).

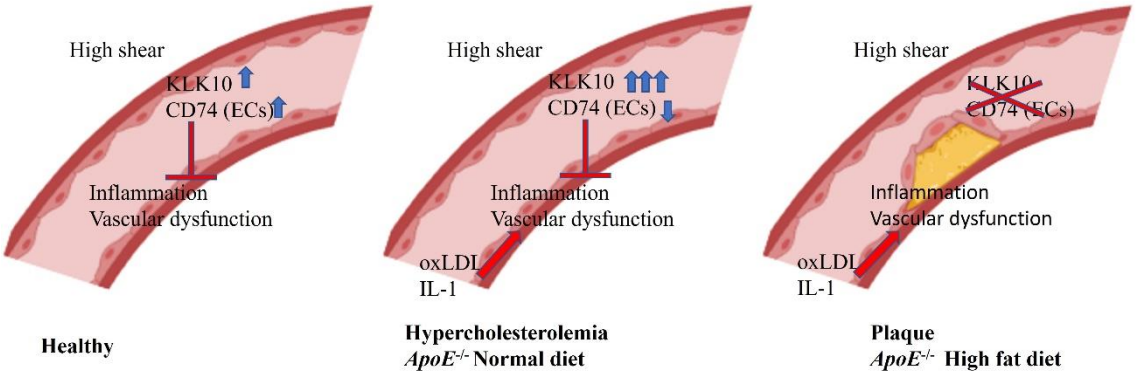

Figure 6. 1 The role of KLK10 and CD74 in atherosclerosis. KLK10 is enriched in HSS in WT mice, and this enrichment is amplified in *ApoE*$^{-/-}$ ND mice. CD74 is enriched in HSS in WT mice, and CD74 expression in ECs is decreased in *ApoE*$^{-/-}$ ND mice. Both KLK10 and CD74 expression is dramatically decreased in plaque. Given their function, it suggests that KLK10 and CD74 may protect high shear regions from damage and this protection is disappeared in plaque (loss of homeostasis).

6.4 Limitations

For the scRNAseq analysis, three types of mice were utilized, including female and male C57BL/6 WT mice (aged 6-8 weeks), female and male *ApoE*$^{-/-}$ ND mice (exposed to normal diet for 8 weeks), female and male *ApoE*$^{-/-}$ HFD mice (exposed to high fat diet for 8 weeks). While Several proteins were validated using these mice, the sex and age of the mice were not standardized across the various conditions. This limitation may be addressed by using mice of the same age and sex in future investigations, nevertheless, this issue was partly addressed in my validation work using en face staining.

6.5 Future work

6.5.1 Expression analysis of GBP3 and CD74

Cells from porcine aortas could be isolated and exposed to HSS and LSS conditions, with or without OA treatment, western blot could be performed to assess protein expression levels of GBP3 and CD74.

6.5.2 Functional analysis of KLK10, GBP3 and CD74 in vitro

Future work can include using inhibitors siRNA to investigate the role of KLK10, GBP3 and CD74. To investigate if these genes have effects on atherosclerosis development, siRNA and inhibitors will be used to silence KLK10, GBP3 and CD74. Furthermore, to assess if these genes have an impact on endothelial apoptosis, proliferation and inflammation, assays including cleaved caspase-3 staining (apoptosis), PCNA staining (proliferation), and assessment of inflammatory genes (inflammation) will be performed.

6.5.3 Functional analysis of KLK10, GBP3 and CD74 in vivo

Following the investigation of KLK10, GBP3 and CD74 *in vitro*, their pathways will be identified through genetic deletion in mice. Atherosclerotic plaque formation will be assessed using oil red O staining after 6-10 weeks. Furthermore, human coronary arteries with atherosclerotic plaques can be used to test GBP3 and CD74 expression to assess their relevance to human atherosclerosis.

6.5.4 3D imaging analysis of KLK10, GBP3 and CD74

The technique optical clearing combined with immunofluorescent light-sheet imaging will be used to assess the expression of KLK10, GBP3 and CD74 in aortic arches from WT mice, *ApoE*$^{-/-}$ ND mice and *ApoE*$^{-/-}$ HFD mice. This method will enable the

visualization of protein expression in both proximal and distal regions of the plaque, indicating the potential roles of KLK10, GBP3 and CD74 in atherosclerosis development.

References

Abbate, A., Toldo, S., Marchetti, C., Kron, J., Tassell, B. W. Van, & Dinarello, C. A. (2020). *Interleukin-1 and the Inflammasome as Therapeutic Targets in Cardiovascular Disease*. 1260–1280. https://doi.org/10.1161/CIRCRESAHA.120.315937

Ahn, J., Berndt, S. I., Wacholder, S., Kraft, P., Kibel, A. S., Yeager, M., Albanes, D., Giovannucci, E., Stampfer, M. J., Virtamo, J., Thun, M. J., Feigelson, H. S., Cancel-Tassin, G., Cussenot, O., Thomas, G., Hunter, D. J., Fraumeni, J. F., Hoover, R. N., Chanock, S. J., & Hayes, R. B. (2008). Variation in KLK genes, prostate-specific antigen and risk of prostate cancer. In *Nature Genetics* (Vol. 40, Issue 9, pp. 1032–1034). https://doi.org/10.1038/ng0908-1032

Al-Soudi, A., Kaaij, M. H., & Tas, S. W. (2017). Endothelial cells: From innocent bystanders to active participants in immune responses. *Autoimmunity Reviews*, *16*(9), 951–962. https://doi.org/10.1016/j.autrev.2017.07.008

Andueza, A., Kumar, S., Kim, J., Kang, D. W., Mumme, H. L., Perez, J. I., Villa-Roel, N., & Jo, H. (2020). Endothelial Reprogramming by Disturbed Flow Revealed by Single-Cell RNA and Chromatin Accessibility Study. *Cell Reports*, *33*(11), 108491. https://doi.org/10.1016/j.celrep.2020.108491

Back, L. H. (1975). Theoretical investigation of mass transport to arterial walls in various blood flow regions- II. oxygen transport and its relationship to lipoprotein accumulation. *Mathematical Biosciences*, *27*(3–4), 263–285. https://doi.org/10.1016/0025-5564(75)90106-6

Baeyens, N., Nicoli, S., Coon, B. G., Ross, T. D., Van Den Dries, K., Han, J., Lauridsen, H. M., Mejean, C. O., Eichmann, A., Thomas, J. L., Humphrey, J. D., & Schwartz, M. A. (2015). Vascular remodeling is governed by a vegfr3-dependent fluid shear stress set point. *ELife*, *2015*(4), 1–35. https://doi.org/10.7554/eLife.04645

Baldrighi, M., Mallat, Z., & Li, X. (2017). NLRP3 inflammasome pathways in atherosclerosis. *Atherosclerosis*, *267*, 127–138. https://doi.org/10.1016/j.atherosclerosis.2017.10.027

Battle, T. E., Lynch, R. A., & Frank, D. A. (2006). Signal transducer and activator of transcription 1 activation in endothelial cells is a negative regulator of angiogenesis. *Cancer Research*, *66*(7), 3649–3657. https://doi.org/10.1158/0008-5472.CAN-05-3612

Benjamin, E. J., Virani, S. S., Callaway, C. W., Chamberlain, A. M., Chang, A. R., Cheng, S., Chiuve, S. E., Cushman, M., Delling, F. N., Deo, R., De Ferranti, S. D., Ferguson, J. F.,

Fornage, M., Gillespie, C., Isasi, C. R., Jiménez, M. C., Jordan, L. C., Judd, S. E., Lackland, D., … Muntner, P. (2018). Heart disease and stroke statistics - 2018 update: A report from the American Heart Association. In *Circulation* (Vol. 137, Issue 12). https://doi.org/10.1161/CIR.0000000000000558

Boshuizen, M. C. S., & De Winther, M. P. J. (2015). Interferons as essential modulators of atherosclerosis. *Arteriosclerosis, Thrombosis, and Vascular Biology*, *35*(7), 1579–1588. https://doi.org/10.1161/ATVBAHA.115.305464

Brauner, S., Jiang, X., Thorlacius, G. E., Lundberg, A. M., Östberg, T., Yan, Z. Q., Kuchroo, V. K., Hansson, G. K., & Wahren-Herlenius, M. (2018). Augmented Th17 differentiation in Trim21 deficiency promotes a stable phenotype of atherosclerotic plaques with high collagen content. *Cardiovascular Research*, *114*(1), 158–167. https://doi.org/10.1093/cvr/cvx181

Brown, A. J., Teng, Z., Evans, P. C., Gillard, J. H., Samady, H., & Bennett, M. R. (2016). Role of biomechanical forces in the natural history of coronary atherosclerosis. *Nature Reviews Cardiology*, *13*(4), 210–220. https://doi.org/10.1038/nrcardio.2015.203

Cai, W.-J., Kocsis, E., Luo, X., Schaper, W., & Schaper, J. (2004). Expression of endothelial nitric oxide synthase in the vascular wall during arteriogenesis. In *Molecular and Cellular Biochemistry* (Vol. 264). Kluwer Academic Publishers.

Chamberlain, J., Francis, S., Brookes, Z., Shaw, G., Graham, D., Alp, N. J., Dower, S., & Crossman, D. C. (2009). Interleukin-1 regulates multiple atherogenic mechanisms in response to fat feeding. *PLoS ONE*, *4*(4), 1–24. https://doi.org/10.1371/journal.pone.0005073

Chen, P. Y., Qin, L., Li, G., Wang, Z., Dahlman, J. E., Malagon-Lopez, J., Gujja, S., Cilfone, N. A., Kauffman, K. J., Sun, L., Sun, H., Zhang, X., Aryal, B., Canfran-Duque, A., Liu, R., Kusters, P., Sehgal, A., Jiao, Y., Anderson, D. G., … Simons, M. (2019). Endothelial TGF-β signalling drives vascular inflammation and atherosclerosis. *Nature Metabolism*, *1*(9), 912–926. https://doi.org/10.1038/s42255-019-0102-3

Chen, P. Y., Schwartz, M. A., & Simons, M. (2020). Endothelial-to-Mesenchymal Transition, Vascular Inflammation, and Atherosclerosis. *Frontiers in Cardiovascular Medicine*, *7*(May), 1–6. https://doi.org/10.3389/fcvm.2020.00053

Cheng, C., Tempel, D., Van Haperen, R., Van Der Baan, A., Grosveld, F., Daemen, M. J. A. P., Krams, R., & De Crom, R. (2006). Atherosclerotic lesion size and vulnerability are determined by patterns of fluid shear stress. *Circulation*, *113*(23), 2744–2753.

https://doi.org/10.1161/CIRCULATIONAHA.105.590018

Cheng, C., Van Haperen, R., De Waard, M., Van Damme, L. C. A., Tempel, D., Hanemaaijer, L., Van Cappellen, G. W. A., Bos, J., Slager, C. J., Duncker, D. J., Van Der Steen, A. F. W., De Crom, R., & Krams, R. (2005). Shear stress affects the intracellular distribution of eNOS: Direct demonstration by a novel in vivo technique. *Blood*, *106*(12), 3691–3698. https://doi.org/10.1182/blood-2005-06-2326

Chikani, G., Zhu, W., & Smart, E. J. (2004). Lipids: Potential regulators of nitric oxide generation. *American Journal of Physiology - Endocrinology and Metabolism*, *287*(3 50-3), 386–389. https://doi.org/10.1152/ajpendo.00106.2004

Chistiakov, D. A., Orekhov, A. N., & Bobryshev, Y. V. (2017). Effects of shear stress on endothelial cells: go with the flow. *Acta Physiologica*, *219*(2), 382–408. https://doi.org/10.1111/apha.12725

Chung, K., Wallace, J., Kim, S. Y., Kalyanasundaram, S., Andalman, A. S., Davidson, T. J., Mirzabekov, J. J., Zalocusky, K. A., Mattis, J., Denisin, A. K., Pak, S., Bernstein, H., Ramakrishnan, C., Grosenick, L., Gradinaru, V., & Deisseroth, K. (2013). Structural and molecular interrogation of intact biological systems. *Nature*, *497*(7449), 332–337. https://doi.org/10.1038/nature12107

Civelek, M., Manduchi, E., Riley, R. J., Stoeckert, C. J., & Davies, P. F. (2009). Chronic endoplasmic reticulum stress activates unfolded protein response in arterial endothelium in regions of susceptibility to atherosclerosis. *Circulation Research*, *105*(5), 453–461. https://doi.org/10.1161/CIRCRESAHA.109.203711

Davis, M. E., Cai, H., Drummond, G. R., & Harrison, D. G. (2001). Shear stress regulates endothelial nitric oxide synthase expression through c-Src by divergent signaling pathways. *Circulation Research*, *89*(11), 1073–1080. https://doi.org/10.1161/hh2301.100806

Davis, M. E., Grumbach, I. M., Fukai, T., Cutchins, A., & Harrison, D. G. (2004). Shear Stress Regulates Endothelial Nitric-oxide Synthase Promoter Activity through Nuclear Factor κB Binding. *Journal of Biological Chemistry*, *279*(1), 163–168. https://doi.org/10.1074/jbc.M307528200

Deng, Y., Zhang, X., Shen, H., He, Q., Wu, Z., Liao, W., & Yuan, M. (2020). Application of the Nano-Drug Delivery System in Treatment of Cardiovascular Diseases. *Frontiers in Bioengineering and Biotechnology*, *7*(January), 1–18. https://doi.org/10.3389/fbioe.2019.00489

Depaola, N., Davies, P. F., Pritchard, W. F., Florez, L., Harbeck, N., & Polacek, D. C. (1999).

Spatial and temporal regulation of gap junction connexin43 in vascular endothelial cells exposed to controlled disturbed flows in vitro. In *Medical Sciences* (Vol. 96). www.pnas.org.

Dimmeler, S. (1999). Activation of nitric oxide synthase in endothelial cells by Akt-dependent phosphorylation. *Nature*, *399*(6736), 601–605.

Ding, Y., Ma, J., Langenbacher, A. D., Baek, K. I., Lee, J., Chang, C. C., Hsu, J. J., Kulkarni, R. P., Belperio, J., Shi, W., Ranjbarvaziri, S., Ardehali, R., Tintut, Y., Demer, L. L., Chen, J. N., Fei, P., Packard, R. R. S., & Hsiai, T. K. (2018). Multiscale light-sheet for rapid imaging of cardiopulmonary system. *JCI Insight*, *3*(16). https://doi.org/10.1172/jci.insight.121396

Donat, S., Lourenço, M., Paolini, A., Otten, C., Renz, M., & Abdelilah-Seyfried, S. (2018). Heg1 and Ccm1/2 proteins control endocardial mechanosensitivity during zebrafish valvulogenesis. *ELife*, *7*, 1–22. https://doi.org/10.7554/eLife.28939

Dunn, J., Thabet, S., & Jo, H. (2015). Flow-dependent epigenetic DNA methylation in endothelial gene expression and atherosclerosis. *Arteriosclerosis, Thrombosis, and Vascular Biology*, *35*(7), 1562–1569. https://doi.org/10.1161/ATVBAHA.115.305042

Ebong, E. E., & Depaola, N. (2013). Specificity in the participation of connexin proteins in flow-induced endothelial gap junction communication. *Pflugers Archiv European Journal of Physiology*, *465*(9), 1293–1302. https://doi.org/10.1007/s00424-013-1245-9

Eren, E., Yates, J., Cwynarski, K., Preston, S., Dong, R., Germain, C., Lechler, R., Huby, R., Ritter, M., & Lombardi, G. (2006). Location of major histocompatibility complex class II molecules in rafts on dendritic cells enhances the efficiency of T-cell activation and proliferation. *Scandinavian Journal of Immunology*, *63*(1), 7–16. https://doi.org/10.1111/j.1365-3083.2006.01700.x

Evans, P. C., Fragiadaki, M., & Morris, P. D. (2021). Shear stress: the dark energy of atherosclerotic plaques. *Cardiovascular Research*, *117*(8), 1811–1813. https://doi.org/10.1093/cvr/cvaa315

Farr, L., Ghosh, S., & Moonah, S. (2020). Role of MIF Cytokine/CD74 Receptor Pathway in Protecting Against Injury and Promoting Repair. *Frontiers in Immunology*, *11*(June), 1–9. https://doi.org/10.3389/fimmu.2020.01273

Förstermann, U., & Li, H. (2011). Therapeutic effect of enhancing endothelial nitric oxide synthase (eNOS) expression and preventing eNOS uncoupling. *British Journal of Pharmacology*, *164*(2), 213–223. https://doi.org/10.1111/j.1476-5381.2010.01196.x

Fukumoto, Y., Hiro, T., Fujii, T., Hashimoto, G., Fujimura, T., Yamada, J., Okamura, T., &

Matsuzaki, M. (2008). Localized Elevation of Shear Stress Is Related to Coronary Plaque Rupture. A 3-Dimensional Intravascular Ultrasound Study With In-Vivo Color Mapping of Shear Stress Distribution. *Journal of the American College of Cardiology*, *51*(6), 645–650. https://doi.org/10.1016/j.jacc.2007.10.030

Gomes, R., Silva, A. L. N., Id, D. M. C., Tu, M., Id, P. B., Zamboni, D. S., & Id, S. C. O. (2018). Guanylate-binding protein 5 licenses caspase- 11 for Gasdermin-D mediated host resistance to Brucella abortus infection. *PLoS Pathogens*, 1–29.

Goo, Y. H., Son, S. H., Yechoor, V. K., & Paul, A. (2016). Transcriptional profiling of foam cells reveals induction of guanylate-binding proteins following western diet acceleration of atherosclerosis in the absence of global changes in inflammation. *Journal of the American Heart Association*, *5*(4). https://doi.org/10.1161/JAHA.115.002663

Hansson, G. K., Libby, P., Schönbeck, U., & Yan, Z. Q. (2002). Innate and adaptive immunity in the pathogenesis of atherosclerosis. *Circulation Research*, *91*(4), 281–291. https://doi.org/10.1161/01.RES.0000029784.15893.10

Heo, K. S., Fujiwara, K., & Abe, J. I. (2011). Disturbed-flow-mediated vascular reactive oxygen species induce endothelial dysfunction. In *Circulation Journal* (Vol. 75, Issue 12, pp. 2722–2730). https://doi.org/10.1253/circj.CJ-11-1124

Hoogendoorn, A., Kok, A. M., Hartman, E. M. J., de Nisco, G., Casadonte, L., Chiastra, C., Coenen, A., Korteland, S. A., Van der Heiden, K., Gijsen, F. J. H., Duncker, D. J., van der Steen, A. F. W., & Wentzel, J. J. (2020). Multidirectional wall shear stress promotes advanced coronary plaque development: comparing five shear stress metrics. *Cardiovascular Research*, *116*(6), 1136–1146. https://doi.org/10.1093/cvr/cvz212

Hu, Y., Dietrich, H., Metzler, B., Wick, G., & Xu, Q. (2000). *Lesions of Cholesterol-Fed Rabbits*. 18–26.

Iwai, N., Yasui, N., Naraba, H., Tago, N., Yamawaki, H., & Sumiya, H. (2005). Klk1 as one of the genes contributing to hypertension in Dahl salt-sensitive rat. *Hypertension*, *45*(5), 947–953. https://doi.org/10.1161/01.HYP.0000161969.65767.0d

Jain, M. K. (2018). *Krüppel-Like Factors in vascular inflammation : Mechanistic insights and Therapeutic Potential*. *5*(February), 1–17. https://doi.org/10.3389/fcvm.2018.00006

Kalluri, Aditya S., Vellarikkal, S. K., Edelman, E. R., Nguyen, L., Subramanian, A., Ellinor, P. T., Regev, A., Kathiresan, S., & Gupta, R. M. (2019). Single-Cell Analysis of the Normal Mouse Aorta Reveals Functionally Distinct Endothelial Cell Populations. *Circulation*, *140*(2), 147–163. https://doi.org/10.1161/CIRCULATIONAHA.118.038362

Kalluri, Aditya Sreemadhav. (2019). *Defining endothelial cell functional heterogeneity and plasticity using single-cell RNA-sequencing*.

Kasikara, C., Cai, B., Tabas, I., Kasikara, C., Doran, A. C., Cai, B., & Tabas, I. (2018). The role of non-resolving inflammation in atherosclerosis Find the latest version : The role of non-resolving inflammation in atherosclerosis. *The Journal of Clinical Investigation*, *128*(7), 2713–2723.

Khan, I. M., Pokharel, Y., Dadu, R. T., Lewis, D. E., Hoogeveen, R. C., Wu, H., & Ballantyne, C. M. (2016). Postprandial monocyte activation in individuals with metabolic syndrome. *Journal of Clinical Endocrinology and Metabolism*, *101*(11), 4195–4204. https://doi.org/10.1210/jc.2016-2732

Kim, C. W., Song, H., Kumar, S., Nam, D., Kwon, H. S., Chang, K. H., Son, D. J., Kang, D. W., Brodie, S. A., Weiss, D., Vega, J. D., Alberts-Grill, N., Griendling, K., Taylor, W. R., & Jo, H. (2013). Anti-inflammatory and antiatherogenic role of bmp receptor ii in endothelial cells. *Arteriosclerosis, Thrombosis, and Vascular Biology*, *33*(6), 1350–1359. https://doi.org/10.1161/ATVBAHA.112.300287

Kioulafa, M., Kaklamanis, L., Stathopoulos, E., Mavroudis, D., Georgoulias, V., & Lianidou, E. S. (2009). Kallikrein 10 (KLK10) methylation as a novel prognostic biomarker in early breast cancer. *Annals of Oncology*, *20*(6), 1020–1025. https://doi.org/10.1093/annonc/mdn733

Kirkby, N. S., Low, L., Wu, J., Miller, E., Seckl, J. R., Walker, B. R., Webb, D. J., & Hadoke, P. W. F. (2015). Generation and 3-dimensional quantitation of arterial lesions in mice using optical projection tomography. *Journal of Visualized Experiments*, *2015*(99), 1–10. https://doi.org/10.3791/50627

Koskinas, K. C., Feldman, C. L., Chatzizisis, Y. S., Coskun, A. U., Jonas, M., Maynard, C., Baker, A. B., Papafaklis, M. I., Edelman, E. R., & Stone, P. H. (2010). Natural history of experimental coronary atherosclerosis and vascular remodeling in relation to endothelial shear stress: A serial, in vivo intravascular ultrasound study. *Circulation*, *121*(19), 2092–2101. https://doi.org/10.1161/CIRCULATIONAHA.109.901678

Kreuk, B. De, Gingras, A. R., Knight, J., Liu, J. J., Gingras, A., & Ginsberg, M. H. (2016). *Heart of glass anchors Rasip1 at endothelial cell-cell junctions to support vascular integrity*. 1–23. https://doi.org/10.7554/eLife.11394

Kwak, B. R., Bäck, M., Bochaton-Piallat, M. L., Caligiuri, G., Daemen, M. J. A. P., Davies, P. F., Hoefer, I. E., Holvoet, P., Jo, H., Krams, R., Lehoux, S., Monaco, C., Steffens, S.,

Virmani, R., Weber, C., Wentzel, J. J., & Evans, P. C. (2014). Biomechanical factors in atherosclerosis: Mechanisms and clinical implications. *European Heart Journal*, *35*(43), 3013–3020. https://doi.org/10.1093/eurheartj/ehu353

Lalitha Nayak, Zhiyong Lin, and M. K. J. (2011). Go With the Flow- How klf2 Regulates the Vasoprotective Effects of Shear Stress.pdf. *Antioxid Redox Signal*, *15*(5), 1449–1461.

Lemaire-Ewing, S., Lagrost, L., & Néel, D. (2012). Lipid rafts: A signalling platform linking lipoprotein metabolism to atherogenesis. *Atherosclerosis*, *221*(2), 303–310. https://doi.org/10.1016/j.atherosclerosis.2011.10.016

Li, L., Xu, N., Fan, N., Meng, Q., Luo, W., Lv, L., Ma, W., Liu, X., Liu, L., Xu, F., Wang, H., Mao, W., & Li, Y. (2015). Upregulated KLK10 inhibits esophageal cancer proliferation and enhances cisplatin sensitivity in vitro. *Oncology Reports*, *34*(5), 2325–2332. https://doi.org/10.3892/or.2015.4211

Li, S., Butler, P., Wang, Y., Hu, Y., Han, D. C., Usami, S., Guan, J. L., & Chien, S. (2002). The role of the dynamics of focal adhesion kinase in the mechanotaxis of endothelial cells. *Proceedings of the National Academy of Sciences of the United States of America*, *99*(6), 3546–3551. https://doi.org/10.1073/pnas.052018099

Lilja, H., Ulmert, D., & Vickers, A. J. (2008). *Prostate-specific antigen and prostate cancer : prediction , detection and monitoring*. *8*(March). https://doi.org/10.1038/nrc2351

Linton, M. F., Hasty, A. H., Babaev, V. R., & Fazio, S. (1998). Hepatic apo E expression is required for remnant lipoprotein clearance in the absence of the low density lipoprotein receptor. *Journal of Clinical Investigation*, *101*(8), 1726–1736. https://doi.org/10.1172/JCI2181

Liu, B. C., Sarhan, J., Panda, A., Muendlein, H. I., Ilyukha, V., Coers, J., Yamamoto, M., Isberg, R. R., & Poltorak, A. (2018). Constitutive Interferon Maintains GBP Expression Required for Release of Bacterial Components Upstream of Pyroptosis and Anti-DNA Responses. *Cell Reports*, *24*(1), 155-168.e5. https://doi.org/10.1016/j.celrep.2018.06.012

Lo Sasso, G., Schlage, W. K., Boué, S., Veljkovic, E., Peitsch, M. C., & Hoeng, J. (2016). The Apoe-/- mouse model: A suitable model to study cardiovascular and respiratory diseases in the context of cigarette smoke exposure and harm reduction. *Journal of Translational Medicine*, *14*(1), 1–16. https://doi.org/10.1186/s12967-016-0901-1

Long, L. X. (1996). Identification of a Novel Serine Protease-like Gene-the Expression of Which Is Down-Regulated during Breast Cancer Progression. *Cancer Research*, *56*(14), 3371–3379.

Lu, J., Goldstein, K. M., Chen, R., Huang, S., Gelbert, L. M., & Nagpal, S. (2005). Transcriptional profiling of keratinocytes reveals a vitamin D-regulated epidermal differentiation network. *Journal of Investigative Dermatology*, *124*(4), 778–785. https://doi.org/10.1111/j.0022-202X.2005.23641.x

Lu, X. B., Wang, Z. X., Liu, S. B., Zhang, X. Y., Lu, L. F., Li, S., Chen, D. D., Nie, P., & Zhang, Y. A. (2019). Interferon regulatory factors 1 and 2 play different roles in MHC II expression mediated by CIITA in grass carp, ctenopharyngodon idella. *Frontiers in Immunology*, *10*(MAY), 1–12. https://doi.org/10.3389/fimmu.2019.01106

Luo, L., Herbrick, J. A., Scherer, S. W., Beatty, B., Squire, J., & Diamandis, E. P. (1998). Structural characterization and mapping of the normal epithelial cell-specific 1 gene. *Biochemical and Biophysical Research Communications*, *247*(3), 580–586. https://doi.org/10.1006/bbrc.1998.8793

Luong, L., Duckles, H., Schenkel, T., Mahmoud, M. M., Tremoleda, J. L., Wylezinska-Arridge, M., Ali, M., Bowden, N. P., Villa-Uriol, M. C., Van Der Heiden, K., Xing, R., Gijsen, F. J., Wentzel, J. J., Lawrie, A., Feng, S., Arnold, N., Gsell, W., Lungu, A., Hose, R., … Evans, P. C. (2016). Heart rate reduction with ivabradine promotes shear stress-dependent anti-inflammatory mechanisms in arteries. *Thrombosis and Haemostasis*, *116*(1), 181–190. https://doi.org/10.1160/TH16-03-0214

Ma, S., Yang, D., Li, D., Tang, B., & Yang, Y. (2011). Oleic acid induces smooth muscle foam cell formation and enhances atherosclerotic lesion development via CD36. *Lipids in Health and Disease*, *10*, 1–9. https://doi.org/10.1186/1476-511X-10-53

Madhavan, S., & Kemmerling, E. M. C. (2018). The effect of inlet and outlet boundary conditions in image-based CFD modeling of aortic flow. *BioMedical Engineering Online*, *17*(1), 1–20. https://doi.org/10.1186/s12938-018-0497-1

Mallat, Z., & Binder, C. J. (2022). The why and how of adaptive immune responses in ischemic cardiovascular disease. *Nature Cardiovascular Research*, *1*(5), 431–444. https://doi.org/10.1038/s44161-022-00049-1

Man, S. M., Karki, R., & Kanneganti, T. D. (2017). Molecular mechanisms and functions of pyroptosis, inflammatory caspases and inflammasomes in infectious diseases. In *Immunological Reviews* (Vol. 277, Issue 1, pp. 61–75). https://doi.org/10.1111/imr.12534

Marquis, J. F., Kapoustina, O., Langlais, D., Ruddy, R., Dufour, C. R., Kim, B. H., MacMicking, J. D., Giguère, V., & Gros, P. (2011). Interferon regulatory factor 8 regulates pathways for Antigen presentation in myeloid cells and during tuberculosis. *PLoS Genetics*, *7*(6).

https://doi.org/10.1371/journal.pgen.1002097

Meyts, E. R., & Jung, K. (2001). *normal and malignant testicular tissue*. *85*, 220–224.

Miteva, K., Madonna, R., De Caterina, R., & Van Linthout, S. (2018). Innate and adaptive immunity in atherosclerosis. *Vascular Pharmacology*, *107*(February), 67–77. https://doi.org/10.1016/j.vph.2018.04.006

Mohmmad-Rezaei, M., Arefnezhad, R., Ahmadi, R., Abdollahpour-Alitappeh, M., Mirzaei, Y., Arjmand, M. H., Ferns, G. A., Bashash, D., & Bagheri, N. (2021). An overview of the innate and adaptive immune system in atherosclerosis. *IUBMB Life*, *73*(1), 64–91. https://doi.org/10.1002/iub.2425

Mundi, S., Massaro, M., Scoditti, E., Carluccio, M. A., Van Hinsbergh, V. W. M., Iruela-Arispe, M. L., & De Caterina, R. (2018). Endothelial permeability, LDL deposition, and cardiovascular risk factors-A review. *Cardiovascular Research*, *114*(1), 35–52. https://doi.org/10.1093/cvr/cvx226

Nakashima, Y., Plump, A. S., Raines, E. W., Breslow, J. L., & Ross, R. (1994). ApoE-deficient mice develop lesions of all phases of atherosclerosis throughout the arterial tree. *ATVB*, *14*(1), 133–140.

Niu, N., Xu, S., Xu, Y., Little, P. J., & Jin, Z. G. (2019). Targeting Mechanosensitive Transcription Factors in Atherosclerosis. *Trends in Pharmacological Sciences*, *40*(4), 253–266. https://doi.org/10.1016/j.tips.2019.02.004

Noonan, J. and A. B. and K. P. (2020). The tandem stenosis mouse model_ Towards understanding, imaging, and preventing atherosclerotic plaque instability and rupture.pdf. *British Journal of Pharmacology*, *179*(18).

Nordlohne, J., Helmke, A., Ge, S., Rong, S., Chen, R., Waisman, A., Haller, H., & von Vietinghoff, S. (2018). Aggravated Atherosclerosis and Vascular Inflammation With Reduced Kidney Function Depend on Interleukin-17 Receptor A and Are Normalized by Inhibition of Interleukin-17A. *JACC: Basic to Translational Science*, *3*(1), 54–66. https://doi.org/10.1016/j.jacbts.2017.08.005

Pammer, J., Reinisch, C., Birner, P., Pogoda, K., Sturzl, M., & Tschachler, E. (2006). Interferon-α prevents apoptosis of endothelial cells after short-term exposure but induces replicative senescence after continuous stimulation. *Laboratory Investigation*, *86*(10), 997–1007. https://doi.org/10.1038/labinvest.3700461

Parmar, K. M., Jr, M. A. G., García-cardeña, G., Parmar, K. M., Larman, H. B., Dai, G., Zhang, Y., Wang, E. T., Moorthy, S. N., Kratz, J. R., Lin, Z., & Jain, M. K. (2006). *Integration of*

flow-dependent endothelial phenotypes by Kruppel-like factor 2. *116*(1), 49–58. https://doi.org/10.1172/JCI24787.development

Peiffer, V., Sherwin, S. J., & Weinberg, P. D. (2013). Does low and oscillatory wall shear stress correlate spatially with early atherosclerosis? A systematic review. *Cardiovascular Research*, *99*(2), 242–250. https://doi.org/10.1093/cvr/cvt044

Pirillo, A., Bonacina, F., Norata, G. D., & Catapano, A. L. (2018). The Interplay of Lipids, Lipoproteins, and Immunity in Atherosclerosis. *Current Atherosclerosis Reports*, *20*(3). https://doi.org/10.1007/s11883-018-0715-0

Rodella, L. F., Favero, G., Rossini, C., Foglio, E., Bonomini, F., Reiter, R. J., & Rezzani, R. (2013). Aging and vascular dysfunction: Beneficial melatonin effects. *Age*, *35*(1), 103–115. https://doi.org/10.1007/s11357-011-9336-z

Rodor, J., Chen, S.-H., Scanlon, J. P., Monteiro, J. P., Caudrillier, A., Sweta, S., Stewart, K. R., Shmakova, A., Dobie, R., Henderson, B. E. P., Stewart, K., Hadoke, P. W. F., Southwood, M., Moore, S. D., Upton, P. D., Morrell, N. W., Li, Z., Chan, S. Y., Handen, A., … Baker, A. H. (2021). Single-cell RNA-seq profiling of mouse endothelial cells in response to pulmonary arterial hypertension. *Cardiovascular Research*. https://doi.org/10.1093/cvr/cvab296

Roy, P., Orecchioni, M., & Ley, K. (2022). How the immune system shapes atherosclerosis: roles of innate and adaptive immunity. *Nature Reviews Immunology*, *22*(4), 251–265. https://doi.org/10.1038/s41577-021-00584-1

Samady, H., Eshtehardi, P., McDaniel, M. C., Suo, J., Dhawan, S. S., Maynard, C., Timmins, L. H., Quyyumi, A. A., & Giddens, D. P. (2011). Coronary artery wall shear stress is associated with progression and transformation of atherosclerotic plaque and arterial remodeling in patients with coronary artery disease. *Circulation*, *124*(7), 779–788. https://doi.org/10.1161/CIRCULATIONAHA.111.021824

Santos, J. C., Dick, M. S., Lagrange, B., Degrandi, D., Pfeffer, K., Yamamoto, M., Meunier, E., Pelczar, P., Henry, T., & Broz, P. (2018). LPS targets host guanylate-binding proteins to the bacterial outer membrane for non-canonical inflammasome activation . In *The EMBO Journal* (Vol. 37, Issue 6). https://doi.org/10.15252/embj.201798089

Schober, A., Nazari-Jahantigh, M., Wei, Y., Bidzhekov, K., Gremse, F., Grommes, J., Megens, R. T. A., Heyll, K., Noels, H., Hristov, M., Wang, S., Kiessling, F., Olson, E. N., & Weber, C. (2014). MicroRNA-126-5p promotes endothelial proliferation and limits atherosclerosis by suppressing Dlk1. *Nature Medicine*, *20*(4), 368–376. https://doi.org/10.1038/nm.3487

Serbanovic-Canic, J., De Luca, A., Warboys, C., Ferreira, P. F., Luong, L. A., Hsiao, S., Gauci, I., Mahmoud, M., Feng, S., Souilhol, C., Bowden, N., Ashton, J. P., Walczak, H., Firmin, D., Krams, R., Mason, J. C., Haskard, D. O., Sherwin, S., Ridger, V., … Evans, P. C. (2017). Zebrafish model for functional screening of flow-responsive genes. *Arteriosclerosis, Thrombosis, and Vascular Biology*, *37*(1), 130–143. https://doi.org/10.1161/ATVBAHA.116.308502

Sharma, D., & Kanneganti, T. D. (2016). The cell biology of inflammasomes: Mechanisms of inflammasome activation and regulation. *Journal of Cell Biology*, *213*(6), 617–629. https://doi.org/10.1083/jcb.201602089

Slagger, C. J., Wentzell, J. J., Gijsen, F. J. H., Thury, A., van der Waal, A. C., Schaar, J. A., & Serruys, P. W. (2005). The role of shear stress in the destabilization of vulnerable plaques and related therapeutic implications. *Nature Clinical Practice Cardiovascular Medicine*, *2*(9), 456–464. https://doi.org/10.1038/ncpcardio0298

Sorescu, G. P., Sykes, M., Weiss, D., Platt, M. O., Saha, A., Hwang, J., Boyd, N., Boo, Y. C., Vega, J. D., Taylor, W. R., & Jo, H. (2003). Bone morphogenic protein 4 produced in endothelial cells by oscillatory shear stress stimulates an inflammatory response. *Journal of Biological Chemistry*, *278*(33), 31128–31135. https://doi.org/10.1074/jbc.M300703200

Sotiropoulou, G., & Pampalakis, G. (2012). Targeting the kallikrein-related peptidases for drug development. *Trends in Pharmacological Sciences*, *33*(12), 623–634. https://doi.org/10.1016/j.tips.2012.09.005

Souilhol, C., Gauci, I., Feng, S., Ayllon, B. T., Mahmoud, M., Canham, L., Fragiadaki, M., Serbanovic-Canic, J., Ridger, V., & Evans, P. C. (2021). Homeobox B9 integrates bone morphogenic protein 4 with inflammation at atheroprone sites. *Cardiovascular Research*, *116*(7), 1300–1310. https://doi.org/10.1093/CVR/CVZ235

Souilhol, C., Gauci, I., Feng, S., Tardajos Ayllon, B., Mahmoud, M., Canham, L., Fragiadaki, M., Serbanovic-Canic, J., Ridger, V., & Evans, P. C. (2020). Homeobox B9 integrates bone morphogenic protein 4 with inflammation at atheroprone sites. *Cardiovascular Research*, *116*(7), 1300–1310. https://doi.org/10.1093/cvr/cvz235

Stone, P. H., Coskun, A. U., Kinlay, S., Clark, M. E., Sonka, M., Wahle, A., Ilegbusi, O. J., Yeghiazarians, Y., Popma, J. J., Orav, J., Kuntz, R. E., & Feldman, C. L. (2003). Effect of endothelial shear stress on the progression of coronary artery disease, vascular remodeling, and in-stent restenosis in humans: In vivo 6-month follow-up study. *Circulation*, *108*(4), 438–444. https://doi.org/10.1161/01.CIR.0000080882.35274.AD

Stone, P. H., Coskun, A. U., Kinlay, S., Popma, J. J., Sonka, M., Wahle, A., Yeghiazarians, Y., Maynard, C., Kuntz, R. E., & Feldman, C. L. (2007). Regions of low endothelial shear stress are the sites where coronary plaque progresses and vascular remodelling occurs in humans: An in vivo serial study. *European Heart Journal*, *28*(6), 705–710. https://doi.org/10.1093/eurheartj/ehl575

Stone, P. H., Maehara, A., Coskun, A. U., Maynard, C. C., Zaromytidou, M., Siasos, G., Andreou, I., Fotiadis, D., Stefanou, K., Papafaklis, M., Michalis, L., Lansky, A. J., Mintz, G. S., Serruys, P. W., Feldman, C. L., & Stone, G. W. (2018). *Role of Low Endothelial Shear Stress and Plaque Characteristics in the Prediction of Nonculprit Major Adverse Cardiac Events*. *11*(3). https://doi.org/10.1016/j.jcmg.2017.01.031

Stone, P. H., Saito, S., Takahashi, S., Makita, Y., Nakamura, S., Kawasaki, T., Takahashi, A., Katsuki, T., Nakamura, S., Namiki, A., Hirohata, A., Matsumura, T., Yamazaki, S., Yokoi, H., Tanaka, S., Otsuji, S., Yoshimachi, F., Honye, J., Harwood, D., … PREDICTION Investigators. (2012). Prediction of progression of coronary artery disease and clinical outcomes using vascular profiling of endothelial shear stress and arterial plaque characteristics: the PREDICTION Study. *Circulation*, *126*(2), 172–181. https://doi.org/10.1161/CIRCULATIONAHA.112.096438

Sun, P. H., Chen, G., Mason, M., Jiang, W. G., & Ye, L. (2017). Dual roles of protein tyrosine phosphatase kappa in coordinating angiogenesis induced by pro-angiogenic factors. *International Journal of Oncology*, *50*(4), 1127–1135. https://doi.org/10.3892/ijo.2017.3884

Suo, J., Ferrara, D. E., Sorescu, D., Guldberg, R. E., Taylor, W. R., & Giddens, D. P. (2007a). Hemodynamic shear stresses in mouse aortas: Implications for atherogenesis. *Arteriosclerosis, Thrombosis, and Vascular Biology*, *27*(2), 346–351. https://doi.org/10.1161/01.ATV.0000253492.45717.46

Suo, J., Ferrara, D. E., Sorescu, D., Guldberg, R. E., Taylor, W. R., & Giddens, D. P. (2007b). Hemodynamic shear stresses in mouse aortas: Implications for atherogenesis. *Arteriosclerosis, Thrombosis, and Vascular Biology*, *27*(2), 346–351. https://doi.org/10.1161/01.ATV.0000253492.45717.46

Susaki, E. A., Tainaka, K., Perrin, D., Yukinaga, H., Kuno, A., & Ueda, H. R. (2015). Advanced CUBIC protocols for whole-brain and whole-body clearing and imaging. *Nature Protocols*, *10*(11), 1709–1727. https://doi.org/10.1038/nprot.2015.085

Tabas, I., & Lichtman, A. H. (2017). Review Monocyte-Macrophages and T Cells in Atherosclerosis. *Immunity*, *47*(4), 621–634. https://doi.org/10.1016/j.immuni.2017.09.008

Taleb, S., Tedgui, A., & Mallat, Z. (2015). IL-17 and Th17 cells in atherosclerosis: Subtle and contextual roles. *Arteriosclerosis, Thrombosis, and Vascular Biology*, *35*(2), 258–264. https://doi.org/10.1161/ATVBAHA.114.303567

Tao, Y., Yang, Y., Zhou, R., & Gong, T. (2020). Golgi Apparatus: An Emerging Platform for Innate Immunity. *Trends in Cell Biology*, *30*(6), 467–477. https://doi.org/10.1016/j.tcb.2020.02.008

Tarbell, J. M. (2003). Mass Transport in Arteries and the Localization of Atherosclerosis. *Annual Review of Biomedical Engineering*, *5*(1), 79–118. https://doi.org/10.1146/annurev.bioeng.5.040202.121529

Theofilis, P., Sagris, M., Oikonomou, E., Antonopoulos, A. S., Siasos, G., Tsioufis, C., & Tousoulis, D. (2021). Inflammatory mechanisms contributing to endothelial dysfunction. *Biomedicines*, *9*(7), 1–21. https://doi.org/10.3390/biomedicines9070781

Thondapu, V., Mamon, C., Poon, E. K. W., Kurihara, O., Kim, H. O., Russo, M., Araki, M., Shinohara, H., Yamamoto, E., Dijkstra, J., Tacey, M., Lee, H., Ooi, A., Barlis, P., & Jang, I. K. (2021). High spatial endothelial shear stress gradient independently predicts site of acute coronary plaque rupture and erosion. *Cardiovascular Research*, *117*(8), 1974–1985. https://doi.org/10.1093/cvr/cvaa251

Timmins, L. H., Molony, D. S., Eshtehardi, P., McDaniel, M. C., Oshinski, J. N., Giddens, D. P., & Samady, H. (2017). Oscillatory wall shear stress is a dominant flow characteristic affecting lesion progression patterns and plaque vulnerability in patients with coronary artery disease. *Journal of the Royal Society Interface*, *14*(127). https://doi.org/10.1098/rsif.2016.0972

Topper, J. N., & Gimbrone, M. A. (1999). Blood flow and vascular gene expression: Fluid shear stress as a modulator of endothelial phenotype. *Molecular Medicine Today*, *5*(1), 40–46. https://doi.org/10.1016/S1357-4310(98)01372-0

Usuba, R., Pauty, J., Soncin, F., & Matsunaga, Y. T. (2019). EGFL7 regulates sprouting angiogenesis and endothelial integrity in a human blood vessel model. *Biomaterials*, *197*(December 2018), 305–316. https://doi.org/10.1016/j.biomaterials.2019.01.022

Varshney, P., Yadav, V., & Saini, N. (2016). Lipid rafts in immune signalling: current progress and future perspective. *Immunology*, *149*(1), 13–24. https://doi.org/10.1111/imm.12617

Wandel, M. P., Kim, B. H., Park, E. S., Boyle, K. B., Nayak, K., Lagrange, B., Herod, A., Henry, T., Zilbauer, M., Rohde, J., MacMicking, J. D., & Randow, F. (2020). Guanylate-binding proteins convert cytosolic bacteria into caspase-4 signaling platforms. *Nature Immunology*,

21(8), 880–891. https://doi.org/10.1038/s41590-020-0697-2

Wang, Y., Qiu, J., Luo, S., Xie, X., Zheng, Y., Zhang, K., Ye, Z., Liu, W., Gregersen, H., & Wang, G. (2016). High shear stress induces atherosclerotic vulnerable plaque formation through angiogenesis. *Regenerative Biomaterials*, *3*(4), 257–267. https://doi.org/10.1093/RB/RBW021

Warboys, C. M., De Luca, A., Amini, N., Luong, L., Duckles, H., Hsiao, S., White, A., Biswas, S., Khamis, R., Chong, C. K., Cheung, W. M., Sherwin, S. J., Bennett, M. R., Gil, J., Mason, J. C., Haskard, D. O., & Evans, P. C. (2014). Disturbed flow promotes endothelial senescence via a p53-dependent pathway. *Arteriosclerosis, Thrombosis, and Vascular Biology*, *34*(5), 985–995. https://doi.org/10.1161/ATVBAHA.114.303415

Warboys, C. M., Ghim, M., & Weinberg, P. D. (2019). Understanding mechanobiology in cultured endothelium: A review of the orbital shaker method. *Atherosclerosis*, *285*(March), 170–177. https://doi.org/10.1016/j.atherosclerosis.2019.04.210

Williams, D., Mahmoud, M., Liu, R., Andueza, A., Kumar, S., Kang, D. W., Zhang, J., Tamargo, I., Villa-Roel, N., Baek, K. I., Lee, H., An, Y., Zhang, L., Tate, E. W., Bagchi, P., Pohl, J., Mosnier, L. O., Diamandis, E. P., Mihara, K., … Jo, H. (2022). Stable Flow-Induced Expression of KLK10 Inhibits Endothelial Inflammation and Atherosclerosis. *ELife*, *11*, 1–23. https://doi.org/10.7554/eLife.72579

Wirtz, T. H., Saal, A., Bergmann, I., Fischer, P., Heinrichs, D., Brandt, E. F., Koenen, M. T., Djudjaj, S., Schneider, K. M., Boor, P., Bucala, R., Weiskirchen, R., Bernhagen, J., & Berres, C. T. M. (2021). *Macrophage migration inhibitory factor exerts pro-proliferative and anti-apoptotic effects via CD74 in murine hepatocellular carcinoma*. *November 2020*, 4452–4467. https://doi.org/10.1111/bph.15622

Xie, G., Myint, P. K., Voora, D., Laskowitz, D. T., Shi, P., Ren, F., Wang, H., Yang, Y., Huo, Y., Gao, W., & Wu, Y. (2015). Genome-wide association study on progression of carotid artery intima media thickness over 10 years in a Chinese cohort. *Atherosclerosis*, *243*(1), 30–37. https://doi.org/10.1016/j.atherosclerosis.2015.08.034

Xu, S., Kamato, D., Little, P. J., Nakagawa, S., Pelisek, J., & Jin, Z. G. (2019). Targeting epigenetics and non-coding RNAs in atherosclerosis: from mechanisms to therapeutics. *Pharmacology and Therapeutics*, *196*, 15–43. https://doi.org/10.1016/j.pharmthera.2018.11.003

Yang, B., & Rizzo, V. (2013). Shear stress activates eNOS at the endothelial apical surface through β1 containing integrins and caveolae. *Cellular and Molecular Bioengineering*, *6*(3),

346–354. https://doi.org/10.1007/s12195-013-0276-9

Yang, Y. M., Huang, A., Kaley, G., & Sun, D. (2009). eNOS uncoupling and endothelial dysfunction in aged vessels. *American Journal of Physiology - Heart and Circulatory Physiology*, *297*(5), 1829–1836. https://doi.org/10.1152/ajpheart.00230.2009

Yeh, C. F., Cheng, S. H., Lin, Y. S., Shentu, T. P., Huang, R. T., Zhu, J., Chen, Y. T., Kumar, S., Lin, M. S., Kao, H. L., Huang, P. H., Roselló-Sastre, E., Garcia, F., Jo, H., Fang, Y., & Yang, K. C. (2022). Targeting mechanosensitive endothelial TXNDC5 to stabilize eNOS and reduce atherosclerosis in vivo. *Science Advances*, *8*(3), 1–16. https://doi.org/10.1126/sciadv.abl8096

Yeung, M. W., Wang, S., Van De Vegte, Y. J., Borisov, O., Van Setten, J., Snieder, H., Verweij, N., Said, M. A., & Van Der Harst, P. (2022). Twenty-Five Novel Loci for Carotid Intima-Media Thickness: A Genome-Wide Association Study in >45 000 Individuals and Meta-Analysis of >100 000 Individuals. In *Arteriosclerosis, Thrombosis, and Vascular Biology* (Vol. 42, Issue 4, pp. 484–501). https://doi.org/10.1161/ATVBAHA.121.317007

Zălar, D.-M., Pop, C., Buzdugan, E., Todea, D., & Mogoșan, C. I. (2019). *THE ATHEROSCLEROSIS-INFLAMMATION RELATIONSHIP – A PATHOPHYSIOLOGICAL APPROACH*. *67*.

Zhang, S. H., Reddick, R. L., Piedrahita, J. A., & Maeda, N. (1992). Spontaneous hypercholesterolemia and arterial lesions in mice lacking apolipoprotein E. *Science*, *258*(5081), 468–471. https://doi.org/10.1126/science.1411543

Zhu, L., Wang, F., Yang, H., Zhang, J., & Chen, S. (2020). Low shear stress damages endothelial function through STAT1 in endothelial cells (ECs). *Journal of Physiology and Biochemistry*, *76*(1), 147–157. https://doi.org/10.1007/s13105-020-00729-1